The Experimental Investigation of a Free-Electron Maser Defined by a Co-axial 2D - 1D Bragg Lasing Cavity

Philip MacInnes

(M.Sci., University of Strathclyde, UK)

(M.Sc., University of Strathclyde, UK)

SUPA Department of Physics

University of Strathclyde

Thesis submitted for the Degree of Ph. D.

September 2009

I would like to dedicate this work to my parents.

Contents

Page

Acknowledgements

I would like to acknowledge my supervisors Dr. A. W. Cross, Dr. I. V. Konoplev and Prof. A. D. R. Phelps for their help and support throughout the course of this work and offer them my sincerest of thanks.

I would also like to acknowledge Dr. C. G. Whyte, Dr. W. He and Dr. K. Ronald for their help in the theoretical and experimental studies presented. My colleagues Dr. C. W. Robertson, Dr. D. Speirs, Mr D. Rowlands and Miss L. Fisher are all offered thanks for their contributions, both direct and indirect, throughout the course of this Ph. D. Thanks are also due to Mr. I. S. Dinwoodie and latterly Mr. D. Barclay for their advice and technical skill in the construction of various parts of the FEM experiment.

I would also like to thank my family and friends for their support through my university career as a whole.

Abstract

This thesis presents the results of the first FEM based on a 2D - 1D Bragg lasing cavity, formed by surface corrugations on the inner conductor of an over-sized co-axial drift-tube. Such over-sized interaction regions allow for the use of high current electron beams, whilst maintaining current densities at a sufficiently low level as to avoid instabilities from self-forces within the beam. In this manner the FEM falls within the High-Gain Compton regime, avoiding the more complex interactions of the Raman regime.

Beginning with an overview of FEL and Bragg reflector theory, the following work presents the theoretical design, numerical modelling and experimental investigation of a proof of principle 2D - 1D Bragg FEM, including the design of two electron beam sources, providing currents of $\sim 1.5kA$ $(350Acm^{-1})$ and $2-3kA$ $(700Acm^{-1})$ respectively. The spectral content of the output microwave pulses was investigated using both high-pass cut-off filters and a heterodyne mixing technique, with the results confirming the excitation and dominance of the fundamental TEM operating mode at a frequency of $\sim 37.5GHz$, in-line with the central resonant frequency of the Bragg reflectors. In addition, the existence of parasitic, competing, cavity resonances was postulated and confirmed experimentally, with suppression achieved through careful tuning of the undulator magnetic field strength. The first detailed analysis of the spectral evolution of microwave pulses from such a cavity is presented, showing preferential coupling to the desired operating mode with proper matching of the undulator field strength to the electron energies.

Best performance was observed using the $1.5kA$ electron beam source, with a guiding axial magnetic field of $0.56T$ and an undulator magnetic field of $0.063T$. The mean electron energy was $\sim 450keV$, resulting in $\gamma \approx 1.8$ and a resonant FEM frequency of $\sim 37.5GHz$. The output microwave pulses were $\sim 150ns$ in duration at an integrated output power of $60MW(\pm 10\%)$, corresponding to a conversion efficiency of 10%.

Nomenclature.

$A_{\pm}(\tau, z)$	Amplitude of the axially propagating partial waves
a	Radius of the inner conductor of a smooth co-axial waveguide
a_0	Mean radius of an inner conductor showing a corrugation
a_u	Undulator parameter
$\vec{B}$	Magnetic flux density; $\vec{B} = \mu\vec{H}$
B_0	Magnitude of the axial magnetic field
B_u	Magnitude of the undulator magnetic field
b	Radius of the outer conductor of a smooth co-axial waveguide
b_0	Mean radius of an outer conductor showing a corrugation
C	Capacitance
C_e	Stray capacitance
C_p	Parallel capacitance
C_s	Series capacitance
c	Speed of EM wave in free-space; $c = (\varepsilon_0\mu_0)^{-1/2} \cong 3 \times 10^8 ms^{-1}$
c_m	Specific heat capacity of shunt material
$\vec{D}$	Electric flux density; $\vec{D} = \varepsilon\vec{E}$
d_e	Axial electrode separation in a spark-gap

d_s	Azimuthal periodicity of a 2D corrugation
d_{sep}	Radial separation between the capacitive probe surface and the centre conductor surface of the folded transmission line.
d_z	Axial periodicity of a Bragg corrugation
$\grave{\vec{E}}$	Electric field strength
E_j	Electric field component in the j^{th} direction
e	Charge on the electron; $e = 1.602 \times 10^{-19} C$
F	Filling factor
$f_{c_{m,n}}$	Cut-off frequencies of the $TM_{m,n}$ modes in co-axial waveguide. $m = 0, 1, 2, \ldots, n = 1, 2, 3, \ldots$
$f_{c_{m,1}}'$	Cut-off frequencies of the $TE_{m,1}$ modes in co-axial waveguide. $m = 1, 2, 3, \ldots, n = 1$
$f_{c_{m,n}}'$	Cut-off frequencies of the $TE_{m,n}$ modes in co-axial waveguide. $m = 1, 2, 3, \ldots, n = 2, 3, 4, \ldots$
$f_{c_{m,n,p}}$	Cut-off frequencies of the $TM_{m,n}$ modes in co-axial cavities. $m = 0, 1, 2, \ldots, n = 1, 2, 3, \ldots, p = 0, 1, 2, \ldots$
$f_{c_{m,1,p}}'$	Cut-off frequencies of the $TE_{m,1}$ modes in co-axial cavities. $m = 1, 2, 3, \ldots, n = 1, p = 1, 2, 3, \ldots$
$f_{c_{m,n,p}}'$	Cut-off frequencies of the $TE_{m,n}$ modes in co-axial cavities. $m = 1, 2, 3, \ldots, n = 2, 3, 4, \ldots, p = 1, 2, 3, \ldots$
f_j	Weighting factor, dependant on polarisation of detector horn
f_{max}	Maximum frequency bandwidth of a DSO
G	Maximum spatial growth rate in a High-Gain Compton / Raman FEL
$G(z_{max})$	Maximum gain of a Low-Gain Compton FEL

$\vec{H}$	Magnetic field strength
H_j	H field component in the j^{th} direction
$\vec{h}_{\pm L,\, R}$	Bragg vectors of a 2D corrugation
h_r	Radial wave-number of corrugation
h_s	Azimuthal wave-number of corrugation
h_τ	Combined transverse wave-number of corrugation; $h_\tau = \sqrt{h_s^2 + h_r^2}$
h_z	Axial wave-number of corrugation
I	Electron beam current
I_0	Alfen current
$I_1(x)$	First order modified Bessel function of the first kind
I_{SCL}	Space charge limited current
$I'_{n_{a,\,b}}$	Current amplitudes of the H field components of the $TM_{m,n}$ modes
$I''_{n_{a,\,b}}$	Current amplitudes of the H field components of the $TE_{m,n}$ modes
J	Beam current density
$J_m(x)$	m^{th} order Bessel function of the first kind
$J'_m(x)$	Spatial derivative of $J_m(x)$
k	EM wave-number; $k = \sqrt{k_z^2 + k_c^2}$
k_c	Cut-off wave-number
$k_{c\pm}$	Transverse wave-numbers of the incident and scattered waves

k'_s	Azimuthal wave-number of the 2D reflector eigenmode
k_u	Undulator wave-number
k_z	Axial EM wave-number
$k_{z\pm}$	Axial wave-numbers of the incident and scattered waves
k'_z	Axial wave-number of the Bragg reflector eigenmode
L	Circuit inductance
L_s	Self inductance
l	Length
l_{1D}	Length of 1D Bragg reflector
l_{2D}	Length of 2D Bragg reflector
l_{det}	Separation of the output and detector horns
l_z	Length of lasing cavity (separation distance of reflectors)
M	Azimuthal index of a Bragg structure
m	Azimuthal index of a waveguide / cavity mode
m'	Azimuthal index of the 2D Bragg reflector eigenmode
m_e	Rest mass of the electron; $m_e = 9.11 \times 10^{-31} kg$
n	Radial index of a waveguide / cavity mode
n_0	Ambient electron beam density
n_t	Number of turns in a coil
P	Perveance of a diode
P_0	Measured power

P_{tot}	Total integrated output microwave power
p	Axial index of a cavity mode
pd_e	Gas pressure (kPa) x axial electrode gap in a spark-gap
$\|R\|$	Magnitude of the reflection co-efficient
$\langle r \rangle$	Mean coil radius of an inductor
r_0	Mean radius of the conductor showing the corrugation
r_1	Amplitude of the corrugation
r_a	Radius of bounding anode can
r_{cyc}	Radius of cyclotron oscillations
r_e	Mean radius of electron beam
r_i	Inner conductor radius of a co-axial transmission line
r_{larmor}	Larmor radius
r_o	Outer conductor radius of a co-axial transmission line
r_{outer}	Outer radius of the electron beam
S	Effective emission surface of cathode
S_0	Surface area of a horn
s	Quasi-cartesian co-ordinate; $s = \theta r_0$
$\|T\|$	Magnitude of the transmission co-efficient
t_1	Rise-time
t_{C_e}	Rise-time from stray capacitance
t_e	Rise-time from self capacitance

t_L	Rise-time from self inductance
t_{min}	Minimum time step of a DSO
t_{trans}	Duration of transmission line pulse
V	Diode potential
V_0	Charging voltage on Marx-bank capacitors
V_b	Townsend breakdown voltage of a spark-gap
$V'_{n_{a,b}}$	Voltage amplitudes of the E field components of the $TM_{m,n}$ modes
$V''_{n_{a,b}}$	Voltage amplitudes of the E field components of the $TE_{m,n}$ modes
v	Total electron velocity; $v = \sqrt{v_z^2 + v_\perp^2}$
v_{ph}	Phase velocity; $v_{ph} = (\varepsilon\mu)^{-1/2}$
v_u	Transverse velocity imparted to the beam electrons by the undulator field
v_z	Axial bulk streaming velocity of the electrons
$v_\perp$	Transverse velocity of the electrons
$Y_m(x)$	m^{th} order Neumann function
$Y'_m(x)$	Spatial derivative of $Y_m(x)$
Z_0	Characteristic impedance of a transmission line; $Z_0 \cong 17\Omega$
Z_d	Impedance of dump resistors on output spark-gap
Z_{fs}	Characteristic impedance of free space; $Z_{fs} \cong 377\Omega$
Z_L	Impedance of the load (electron gun-diode)
Z_{source}	Impedance of the source (Marx-bank)

Z_w	Wave impedance in co-axial waveguide
z_{max}	Position of maximum gain in a Low-Gain Compton FEL

Greek:

β	Normalised electron velocity; $\beta = \sqrt{\beta_z^2 + \beta_\perp^2} = \sqrt{v_z^2 + v_\perp^2/c^2}$
β_{crit}	Value of β_u at which one moves from High-Gain Compton to Raman regimes in a high-current FEL
β_u	Normalised transverse velocity imparted to electrons by the undulator magnetic field; $\beta_u = v_u/c$
β_z	Normalised electron bulk streaming velocity; $\beta_z = v_z/c$
β_{z0}	Normalised initial (unperturbed) bulk streaming velocity; $\beta_z = v_{z0}/c$
$\beta_\perp$	Normalised electron transverse velocity; $\beta_\perp = v_\perp/c$
Γ	Townsend breakdown criterion of a spark-gap
Γ_{horn}	Reflection due to impedance miss-match
γ	Lorentz relativistic mass factor; $\gamma = 1 + [eV/m_e c^2] = 1/(\sqrt{1-\beta^2})$
γ_z	Axial component of γ; $\gamma_z = 1/(\sqrt{1-\beta_z^2})$
γ_0	$\gamma_0 = \gamma_z\sqrt{\gamma}$
Δr	Radial spread of the electron beam
ΔT	Temperature change (in Kelvin) over pulse duration
$\Delta\psi$	Range of measurement angle (in radians)
δ_j	Detuning of k_j from h_j in the j^{th} direction; $\delta_j = k_j - h_j$

δ_{skin}	Skin depth of a material
ε	Permittivity of a dielectric; $\varepsilon = \varepsilon_0 \varepsilon_r$
ε_0	Permittivity of free-space; $\varepsilon_0 = 8.854 \times 10^{-12} Fm^{-1}$
ε_r	Relative permittivity of a given media
ε_m	Electric field parameter; $\varepsilon_m = 1$ if $m = 0$, else $\varepsilon_m = 2$
ζ_n	n^{th} root of the m^{th} order Bessel-Neumann function $J_m\left(\frac{b}{a}\zeta_n\right) Y_m(\zeta_n) - Y_m\left(\frac{b}{a}\zeta_n\right) J_m(\zeta_n) = 0$
ζ'_n	n^{th} root of the m^{th} order Bessel-Neumann function $J'_m\left(\frac{b}{a}\zeta'_n\right) Y'_m(\zeta'_n) - Y'_m\left(\frac{b}{a}\zeta'_n\right) J'_m(\zeta'_n) = 0$
θ_f	Pitch angle of the electron orbits
κ	Coupling co-efficient between the EM waves due to the presence of a Bragg reflector
Λ	Solutions of the eigenmodes in a Bragg reflector ($\Lambda = -ik'_z$)
λ	EM Wave-length
λ_u	Wave-length (period) of the undulator
μ	Permeability of a dielectric; $\mu = \mu_0 \mu_r$
μ_0	Permeability of free-space; $\mu_0 = 4\pi \times 10^{-7} Hm^{-1}$
μ_r	Relative permeability of a given media
σ	Conductivity of a resistive media ($i\sigma_j$ corresponds to losses in the j^{th} direction)
σ_b	Cross-sectional area of the electron beam

σ_r	Cross-sectional area of the radiation beam
τ	Combined transverse co-ordinate; $\tau(r, \theta)$
Φ_j	Scalar potential on the j^{th} conductor surface of a multi-conductor waveguide
ϕ	Phase difference between the transverse E field components in an EM mode
χ	Ratio of the corrugation amplitude to the mean radius; $\chi = r_1 / r_0$
ψ	Measurement angle of detector horn (in radians)
$\lvert\Omega\rvert$	Magnitude of the total system losses
ω	Angular frequency; $\omega = kc$
ω_b	Beam plasma frequency
ω_{cyc}	Relativistic cyclotron frequency
ω_{FEL}	Frequency of the FEL instability
ω_{low}	Frequency of the Lowbitron instability
ω_h	Highest frequency component of the measured signal

List of Figures

Chapter 1: Introduction.

1.1 Introduction.

This Chapter presents the original basis for the 2D - 1D Bragg Free Electron Maser (FEM) experiment, followed by a review of FEM research carried out at the University of Strathclyde (c.f. Section 1.3). The authors contribution to the experiment, in terms of the development of apparatus required, is presented in Section 1.4, along with a summary of the thesis content presenting the main sections of the following chapters.

1.2 Basis for Research.

The following work describes the first operation of a Free Electron Maser (FEM) with a lasing cavity defined by 2D and 1D Bragg reflectors. These were implemented in an over-sized co-axial drift-tube, allowing for high power ($\sim 60MW$) operation without the risk of breakdown, due to high electrical stresses, or the generation of spurious beam instabilities, due to overly high beam current densities.

The application basis for this work came from the initial design brief for the proposed Compact Linear Collider (CLIC), under development at the European Organisation for Nuclear Research (CERN), which required high power microwave sources, operating in the Ka-Band ($26.4 - 40GHz$) to test the power handling capabilities of the accelerating cavities and ancillary components. While it should be noted that following commencement of the project the operating frequency of CLIC was revised from $35GHz$ to $12GHz$, this in no way degrades the impact of the results presented, rather, given the scalability of the technology advanced a suitably redesigned 2D - 1D Bragg FEM operating at $12GHz$ could potentially offer GW-class operation.

1.3 Historical Review of Research.

Free Electron Maser (FEM) experiments, based around the use of Bragg reflector defined lasing cavities, began at the University of Strathclyde in the late 1990's following the establishment of a collaboration with the Institute of Applied Physics (IAP), in Nizhny Novgorod, Russia. By 1998 this resulted in the operation of the first FEM oscillator in the UK (Cross et al. 1998) which provided $\sim 0.5MW$ of output power at $32GHz$ with a conversion efficiency of $\sim 5\%$.

Collaborative work investigating the use of 2D Bragg structures began in 1999 (Ginzburg et al. 1999), with the theoretical basis for a 2D - 2D Bragg reflector based FEM presented in 2001 (Konoplev 2001). This was later experimentally verified, with the generation of nominally single frequency pulses at $\sim 37.5GHz$ and power level of $\sim 15MW$, corresponding to energy extraction efficiencies of $\sim 6\%$ (McGrain 2006, Konoplev 2007).

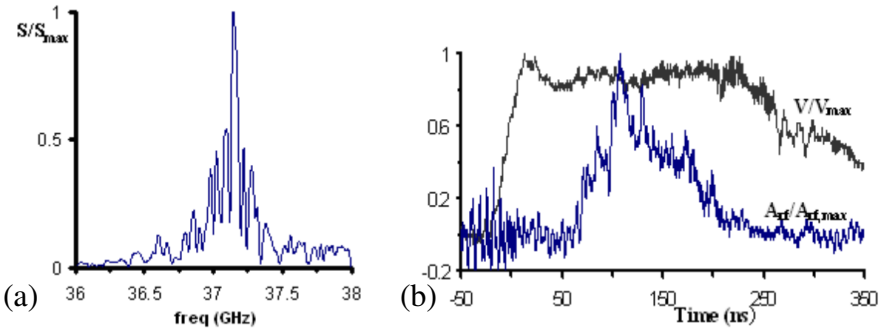

Figure 1.1: Shows (a) the spectral content of a microwave pulse generated by the 2D - 2D Bragg FEM experiment, (b) the voltage pulse applied to the gun diode (black curve) and resultant microwave pulse measured at the FEM output (blue curve). All units are normalised.

This experiment was the progenitor of the 2D - 1D Bragg FEM presented in this thesis, which builds on the success of the purely 2D Bragg based lasing cavity by providing a similar degree of spectral purity, with an enhanced power output of $\sim 60MW$ and energy conversion efficiency of $\sim 10\%$. Portions of this work have been reported by Konoplev et al. (2006a, 2008).

1.4 The 2D - 1D Bragg FEM Experiment.

The 2D - 1D Bragg FEM experiment utilised many of the components of the previous 2D - 2D Bragg FEM, though much of the experimental infrastructure was redesigned to offer enhanced performance and stability in operation. The main advancements of the experiment are summarised as follows:

The High Voltage Power Supply:

The 2D - 2D Bragg FEM experiment utilised a 15 stage inverting Marx-bank, connected to a folded transmission-line pulse former, as the driving supply for the electron beam source. Whilst functioning adequately for the experiment at hand, the Marx-bank was prone to electrical breakdown between the bank output and its

grounded insulation tank, despite the use of highly dielectric ($> 100 kV cm^{-1}$) oil as the insulation medium in the tank:

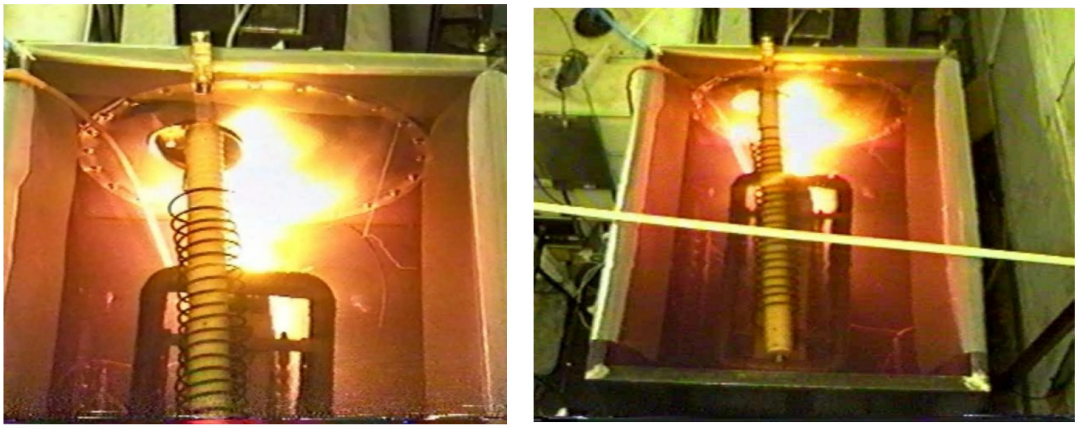

Figure 1.2: Shows examples of flashover between the output of the Marx-bank and the grounded insulation tank.

Such failure of the insulation medium results in the formation of carbon particles in the oil, exacerbating the issue and risking severe damage to the Marx-bank capacitors. For the 2D - 1D Bragg experiment the power supply as a whole was stripped, redesigned and rebuilt (compare Figures 1.2 and 5.5). This included modifications to the Marx-bank base assembly and positioning within a newly designed insulation tank along with improved field suppression structures added to the transmission line and an improved deionised water system to maintain the dielectric strength of the transmission line at a higher, more consistent value.

The redesigned power supply showed a marked increase in stability with no signs of dielectric failure in the insulation oil noted throughout the course of the 2D - 1D Bragg FEM experiment. This allowed for proper calibration of the power supply output, yielding in turn a higher reproducibility in the observed output from the FEM.

The Explosive Electron Emission Gun.

The FEM experiment utilises a space-charge limited electron source, based around an annular explosive electron emission (EEE) cathode. The source used in the 2D - 2D

Bragg FEM experiments suffered from high losses due to the formation of a secondary electron beam from a set of focus electrodes, limiting the beam current to $\sim 500A$ with a degraded pulse shape.

For the 2D - 1D Bragg FEM experiment the design of both the cathode stalk and the bounding anode can were revised, first removing the focus electrodes, then reducing the anode-can diameter, resulting in the construction and experimental verification of two separate electron sources, operating at $1.5kA$ and $2-3kA$ respectively. Reproducibility between shots with similar operating parameters was observed to remain high even when comparing measurements taken from different experimental runs (c.f. Sections 7.3.2 & 7.4.2) allowing for tuning of the electron beam parameters, in successive shots, to achieve resonance with the undulator field in the interaction region.

The 2D - 1D Bragg FEM Cavity and Magneto-optical Systems.

Purely 1D and 2D Bragg reflector based FEM's have been investigated in a variety of forms (Bratman et al. 1983, Wang et al. 1986, Chu et al. 1994, Kaminsky et al. 1996, Ginzburg et al. 1998b, Arzhannikov et al. 1995, Agafonov et al. 1997, Agafonov et al. 1998, Konoplev 2001, McGrain 2006, Konoplev et al. 2007), however the 2D - 1D Bragg lasing cavity used in the FEM experiment is unique, both in its co-axial over-sized design and in that its operation has been proven experimentally. The measurement of $>100ns$ pulses, peaked strongly at their centre frequency of $\sim 37.5GHz$, combined with an observed peak power output $>60MW$ shows that the combination of the 2D and 1D Bragg reflectors results in a marked improvement in performance over a purely 2D Bragg based design whilst maintaining the mode selectivity and phase synchronisation advantages offered by the 2D Bragg reflector.

The magneto-optics employed in the FEM experiment, namely the guide solenoid and undulator circuits, remained largely untouched from that used in the earlier 2D - 2D Bragg FEM, though both circuits were fully stripped, checked and reassembled before commencement of the work presented.

1.4.1 Thesis Structure.

The main features of the thesis are presented as follows:

Chapter 2:

Presents a brief history of the FEL, with a bias towards FEM's in-line with the experiment presented. This is followed by a review of base FEL physics and its relation to the 2D - 1D Bragg experiment.

Chapter 3:

Presents theory relevant to the operation of an FEM lasing cavity defined by 2D and 1D Bragg reflectors, beginning with an over-view of waveguide mode theory as a precursor to discussion of the different Bragg reflectors and the modifications these induce to the EM dispersion relation. The creation of a lasing cavity defined by such Bragg reflectors is then considered, with the performance for a given set of experimental parameters estimated. Full derivations of the 1D and 2D Bragg theory are included in Appendices A and B respectively.

Chapter 4:

Presents numerical simulations of the gun diode, used as the source of the electron beam in the FEM experiments, for two different gun geometries, one operating with beam currents in the region of $1 - 1.5kA$ and one with beam currents of $3 - 4kA$. The required guiding field strength in each case was determined to provide the optimum achievable beam quality for insertion into the drift-tube (interaction) region. All modelling of the gun diode was carried out using the 2.5D Particle in Cell (PiC) code KARAT.

Numerical simulations of the 2D - 1D Bragg cavity are also presented in Chapter 3, this time using the 3D PiC code MAGIC. Simulations are presented for the same cavity geometry, with beam currents and magnetic field strengths adjusted to correspond to that simulated for the two gun geometries. The chapter concludes with a comparison of the performance expected from the lasing cavity for the two beam current densities

and a short summary of the expected operating parameters for the physical experiment based on the simulation results.

Chapter 5:

Presents the construction of the 2D - 1D Bragg experiment, beginning with the high-voltage pulsed-power supply, covering the operation of a $1.5MeV$ inverting Marx-bank and a passively switched folded co-axial pulse forming line controlled by a high-voltage pressurised spark-gap.

The construction of both diode geometries is presented along with discussion of the physics behind the operation of the plasma-flare cathode. The construction of the co-axial drift-tube (incorporating the lasing cavity) along with the undulator and guide solenoid circuits are presented together, as the interaction region of the experiment is defined properly by all three in conjunction.

Operational parameters for the guide solenoid and undulator circuits are provided as is the experimentally determined performance of the co-axial output horn used throughout the FEM experiments. The chapter concludes with a summary of the experimental parameters.

Chapter 6:

Presents the different diagnostic techniques employed in measurement in the FEM experiment. These include shielded and non-shielded resistive-divider and capacitive-divider voltage probes, used to measure the developing voltage pulse (ultimately applied across the diode electrodes).

The beam current was measured using both a Rogowski coil and a current-shunt, with Rogowski coils and current shunts also measuring the magnetic fields (indirectly) of the undulator and guide solenoid respectively.

The microwave power emitted by the FEM experiment was measured using rectifying crystal detectors, with the spectral content analysed using high-pass frequency cut-off

filters and a Ka-band mixer crystal. In each case relevant theory and design is presented along with typical performance / calibration curves as appropriate.

Chapter 7:

Presents the results of the physical FEM experiments, beginning with a description of the triggered timing circuit used to synchronise the discharges from the various power supplies used in the experiment. This is followed by the results obtained for the 2D - 1D Bragg FEM operating with the $\sim 1.5kA$ diode geometry, covering the reproducibility of the diode voltage / beam current pulses, the spectral content of the output microwave pulses and the total output power from the FEM.

The second stage of the FEM experiment, incorporating the $3 - 4kA$ diode geometry, is then presented covering the same measurements as in the earlier stage though with some alterations to the techniques employed. In the latter experimental case, the availability of a Ka-band mixer crystal allowed for a more in-depth examination of the spectral content of the microwave pulses generated by the FEM, specifically allowing the spectral evolution of the pulses with time to be examined. Improved diagnostics implemented in the power supply also allowed for more complete characterization of the power supply performance, a summary of these results is included in Appendix C.

The chapter concludes with a discussion and comparison of results from the two 2D - 1D Bragg FEM experiments, utilising $1.5kA$ and $3kA$ electron beams respectively.

Chapter 8:

Presents a summation of the results obtained in the study of the 2D - 1D Bragg FEM, followed by a brief look at potential future work.

Chapter 2: Historical Review and FEL Physics.

2.1 Introduction

Free Electron Lasers (FEL's) trace their roots back to the early 1930's and have shown great versatility in terms of power output and spectral range, operating from the millimetre wavelengths (mildly relativistic) up to that of X-rays (highly relativistic). When working within the millimetre wave region FEL's are commonly designated within the sub-group Free Electron Masers (FEM's) though the guiding principles of operation remain the same.

This chapter begins with a brief historical review of FEL's focusing on those sources operating in the millimetre wave region, more precisely known as Free Electron Masers (FEM's) (c.f. Section 2.2) in keeping with the type of FEL presented in the main body of work. A brief review of the three, broadly defined, FEL operational regimes is presented in Section 2.4, followed by a review of relevant FEL theory in Section 2.5.

2.2 Historical Review.

The theoretical basis for what would become the Free Electron Laser (FEL) lies with Kapitza and Dirac's theoretical investigation into stimulated Thomson and Compton scattering of electrons by standing light waves (Kapitza & Dirac 1933) and Ginzburg's work on the Doppler upshift of radiation emitted from relativistic electron oscillators (Benford & Swegle 1992). A device making use of these observations was in fact designed in the same year as Ginzburg's work; Gorn submitted a patent, in the United States of America, for a device which generated electromagnetic (EM) radiation from an oscillating electron beam (Gorn 1952).

Between the submission of Gorn's patent (in 1947) and its acceptance in 1952, Motz, along with co-workers at the Stanford Linear Accelerator Centre (SLAC), constructed and tested a device based on the same principles, passing a relativistic electron beam, from an RF linac, through a multi-period undulator (Motz 1951, Motz et al. 1953, Robertson & Sprangle 1988). In 1953 further detail of the electron beam - EM wave interaction was presented by Birdsall et al. (1953), in their work on a resistive-wall amplifier, describing the creation of what would become known as the pondermotive wave in the FEL interaction (c.f. Section 2.3). By 1960 a functioning FEL had been constructed by Phillips, which he termed the "Undulated Beam Interaction elecTRON" (Ubitron) tube (Phillips 1960). This produced peak powers of $\sim 150kW$ at wavelengths of $5mm$ $(60GHz)$, with improved performance theorised through the use of a tapered undulator field (O'Shea & Freund 2001).

An alternative to the Ubitron, the "Compton laser" was proposed in a paper by Pantell et al. theorising the construction of a device which used stimulated Compton scattering of electrons to generate Infra-Red (IR) radiation (Pantell et al. 1968). The operation of such a device was reported by Madey in 1971, in a paper detailing the stimulated emission of Bremsstrahlung radiation from electrons moving through a periodic magnetic field (Madey 1971). This was followed by demonstration of what he termed a "Free-Electron Laser", operating as both an IR amplifier (Elias et al. 1976) and oscillator (Deacon et al. 1977).

These early devices operated in the low-gain Compton (or simply "Compton") regime (c.f. Section 2.4.1), essentially functioning as single particle interactions with the EM field; Colson's work in 1974 determined that such FEL's could be considered as dynamic models of the pendulum equation (Colson 1974). Compton FEL's are characterised by highly relativistic electron energies, coupled with low beam currents, minimising space-charge effects. Typically these are powered by RF linacs (Deacon et al. 1977, Edinghoffer et al. 1984), storage rings (Billardon et al. 1985, Poole 2000) or microtrons (Elias et al. 1986, Shaw et al. 1986). The term "low-gain" is attached to this regime as the low current density of the beam limits the energy conversion efficiency to $\sim 1\%$, though this may be increased in the case of multi-pass FEL's (Robertson & Sprangle 1988).

Development of FEL's showing exponential gain began at roughly the same time as Madey's work, sub-dividing into Raman and high-gain Compton regime FEL's dependant on the dominance of the pondermotive or space-charge forces in the FEL interaction respectively (discussion of the differences between these regimes is given in Section 2.4.2).

One such FEL was developed at the Naval Research Laboratory (NRL) in the early 1970's, when Friedman et al. constructed a working millimetre wavelength Ubitron like device, providing microwave intensity of $\geq 70dB$ above noise level at X-band ($8 - 12.4GHz$), with power levels in the region of $10 - 20MW$ in X-band and Ka-band ($26 - 40GHz$) respectively. Again the energy conversion efficiency was in the region of 1% (Friedman & Herndon 1972a, 1972b).

In 1977, Efthimion & Schlesinger reported the first coupling between a fast wave structure and an intense relativistic electron beam through what they termed "stimulated Raman scattering" (Efthimion & Schlesinger 1977). This was followed quickly by the report of an FEL operating in the Raman regime by McDermott et al. at Columbia University, in collaboration with NRL. This generated $0.5 - 1MW$ output EM power levels, from a $25kA$ $1.2MeV$ electron beam, at sub-millimetre wavelengths (McDermott et al. 1978). This was also an early example of super-radiant EM emission

(operation in the Self-Amplifying Spontaneous Emission (SASE) regime), meaning the FEL operated as an amplifier without the inclusion of a seed EM signal for amplification.

The first mention of the use of Bragg structures as potential reflectors in FEL's came in 1977 (Yariv & Nakamura 1977), forming what they termed a "distributed feedback laser". It should be noted here that by the close of the 1970's separation of FEL's into the three known regimes was not yet formalised, rather FEL's were roughly divided into low-gain and high-gain regime only (Sprangle et al. 1979).

Development of FEL's in the 1980's increased greatly from the early work of the 1970's, both in terms of theory (Sprangle & Smith 1980, Colson 1981, Yin & Bekefi 1983, Luchini & Solimeno 1985, Grover & Pantell 1985, Tang & Sprangle 1985) and experiment (Kroll et al. 1981, Jackson et al. 1983, Sheffield et al. 1985, Pasour & Gold 1985, Billardon et al. 1985, Shraga et al. 1986, Orzechowski et al. 1986, Kirkpartrick et al. 1989, Antonsen Jr. & Levush 1989). Those operating in the high-gain regimes generally fall into the sub-category of Free-Electron Masers (FEM's) rather than FEL's, due to the relatively low electron energies (sub-MeV) and resultant long wavelength output radiation. FEM's, which are theoretically identical to FEL's, in some ways can be considered as the more direct descendents of Phillips' Ubitron, which also functioned in the millimetre wave region.

In relation to the FEM presented here, some of the most important work from the 1980's relates to the development and testing of different forms of magneto-optical systems, to both confine high current electron beams and extract as much energy from them as possible. The use of a collimator combined with a guiding axial magnetic field (Parker et al. 1982, Jackson et al. 1983) allowed for the extraction of a high quality beam (at the expense of over-all efficiency) from an apertured diode, achieving 2.5% electrical efficiency in a FEM operating at $\sim 75 GHz$ in the Raman regime. Other routes for efficiency enhancement were pursued via tuning of the guiding magnetic field and /or the undulator field (Jacobs et al. 1981, Gold et al. 1983, Freund & Gold 1984, Gold et al 1984, Fajans et al 1985, Fajans et al 1986), with the inclusion of the

guiding magnetic field becoming fairly standard in high power FEM's, though some exceptions remained, such as SASE amplifiers (Pasour & Gold 1985, Kirkpartrick et al. 1989) and the helical FEM of Mathew & Pasour (1986) which made use of a collimator but no axial field.

The first instances of Bragg reflector based FEM's were reported in 1983 (Bratman et al. 1983) and 1986 (Wang et al. 1986) detailing the use of 1D Bragg corrugations in over-sized waveguide structures. The early 1980's also saw the conceptual emergence of the Lowbitron (McMullin & Bekefi 1981, McMullin & Bekefi 1982, Shraga et al 1986), which shared many similarities with the FEM and the Cyclotron Auto-Resonance Maser (CARM), operating as a semi-hybrid of the two. The Lowbitron will be discussed in Section 2.3.2 due to similarities in the undulator field employed with that of the 2D-1D Bragg FEM experiment.

The 1990's saw great advances in the operation of FEM's incorporating a helical undulator; the use of a reversed axial guide field (one in which the current flowing in the guide solenoid opposes that flowing in the undulator) was found to increase energy extraction efficiency by an order of magnitude (Conde & Bekefi 1991, Kaminsky et al. 1996, Ginzburg et al. 1998a) from a few percent to $20 - 30\%$. The 1990's also saw the appearance of theoretical FEM's based on co-axial undulators, proposed by Freund et al. (1993) at NRL and McDermott et al. (1995) at the University of California, with the latter developing the concept throughout the 1990's (Balkum et al. 1996, Balkum et al. 1998) though a working model was never presented. The inclusion of Bragg structures to form resonant lasing cavities (Chu et al. 1994, Kaminsky et al. 1996, Ginzburg et al. 1998b) and novel drift-tube regions (Freund et al. 1997) were developed, with collaborative work between the Institute of Applied Physics (IAP) and the Budker Institute of Nuclear Physics (BINP), in Russia, resulting in the creation of a sheet beam FEM, operating with a resonator defined by a 1D Bragg grating (Arzhannikov et al. 1995, Agafonov et al. 1997, Agafonov et al. 1998) producing $\sim 200J$ microsecond pulses at wavelengths of $4mm$.

The late 1990's also saw the beginning of a collaboration between the IAP and the University of Strathclyde, investigating the development of high power masers, utilising the distributed feedback mechanisms offered by different Bragg structures. By 1998 this resulted in the operation of the first FEM oscillator in the UK (Cross et al. 1998) which provided $\sim 0.5MW$ of output power at $32GHz$ with a conversion efficiency of $\sim 5\%$. Collaborative work investigating the use of 2D Bragg structures began in 1999 (Ginzburg et al. 1999).

Development of FEM's using distributed feedback, by both Strathclyde and the IAP, is ongoing, particularly into the application of 2D distributed feedback due to its increased mode selection and synchronism properties in over-sized structures. The first FEM using a 2D - 2D over-sized co-axial Bragg lasing cavity was experimentally verified at the University of Strathclyde in 2005, reported in McGrain (2006) and Konoplev et al. (2007). This showed single frequency operation at $\sim 37.5GHz$ at power levels of $\sim 15MW$ and conversion efficiencies of $\sim 6\%$.

The IAP / BINP sheet beam FEM (located at the BINP in Novosibirsk, Russia) developed in the 1990's was upgraded to include 2D, rather than 1D, Bragg reflectors. This generated $\sim 100MW$ pulses for $\sim 1\mu s$ at $75GHz$ (Agarin et al. 2000). The action of co-axial Bragg structures has also been independently investigated by a group based at Southwest Jiaotong University, China, looking at the effects of off-axis positioning of the two conductor surfaces (Ying-Xin & Shi-Chang 2007, Shi-Chang et al 2007, Ying-Xin & Shi-Chang 2008). The theoretical development of a co-axial Raman regime FEM, operating at wavelengths of $\sim 6mm$ was also carried out at the Bu-Ali Sina University in Iran (Maraghechi & Sepehri Javan 2001, Farokhi & Maraghechi 2005) though at present only simulation results have been presented.

2.3 The Free Electron Laser Instability.

The operation of the FEL, or FEM as is more apt in this case, is conceptually quite simple. Figure 2.1 represents a simple planar FEL, widely used for descriptive purposes (Pasour 1987, Robertson & Sprangle 1989, Luchini & Motz 1990, Benford & Swegle 1992, Freund & Antonsen 1996, Bonifacio 1997):

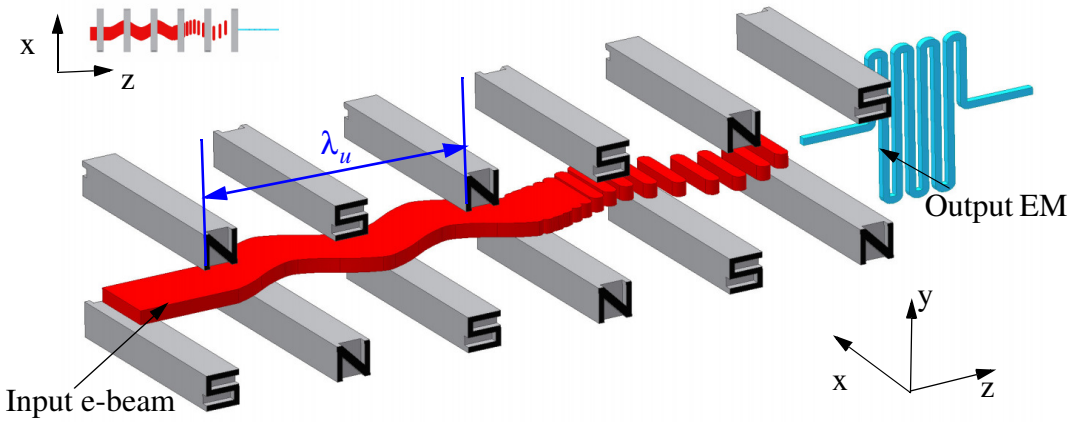

Figure 2.1: Shows a schematic of a planar magnetostatic undulator, noting the axial bunching of the on-axis electron beam as it moves through a periodic magnetic field. The insert shows the (x,z) cross-section for clarity.

Here an electron beam propagates in the +z direction, on-axis through a linearly polarised transverse magnetostatic field. This is provided by a series of alternating polarity magnets (or alternately wound coils), collectively known as either an "undulator" or a "wiggler".

The choice of which term should be used, for a given situation, is an on-going matter of discussion, with the most common consensus made in reference to the "undulator parameter" a_u (c.f equation 2.5) which differentiates dependant on the magnitude of the "bounce" imparted to the electrons (Luchini & Motz 1990, Benford & Swegle 1992), however such distinctions are not universally applied. As a matter of preference the term undulator will be used throughout the following text, however this should be understood to apply equally to devices noted as wigglers in the literature.

For the case presented above, the static field of the linear undulator ($\vec{B}_u$) can be described by the function:

$$\vec{B}_u \cong B_u \cos(k_u z)\hat{y} \qquad \textbf{2.1}$$

where B_u is the peak magnitude of the magnetic field and $k_u = 2\pi/\lambda_u$ is the wave-number of an undulator with axial period λ_u.

The electrons entering the undulator from the left have an initial velocity spread close to zero, giving the initial electron velocity as $\vec{v}_0 \cong v_{z0}\hat{z}$. As the electrons pass through the polarised magnetic field, they are subject to a Lorentz force of $e\vec{v}_0 \wedge \vec{B}_u$, inducing oscillatory motion on the x axis with velocity:

$$\vec{v}_u = \frac{|e|B_u}{\gamma m_e k_u}\sin(k_u z)\hat{x} \qquad \textbf{2.2}$$

where $|e| = 1.602 \times 10^{-19} C$ is the magnitude of the charge on the electron, $\gamma = (1 - (v_0/c)^2)^{-1/2}$ is the Lorentz relativistic mass factor, $m_e = 9.11 \times 10^{-31} kg$ is the electron rest mass.

The resultant $\vec{v}_u \wedge \vec{B}_u$ term in the force equation yields a sinusoidal axial force which the incoming electrons perceive as a counter-propagating "pondermotive" wave travelling with a phase velocity of:

$$v_{ph} = \frac{\omega}{k + k_u} \qquad \textbf{2.3}$$

where ω is the angular frequency, k is the free-space wave-number and $v_{ph} < c$.

Through tuning of the electron energy the condition $v_z \cong v_{ph}$ can be approached, where v_z is the electron bulk streaming velocity, producing a resonance between the beam electrons and the pondermotive potential. This leads to the formation of an axial bunching mechanism known as the "FEL instability" which, as is discussed in Section 2.3.2, is distinct from the two Gyrotron instabilities (namely the cyclotron and associated Weibel instabilities).

As the FEL instability becomes more established, the beam electrons begin to form axial bunches, with the electrons of each bunch lying close in phase. This leads to an increase in the coherence of the radiated output, occurring at a Doppler up-shifted wavelength of:

$$\lambda = \frac{\lambda_u}{\beta_z(1+\beta_z)\gamma^2}\left(1+\frac{a_u^2}{2}\right) \qquad \textbf{2.4}$$

where $\beta_z = v_z/c$ and the quantity a_u is the undulator parameter:

$$a_u = \frac{eB_u}{m_e c k_u} \qquad \textbf{2.5}$$

which denotes the magnitude of the undulation imparted to the electrons. When used to differentiate between "undulators" and "wigglers", typically a "wiggler" has $a_u > 1$ and an "undulator" has $a_u < 1$.

2.3.1 The Azimuthally Symmetric Undulator.

The co-axial nature of the 2D - 1D Bragg FEM experiment precludes the use of a linear undulator, such as that shown in Figure 2.1, though similar operation may be achieved through the use of an azimuthally symmetric undulator, shown schematically in Figure 2.2:

.

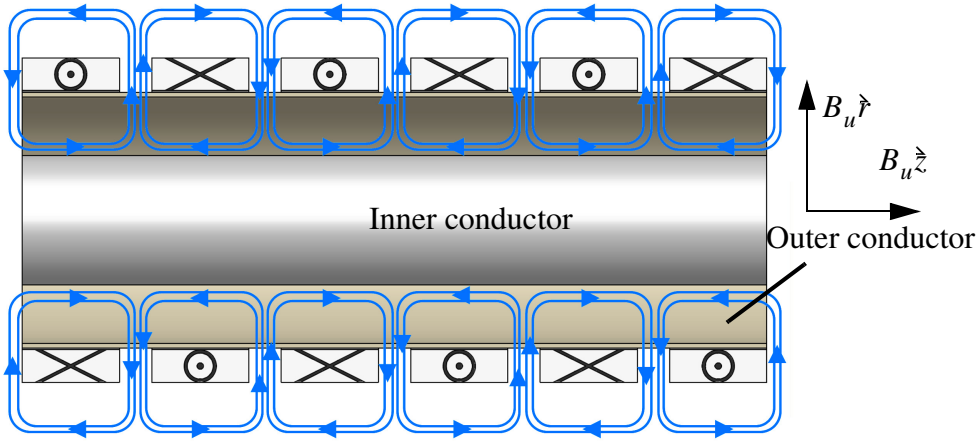

Figure 2.2: Shows a co-axial drift-tube in cross-section with an azimuthally symmetric undulator fitted on the outer surface of the outer conductor. The direction of current flow in the undulator coils and resultant magnetic field lines are shown.

Here a series of alternately wound coils are placed along the outer-conductor of the co-axial drift-tube, producing a periodic, magnetostatic field described by:

$$\vec{B}_u = [B_u \cos(k_u z)\hat{r} + B_u \sin(k_u z)\hat{z}] I_1(k_u r_e) \qquad \textbf{2.6}$$

where the axial term arises from the alternating axial magnetic fields induced by the flow of current in successive coils and the radial term arises from the localised reversal of the magnetic field, similar to the action of a magnetic cusp (Sinnis & Schmidt 1963, Rhee & Destler 1974, Gallagher et al. 2000).

Noting that the electrons, in the co-axial channel, propagate at a radial position removed from the "on-axis" case of the linear undulator, the electrons should be considered as having an induced sinusoidal oscillation in the azimuthal direction due to the action of successive alternately polarised radial cusps, as opposed to the defined direction of rotation about the azimuth delivered by a single cusp. $I_1(k_u r_e)$ is the first order modified Bessel function of the first kind. The resultant $v_\theta \wedge B_z$ force on the electrons, from the azimuthal oscillations, imparts a similarly sinusoidal radial oscillation on the electron motion, producing a spiralling motion as the electrons propagate along z (c.f. Section 4.3.2). As will be shown in Section 4.3.2, the difference in the magnetic field seen by two initially co-propagating electrons, with differing radial positions, has an effect on both the beam - wave coupling strength and on the propagation of the electrons through the beam-channel.

When working in the millimetre-wave range a common addition in FEM's is the introduction of a guiding axial magnetic field, used as a means of confining high-current electron beams (Pasour 1987, Peskov et al. 1998, Cross et al. 1998, Konoplev et al. 2007), however this introduces some complications to the case described above; as the axial guide field constrains the transverse motion of the electrons, the perturbation induced by the undulator field is reduced.

It is worth noting that other forms of co-axial undulator exist, such as the co-axial periodic-permanent magnet (PPM) systems of Freund (1993), McDermott et al. (1995) and Balkum et al. (1996, 1998), however such a system was discounted for use in the

FEM experiment as they require alignment of static magnetic components on both co-axial conductors, negating the ability to tune the undulator magnetic field strength fully independently of the guiding magnetic field.

2.3.2 Inclusion of an Axial Guiding Magnetic Field.

To account for the presence of the guiding magnetic field, the relation between the applied guide solenoid field and the required undulator field is (Konoplev et al. 2000):

$$B_u = \frac{B_0 k_u r_e}{2I_1(k_u r_e)}\left(\frac{2v_u}{\omega_{cyc} r_e} - 1\right) \qquad \textbf{2.7}$$

in the limit where the FEM frequency $\omega_u \neq \omega_{cyc}$ where $\omega_{cyc} = (eB_0)/(m_e\gamma)$ is the relativistic cyclotron frequency, B_0 is the magnitude of the axial magnetic field and r_e is the mean radius of the electron beam.

The inclusion of a static axial magnetic field does however introduce some important considerations, most importantly the production of Larmor rotation (cyclotron motion) in the beam electrons. This arises naturally due to the magnetic moment of the electrons as they propagate along the field lines of the axial guide field, with the oscillatory motion corresponding to ω_{cyc} and an associated amplitude of:

$$r_{cyc} = \frac{\gamma v}{\omega_{cyc}} \qquad \textbf{2.8}$$

where v is the electron velocity (Humphries 2002).

This oscillation has the potential to lead to the creation of two parasitic beam instabilities, namely the cyclotron and Weibel instabilities, which compete with the FEL instability and degrade the efficiency of the maser. It is certainly not the case that such instabilities are uniformly taken to be parasitic; the cyclotron instability in particular is of interest for devices such as the gyrotron or the Cyclotron Auto-Resonance Maser (CARM), in which it forms the means of coupling energy from the beam electrons to the EM wave. However in this case, as they are in direct competition with the desired FEL instability, it is necessary to reduce the effects of Larmor rotation in the beam as much as possible.

Depending on the type of undulator used, there are various means of achieving this end. The first and most universal means is to ensure the strength of the axial magnetic field is such that the resultant resonant cyclotron (and by inference Weibel) frequencies lie far from the FEL operating frequency. A typical example of this is shown in Figure 2.3, with parameters chosen such that the resonant cyclotron, Weibel and FEL frequencies, with a given waveguide mode (c.f. Section 3.2) are clearly defined.

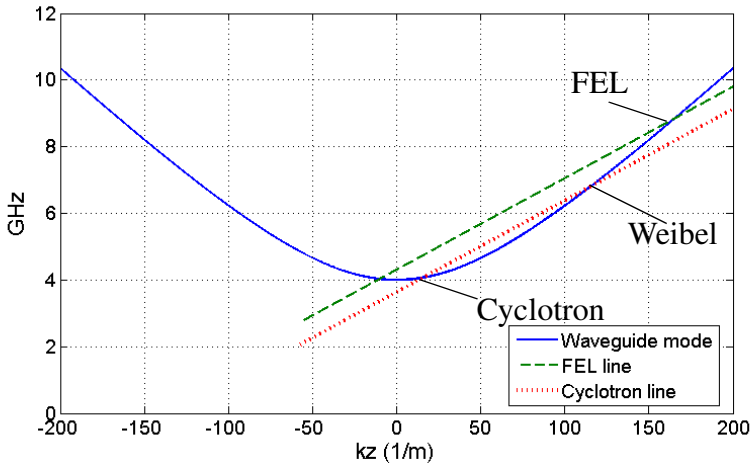

Figure 2.3: Shows a typical waveguide mode along with beam lines denoting FEL and cyclotron interactions. The frequencies of the FEL, cyclotron and Weibel instabilities are indicated.

The initial magnetic field of the undulator may also be tapered to allow a more adiabatic change in the electron trajectories as they enter the FEL and reduce the risk of "kicking" the electrons into a rotational trajectory as one would do, for example, with a gyrotron.

For FELs employing a bifilar helical undulator, where both the FEL and cyclotron instabilities interact with the E_θ field, reversal of the guide field, relative to the direction of rotational motion of the electrons, greatly reduces the sensitivity of the FEL to spread in $v_\perp$, dramatically increasing the energy conversion efficiency, from the beam to the EM wave, from ~1% to ~30% (Conde & Bekefi 1991, Kaminsky et al. 1996, Ginzburg et al. 1998a). The above conditions in regards to the tuning of the axial magnetic field should, however, still be employed, as the positioning of either parasitic

instability close to the operating frequency of the FEL introduces a degree of uncertainty in the results. Once produced the EM radiation shows no sign of which mechanism generated it from the beam, meaning differentiation between radiation generated by cyclotron motion in the electrons may not be fully discernible from that generated by the FEL instability (Gold et al. 1983, Bekefi & Fajans 1985, Gold et al. 1985, Aitken et al. 1998).

With an azimuthally symmetric undulator, contrary to the case of the helical undulator, no reversal of the guide field can be performed, as the orbits of the individual electrons in the undulator field do not encircle the axis and so no "reverse" field direction can be defined. Rather suppression of the cyclotron instabilities can be achieved by following the initial two conditions of proper selection of the guide field strength and tapering of the input to the undulator itself. If conditions allow one may in fact set B_0 such that the ω_{cyc} falls below the "cut-off frequency" for the electron beam drift-tube.

In setting these conditions an additional beam instability, which may be excited by the azimuthal undulator field, must be considered. The Lowbitron instability, investigated conceptually in the early 1980's at the Massachusetts Institute of Technology (MIT) (McMullin & Bekefi 1981, Jacobs et al. 1981, McMullin & Bekefi 1982, Davidson & McMullin 1982, McMullin et al. 1983) shares characteristics with both the cyclotron and FEL instabilities. The Lowbitron frequency is defined as:

$$\omega_{low} = \frac{(1+\beta_z)\gamma^2}{(1+\gamma^2\beta_\perp^2)}(k_u c\beta_z + \omega_{cyc}) \qquad \textbf{2.9}$$

where $\beta_z = v_z/c$ and $\beta_\perp = v_\perp/c$ are the axial and transverse electron velocities normalised to the speed of light $c \cong 3\times10^8 ms^{-1}$.

Typically this is much higher in frequency than the other beam instabilities and can be avoided provided the magnitude of $v_\perp$ is low compared to v_z.

It is worth noting that as the case presented uses a co-axial beam-channel, with the operating mode being the fundamental TEM mode, growth of the E_θ field in itself

indicates coupling of energy into modes other than that desired and may be symptomatic of generation of the cyclotron or Weibel instabilities, as the TEM mode is described by E_r and B_θ field components exclusively. The concept of different modes in waveguide (synonymous with drift-tubes in this instance) is discussed in Section 3.2.

2.4 Operational Regimes of FEL's / FEM's.

FEL's are typically described in relation to their "operational regime", that is, the form that the beam - wave interaction takes within the device. There are three broadly defined regimes, namely the low-gain Compton, high-gain Compton and Raman regimes (equations in the following section use cgs Electro-Static Units (esu)).

2.4.1 The Low-Gain Compton Regime.

The low-gain Compton regime is named for the similarity of the beam - wave interaction to that of Compton scattering of electrons by an EM wave. In a low-gain Compton FEL space-charge effects in the beam play a minor role, as beam currents are low ($< 1kA$), allowing single particle scattering physics to be applied (Sprangle & Smith 1980), though individual electron energies can be highly relativistic. The highly relativistic electron energies allow low-gain Compton FEL's to operate into the IR and X-ray regions of the EM spectrum, though the single-pass efficiency is typically $\leq 1\%$ (Elias et al. 1976, Deacon et al. 1977).

Such FEL's show a maximum gain of (Robertson & Sprangle 1989):

$$G(z_{max}) \cong \frac{\beta_u^2 \omega_b^2}{\gamma_0} F k_u z_{max}^3 \qquad \textbf{2.10}$$

where $z_{max} = (2.6 v_{z0})/(v_{z0}(k + k_u) - \omega)$ is the axial location of maximum gain, k is the free-space EM wave-number, $\omega = kc$ where c is the speed of light, k_u is the undulator wave-number, $\beta_u = v_u/c$ is the normalised velocity of the oscillation on the electrons, $\gamma_0 = \gamma_z \sqrt{1 + (eB_u/[k_u m_e c^2])^2}$, $\gamma_z = (1 - v_{z0}/c)^{-1/2}$, e is the

electron charge, B_u is the magnetic field strength of the undulator, k_u is the undulator wave-number, $\omega_b = \sqrt{(4\pi e^2 n_0)/m_e}$ is the beam plasma frequency, n_0 is the ambient beam density, m_e is the electron rest mass and $F = \sigma_b/\sigma_r$ is the filling factor, where $\sigma_{b,r}$ are the cross-sectional areas of the electron and radiation beams respectively.

While the FEM presented in this work falls out-with that defined by the low-gain Compton regime, this regime is often used for describing FEL operation due to the single particle nature of the interaction (c.f. Section 2.3).

2.4.2 The High-Gain Regimes.

The high-gain operational regimes are both defined by the presence of high beam currents $> 1kA$ and mildly relativistic electron energies (subGeV). Both the high-gain Compton and Raman regimes show exponential growth of the EM field profile, markedly higher than that shown in the low-gain Compton regime. Differentiation, between the Raman and high-gain Compton regimes, is determined by the relative strength of the beam space-charge forces compared to the strength of the pondermotive wave.

2.4.2.1 The High-Gain Compton Regime.

When the forces on the beam electrons from the pondermotive wave dominate the collective space-charge forces, the FEL is considered to operate in the high-gain Compton regime.

This holds provided the following condition is met (Robertson & Sprangle 1988):

$$\beta_u \gg \beta_{crit} \equiv \sqrt{\frac{2\omega_b c^2}{F v_{z0}^3 \gamma_0^{1/2} \gamma_z^3 k_u}} \qquad \textbf{2.11}$$

where v_{z0} is the initial electron axial velocity and all other terms share common meanings with equation 2.10.

β_{crit} increases with ω_b (and so n_0) and β_u can be expressed in terms of the undulator field amplitude (B_u) as:

$$\beta_u = \frac{|e|B_u}{\gamma_0 m_e c^2} \qquad \textbf{2.12}$$

The maximum spatial growth rate for the high-gain Compton regime is given as:

$$G = \frac{\sqrt{3}}{2}\sqrt[3]{F\frac{\beta_u^2\omega_b^2 k_u}{2\gamma_0 c^2}} \qquad \textbf{2.13}$$

with an associated frequency for the emitted EM radiation being:

$$\omega_{FEL} = (1+\beta_{z0})\gamma_z^2 v_{z0} k_u \cong 2\gamma_z^2 k_u c \qquad \textbf{2.14}$$

2.4.2.2 The Raman Regime.

When the space-charge forces dominate, the FEL is considered to function in the Raman regime, meaning the beam-wave interaction is treated as an interaction between all the electrons collectively, as a plasma wave, and the EM wave. In this case the inverse of equation 2.11 should be met:

$$\beta_u \ll \beta_{crit} \qquad \textbf{2.15}$$

with β_{crit} and β_u defined as in equations 2.11 and 2.12 respectively.

The maximum growth rate in this case is:

$$G = \beta_u\sqrt{F\frac{\omega_b\gamma_z k_u}{4\sqrt{\gamma_0 c}}} \qquad \textbf{2.16}$$

where the resonant frequency of the beam-wave interaction is:

$$\omega = v_{z0}(k + k_u) - \frac{\omega_b}{\gamma_{z0}\sqrt{\gamma_0}} \qquad \textbf{2.17}$$

occurring in the region of the intersection between the negative energy beam mode and the EM mode:

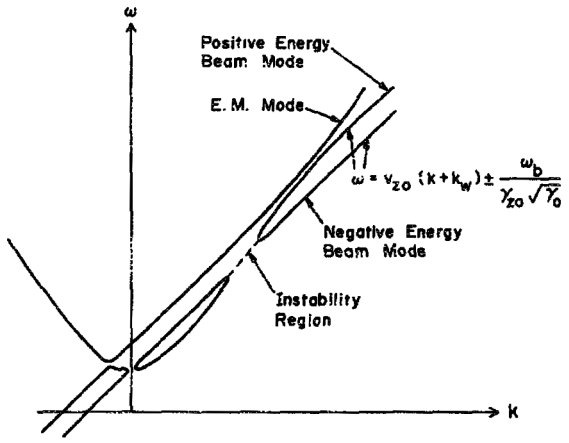

Figure 2.4: Shows a schematic ω - k diagram of the Raman FEL instability forming between the negative energy beam mode and a standard waveguide EM mode. (Robertson & Sprangle 1989).

2.4.2.3 Indeterminate High-Gain Regimes.

The cases presented in Sections 2.4.2.1 and 2.4.2.2 are representative of two well defined operational regimes; $\beta_u \gg \beta_{crit}$ and $\beta_u \ll \beta_{crit}$ respectively. When $\beta_u \leq \beta_{crit}$ or $\beta_u \geq \beta_{crit}$ the regime is less well defined and the FEL may show aspects of both in its operation, though more Raman or high-gain Compton "like" operation may be inferred respectively. When close to $\beta_u \approx \beta_{crit}$ increases or decreases in the beam density may result in switching between approximate operational regimes, though small changes in n_0 should not greatly effect operation, i.e. if one considers a spread in current density resulting in variations in the beam current of a few hundred amps the operational regime should remain largely unaffected.

2.5 Parameters of the 2D - 1D Bragg Free Electron Maser.

An estimation for the operational regime of FEM experiment can be obtained in reference to equations 2.11 and 2.12.

Noting that the electron charge in this case is expressed as $e = 4.8032 \times 10^{-10} esu$, assume a beam cross-section $\sim 4.4 cm^2$, with a drift-tube cross-section of $\sim 22 cm^2$, an estimated beam current density of $\sim 350 A cm^{-1}$ and an undulator field strength of $\sim 650 Gauss$ (these are in-line with the specification for the earlier 2D - 2D Bragg FEM experiment noted in Konoplev (2001) and McGrain (2006)). For electron energies of $\sim 450 keV$, propagating with $v_z \gg v_\perp$ through an undulator field with a periodicity of $4 cm$ (c.f. Section 5.4.1), equation 2.12 gives $\beta_u \approx 0.64$ with $\beta_{crit} \approx 0.0032$. This indicates operation in the High-Gain Compton regime, which may be assumed applicable to the 2D - 1D Bragg FEM experiment as the operational paramters were not much changed from the case of the 2D - 2D Bragg FEM experiment.

Looking back at equations 2.4, 2.5 and 2.7, if one assumes a guiding magnetic field strength of $\sim 0.6 T$ and a thin annular electron beam with a nominal radius of $\sim 3.5 cm$, for electron energies in the region of $\sim 450 keV$ an undulator field of $0.065 - 0.067 T$ ($650 - 670 Gauss$) should provide coupling between the electron beam and the fundamental TEM mode of the interaction region, with radiated emission at $\sim 37.5 GHz$ ($8 mm$). This is advantageous in terms of construction, for what is in essence a proof of principle experiment, though it should be noted that both the magneto-optics and the Bragg structures (discussed in the following chapter) are fully scalable to higher or lower frequencies.

Chapter 3: Theory of the 2D - 1D Bragg Free-Electron Maser.

3.1 Introduction.

The lasing cavity used in the FEM experiment was defined by novel Bragg reflector structures, positioned on the inner conductor of an oversized co-axial waveguide. The following chapter begins with a review of co-axial waveguide theory (c.f. Section 3.2) as a preface to discussion of the operation of both 1D and 2D Bragg reflectors (c.f. Section 3.3). The Chapter concludes with a description of a 2D - 1D Bragg lasing cavity, defined by surface corrugations on the inner conductor of a co-axial waveguide (c.f. Section 3.4). Further detail regarding the derivation of parameters for the 1D and 2D Bragg reflectors may be found in Appendices A and B respectively.

3.2 The Propagation of Electromagnetic Waves in Waveguides.

An EM wave propagating in an unbound media is known to follow the dispersive relation:

$$\omega^2 = \frac{k^2}{\mu\varepsilon} \tag{3.1}$$

where k is the wave-number, $\varepsilon = \varepsilon_0\varepsilon_r$ and $\mu = \mu_0\mu_r$ are the permittivity and permeability of the medium respectively. The subscript 0 denotes the free space values $\varepsilon_0 \cong 8.854 \times 10^{-12} Fm^{-1}$ and $\mu_0 = 4\pi \times 10^{-7} Hm^{-1}$, while the subscript r denotes the relative weighting factor of the propagation medium from the free space values. The phase velocity of the wave is typically expressed as $v_{ph} = 1/\sqrt{\mu\varepsilon}$ with $v_{ph} = c$ in free space (i.e. $v_{ph} = 1/\sqrt{\mu_0\varepsilon_0}$).

Moving to the case where the propagation medium has a defined geometry, the boundary of the medium introduces a maximum limit on the wavelength of radiation that can propagate for a given field profile. This leads to a modification of equation 3.1 to account for the cut-off wave-number (k_c):

$$\omega^2 = k^2 v_{ph}^2 \tag{3.2}$$

where $k = \sqrt{k_z^2 + k_c^2}$ is the magnitude of the EM wave-vector and we take the wave as propagating in the $+z$ direction with a propagation constant of k_z.

In the work presented the bounding media were hollow metallic waveguides, with the cut-off wave-number determined by the transverse cross-section of the guide:

$$k_z = \sqrt{k^2 - k_c^2} = \begin{cases} If & k < k_c = \sqrt{k^2 - k_c^2} < 0 = \text{Evanescent wave} \\ If & k = k_c = \sqrt{k^2 - k_c^2} = 0 = \text{Cut-off wave} \\ If & k > k_c = \sqrt{k^2 - k_c^2} > 0 = \text{Propagating wave} \end{cases} \tag{3.3}$$

therefore an EM wave can be considered to be “cut-off” if the transverse component of its wave-number $k_c \geq k$. The introduction of this boundary condition gives rise to the existence of different EM “modes”; EM waves differentiated by variations in the transverse wave amplitude profile.

In single conductor waveguides the modes supported take two general forms:

- Transverse Electric (TE) modes, characterized by the lack of an E_z field component.
- Transverse Magnetic (TM) modes, characterized by the lack of an axial H_z field component.

with the addition of a purely transverse TEM mode in the case of multi-conductor waveguides to be discussed later.

Equation 3.3 defines the limit for the fundamental (lowest order) mode of the waveguide, with successive higher order modes having larger values of k_c. An example of a typical waveguide mode, along with the case where $k_c = 0$ (the free-space relation), is given in Figure 3.1.

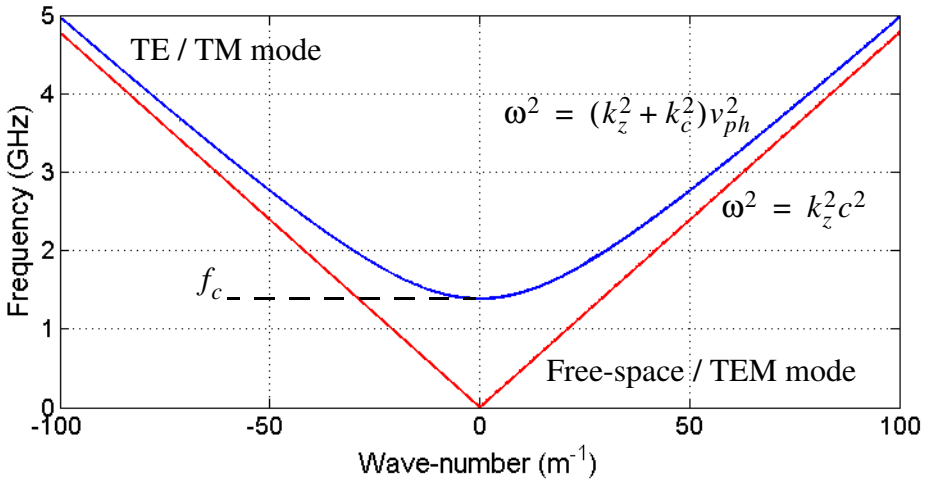

Figure 3.1: Shows the dispersion curve of a typical TE / TM mode in a waveguide, noting the free-space relation for comparison.

Successive modes are differentiated through the inclusion of a set of indices after the modal designation ($TE_{m,n}$ and $TM_{m,n}$).

The meanings of these indices varies dependant on the waveguide, however for the most common types they are defined as:

Table 1:

	m	n	Fundamental mode
Rectangular waveguide	Number of half-wave variations along the long transverse co-ordinate	Number of half-wave variations along the short transverse co-ordinate	$TE_{1,0}$
Circular and co-axial waveguide	Number of full-wave azimuthal variations	Number of half-wave radial variations	$TE_{1,1}$ / TEM respectively

Detailed discussion on the classification of different modes and their structures is given in Harvey (1963), Thumm (1997) and Pozar (1998).

An alternative notation scheme exists, which should be noted due to its prevalence in older literature and some facets of contemporary work, which delineate the two mode types based on the extant axial field component; i.e. a TE mode would be designated a magnetic (H) mode and a TM mode would be designated an electric (E) mode. While this notation has been largely supplanted by the TE / TM notation, it does offer a useful alternative when dealing with so-called “hybrid” waveguide modes, that is modes which are not clearly defined as TE or TM but show characteristics of both. In these cases the designations HE and EH can be used to clearly specify which modal type the hybrid mode is closest to and as such remain in fairly common usage.

The behaviour of modes as they propagate through a waveguide can be understood in reference to Maxwell’s third and fourth equations, which are respectively:

$$\vec{\nabla} \wedge \vec{E} = -\mu \frac{\partial \vec{H}}{\partial t} \qquad \textbf{3.4}$$

where $\vec{E}$ and $\vec{H}$ are the strengths of the electric and magnetic fields respectively,

and:

$$\vec{\nabla} \wedge \vec{H} = \vec{J} + \varepsilon \frac{\partial \vec{E}}{\partial t} \quad \textbf{3.5}$$

where $\vec{J}$ is sum of the convection and conduction current densities, while $\varepsilon \frac{\partial \vec{E}}{\partial t}$ represents the displacement current density.

For a mode propagating in the +z direction ($e^{-ik_z z}$ dependence) in a source-free waveguide these may be expressed as:

$$\vec{\nabla} \wedge \vec{E} = -i\omega\mu\vec{H} \quad \textbf{3.6}$$

$$\vec{\nabla} \wedge \vec{H} = i\omega\varepsilon\vec{E} \quad \textbf{3.7}$$

with individual field components defined as:

$$\frac{\partial E_z}{\partial y} + ik_z E_y = -i\omega\mu H_x \quad \textbf{3.8a}$$

$$-ik_z E_x - \frac{\partial E_z}{\partial x} = i\omega\mu H_y \quad \textbf{3.8b}$$

$$\frac{\partial E_y}{\partial x} - \frac{\partial E_x}{\partial y} = -i\omega\mu H_z \quad \textbf{3.8c}$$

$$\frac{\partial H_z}{\partial y} + ik_z H_y = i\omega\varepsilon E_z \quad \textbf{3.8d}$$

$$-k_z H_x - \frac{\partial H_z}{\partial x} = i\omega\varepsilon E_y \quad \textbf{3.8e}$$

$$\frac{\partial H_y}{\partial x} - \frac{\partial H_x}{\partial y} = i\omega\varepsilon E_z \quad \textbf{3.8f}$$

Typically these are solved for E_z and H_z, giving the transverse field components the form:

$$E_x = -\frac{i}{k_c^2}\left(k_z \frac{\partial E_z}{\partial x} + \omega\mu \frac{\partial H_z}{\partial y}\right) \quad \textbf{3.9a}$$

$$E_y = \frac{i}{k_c^2}\left(-k_z\frac{\partial E_z}{\partial y} + \omega\mu\frac{\partial H_z}{\partial x}\right) \quad \textbf{3.9b}$$

$$H_x = \frac{i}{k_c^2}\left(\omega\varepsilon\frac{\partial E_z}{\partial y} - k_z\frac{\partial H_z}{\partial x}\right) \quad \textbf{3.9c}$$

$$H_y = -\frac{i}{k_c^2}\left(\omega\varepsilon\frac{\partial E_z}{\partial x} + k_z\frac{\partial H_z}{\partial y}\right) \quad \textbf{3.9d}$$

with an exception being the case of the transverse electromagnetic (TEM) mode, which as its name suggests has purely transverse field components; $E_z = H_z = 0$. Looking at equations 3.9a - 3.9d, this condition means all the transverse components would also be zero, unless $k_c = 0$, which leads to an indeterminate result. If one returns equations 3.8a - 3.8f and solves for $E_z = H_z = 0$, one can recover the relation:

$$k_z^2 = \omega\mu\varepsilon = k^2 \quad \textbf{3.10}$$

implying that k_c is indeed zero for the TEM mode.

In this case the potential on the surface of a single conductor waveguide would be a constant, i.e. an equipotential, meaning the TEM mode cannot propagate; an equipotential on the waveguide surface results in cancellation of the transverse electric field; $\vec{E}(x, y) = 0$. The TEM mode can however exist when using waveguides constructed from multiple conductors, this is described in the following section.

3.2.1 Electromagnetic Modes in Smooth Co-axial Waveguide.

For waveguides constructed from multiple conductors, such as co-axial waveguides, the TEM mode can be supported as a static potential between the conductors, i.e. although the potential on a given surface is constant, a potential difference exists between adjacent surfaces, forming an electrostatic field.

In this case $\vec{E}(x, y)$ can be expressed as the gradient of the scalar potential $\Phi(x, y)$:

$$\vec{E}(x, y) = -\vec{\nabla}_{\perp}\Phi(x, y) \qquad \textbf{3.11}$$

where $\vec{\nabla}_{\perp} = \hat{x}\frac{\partial}{\partial x} + \hat{y}\frac{\partial}{\partial y}$ is the transverse component of the gradient operator.

In this case the divergence and curl of equation 3.11:

$$\vec{\nabla}_{\perp} \wedge \vec{E}(x, y) = \vec{\nabla}_{\perp} \wedge (-\vec{\nabla}_{\perp}\Phi(x, y)) = 0 \qquad \textbf{3.12a}$$

and

$$\vec{\nabla}_{\perp} \cdot \vec{E}(x, y) = \vec{\nabla}_{\perp} \cdot (-\vec{\nabla}_{\perp}\Phi(x, y)) = -\vec{\nabla}_{\perp}^{2}\Phi(x, y) = 0 \qquad \textbf{3.12b}$$

express Maxwell's first and third equations for electrostatics respectively (Greiner 1998).

Taking the line integral between the two conductor surfaces, the potential difference can be determined as:

$$V_{12} = \int_{1}^{2} \vec{E} \cdot d\vec{l} = \Phi_1 - \Phi_2 \qquad \textbf{3.13}$$

where Φ_1 and Φ_2 are the potentials on conductors 1 and 2 respectively, with the associated surface currents determined as:

$$I_{1,2} = \oint_{S_1, S_2} \vec{H} \cdot d\vec{l} \qquad \textbf{3.14}$$

taken across the cross-sectional contour of the relevant conductor surface (S_1, S_2).

This electrostatic TEM mode, showing $k_c = 0$ forms the fundamental mode in multi-conductor waveguides, which for circular cross-section co-axial waveguide is described by the field components:

$$E_r = \frac{V}{r\ln(b/a)} \qquad \textbf{3.15a}$$

$$H_\theta = \frac{I}{2\pi r} \qquad \textbf{3.15b}$$

where $E_\theta = E_z = H_r = H_z = 0$. A schematic (r, θ) cross-section of a circular co-axial waveguide is given in Figure 3.2:

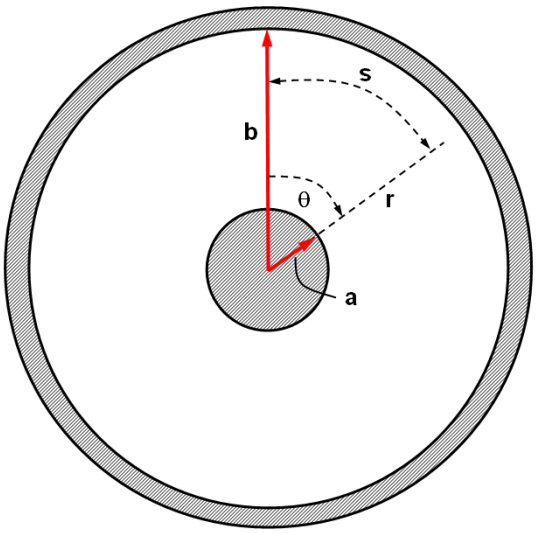

Figure 3.2: Shows the *(r,θ)* schematic cross-section of a circular co-axial waveguide. Here *a* is the radius of the inner conductor *b* is the radius of the outer conductor and *s* is the arc-length subtended by the angle θ at a radius of *r*.

When looking at the higher order modes in co-axial waveguide the cut-off frequencies can be determined via the solutions of equations 3.16a and 3.16b for the TM and TE modes respectively (Marcuvitz 1986):

$$J_m\left(\frac{b}{a}\zeta_n\right) Y_m(\zeta_n) - Y_m\left(\frac{b}{a}\zeta_n\right) J_m(\zeta_n) = 0 \qquad \textbf{3.16a}$$

$$J'_m\left(\frac{b}{a}\zeta'_n\right) Y'_m(\zeta'_n) - Y'_m\left(\frac{b}{a}\zeta'_n\right) J'_m(\zeta'_n) = 0 \qquad \textbf{3.16b}$$

where J_m is the m^{th} order Bessel function of the first kind, Y_m is the m^{th} order Neumann function (Bessel function of the second kind), J'_m and Y'_m are the respective first-order spatial differentials and ζ_n and ζ'_n are the n^{th} non-vanishing root of the relevant Bessel-Neumann combinations. a and b correspond to the radii of the inner and outer conductor surfaces respectively.

Here the "m, n" terminology is synonymous with that presented in Table 1, where, for equation 3.16a, the n^{th} root of the m^{th} Bessel-Neumann combination is associated with the cut-off wave-number of the $TM_{m,n}$ mode, via (Marcuvitz 1986):

$$f_{c_{m,n}} = \frac{v_{ph}\zeta_n}{2\pi(b-a)}\left(\frac{b}{a}-1\right) = \frac{v_{ph}\zeta_n}{2\pi a} \qquad \textbf{3.17}$$

where"m, n" may take the values $m = 0, 1, 2, \ldots$, $n = 1, 2, 3, \ldots$.

The case for the TE modes is a little more complex. For TE modes, with a radial index of $n = 1$ and $m = 1, 2, 3, \ldots$, the cut-off frequencies are determined as:

$$f_{c_{m,1}}' = \frac{v_{ph}\zeta'_1}{2\pi(b+a)}\left(\frac{b}{a}+1\right) = \frac{v_{ph}\zeta'_1}{2\pi a} \qquad \textbf{3.18}$$

where ζ'_1 is the first non-vanishing root, of the m^{th} order Bessel-Neumann combination, given by equation 3.16b. The cut-off frequency of the first higher-order mode, the $TE_{1,1}$ mode, is therefore given by this equation. It should be noted that in the limit $(b/a) \to 1$ this mode approximates better as the $TE_{1,0}$ mode of a rectangular waveguide, where the long transverse dimension is defined by half the circumference of the co-axial line, with a smooth transition to the $TE_{1,1}$ mode of circular waveguide as $a \to 0$ (Harvey 1963).

In contrast, for TE modes where $n > 1$ and $m = 1, 2, 3, \ldots$, the cut-off frequencies are determined using:

$$f_{c_{m,n}}' = \frac{v_{ph}\zeta'_n}{2\pi(b-a)}\left(\frac{b}{a}-1\right) = \frac{v_{ph}\zeta'_n}{2\pi a} \qquad \textbf{3.19}$$

where again, ζ'_n is the n^{th} root of equation 3.16b for a given value of $m > 0$.

For the case where $m = 0$ and $n = 1, 2, 3, \ldots$, the following applies; the $TE_{0,1}$ mode is degenerate with the $TM_{1,1}$ mode (i.e. they share the same cut-off frequency), the $TE_{0,2}$ mode is degenerate with the $TM_{0,1}$ mode, the $TE_{0,3}$ with the $TM_{0,2}$ and so on (Marcuvitz 1986).

Table 2 gives the relevant cut-off frequencies for TE and TM modes in an oversized co-axial line such as that used in the FEM experiment:

Table 2:

TE modes (GHz)

m\n	1	2	3
0	15.05	14.89	29.99
1	1.36	2.15	30.06
2	2.73	15.30	30.15
.	.	.	.
.	.	.	.
.	.	.	.
.	.	.	.
.	.	.	.
24	31.41	37.46	44.92

TM modes (GHz)

m\n	1	2	3
0	14.98	29.99	45.00
1	15.05	30.02	45.02
2	15.24	30.12	45.08
.	.	.	.
.	.	.	.
.	.	.	.
.	.	.	.
.	.	.	.
24	35.88	44.67	55.86

where $a = 30(\pm 0.5)mm$ and $b = 40(\pm 0.5)mm$, giving $b/a \cong 1.33$. The values quoted in table 2 are for the mean values of a and b, with maximum deviations in the cut-off frequencies of $\pm 2\%$ determined across the frequency range of interest $(30 - 40GHz)$.

The constituent field components for the different higher order modes, in co-axial waveguide, are, for the TE modes (Marcuvitz 1986):

$$E_r = \frac{m}{r} Z_m\left(\zeta'_n \frac{r}{a}\right)\left(V_{nA}'' \sin(m\theta) - V_{nB}'' \cos(m\theta)\right) \qquad \textbf{3.20a}$$

$$E_\theta = \frac{\zeta_n}{a} Z'_m\left(\zeta_n \frac{r}{a}\right)\left(V_{nA}'' \cos(m\theta) + V_{nB}'' \sin(m\theta)\right) \qquad \textbf{3.20b}$$

$$E_z = 0 \qquad \textbf{3.20c}$$

$$H_r = -\frac{\zeta'_n}{a} Z'_m\left(\zeta'_n \frac{r}{a}\right)\left(I_{nA}'' \cos(m\theta) + I_{nB}'' \sin(m\theta)\right) \qquad \textbf{3.20d}$$

$$H_\theta = \frac{m}{r} Z_m\left(\zeta'_n \frac{r}{a}\right)\left(I_{nA}'' \sin(m\theta) - I_{nB}'' \cos(m\theta)\right) \qquad \textbf{3.20e}$$

$$H_z = -i\sqrt{\frac{\varepsilon}{\mu}}\frac{\lambda}{\lambda_{cn}}\frac{\zeta'_n}{a}Z_m\left(\zeta'_n\frac{r}{a}\right)(V_{nA}''\cos(m\theta) + V_{nB}''\sin(m\theta)) \qquad \textbf{3.20f}$$

and for the TM modes:

$$E_r = -\frac{\zeta_n}{a}X'_m\left(\zeta_n\frac{r}{a}\right)(V_{nA}'\cos(m\theta) + V_{nB}'\sin(m\theta)) \qquad \textbf{3.21a}$$

$$E_\theta = \frac{m}{r}X_m\left(\zeta_n\frac{r}{a}\right)(V_{nA}'\sin(m\theta) - V_{nB}'\cos(m\theta)) \qquad \textbf{3.21b}$$

$$E_z = -i\sqrt{\frac{\mu}{\varepsilon}}\frac{\lambda}{\lambda'_{cn}}\frac{\zeta_n}{a}X_m\left(\zeta_n\frac{r}{a}\right)(I_{nA}'\cos(m\theta) + I_{nB}'\sin(m\theta)) \qquad \textbf{3.21c}$$

$$H_r = -\frac{m}{r}X_m\left(\zeta_n\frac{r}{a}\right)(I_{nA}'\sin(m\theta) - I_{nB}'\cos(m\theta)) \qquad \textbf{3.21d}$$

$$H_\theta = -\frac{\zeta_n}{a}X'_m\left(\zeta_n\frac{r}{a}\right)(I_{nA}'\cos(m\theta) + I_{nB}'\sin(m\theta)) \qquad \textbf{3.21e}$$

$$H_z = 0 \qquad \textbf{3.21f}$$

where $V_{nA,B}''$ and $V_{nA,B}'$ are the (independently varying) z-dependant voltage amplitudes of the TM and TE modes respectively, $I_{nA,B}''$ and $I_{nA,B}'$ are the corresponding z-dependant current amplitudes and ζ_n and ζ'_n are the relevant roots of equations 3.16a - 3.16b. λ is the free-space wavelength and $\lambda_{cn} = f_{m,n}/v_{ph}$, $\lambda'_{cn} = f_{m,n}'/v_{ph}$.

The functions $Z_m\left(\zeta'_n\frac{r}{a}\right)$ and $X_m\left(\zeta_n\frac{r}{a}\right)$ are defined as:

$$Z_m\left(\zeta'_n\frac{r}{a}\right) = \frac{\sqrt{\pi\varepsilon_m}}{2}\frac{J_m\left(\zeta'_n\frac{r}{a}\right)Y'_m(\zeta'_n) - Y_m\left(\zeta_n\frac{r}{a}\right)J'_m(\zeta'_n)}{\sqrt{\left[J'_m(\zeta'_n)/J'_m\left(\frac{b}{a}\zeta'_n\right)\right]^2(1-[ma/b\zeta_n]^2)(1-[m/\zeta'_n]^2)}} \qquad \textbf{3.22a}$$

and

$$X_m\left(\zeta_n\frac{r}{a}\right) = \frac{\sqrt{\pi\varepsilon_m}}{2}\frac{J_m\left(\zeta'_n\frac{r}{a}\right)Y_m(\zeta'_n) - Y_m\left(\zeta_n\frac{r}{a}\right)J_m(\zeta'_n)}{\sqrt{\left[\frac{J'_m(\zeta'_n)}{J'_m((b/a)\zeta'_n)}\right]^2 - 1}} \qquad \textbf{3.22b}$$

where $\varepsilon_m = 1$ if $m = 0$, otherwise $\varepsilon_m = 2$ and $m = 1, 2, 3, \ldots$.

A schematic of the field lines of the first few modes in co-axial waveguide is given in Figure 3.3 (Harvey 1969):

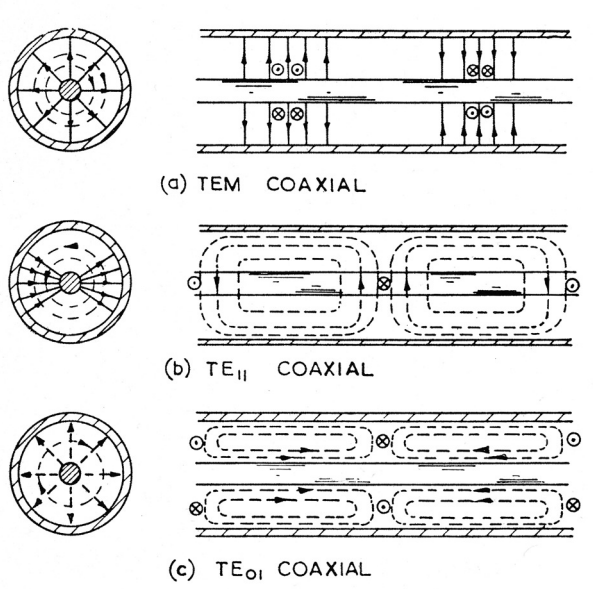

Figure 3.3: Shows the field lines for the TEM, TE_{11} and TE_{01} modes, in co-axial waveguide, in different cross-sections (Harvey 1969).

which can be compared with those of circular waveguide (see Figure 3.4 (Thumm 1997)).

When comparing similar modes in co-axial waveguide and cylindrical waveguide a note on nomenclature is again needed here. In addition to the TE-TM, H-E nomenclatures for basic waveguide modes, the two extreme limiting cases of $a \to b$ and $a \to 0$ in the ratio b/a has resulted in the existence of two distinct reference schemes for the radial mode index. Where the radial indices are determined from the case $a \to b$ (Waldron 1969) the mode profiles most closely resemble those of rectangular waveguide, giving the first higher order mode the designation $TE_{1,0}$. This leads to the relation $n_{\text{circ}} = n_{\text{co-ax}} + 1$. Given that the $TE_{m,0}$ modes only truly exist in co-axial waveguide when one operates in the $a \to b$ limiting case (Kirkman & Kline 1946, Harvey 1963), this work follows the more common assumption of $a \to 0$ as its basis, giving the relation $n_{\text{circ}} = c_{\text{co-ax}}$ (Kirkman & Kline 1946, Harvey 1963,

Marcuvitz 1986, Pozar 1998) as the resultant field profiles most closely approximate those of circular waveguide. As one moves from one of these two limiting cases to the other, the field profiles are considered to move smoothly from one (say $n_{\text{circ}} = n_{\text{co-ax}} + 1$) reference scheme to the other ($n_{\text{circ}} = n_{\text{co-ax}}$) (Bracewell 1947, Harvey 1963).

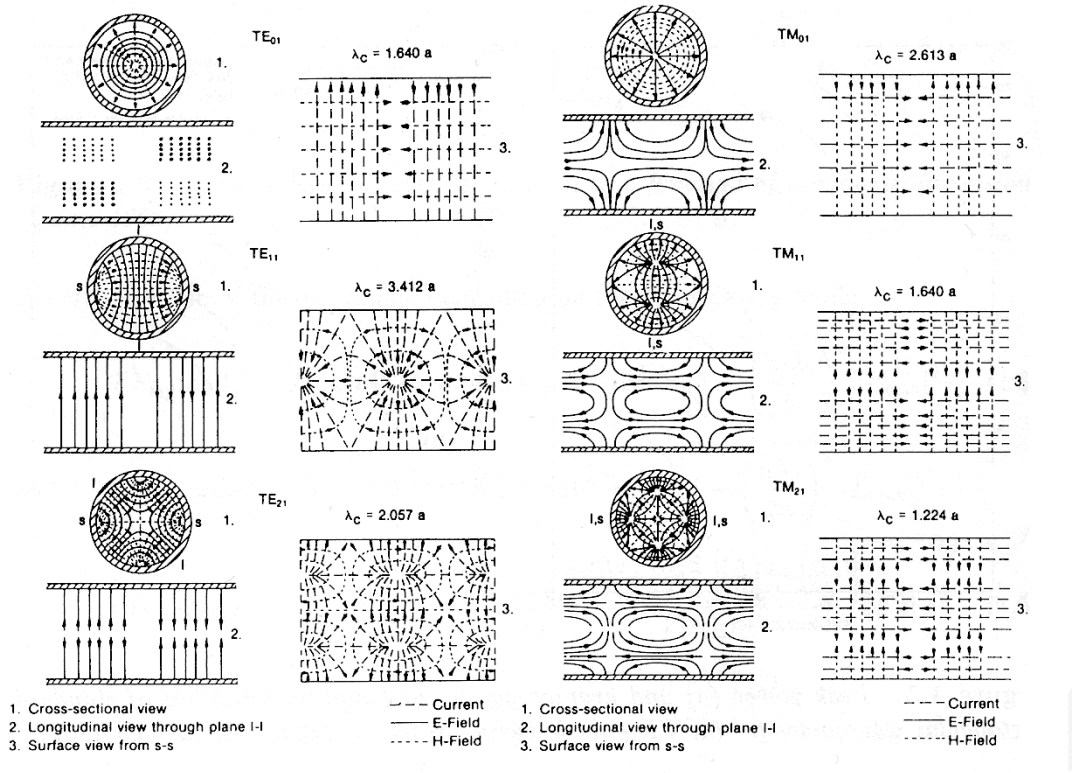

Figure 3.4: Shows the field lines for some circular waveguide modes, noting the first few TE and TM modes in different cross-section views (Thumm 1997).

The distinction between the two reference schemes is worthy of note as both are used with the H-E and TE-TM nomenclature throughout the relevant literature, meaning the $H_{m,0}$, $TE_{m,0}$, $H_{m,1}$ and $TE_{m,1}$ modes, read across different texts, may in fact all refer to the same mode (for a given value of m).

3.2.2 Propagation of EM Waves in Smooth Co-axial Waveguide.

The propagation of an EM wave through a given medium can be described via the Helmholtz equation (Grant & Phillips 1990, Jackson 1999, Vanderlinde 2004), expressed in phasor form for the E field as the curl of equation 3.6:

$$\nabla^2 E + \omega^2 \mu \varepsilon E = 0 \qquad \textbf{3.23}$$

with a similar equation derivable for the H field if required. The form shown corresponds to the case where the EM wave profile is invariant with time, allowing suppression of the common $e^{i\omega t}$ factor (Harvey 1969, Pozar 1998).

If we now consider the characteristic impedance (Z_0) of the co-axial line (which is set purely by the geometry of the line) as:

$$Z_0 = \frac{\ln(b_0/a_0)}{2\pi}\sqrt{\frac{\mu}{\varepsilon}} \qquad \textbf{3.24}$$

where a_0 and b_0 are the radii of the unperturbed inner and outer conductor surfaces, respectively.

and assume operation in the fundamental TEM mode, where the wave-impedance (Z_w) takes the form:

$$Z_w = \frac{E_r}{H_\theta} = \frac{\omega\mu}{k} = \sqrt{\frac{\mu}{\varepsilon}} \qquad \textbf{3.25}$$

substitution of equation 3.25 into equation 3.24 yields a relation for the wave-number as:

$$k = \omega\sqrt{\mu\varepsilon} = \frac{\omega\mu \ln(b/a)}{2\pi Z_0} \qquad \textbf{3.26}$$

giving the Helmholtz equation the form:

$$\nabla^2 E + k^2 E = \nabla^2 E + \frac{\omega^2\mu^2}{4\pi^2 Z_0^2}\ln^2\left(\frac{b_0}{a_0}\right)E = 0 \qquad \textbf{3.27}$$

If the waveguide incorporates a region where the ratio b_0/a_0 shows some periodic variation, this is reflected in the natural log term of equation 3.27, expressing the Helmholtz equation accounting for the changing geometry of the waveguide. Sections 3.3.1 and 3.3.2 describe the modifications incurred to equation 3.27 resulting from the introduction of 1D and 2D periodic structures within co-axial waveguide.

3.3 Bragg Reflectors Formed by Surface Corrugations.

A Bragg reflector, in the simplest sense, is a frequency selective mirror, formed by introducing some periodicity in propagation path of an EM wave. They operate over a a finite band-width, for a given interacting mode, out-with which the reflector appears transparent to the incident EM wave, allowing it to radiate through. The operational band-width and interacting mode(s), varies dependant on the form of Bragg reflector used, as discussed in the following section.

The Bragg structures used in this work were formed by introducing corrugations on the inner conductor surface of an over-sized co-axial waveguide. Such corrugations allow the introduction of periodicities in the axial and azimuthal directions, which may or may not result in the formation of stop-bands (reflection zones) depending on the form of corrugation presented. Examples of two so-called 1D Bragg corrugations are shown in Figure 3.5, both of which are described by the sinusoidal function given in equation 3.28 (though it can be readily seen only the $M = 0$ case results in the formation of a reflector):

$$r(\theta, z) = r_0 + r_1 \cos(M\theta + h_z z) \qquad \textbf{3.28}$$

where r_0 is the mean radius of the conductor surface, r_1 is the amplitude of the corrugation, $h_z = 2\pi/d_z$ is the axial corrugation wave-number and d_z is the axial period. M is the total number of periodic variations seen across the azimuth, while θ is the angle (in radians), subtended along the conductor surface (s) with mean radius r_0.

For corrugations where both M and h_z are non-zero equation 3.28 describes a helical corrugation of order M, which rotates in a clockwise ($-M$) or anti-clockwise ($+M$) direction along z. The introduction of such a corrugation, to the surface of a waveguide, allows for "scattering" of EM waves as they propagate through the perturbed waveguide region.

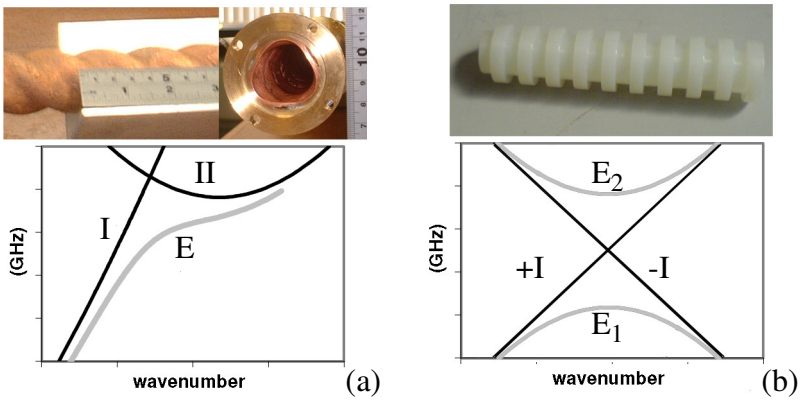

Figure 3.5: (a) Shows a three-fold helix (*M=3*)along with its dispersion diagram, noting coupling between spatial harmonics of a lower (I) and upper (II) waveguide mode, forming the eigenmode (E). (b) Shows a 1D Bragg reflector (*M=0*) formed by a corrugated dielectric insert, noting coupling between successive spatial harmonics of the same mode (+I & -I), resulting in the creation of a band-gap defined between the eigenmode (E_1 & E_2).

The eigenmodes produced in such structures can be used to aid EM pulse compression (Danilov et al. 2000, Burt et al. 2004, Samsonov et al. 2004), as the operating modes in active devices (McDermott et al. 1996, Denisov et al. 1998, Wei et al. 2002) and in the low-loss operation of antenna feeders (Jecko & Papiernik 1983). Corrugations with $M = 0$ result in the formation of 1D Bragg reflectors (Denisov & Reznikov 1982, Bratman et al. 1983, Swegle et al. 1985, Fuks et al. 2004, Ginzburg et al. 2006) while corrugations with $h_z = 0$ are used as high-order mode suppressors in high-power, high frequency gyrotrons (Kononenko & Gandel 2006, Ioannidis et al. 2008). The $M = 0$ case will be developed further in Section 3.3.1. Examples of a three-fold ($M = -3$) helix and a 1D Bragg reflector ($M = 0$) are given in Figure 3.5.

The difference in operation is clearly evident in the accompanying dispersion diagrams; in the case of the helical Bragg structure the eigenmode E is continuous in its transition between modes I and II, meaning no stop-band (band-gap) is created, making structures described by equation 3.28, with $M \neq 0$, unsuitable for use as reflectors. In the case of the 1D Bragg reflector the eigenmodes $E_{1,2}$ do result in the formation of a stop-band, in the region of the intersection between the incident (+I) and scattered (-I) waves. A corrugation where $M \neq 0$ which does generate band-gaps will be discussed later.

In all cases, provided the amplitude of the corrugation conforms to the limit:

$$\delta_{skin} < r_1 < \lambda/4 \qquad \textbf{3.29}$$

where δ_{skin} is the skin depth and λ is the resonant EM wavelength, the introduction of a corrugation can be considered to create a series of "spatial" harmonics of the waveguide modes, separated regularly in k_z by integer values of h_z.

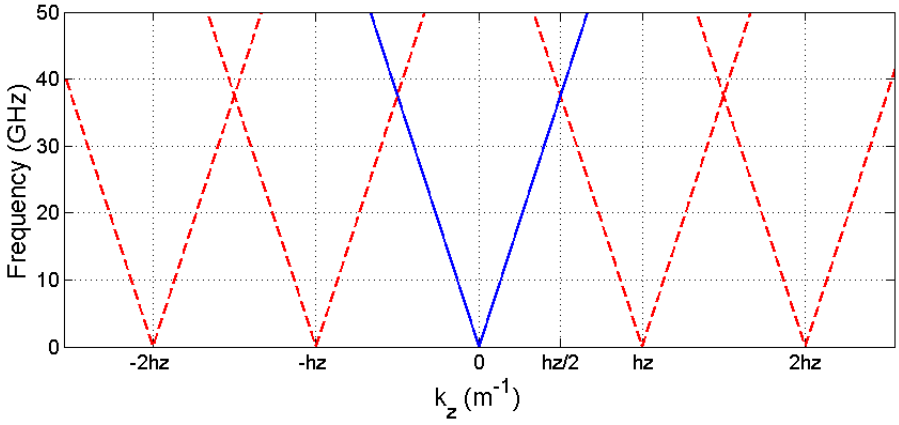

Figure 3.6: Shows the uncoupled spatial harmonics of the TEM mode in co-axial waveguide, with a corrugation wave-number of h_Z. Resonant coupling occurs at the intersections of the spatial harmonics, occurring at $k_Z = nh_Z/2$ where $n = +/-1, +/-3,...$

Considering the 1D Bragg reflector, coupling between spatial harmonics occurs at the intersection of successive harmonics of the same mode at $k_z = nh_z/2$, where $n = \pm 1, \pm 3, \pm 5, \ldots$. In the limit $r_1 \cong \delta_{skin}$ the degree of coupling can be considered

negligible, allowing the dispersion curves to be considered to follow that of the unperturbed case (see Figure 3.6).

As the amplitude of the corrugation increases away from δ_{skin}, the coupling between harmonics increases, forming eigenmodes (see Figure 3.5(b)). The limit $r_1 < \lambda/4$ is chosen to ensure the corrugation amplitude is not comparable to the axial period of the corrugation itself. As this upper limit is approached the waveguide begins to approximate better as a series of conjoined cavities and the eigenmode solution would no-longer apply.

Provided one works within the limits imposed by equation 3.29, perturbation theory may be used in calculating the wave equations for the resultant eigenmodes (Yariv & Nakamura 1977, Konoplev 2001, Burt 2004, Burt et al. 2004, Nusinovich 2004, McGrain 2006, Yariv & Yeh 2006), with effective coupling between successive spatial harmonics occurring when the Bragg resonance conditions are met. In the case of 1D Bragg reflectors, where the interaction is simply between a $+z$ propagating incident wave and a $-z$ propagating scattered wave, these conditions are expressed as:

$$h_z = k_{+z} + k_{-z} \qquad \textbf{3.30a}$$

and

$$M = m_+ - m_- \qquad \textbf{3.30b}$$

where the $\pm$ subscripts denote quantities associated with the forward propagating (incident) and backward propagating (scattered) partial-waves respectively. Here m shares its definition with that given in Table 1, corresponding to the azimuthal periodicities of the interacting waves (i.e. the $TE_{24,1}$ mode has $m = 24$).

At this stage it is useful to consider a slightly different representation of equation 3.28. Taking that a single azimuthal period has an arc-length of $d_s = (2\pi r_0)/M$ which, moving to the quasi-cartesian co-ordinate $s = \theta r_0$, gives the azimuthal period a wave-number $h_s = M/r_0$.

Noting the relation between s and θ one may then express equation 3.28 as:

$$r(s, z) = r_0 + r_1 \cos(h_s s + h_z z) \qquad \textbf{3.31}$$

In practical terms either $M\theta$ or $h_s s$ may be used in defining the azimuthal periodicity, as $h_s s = M\theta$, however for substitution into the Helmholtz equation there are some advantages in choosing the $h_s s$ definition as this allows a clearer relation to the transverse (cut-off) wave-numbers of the interacting modes to be seen. This is particularly true when dealing with the case of a 2D Bragg reflector, where the cut-off wave-number of the higher order mode is important for proper operation of the reflector.

As stated, corrugations described by equation 3.28, showing $h_s \neq 0$ $(M \neq 0)$ do not produce band-gaps in their dispersion profiles. Such a reflector may however be realised using a Bragg structure described by:

$$r(\theta, z) = r_0 + r_1(\cos(h_s s + h_z z) + \cos(h_s s - h_z z)) \qquad \textbf{3.32}$$

where the axial and azimuthal wave-numbers of the corrugation should satisfy the relation $h_z \cong h_s$, with the ideal case being $h_z = h_s$.

These so-called 2D Bragg structures (due to the 2D nature of the corrugation) are more commonly described in the form:

$$r(s, z) = r_0 + 2r_1 \cos(h_s s)\cos(h_z z) \qquad \textbf{3.33}$$

where all terms share common meanings with those of equation 3.31.

This produces a structure which has Bragg-vectors $\vec{h}_{+\mathrm{L,R}}$ and $\vec{h}_{-\mathrm{L,R}}$, where the $\pm$ subscripts denote propagation in the $\pm z$ direction as before and the subscripts L,R denote the polarisation of the vector as either Left or Right-handed respectively. These are shown schematically in Figure 3.7, expressed on a square-wave 2D Bragg structure, similar to that used in the FEM experiment (c.f. Section 5.4.2).

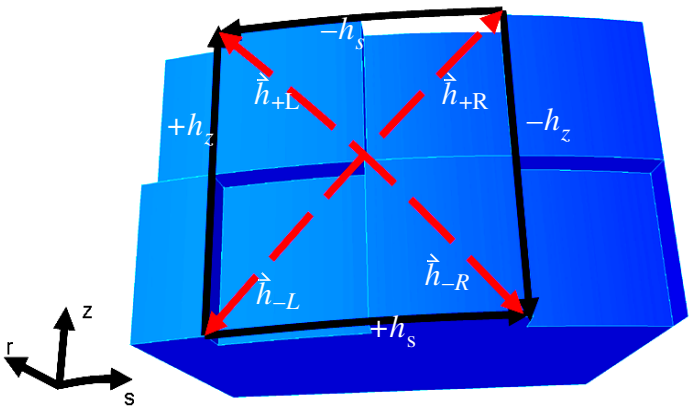

Figure 3.7: Schematic of the 2D Bragg vectors across one period of a square-wave 2D Bragg structure. The Bragg wave-numbers h_s and h_z are shown along with the resultant Bragg-vectors h_+ and h_-.

As may be inferred from Figure 3.7, the coupling mechanism for such structures is markedly more complex than that of 1D Bragg structures, as the Bragg resonance condition has to be satisfied for both Bragg-vectors for coupling to occur. This is achieved through the scattering of a $+z$ propagating A_+ wave into a close to cut-off $B_\pm$ mode, which in turn scatters into a $-z$ propagating A_- wave (Ginzburg et al. 1996, Ginzburg et al 1999, Konoplev et al. 2000, Konoplev 2001, Cross et al. 2003, Ginzburg et al. 2004), noting that all waves here are considered to be linearly polarised. This forms a 2D "feedback loop" $A_+ \leftrightarrow B_\pm \leftrightarrow A_-$ giving indirect coupling of the A_+ and A_- waves, creating a band-gap similar to that of the 1D Bragg reflector.

This feedback loop is intrinsic to the special nature of 2D Bragg reflectors. If one considers an over-sized co-axial drift-tube, incorporating a 2D corrugation of the form described by equation 3.33, with a +z propagating electron beam, the $A_+ \leftrightarrow B_\pm \leftrightarrow A_-$ feedback loop allows for synchronisation of radiation emitted across the azimuth. This greatly improves phase stability and mode control over the azimuthal index when compared to conventional 1D Bragg reflectors, allowing a move to increasingly over-sized interaction regions and so increased potential output powers, with little degradation in the quality of the output.

Efficient coupling between the $A_{\pm}$ and $B_{\pm}$ partial-waves only occurs when the Bragg resonance conditions are met, which in this case take the form:

$$\hat{h}_{+\mathrm{L}} = -k_z\hat{z} + k_s\hat{s} \qquad \textbf{3.34a}$$

$$\hat{h}_{+\mathrm{R}} = -k_z\hat{z} - k_s\hat{s} \qquad \textbf{3.34b}$$

$$\hat{h}_{-\mathrm{L}} = k_z\hat{z} + k_s\hat{s} \qquad \textbf{3.34c}$$

$$\hat{h}_{-\mathrm{R}} = k_z\hat{z} - k_s\hat{s} \qquad \textbf{3.34d}$$

Noting that the incident (A_+) and reflected (A_-) partial waves in the 2D Bragg reflector are of the same mode (namely the TEM mode in the work presented), the relation between the resonant wave-numbers of the EM waves and the corrugation can be rewritten in scalar form as $k_{+z} \approx k_{-z} \approx h_z$ and $k_{+s} \approx k_{-s} \approx h_s$.

As in the case of the 1D Bragg reflector, interaction of the EM wave with the corrugation produces spatial harmonics stepped in k_z by integer values of the corrugation wave-vector. Figure 3.8 shows the uncoupled ($\delta_z \approx r_1$) spatial harmonics of the TEM mode in a 2D Bragg reflector, stepped in k_z by integer values of h_z over the same range as that shown in Figure 3.6 for the 1D Bragg reflector:

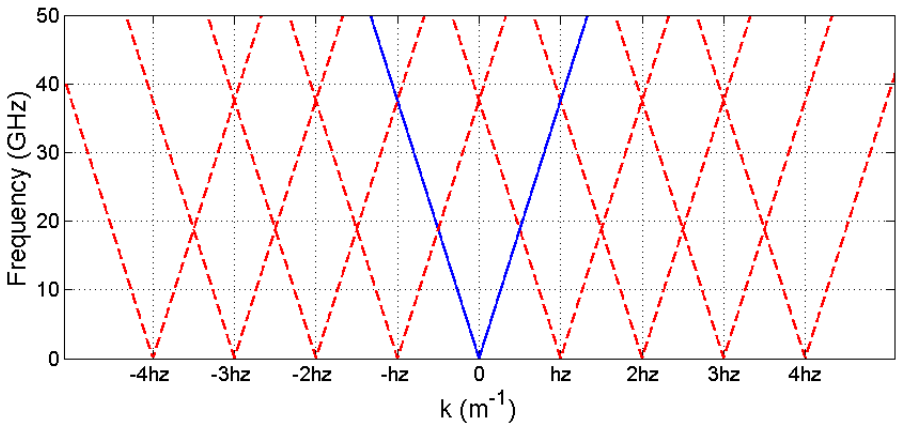

Figure 3.8: Shows the uncoupled spatial harmonics of the TEM mode in co-axial waveguide, with an axial corrugation wave-number of h_z, for the same range in k as Figure 3.6. Resonant coupling occurs only at $k_z = nh_z$ where n = *+/-1, +/-2, +/-3,...*

In this case resonant coupling only occurs at intersections satisfying equations 3.34a - 3.34d, i.e. $k_{s,z} = nh_{s,z}$ with $n = \pm 1, \pm 2, \pm 3, \ldots$. As before, when $\delta_z < r_1$ the resonant modes begin to couple, forming stop-bands centred on $k_z = nh_z$. As will be shown in Section 3.3.2.2 these stop-bands show different dependences on the corrugation parameters than in 1D Bragg reflectors (c.f. Section 3.3.1.2), allowing for the production of much tighter reflection zones which only form via the interaction of a highly selective set of mode couplings.

In terms of FEM operation, the initial implication of this, along with the advantages of increased stability due to increased mode selectivity, is that a lasing cavity defined by 2D Bragg input and output reflectors, would result in a marked improvement in spectral purity and microwave output power. While the single frequency operation of such a cavity has been verified, power losses to the transverse fluxes in the input and output mirrors reduced the available output power to $\sim 15MW$ (McGrane 2006, Konoplev et al. 2006b, Konoplev et al. 2007).

If one instead constructs a lasing cavity defined by a 2D Bragg input mirror and a 1D Bragg output mirror, the losses to the transverse fluxes can be halved, along with an overall reduction of the cavity Q-factor. Such a cavity should allow for improvement to both the output power observed and the profile of the microwave pulse, without any appreciable degradation in the spectral content. The following sections describe the relevant theory for both 1D and 2D Bragg reflectors, required to design such a cavity, with more complete derivations provided in Appendices A and B for the 1D and 2D Bragg reflectors respectively.

3.3.1 Mode Propagation and Coupling in 1D Bragg Reflectors.

For a corrugation, defined as in equation 3.28, presented on either the inner or outer conductor of a co-axial waveguide, the Helmholtz equation (equation 3.27) can be shown to reduce to:

$$\nabla^2 E + k_z^2 E + \frac{2k_z^2}{\ln(b_0/a_0)} \ln(1 + \chi\cos(M\theta + h_z z))E = 0 \qquad \textbf{3.35}$$

where a_0 and b_0 are the unpertubed radii of the inner and outer conductors respectively, r_1 is the corrugation amplitude and $\chi = r_1/b_0$ or $\chi = r_1/a_0$ depending on the surface showing the corrugation.

Taking $M = 0$, with the magnitude of the E field considered as:

$$E(z) = Re(A_+ e^{-ik_{z+}z} + A_- e^{ik_{z-}z})e^{-i\omega t} \qquad \textbf{3.36}$$

where $A_\pm$ are, respectively, the amplitudes of the incident and scattered partial waves, substituting equation 3.36 into equation 3.35 and following the steps laid out in Appendix A yields:

$$\frac{dA_+}{dz} + i\kappa k_z A_- e^{2i(\delta_z - i\sigma_z)z} = 0 \qquad \textbf{3.37a}$$

$$\frac{dA_-}{dz} - i\kappa k_z A_+ e^{-2i(\delta_z - i\sigma_z)z} = 0 \qquad \textbf{3.37b}$$

where κ is the coupling co-efficient:

$$\kappa = \frac{\chi}{2\ln(b_0/a_0)} \qquad \textbf{3.38}$$

and $(\delta_z - i\sigma_z)$ is the detuning from resonance, defined as:

$$\delta_z - i\sigma_z = k_z - \frac{h_z}{2} - i\sigma_z \qquad \textbf{3.39}$$

where δ_z is the detuning from Bragg resonance in a loss less system and $i\sigma_z$ represents the losses due to the finite conductivity of the waveguide walls.

Taking the amplitudes of the partial-waves to be functions of the detuning from h_z, equations 3.37a and 3.37b become:

$$\frac{dA'_+}{dz} + i(\delta'_z - i\sigma)A'_+ + i\kappa k_z A'_- = 0 \qquad \textbf{3.40a}$$

$$\frac{dA'_-}{dz} - i(\delta'_z - i\sigma)A'_- - i\kappa k_z A'_+ = 0 \qquad \textbf{3.40b}$$

Equations 3.40a and 3.40b represent the wave equations for the incident and scattered waves as they propagate along z.

3.3.1.1 Dispersion Relation of 1D Corrugated Co-axial Waveguide.

Consider the partial-wave amplitudes to be functions of the solutions of the eigenmodes (Λ) within the waveguide:

$$A'_\pm(z) = a_\pm e^{\Lambda z} \qquad \textbf{3.41}$$

where Λ is unknown and considered to be complex.

Substitution of Λ into equations 3.40a and 3.40b, leads to the relation:

$$\pm\Lambda = \pm\sqrt{\kappa^2 k_z^2 - (\delta'_z - i\sigma)^2} \qquad \textbf{3.42}$$

where Λ is related to the perturbed wave-number (k'_z) of the eigenmodes by $\Lambda = -ik'_z$.

Rearranging for δ_z and combining with equation 3.39 leads to the dispersion relation:

$$\omega_{1,2} = \frac{h_z}{2}\left(n + \frac{1}{1-\kappa^2}\left[1 \pm \sqrt{\kappa^2 + \frac{4[k'^2_z + \sigma_z^2 + i\sigma_z h_z](1-\kappa^2)}{h_z^2}}\right]\right)c \qquad \textbf{3.43}$$

where $n = 0, 1, 2, \ldots$ is an integer referring to the order of the spatial harmonic.

Figures 3.9 and 3.10, show the dispersion plots for similar corrugations, placed independently on the outer and inner conductor surfaces respectively.

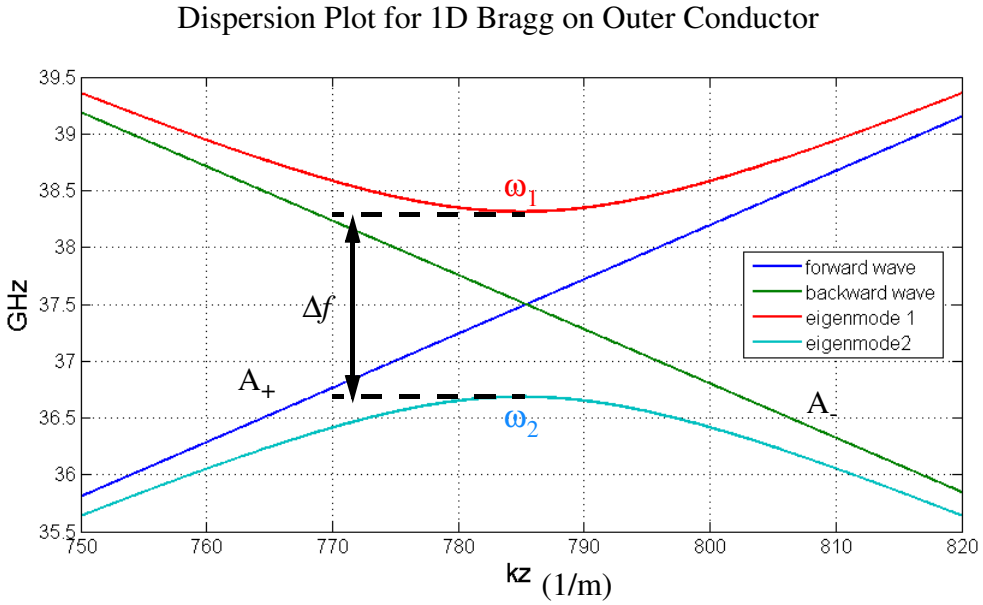

Figure 3.9: Shows the dispersion curves for a_0 = *30mm,* b_0 = *40mm, d = 4mm* with a corrugation amplitude on the outer conductor surface of *+/-0.5mm.* $\kappa k_z = 17.06m^{-1}$, Δf *= 815MHz,* $k_{z0} \sim 785m^{-1}$**.**

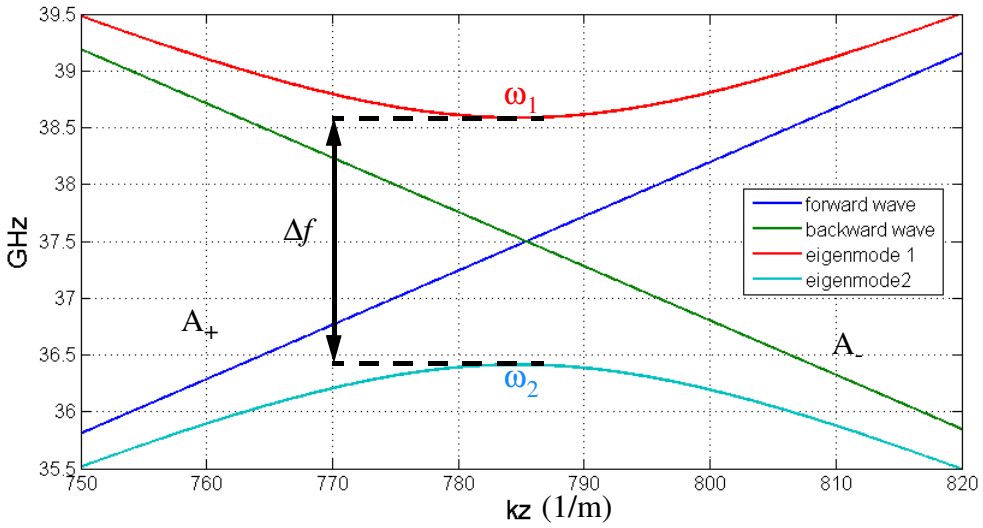

Figure 3.10: Shows the dispersion curves for a_0 = *30mm,* b_0 = *40mm, d =4mm,* with a corrugation amplitude on the inner conductor surface of *+/-0.5mm.* $\kappa k_z = 22.76m^{-1}$, f *= 1.09GHz,* $k_{z0} \sim 785m^{-1}$.

This shows that for a given corrugation amplitude the coupling between the incident and scattered waves is stronger when the corrugation is presented on the inner conductor surface, indicating a shallower corrugation can be employed on the inner surface to obtain a given value of Δf, where Δf corresponds to the spectral width of the reflection band.

3.3.1.2 Reflection and Transmission Co-efficients of 1D Reflectors

The reflection zones shown in Figures 3.9 and 3.10, correspond to regions where the solutions of Λ are real. The magnitude of such zones can be determined in reference to the reflection($R(z)$) and transmission ($T(z)$) coefficients, related by:

$$|T|^2 = 1 - |R|^2 - |\Omega|^2 \qquad \textbf{3.44}$$

where Ω denotes the total system losses.

For an incident wave entering the reflector at $z = 0$, the amplitudes of the partial-waves obey the limits $A'_+(z)\big|_{z=0} = 1$ and, $A'_-(z)\big|_{z=l_{1D}} = 0$, where l_{1D} is the axial length of the corrugation.

If the partial-wave amplitudes are taken as functions of Λ, where Λ has solutions of the form given in equation 3.42, one obtains a general form for the reflection co-efficient as:

$$|R(z)| = \left|\frac{A'_-(z)}{A'_+(z)}\right| = \left|i\kappa k_z\left[\frac{1}{\Lambda\coth(\Lambda(z-L_{1D})) - i(\delta_z - i\sigma_z)}\right]\right| \qquad \textbf{3.45}$$

which shows a maximum at $z = 0$.

The performance of the reflector can be varied by altering the amplitude of the corrugation and / or the number of axial periods. Figure 3.11 shows $|R(z)|$ for a set corrugation length of 75 periods ($30cm$) and corrugation amplitudes in the range $0.1 - 0.3mm$. In contrast Figure 3.12 shows $|R(z)|$ for a set amplitude of $0.3mm$ and corrugation lengths of $20 - 80$ periods. In both cases $d_z = 4mm$ and $\Omega = 0.2$.

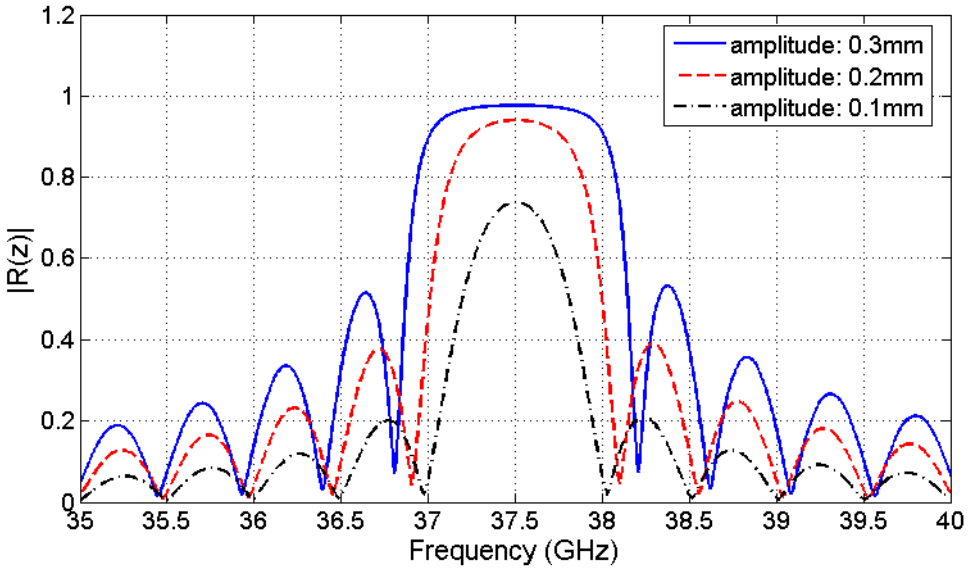

Figure 3.11: Shows the reflection co-efficient for 1D Bragg reflectors, *30cm* long, with periodicities of *4mm* and corrugation amplitudes of *0.3mm, 0.2mm and 0.1mm.* $\Omega = 0.2$.

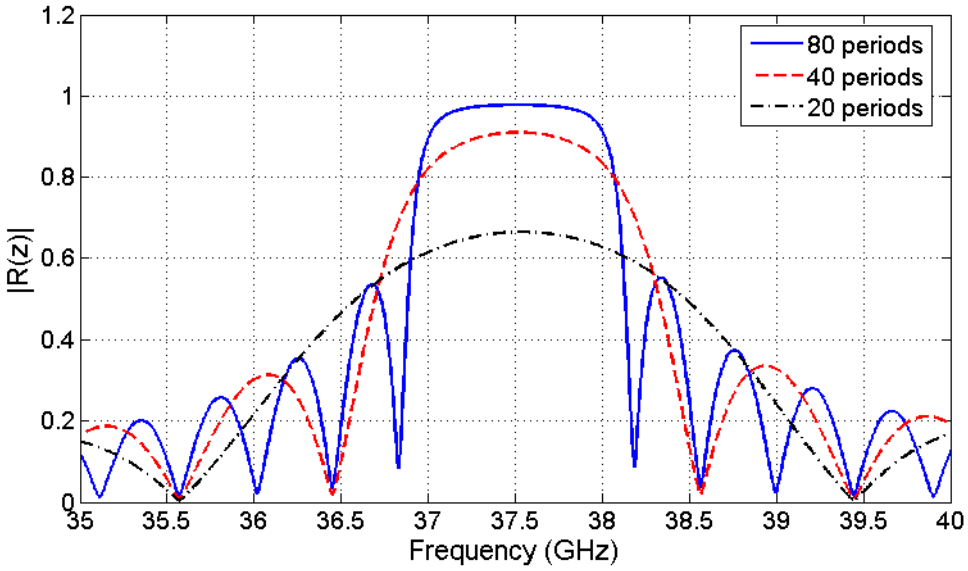

Figure 3.12: Shows the reflection co-efficient for 1D Bragg reflectors, with a set amplitude of *0.3mm*, for corrugations *20, 40* and *80* periods in length. The periodicity is again *4mm* with $\Omega = 0.2$.

Looking at Figure 3.11 it can be seen that, for a given corrugation length, increasing the amplitude of the corrugation results in a slight broadening of the reflection band along with a marked increase in the magnitude of the reflection. From Figure 3.12 it can be seen that, for a given corrugation amplitude, increasing the number of periods also results in an increase in the magnitude of the reflection, along with a narrowing of the reflection band, but for a marked change the corrugation length has to be roughly doubled, i.e. the reflection band-width depends most strongly on the amplitude of the corrugation.

It should be noted that for over-sized waveguides, multiple propagating modes may satisfy the Bragg resonance conditions. Provided any overlap between successive band-gaps is negligible, the reflection co-efficient takes the form $R(z) = \sum R_i(z)$, where $R_i(z)$ correspond to the reflection co-efficient due to the $i'th$ set of eigenmodes, with the consequence $T(z) = \sum T_i(z)$. Figure 3.13 compares the numerically determined and experimentally measured transmission profiles of such a waveguide (Konoplev et al. 2005).

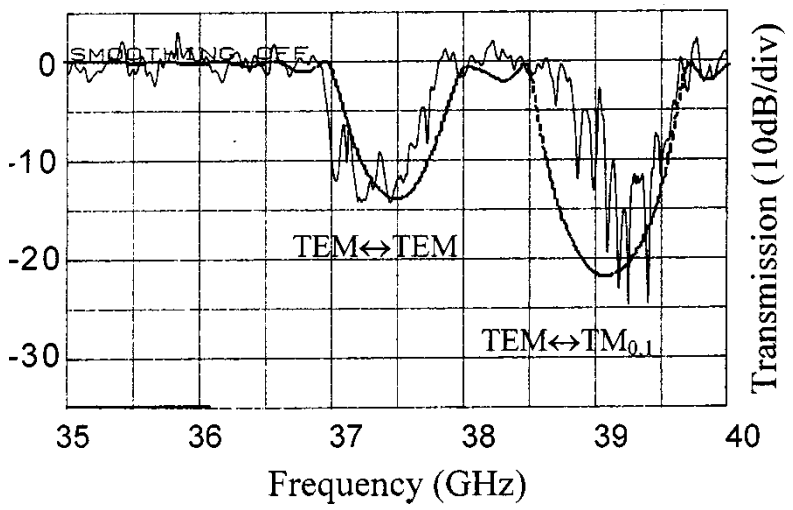

Figure 3.13: Shows the experimentally measured and numerically determined transmission profile for a *30cm* long 1D Bragg reflector with a corrugation amplitude of *+/-0.3mm*, located on the inner conductor surface of an over-sized Ka-band (*26.4 - 40GHz*) co-axial waveguide.

The presence of higher order mode coupling is clearly evident in Figure 3.13, however purely fundamental operation (TEM - TEM) of the reflector is also readily observed. This indicates TEM - TEM operation may be maintained, with limited loss of energy to the TEM - $TM_{0,1}$ interaction, provided the operating frequency of a system using such a mirror is kept in the region of $37 - 38 GHz$.

3.3.2 Mode Propagation and Coupling in 2D Bragg Reflectors.

Following a similar process as for the 1D Bragg reflector, to determine the effect the presence of a 2D Bragg reflector on the Helmholtz equation, one can express the periodic variation induced by a structure of the form:

$$r(z, s) = r_0 + 2r_1 \cos(h_s s)\cos(h_z z) \qquad \textbf{3.46}$$

within the natural log term of equation 3.27.

With this in mind, consider that the radial wave-number of the Bragg structure is undefined here, i.e. $h_r = 0$. Therefore:

$$h_\tau = \sqrt{h_s^2 + h_r^2} = h_s \qquad \textbf{3.47}$$

where h_τ is the combined transverse co-ordinate of the Bragg structure.

The Helmholtz equation can therefore be expressed as:

$$\nabla^2 E + k^2 E + \frac{4k^2\chi}{\ln(b_0/a_0)}\cos(h_\tau \tau)\cos(h_z z)E = 0 \qquad \textbf{3.48}$$

as outlined in Appendix B, where τ is the combined transverse co-ordinate.

Recalling that a helical Bragg structure results in coupling of spatial harmonics of different waveguide modes and that a 2D Bragg reflector is essentially a super-position of two such structures, the E field in this case is composed of four, rather than two partial waves, corresponding to the axial incident and scattered waves found in the 1D

Bragg reflector ($A_{\pm}$) and the counter-rotating partial waves of a higher-order mode which satisfies the Bragg resonance conditions with the incident wave ($B_{\pm}$):

$$E(\tau, z) = (A_{+}e^{-ik_{zA}z} + A_{-}e^{ik_{zA}z})e^{\pm ik_{cA}\tau} + (B_{+}e^{-ik_{zB}z} + B_{-}e^{ik_{zB}z})e^{\pm ik_{cB}\tau} \qquad \textbf{3.49}$$

where k_{zA} & k_{zB} are the axial wave-numbers of partial-waves A and B respectively and k_{cA} & k_{cB} are the corresponding partial-wave cut-off wave-numbers.

Equation 3.49 can be further expanded in terms of the degenerate counter-polarised modes as:

$$E(\tau, z) = \begin{bmatrix} (A_{+\mathrm{R}}e^{-ik_{cA}\tau} + A_{+\mathrm{L}}e^{ik_{cA}\tau})e^{-ik_{zA}z} + (A_{-\mathrm{R}}e^{-ik_{cA}\tau} + A_{-\mathrm{L}}e^{ik_{cA}\tau})e^{ik_{zA}z} \\ + (B_{+\mathrm{R}}e^{-ik_{cB}\tau} + B_{+\mathrm{L}}e^{ik_{cB}\tau})e^{-ik_{zB}z} + (B_{-\mathrm{R}}e^{-ik_{cB}\tau} + B_{-\mathrm{L}}e^{ik_{cB}\tau})e^{ik_{zB}z} \end{bmatrix} \qquad \textbf{3.50}$$

where the L and R subscripts denote the chirality of the degenerate mode and the $\pm$ subscripts denote waves travelling in the +ve and −ve z-direction respectively.

with the wave propagation equations for the partial waves becoming:

$$\left(k_{zA}\left(i(\delta_z - i\sigma_z)A'_{+\mathrm{R}} + \frac{\partial A'_{+\mathrm{R}}}{\partial z} \right) + k_{cA}\frac{\partial A'_{+\mathrm{R}}}{\partial \tau} + \frac{i}{2}\frac{\partial^2 A'_{+\mathrm{R}}}{\partial \tau^2} + i\frac{k^2\chi}{2\ln(b_0/a_0)}\begin{bmatrix} B'_{+\mathrm{R}} + B'_{+\mathrm{L}} \\ + B'_{-R} + B'_{-L} \end{bmatrix} \right) = 0 \qquad \textbf{3.51a}$$

$$\left(k_{zA}\left(i(\delta_z - i\sigma_z)A'_{+\mathrm{L}} + \frac{\partial A'_{+\mathrm{L}}}{\partial z} \right) - k_{cA}\frac{\partial A'_{+\mathrm{L}}}{\partial \tau} + \frac{i}{2}\frac{\partial^2 A'_{+\mathrm{L}}}{\partial \tau^2} + i\frac{k^2\chi}{2\ln(b_0/a_0)}\begin{bmatrix} B'_{+\mathrm{R}} + B'_{+\mathrm{L}} \\ + B'_{-R} + B'_{-L} \end{bmatrix} \right) = 0 \qquad \textbf{3.51b}$$

$$\left(k_{zA}\left(i(\delta_z - i\sigma_z)A'_{-\mathrm{L}} - \frac{\partial A'_{-\mathrm{L}}}{\partial z} \right) - k_{cA}\frac{\partial A'_{-\mathrm{L}}}{\partial \tau} + \frac{i}{2}\frac{\partial^2 A'_{-\mathrm{L}}}{\partial \tau^2} + i\frac{k^2\chi}{2\ln(b_0/a_0)}\begin{bmatrix} B'_{+\mathrm{R}} + B'_{+\mathrm{L}} \\ + B'_{-R} + B'_{-L} \end{bmatrix} \right) = 0 \qquad \textbf{3.51c}$$

$$\left(k_{zA}\left(i(\delta_z - i\sigma_z)A'_{-\mathrm{R}} - \frac{\partial A'_{-\mathrm{R}}}{\partial z} \right) + k_{cA}\frac{\partial A'_{-\mathrm{R}}}{\partial \tau} + \frac{i}{2}\frac{\partial^2 A'_{-\mathrm{R}}}{\partial \tau^2} + i\frac{k^2\chi}{2\ln(b_0/a_0)}\begin{bmatrix} B'_{+\mathrm{R}} + B'_{+\mathrm{L}} \\ + B'_{-R} + B'_{-L} \end{bmatrix} \right) = 0 \qquad \textbf{3.51d}$$

$$\left(k_{zB}\frac{\partial B'_{+\mathrm{R}}}{\partial z} + k_{cB}\left(i(\delta_\tau - i\sigma_\tau)B'_{+\mathrm{R}} + \frac{\partial B'_{+\mathrm{R}}}{\partial \tau}\right) + \frac{i}{2}\frac{\partial^2 B'_{+\mathrm{R}}}{\partial z^2} + i\frac{k^2\chi}{2\ln(b_0/a_0)}\left[\begin{array}{c} A'_{+\mathrm{R}} + A'_{+\mathrm{L}} \\ + A'_{-\mathrm{R}} + A'_{-\mathrm{L}} \end{array}\right] \right) = 0 \qquad \textbf{3.51e}$$

$$\left(k_{zB}\frac{\partial B'_{-\mathrm{R}}}{\partial z} - k_{cB}\left(i(\delta_\tau - i\sigma_\tau)B'_{-\mathrm{R}} + \frac{\partial B'_{-\mathrm{R}}}{\partial \tau}\right) - \frac{i}{2}\frac{\partial^2 B'_{-\mathrm{R}}}{\partial z^2} - i\frac{k^2\chi}{2\ln(b_0/a_0)}\left[\begin{array}{c} A'_{+\mathrm{R}} + A'_{+\mathrm{L}} \\ + A'_{-\mathrm{R}} + A'_{-\mathrm{L}} \end{array}\right] \right) = 0 \qquad \textbf{3.51f}$$

$$\left(k_{zB}\frac{\partial B'_{-\mathrm{L}}}{\partial z} - k_{cB}\left(i(\delta_\tau - i\sigma_\tau)B'_{-L} - \frac{\partial B'_{-L}}{\partial \tau}\right) - \frac{i}{2}\frac{\partial^2 B'_{-\mathrm{L}}}{\partial z^2} - i\frac{k^2\chi}{2\ln(b_0/a_0)}\left[\begin{array}{c} A'_{+\mathrm{R}} + A'_{+\mathrm{L}} \\ + A'_{-\mathrm{R}} + A'_{-\mathrm{L}} \end{array}\right] \right) = 0 \qquad \textbf{3.51g}$$

$$\left(k_{zB}\frac{\partial B'_{+\mathrm{L}}}{\partial z} + k_{cB}\left(i(\delta_\tau - i\sigma_\tau)B'_{+\mathrm{L}} - \frac{\partial B'_{+\mathrm{L}}}{\partial \tau}\right) + \frac{i}{2}\frac{\partial^2 B'_{+\mathrm{L}}}{\partial z^2} + i\frac{k^2\chi}{2\ln(b_0/a_0)}\left[\begin{array}{c} A'_{+\mathrm{R}} + A'_{+\mathrm{L}} \\ + A'_{-\mathrm{R}} + A'_{-\mathrm{L}} \end{array}\right] \right) = 0 \qquad \textbf{3.51h}$$

where:

$$\delta_i = k_i - h_i \qquad \textbf{3.52}$$

represents the detuning of the EM wave-number and the relevant Bragg wave-number and σ_i is the ohmic losses along the $i'th$ co-ordinate.

3.3.2.1 Dispersion Relation of 2D Corrugated Co-axial Waveguide.

As may be inferred from comparison of equations 3.40a-3.40b & 3.51a-3.51h, the description of the dispersion relation in a 2D Bragg reflector is markedly more complex than that of the 1D Bragg reflector. A similar procedure may, however, be employed in determining the resultant eigenmodes, from the indirect coupling of the $A_{\pm}(\tau, z)$ waves, providing one accounts for the azimuthal structure, as well as the axial structure.

The azimuthal structure may be defined as:

$$A'_{\pm R}(\tau, z) = \sum_{m'=-\infty}^{\infty} A^{m'}_{\pm R}(z) e^{ik'_s \tau} \quad \textbf{3.53a}$$

$$A'_{\pm L}(\tau, z) = \sum_{m'=-\infty}^{\infty} A^{m'}_{\pm L}(z) e^{-ik'_s \tau} \quad \textbf{3.53b}$$

$$B'_{\pm R}(\tau, z) = \sum_{m'=-\infty}^{\infty} B^{m'}_{\pm R}(z) e^{ik'_s \tau} \quad \textbf{3.53c}$$

$$B'_{\pm L}(\tau, z) = \sum_{m'=-\infty}^{\infty} B^{m'}_{\pm L}(z) e^{-ik'_s \tau} \quad \textbf{3.53d}$$

where m' is the azimuthal variation of the wave envelope and $k'_s = m'/r_0$ relates to the azimuthal field structure of the m' eigenmode.

Following the steps outlined in Appendix B the set of equations 3.51a - 3.51h can be reduced to:

$$\frac{\partial A^{m'}_{+R,L}}{\partial z} + i\left[(\delta_z - i\sigma_z) + \frac{k_{cA} k'_c}{k_{zA}} - \frac{k'^2_c}{2k_{zA}}\right] A^{m'}_{+R,L} = -i\frac{k^2}{k_{zA}} \kappa [B^{m'}_{\pm R} + B^{m'}_{\pm L}] \quad \textbf{3.54a}$$

$$\frac{\partial A^{m'}_{-R,L}}{\partial z} - i\left[(\delta_z - i\sigma_z) + \frac{k_{cA} k'_c}{k_{zA}} - \frac{k'^2_c}{2k_{zA}}\right] A^{m'}_{-R,L} = i\frac{k^2}{k_{zA}} \kappa [B^{m'}_{\pm R} + B^{m'}_{\pm L}] \quad \textbf{3.54b}$$

$$\frac{k_{zB}}{k_{cB}} \frac{\partial B^{m'}_{+R,L}}{\partial z} + i[(\delta_\tau - i\sigma_\tau) + k'_c] B^{m'}_{+R,L} + \frac{i}{2k_{cB}} \frac{\partial^2 B^{m'}_{+R}}{\partial z^2} = -i\frac{k^2}{k_{cB}} \kappa [A^{m'}_{\pm R} + A^{m'}_{\pm L}] \quad \textbf{3.54c}$$

$$\frac{k_{zB}}{k_{cB}} \frac{\partial B^{m'}_{-R,L}}{\partial z} - i[(\delta_\tau - i\sigma_\tau) + k'_c] B^{m'}_{-R,L} - \frac{i}{2k_{cB}} \frac{\partial^2 B^{m'}_{-R}}{\partial z^2} = i\frac{k^2}{k_{cB}} \kappa [A^{m'}_{\pm R} + A^{m'}_{\pm L}] \quad \textbf{3.54d}$$

where:

$$\kappa = \frac{\chi}{4\ln(b_0/a_0)} \quad \textbf{3.55}$$

is the coupling co-efficient.

One may now consider the wave-amplitudes in a similar manner to the 1D Bragg reflector case as:

$$A^{m'}_{+\mathrm{R,L}}(z) = a_{+1\mathrm{R},1\mathrm{L}}e^{-ik'_z z} + a_{+2\mathrm{R},2\mathrm{L}}e^{ik'_z z} \quad \textbf{3.56a}$$

$$A^{m'}_{-\mathrm{R,L}}(z) = a_{-1\mathrm{R},1\mathrm{L}}e^{-ik'_z z} + a_{-2\mathrm{R},2\mathrm{L}}e^{ik'_z z} \quad \textbf{3.56b}$$

$$B^{m'}_{+\mathrm{R,L}}(z) = b_{+1\mathrm{R},1\mathrm{L}}e^{-ik'_z z} + b_{+2\mathrm{R},2\mathrm{L}}e^{ik'_z z} \quad \textbf{3.56c}$$

$$B^{m'}_{-\mathrm{R,L}}(z) = b_{-1\mathrm{R},1\mathrm{L}}e^{-ik'_z z} + b_{-2\mathrm{R},2\mathrm{L}}e^{ik'_z z} \quad \textbf{3.56d}$$

where $a_{\pm(1,2)}$, $b_{\pm(1,2)}$ are functions of the corrugation length (l_{2D}) only.

This leads to the relation:

$$q_1 q_2 q_3 q_4 = 4k^4\kappa^2(q_1 + q_2)(q_3 + q_4) \quad \textbf{3.57}$$

where:

$$q_1 = k_{zA}(\delta_z - i\sigma_z - k'_z) + k_{cA}k'_c - \frac{k'^2_c}{2} \quad \textbf{3.58a}$$

$$q_2 = k_{zA}(\delta_z - i\sigma_z + k'_z) + k_{cA}k'_c - \frac{k'^2_c}{2} \quad \textbf{3.58b}$$

$$q_3 = k_{cB}[(\delta_\tau - i\sigma_\tau) + k'_c] - \frac{k'^2_z}{2} - k_{zB}k'_z \quad \textbf{3.58c}$$

$$q_4 = k_{cB}[(\delta_\tau - i\sigma_\tau) + k'_c] - \frac{k'^2_z}{2} + k_{zB}k'_z \quad \textbf{3.58d}$$

and:

$a_{+1} = a_{+1\mathrm{R}} + a_{+1\mathrm{L}}$, $a_{-1} = a_{-1\mathrm{L}} + a_{-1\mathrm{R}}$, $a_{+2} = a_{+2\mathrm{R}} + a_{+2\mathrm{L}}$, $a_{-2} = a_{-2\mathrm{L}} + a_{-2\mathrm{R}}$,
$b_{+1} = b_{+1\mathrm{R}} + b_{+1\mathrm{L}}$, $b_{-1} = b_{-1\mathrm{R}} + b_{-1\mathrm{L}}$, $b_{+2} = b_{+2\mathrm{R}} + b_{+2\mathrm{L}}$, $b_{-2} = b_{-2\mathrm{R}} + b_{-2\mathrm{L}}$.

Equation 3.57 therefore forms a quartic equation, yielding four roots for the solutions of the eigenmodes. These were solved numerically using the mathematical program MatLAB. The resultant dispersion profiles for 2D Bragg reflectors, positioned independently on the inner and outer conductor surfaces of a co-axial waveguide, are

shown in Figures 3.14 and 3.15 respectively. In both cases the incident mode was taken to be the TEM mode:

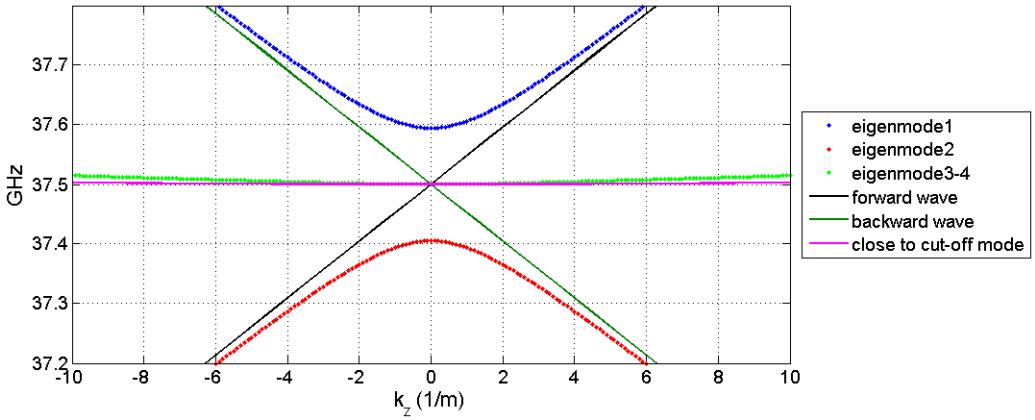

Figure 3.14: Shows the dispersion curves for a 2D Bragg reflector, given a_0 = *30mm,* b_0 = *40mm,* d_z =*8mm, M = 24, m'= 0,* σ_z = *0.1,* σ_τ= *0.01* with a corrugation amplitude on the inner conductor surface of *+/-0.8mm.* Δf =*190MHz,* k_{z0} ~*785m*$^{-1}$.

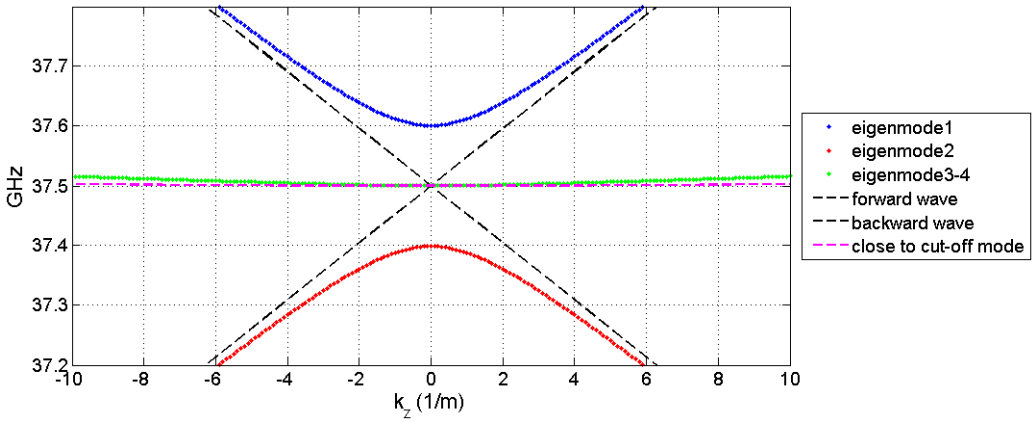

Figure 3.15: Shows the dispersion curves for a 2D Bragg reflector, given a_0 = *30mm,* b_0 = *40mm,* d_z =*8mm, M = 28, m'=0,* σ_z = *0.1,* σ_τ= *0.01* with a corrugation amplitude on the outer conductor surface of *+/-0.8mm.* Δf =*200MHz,* k_{z0} ~*785m*$^{-1}$.

In this case the choice of conductor surface on which the Bragg reflector is formed can be seen to be largely arbitrary, with both corrugations on the inner and outer conductor surface yielding very similar dispersion characteristics for the eigenmodes. It should

be noted that M for the 2D Bragg reflector positioned on the outer conductor surface is greater than that for a similar conductor positioned on the inner conductor, as this maintains the relation $h_\tau \approx h_z$. For simplicity a 2D Bragg reflector designed to form part of the inner conductor will be considered, as the design of such a reflector lends itself more readily to the experimental environment that one designed to be part of the outer conductor surface.

3.3.2.2 Reflection and Transmission Co-efficients of 2D Reflectors.

In calculating the reflection co-efficient of a 2D Bragg reflector we may neglect the diffractive effects considered in Section 3.3.2.1, reducing equations 3.51a-3.51h to:

$$\frac{\partial A'_+}{\partial z} + i(\delta_z - i\sigma_z)A'_+ + ik\kappa(B'_+ + B'_-) = 0 \qquad \textbf{3.59a}$$

$$\frac{\partial A'_-}{\partial z} - i(\delta_z - i\sigma_z)A'_- - ik\kappa(B'_+ + B'_-) = 0 \qquad \textbf{3.59b}$$

$$\frac{\partial B'_+}{\partial \tau} + i(\delta_\tau - i\sigma_\tau)B'_+ + ik\kappa(A'_+A'_-) = 0 \qquad \textbf{3.59c}$$

$$\frac{\partial B'_-}{\partial \tau} - i(\delta_\tau - i\sigma_\tau)B'_- - ik\kappa(A'_+ + A'_-) = 0 \qquad \textbf{3.59d}$$

where $B'_+ = B'_{+\mathrm{R}} + B_{+\mathrm{L}}$ and $B'_- = B'_{-\mathrm{R}} + B'_{-\mathrm{L}}$, taking $k_{zA} \approx h_z$ $(k_{zB} \approx 0)$ and $k_{cB} \approx h_\tau$ $(k_{cA} \approx 0)$.

Following the steps laid out in Appendix B, these reduce to:

$$\frac{\partial A'^{m}_+}{\partial z} + i(\delta_z - i\sigma_z)A'^{m}_+ - 2i\frac{k^2\kappa^2}{(\delta_\tau - i\sigma_\tau)^2 - k'^2_s}(A'^{m}_+ + A'^{m}_-) = 0 \qquad \textbf{3.60a}$$

$$\frac{\partial A'^{m}_-}{\partial z} - i(\delta_z - i\sigma_z)A'^{m}_- + 2i\frac{k^2\kappa^2}{(\delta_\tau - i\sigma_\tau)^2 - k'^2_s}(A'^{m}_+ + A'^{m}_-) = 0 \qquad \textbf{3.60b}$$

where:

$$A_{+}^{m'} = a_{+1}e^{\Lambda z} + a_{+2}e^{-\Lambda z} \quad \textbf{3.61a}$$

$$A_{-}^{m'} = a_{-1}e^{\Lambda z} + a_{-2}e^{-\Lambda z} \quad \textbf{3.61b}$$

define the wave-amplitudes in terms of the solutions of the eigenmodes (these may be compared with equations A.33a-A.33b in Appendix A for the case of the 1D Bragg reflector).

Noting the boundary conditions:

$$A_{+}^{m'}(z)\big|_{z=0} = 1 \quad \textbf{3.62a}$$

$$A_{-}^{m'}(z)\big|_{z=l_{2D}} = 0 \quad \textbf{3.62b}$$

where l_{2D} is the length of the corrugation, equations 3.61a-3.61b take the form:

$$A_{+}^{m'}(z) = 2i\frac{k^2\kappa^2}{q_1 q_2}(q_1 e^{-\Lambda z} - q_2 e^{\Lambda(z-2l_{2D})})a_{-2} \quad \textbf{3.63a}$$

$$A_{-}^{m'}(z) = a_{-2}(e^{-\Lambda z} - e^{\Lambda(z-2L)}) \quad \textbf{3.63b}$$

where:

$$q_1 = [([\delta_\tau - i\sigma_\tau]^2 - k'^2_s)(\Lambda + i[\delta_z - i\sigma_z]) - 2ik^2\kappa^2] \quad \textbf{3.64a}$$

$$q_2 = [([\delta_\tau - i\sigma_\tau]^2 - k'^2_s)(i[\delta_z - i\sigma_z] - \Lambda) - 2ik^2\kappa^2] \quad \textbf{3.64b}$$

The reflection co-efficient can then be calculated, as in the 1D Bragg reflector case, as:

$$|R(z)| = \left| -i\frac{q_1 q_2}{2k^2\kappa^2[(q_1 - q_2)\coth(\Lambda(z - l_{2D})) + q_1 + q_2]} \right| \quad \textbf{3.65}$$

For a set corrugation length of 6 periods ($4.8cm$), varying the amplitude of the coupling co-efficient (noting this is directly proportional to the corrugation amplitude) results in a marked change in performance when compared to the case of the 1D Bragg reflector (c.f. Figure 3.11).

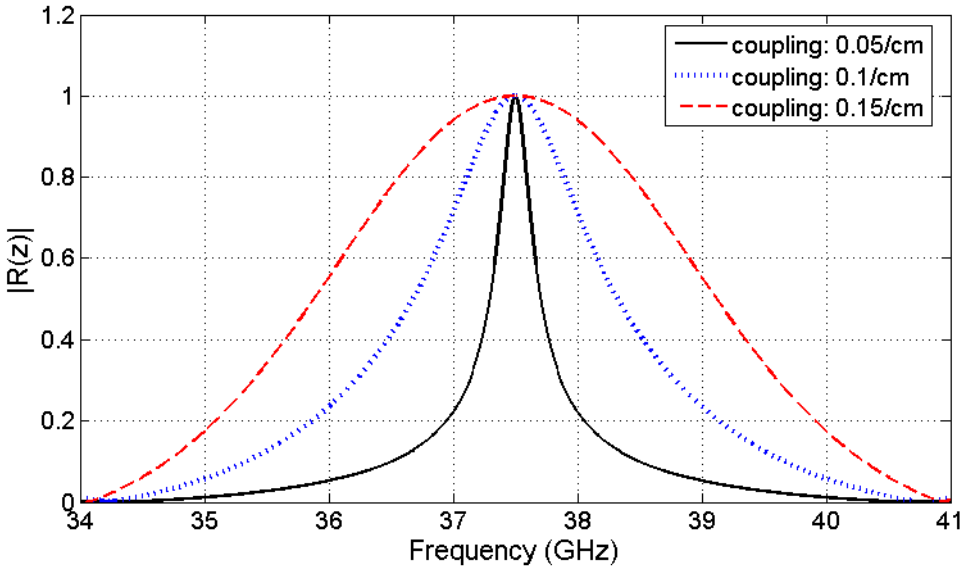

Figure 3.16: Shows the reflection band produced by *4.8cm* long (6 period) 2D Bragg reflectors, located on the inner conductor of a co-axial waveguide with mean radius a_0= *3cm*, with coupling strengths κk = *0.05/cm, 0.1/cm* and *0.15/cm*.

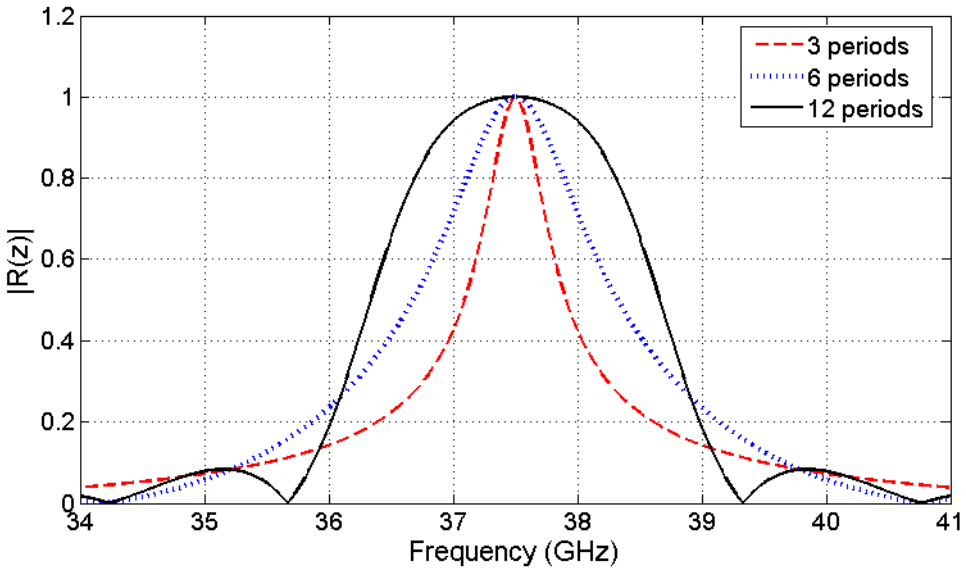

Figure 3.17: Shows the reflection band produced by 2D Bragg reflectors of l_{2D}=*2.4cm, 4.8cm* and *9.6cm* (*3, 6* and *12* periods respectively), located on the inner conductor of a co-axial waveguide with mean radius a_0= *3cm*. In each case the coupling strength κk=*0.1/cm.*

Alternatively, varying the length of the corrugation, for a fixed coupling strength of $k\kappa = 0.1/cm$ results in the curve shown in Figure 3.17 (compare with Figure 3.12).

From Figures 3.16 & 3.17 it can be seen that increasing the amplitude of the corrugation (for a given value of l_{2D}) rapidly broadens the reflection band, with the centre of maximum reflection remaining constant. This is true when one sets the amplitude of the corrugation but varies l_{2D}, however in this case the broadening of the reflection band is less marked and the location of the side-bands begin to shift closer to the central resonant frequency. This is in contrast to the case of the 1D Bragg reflector, where longer corrugations result in tighter, better defined reflection bands. Noting that the desired performance from the 2D corrugation is to provide a highly-reflective, narrow band-width, reflector, for a given corrugation amplitude best performance is observed using relatively short structures. The numerically determined and experimentally measured transmission co-efficients, for two different lengths of similar 2D Bragg reflector, are shown in Figure 3.18 (Cross et al. 2001):

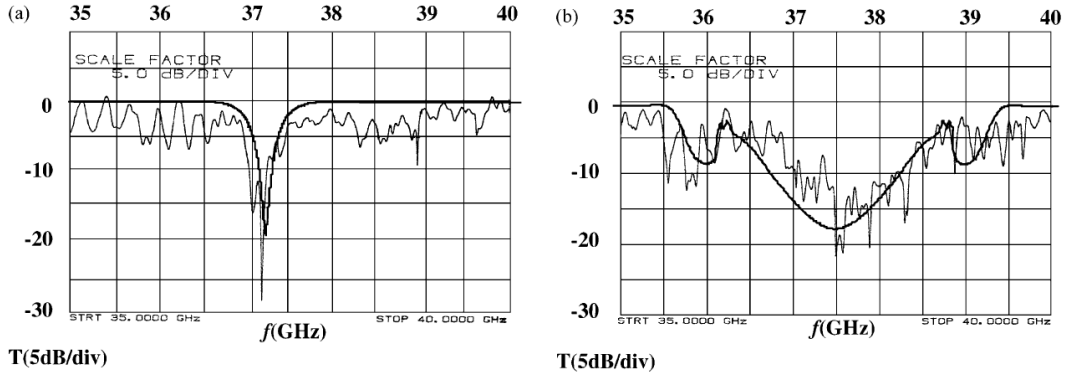

Figure 3.18: Shows the numerical (bold-line) and experimentally measured (thin-line) transmission profiles for two 2D Bragg reflectors, with a_0=*3.02cm,* b_0=*3.95cm,* κk=*0.1/cm,* $\sigma_{\tau,z}$=*6x10-4/cm,* d_z=*0.8cm* and (a) l_{2D}=*4cm*, (b) l_{2D}=*10.4cm.*

The structures used were similar to those employed in the 2D - 1D Bragg FEM experiment itself, formed on the inner conductor of an over-sized Ka-band $(26.4 - 40GHz)$ co-axial waveguide. The expected increase in the reflection bandwidth for the longer corrugation is noted, with the associated appearance of a

parasitic side-band evident in the region of $35.5 - 36GHz$ (see Figure 3.18(b)). The upper side-band is less clearly defined, however this lack of uniformity does not negate the side-band's existence. The measured transmission profiles were obtained using a 8757D Scalar Network Analyser (SNA) with a frequency-doubler head positioning the operational bandwidth across the Ka-band range. As the higher side-band lies close to the upper limit of efficient performance for the Ka-band detector head, some degradation in the measured signal amplitude is to be expected, even following calibration of the SNA.

The structures discussed, for both 1D and 2D Bragg reflectors, present only one half of the case required for the design of a lasing cavity, as the effective bandwidth of such a cavity is defined by the overlap of the reflection-bands of the constituent reflectors and the resonant modes there in. Such a cavity is discussed in the following section.

3.4 Co-axial Cavities Defined by 2D and 1D Bragg Reflectors.

If one places a Bragg reflector at either end of a length of waveguide this forms a finite bandwidth cavity, defined by the overlap of the reflectors' stop-bands:

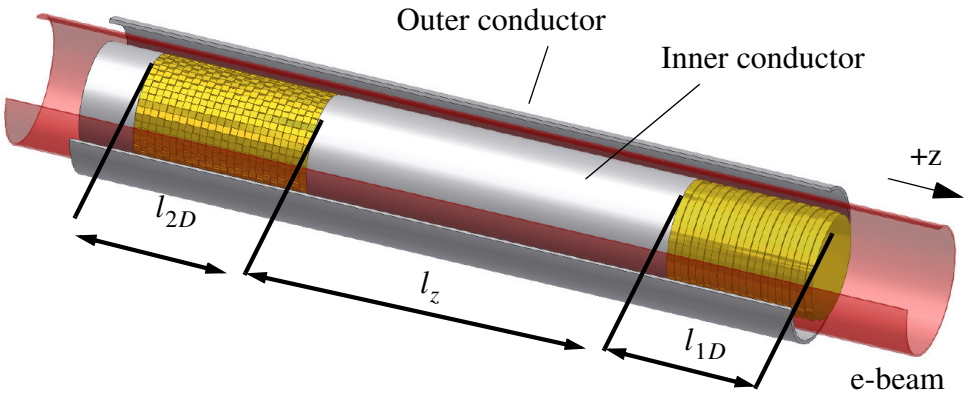

Figure 3.19: Shows a cross-sectional schematic of a co-axial 2D - 1D Bragg lasing cavity, defined on the inner-conductor with reflector lengths l_{2D} and l_{1D} respectively, separated by a distance l_z (the effective cavity length). The annular electron beam propagates in the $+z$ direction.

The cavity itself only becomes resonant at discrete frequencies within this overlap, resulting in the introduction of a third subscript to the modal designations; "p" which is an integer corresponding to the number of half-wave variations along z (Kirkman & Kline 1946, Harvey 1963, Waldron 1969). This is reflected in the calculation of the resonance frequencies for the different TE and TM cavity modes, giving equations 3.17 - 3.19 the form:

$$\frac{\omega_c^2}{c^2} = \frac{\zeta_n^2}{(b-a)^2}\left(\frac{b}{a}-1\right)^2 + \frac{p^2\pi^2}{l_z^2} = \frac{\zeta_n^2}{a^2} + \frac{p^2\pi^2}{l_z^2} \qquad \textbf{3.66}$$

for the $TM_{m,n,p}$ modes, where $m = 0, 1, 2, \ldots$, $n = 1, 2, 3, \ldots$, $p = 0, 1, 2, \ldots$ and m and p may both be zero together.

$$\frac{\omega_c^2}{c^2} = \frac{\zeta'^2_1}{(b+a)^2}\left(\frac{b}{a}+1\right)^2 + \frac{p^2\pi^2}{l_z^2} = \frac{\zeta'^2_1}{a^2} + \frac{p^2\pi^2}{l_z^2} \qquad \textbf{3.67}$$

for the $TE_{m,n,p}$ modes, where $m = 1, 2, 3, \ldots$, $n = 1$ and $p = 1, 2, 3, \ldots$.

and:

$$\frac{\omega_c^2}{c^2} = \frac{\zeta'^2_n}{(b-a)^2}\left(\frac{b}{a}-1\right)^2 + \frac{p^2\pi^2}{l_z^2} = \frac{\zeta'^2_n}{a^2} + \frac{p^2\pi^2}{l_z^2} \qquad \textbf{3.68}$$

for the $TE_{m,n,p}$ modes, where $m = 1, 2, 3, \ldots$, $n = 2, 3, 4, \ldots$ and $p = 1, 2, 3, \ldots$.

As in the case of co-axial waveguides the $TE_{0,n,p}$ modes are degenerate with the $TM_{0,n+1,p}$ modes, with the exception of the $TE_{0,1,p}$ modes which are degenerate with the $TM_{1,1,p}$ modes. For the TEM_p and the $TM_{0,0,p}$ modes, the resonant frequencies can be found from equation 3.66 by setting $\zeta_n = 0$.

Taking the separation between the cavity reflectors to be, for example $l_z = 60cm$ (as in the physical cavity) the resonant TEM_p cavity mode with the required FEM frequency of $\sim 37.5GHz$ would be the TEM_{150} mode. From this it may be inferred that multiple longitudinal resonances may occur for a given beam-wave interaction, as a relatively small spread in v_z of the beam electrons is likely to allow for the excitement of "satellite" resonances, separated in frequency by $\pm c\lambda/l_z$, where λ is the central resonant frequency of the interaction.

In addition, the over-moded nature of cavities, such as that used in the 2D-1D Bragg FEM experiment, allows for the excitement of separate cavity resonances from competing beam - wave interactions, which are distinct from the satellite modes described above (for an example see Figure 4.19). In the work presented these parasitic resonances must satisfy the Bragg resonance conditions of both the 1D and 2D Bragg reflectors in order to be confined within the lasing cavity, with their location determined by the parameters of the two mirrors.

In the case of the 1D Bragg reflector the closest eigenmode to the desired TEM-TEM interaction occurs due to TEM-$TM_{0,1}$ coupling which, as can be seen in Figure 3.13 lies close by, with a central frequency of $\sim 39 GHz$.

In the case of the 2D Bragg reflector the fundamental eigenmode ($m' = 0$) has near-by parasitic eigenmodes positioned as described by $m' = 0, \pm 1, \pm 2$ in equation 3.65:

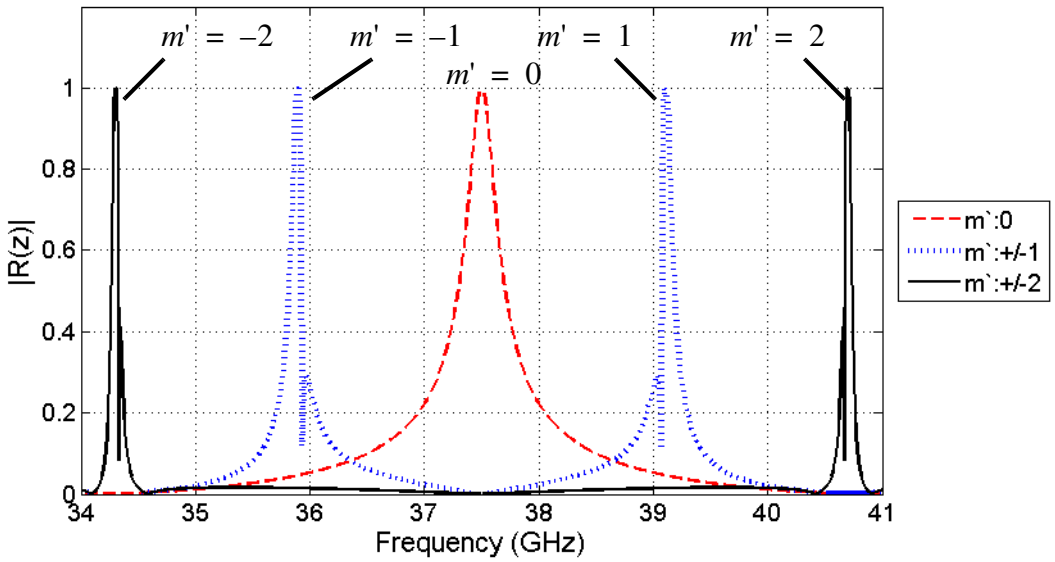

Figure 3.20: Shows the reflection bands for *m'=0,+/-1,+/-2* for a 3 period long 2D Bragg reflector sharing parameters with that shown in Figure 3.17.

It should be noted that the amplitudes of the different eigenmode solutions in Figure 3.20 do not represent the physical magnitudes in a multi-mode system, rather it is the central positioning of the reflection bands which is of interest. Given that each of these

eigenmodes satisfy the resonance conditions of the 1D Bragg reflector, all will be resonant within the lasing cavity.

If we consider a 2D - 1D Bragg lasing cavity, with mean waveguide dimensions of $a_0 = 30mm$ and $b_0 = 40mm$, the fundamental eigenmode of the 2D reflector corresponds to coupling between the TEM mode and the close to cut-off $TE_{24,2}$ mode at $\sim 37.5GHz$. Back-scattering of the $TE_{24,2}$ mode into the TEM mode then leads to the creation of an absolute instability between the reflected TEM waves of the 2D and 1D Bragg mirrors, with the exact frequency determined by l_z. This then forms the operating mode of the FEM, with proper selection of V_0, B_0 and B_u resulting in efficient beam-wave coupling.

As noted in Section 2.5, the TEM mode should be excitable at $\sim 37.5GHz$, within the interaction region, using an electron beam of $\gamma \approx 1.8 - 2$ ($V_0 \approx 450 - 500kV$), a guide solenoid field strength of $\sim 0.6T$ and an undulator field strength of $\sim 0.067T$. For a cavity length of $\sim 60cm$, operation at $\sim 37.5GHz$ should be obtainable in the TEM_{150} cavity mode, with some satellite longitudinal harmonics (side-lobes) expected at integer values of $\pm 0.5GHz$, decreasing in amplitude as one moves further away from the central resonance. If multi-mode operation was observed, it was expected that similar behaviour would occur for each solution of equation 3.65 ($m' = 0, \pm 1, \pm 2, \ldots$).

Chapter 4: The Design and Simulation of the 2D-1D Bragg Free-Electron Maser Experiment.

4.1 Introduction

Modelling of the 2D - 1D Bragg FEM experiment was carried out using two separate Finite Difference Time Domain (FDTD) Particle in Cell (PiC) codes; KARAT (Tarakanov 1997) and MAGIC (ATK Mission Systems 2004). The former was used to model the generation and transportation of the electron beam, from a plasma-flare cathode through to the drift-tube. The latter was used to model the lasing cavity and the resonant coupling between the magneto-optical systems, of the guide solenoid and undulator, with a simulated electron beam.

The following chapter describes the simulations carried out over both stages of the FEM experiment. In Section 4.2 simulations of the plasma-flare gun, carried out using KARAT, are presented, beginning with a brief over-view of the operation of a plasma-flare cathode, followed by a description of the two gun geometries used and the corresponding changes in the expected performance. Both guns modelled had a cathode stalk with a mean diameter of $7cm$ with the anode can diameter of the first gun being $29cm$ and that of the second gun being $12cm$. The axial electrode separation was kept constant at $10cm$ throughout.

Section 4.3 presents simulations of an idealised 2D - 1D Bragg lasing cavity, operating with electron beam currents of $\sim 1.5kA$ and $\sim 3.5kA$ (corresponding to those generated by the two gun geometries). In this case modelling was done using the PiC code MAGIC, as this allowed for modelling over a single azimuthal period, rather than modelling of the full 3D cavity as would be required with KARAT. Modelling of an idealised cavity is presented as opposed to modelling of the experimental cavity, as this latter case required computer processing power in excess of that available at the time of writing. In addition, deviation between the results of an idealised cavity and that of the experimental cavity were assumed to be significant only in terms of conversion efficiency between the electron beam and the EM wave, with the idealised cavity providing a higher efficiency and subsequently higher output power.

4.2 The Plasma-Flare Electron gun.

The electron gun used in the 2D - 1D Bragg FEM experiments was based on the use of a plasma-flare cathode (also known as an explosive electron emission (EEE) cathode). This was based on an existing gun, designed by Konoplev (2001) and implemented by McGrain (2006) in a previous FEM experiment using a 2D - 2D Bragg lasing cavity.

The reasons for the choice of a plasma-flare cathode over, for example, a thermionic cathode is explained in more detail in Section 5.3.1, however for the discussion that follows, the most important property of such cathodes is their ability to provide emission current densities $> 10 kA cm^{-2}$ (Milton 1974, Barker & Schamiloglu 2001), with the space-charge current limit determining the maximum beam current for a given applied accelerating potential. In contrast, thermionic and field emission based guns have emission current densities limited to $\sim 50 A cm^{-2}$ (Cross 1993), making plasma-flare guns more attractive for use in high power microwave devices, such as cyclotron auto-resonance masers (CARMs), FELs and high power Gyrotrons (Gold et al. 1988, Conde & Bekefi 1991, Bratman et al. 1992, Spark et al. 1994, Bratman et al. 1996, Glyavin et al. 1999, Konoplev 2001, McGrain 2006).

In its simplest form a plasma-flare gun takes the form of a parallel plate diode, where the electrode plates have dimensions far in excess of the electrode separation. The emitted current density from such a diode follows the Child-Langmuir law:

$$J = \frac{4\varepsilon_0}{9d^2} V^{3/2} \sqrt{\frac{2e}{m_e}} \qquad \textbf{4.1}$$

where d is the axial anode-cathode gap, $e = 1.602 \times 10^{-19} C$ is the electron charge, $m_e = 9.11 \times 10^{-31} kg$ is the rest electron mass, V is the potential difference across the gap and the current in the beam is determined via $I = JS$, where S is the effective emission surface of the cathode (Pierce 1954, Gilmour 1986, Barker & Schamiloglu 2001).

While this is insufficient to accurately model complex gun geometries, the trends implied by equation 4.1 holds, specifically that one would expect the electron beam

current to increase with decreasing anode-cathode separation, or to increase with increases in the applied diode potential. In the latter case a related equation, typically used to estimate the space-charge limit in hollow metallic waveguide, may be used to estimate the maximum current which may be transferred through the inter-electrode region before instabilities are likely to occur (Mesyats 1991, Barker & Shamiloglu 2001):

$$I_{SCL} = I_0 \frac{(\gamma^{2/3} - 1)^{3/2}}{1 - f + 2\ln(r_a / r_{outer})} \qquad \textbf{4.2}$$

where $I_0 = (4\pi\varepsilon_0 m_0 c^3)/e \cong 17.1kA$, r_a is the radius of the anode can, r_{outer} is the outer radius of the electron beam and f is a function dependent on the geometry of the cathode emitter. The function f tends to 1 as the inner radius of the beam tends to r_{outer} and to zero for a solid (pencil) beam. A general approximation for a thin annular beam is to take $f = 1$, i.e.:

$$I_{SCL} \cong I_0 \frac{(\gamma^{2/3} - 1)^{3/2}}{2\ln(r_a / r_{outer})} \qquad \textbf{4.3}$$

In dealing with the electron emission from a cathode, the relations of equations 4.1 and 4.2 can be quantified in terms of the gun's perveance (P), which is a function purely of the gun geometry:

$$P = \frac{I}{V^{3/2}} \qquad \textbf{4.4}$$

where I is the beam current and V is the potential difference applied between the anode and the cathode.

The perveance for a set geometry is generally taken to be a constant (Gilmour 1986), with a V^X dependence of $X = 1.5$ assumed, though some deviation has been noted, such as Jory & Trivelpiece (1969) and Barker & Schamiloglu (2001), the latter giving $1.33 \leq X \leq 1.52$ for the case of an annular plasma-flare cathode. For complex gun geometries, such as that used in the 2D-1D Bragg FEM experiment, the perveance is better predicted through numerical simulation than analytic calculation, as this better accounts for the geometry of the electrodes in calculating the space-charge forces on the beam and the resultant current limit for a given driving potential.

4.2.1 The FEM Electron Gun.

The gun used in the FEM experiment was based on an existing plasma-flare cathode, used in earlier 2D - 2D Bragg FEM experiments (Konoplev 2001, McGrain 2006). Alterations to the gun were carried out in two stages resulting in the construction and testing of two separate gun topologies. For ease of designation the abbreviations EEE1 and EEE2 will be used to specify which of the two guns is under consideration, where "EEE" relates to the alternate name for plasma-flare cathodes; Explosive Electron Emission cathodes.

4.2.1.1 Modelling of the EEE1 2D - 1D Bragg FEM Electron Gun.

Working from the physical geometry of the plasma-flare gun, a model was constructed using the PiC code KARAT, with the cathode-stalk radius adjusted to match the radial dimensions of the emitter ring. An example of the modelled geometry is given in Figure 4.1, including an example of the electron beam propagating through the drift tube region:

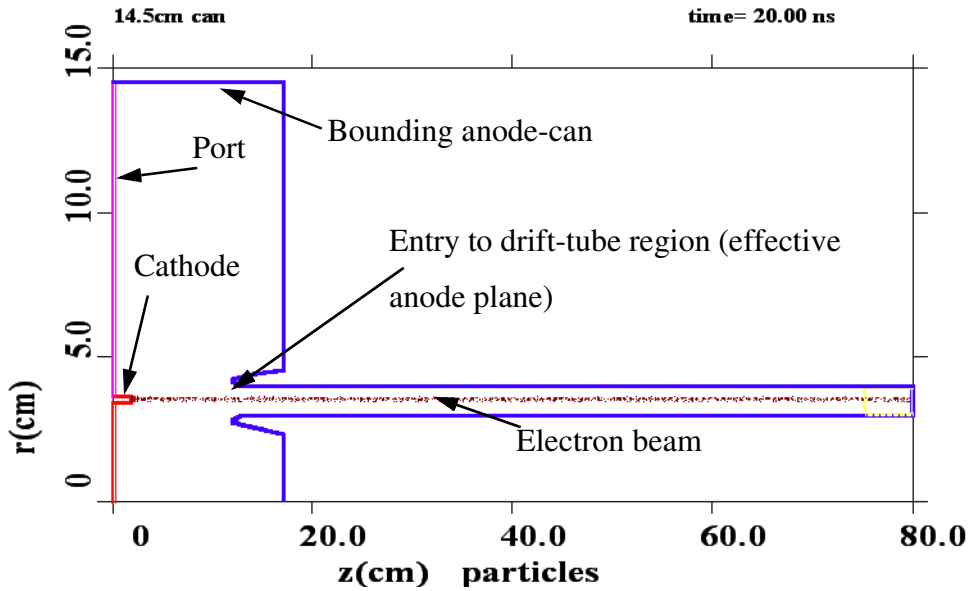

Figure 4.1: Shows the geometry of the FEM plasma-flare gun as modelled in KARAT. The beam shown corresponds to an applied voltage of *450kV* with a guide field of *0.64T*.

It should be noted that KARAT does not model the plasma-flare process directly, i.e. it does not model the explosive sublimation of the cathode surface and resultant creation of a zero work-function plasma cloud (c.f. Section 5.3.1). The modelled emitter surface was therefore increased from its physical value of ~$0.5mm$ to $2mm$, giving an effective emitter annulus more analogous with that of the plasma cloud of the experiment. The distance between the emitter surface and the entry to the drift-tube region was kept at $10cm$, in-line with previous experimental work, with the radii of the inner and outer conductors of the drift tube set at $2.95cm$ and $3.95cm$ respectively, corresponding to the physical values in the experiment. Similarly the anode-can radius was set as $14.5cm$.

A peculiarity of KARAT in estimating the beam current, associated with a given diode potential, is that the code does not estimate this current directly, rather an upper limit is set for the current which the code attempts to implement (Tarakanov 1997). To properly model space-charge limited emission from the plasma-flare cathode it was therefore necessary to perform a series of simulations, for each relevant diode potential, with the available current varied incrementally between 500 – $4500A$. Space charge limited emission was taken to occur when increases in the available current setting resulted in no appreciable change in the simulated beam current:

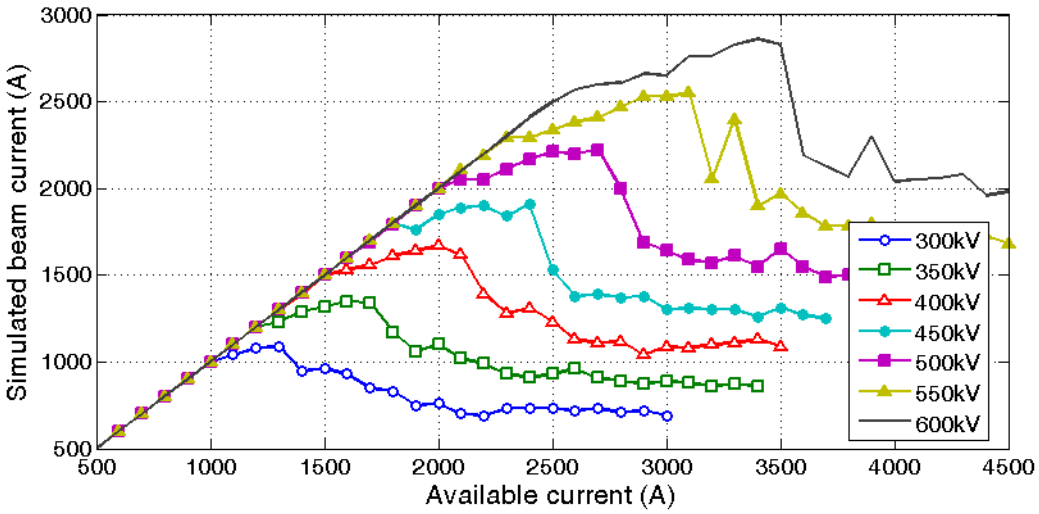

Figure 4.2: Shows the trend in the simulated beam current, using KARAT, for different diode voltages over a range of available current settings.

The simulations were performed with a radial resolution of $0.4mm$ and an axial resolution of $0.8mm$, for applied diode voltages of $300 – 600kV$. The simulated beam current was measured at a distance of $40cm$ along z (see Figure 4.1), placing it within the drift tube region. This was done as an approximation of the position of the Rogowski coil and current shunt diagnostics used in the experiment. From Figure 4.2, beginning with the $300kV$ trace, it can be seen that an increase of $\sim 500A$ is required in the available current to remain in the saturated region if the diode potential is increased by $50kV$, with similar incremental increases required as the diode potential is raised, in $50kV$ steps, to $600kV$. The required current setting for a diode potential of $700kV$ would therefore be in the region of $5.5 – 6kA$. Taking a mean of the simulated beam currents, in the saturated regions for each diode potential, allows for an estimation of the EEE1 gun's performance across the voltage range $300 – 600kV$:

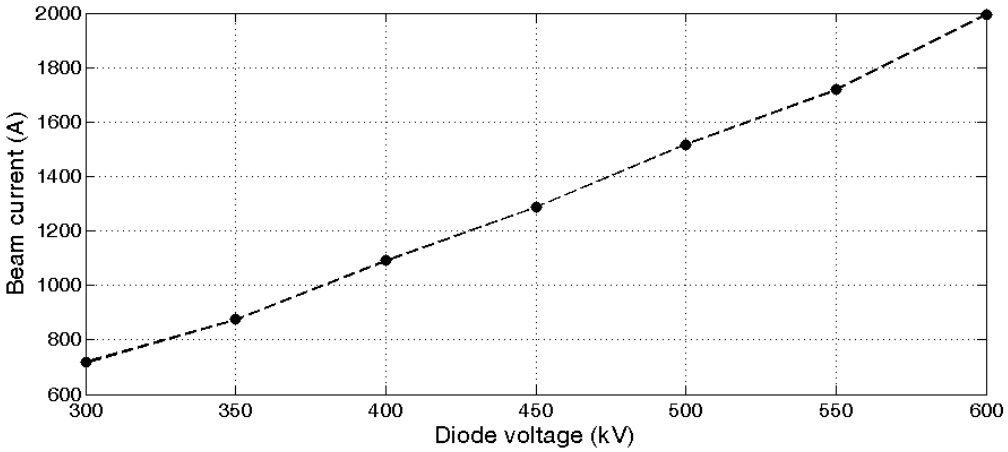

Figure 4.3: Shows the simulated space charge limited beam current for the FEM gun, operating with an anode can of radius *14.5cm* with an axial electrode gap of *10cm*.

This shows the expected trend of increasing in limiting current with increasing diode voltage. Using equation 4.4 one can then estimate the perveance for the EEE1 gun to be in the region of $4.3(\pm 0.1)\mu P$.

For efficient interaction of the electron beam with the undulator field, the axial electron beam velocity should remain essentially uniform, with little transverse velocity spread ($\beta_z \gg \beta_\perp$), i.e. the beam emittance should be low, with the effective cross-sectional

area of the propagating beam kept to a minimum. The quality of the electron beam transported into the drift tube region can be determined in the first instance by looking at the degree of variation in the axial electron velocities through the system. In addition, by comparing the axial component of the electron relativistic energy factor $\gamma_z = (1-(v_z/c)^2)^{-1/2}$ to the total relativistic energy factor $\gamma = (1-(v/c)^2)^{-1/2}$ (where $v^2 = v_z^2 + v_\perp^2$), the spread in electron energies resulting from deviations in v_z can be readily observed. Evidence of potential depression may also be observed, where the axial velocity of the electrons may indeed remain fairly constant but the electron energy is lower than that expected for the applied diode potential. In the idealised case the beam electrons should show negligible variation in v_z and have $\gamma - \gamma_z \cong 0$.

Traces of the normalised axial electron velocity (β_z) and the total γ for an applied potential of $450kV$ on the EEE1 gun are given in Figures 4.4 (a) and (b) respectively. γ, rather than γ_z is plotted here as deviation between γ and γ_z was found to be on the order of $\pm 0.5\%$, too small for any meaningful difference to be observed. The electrons were subject to a $0.64T$ axial guiding magnetic field

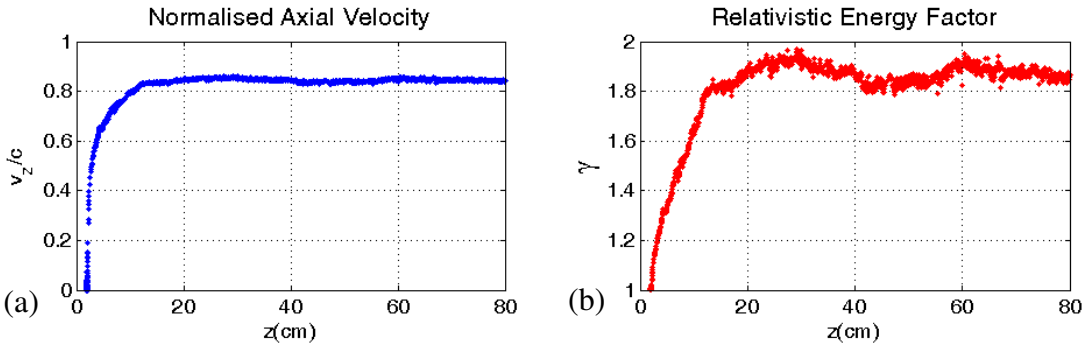

Figure 4.4: (a) Shows β_z for the electrons travelling through the plasma-flare gun. (b) Shows the total relativistic electron energy factor γ.

Looking at Figure 4.4(a), it can be seen that once the electrons pass the anode and enter the drift-tube region ($15cm$ along z) they maintain a relatively uniform velocity of $\sim 2.5 \times 10^8 ms^{-1}$. The slight ripple in β_z is reflected in the variation in γ shown in Figure 4.4(b), which corresponds to electron energies of $450keV(\pm 7\%)$.

This implied that for an axial guiding field strength of $0.64T$ and an applied diode voltage of $\sim 450kV$ the EEE1 gun would provide a $\sim 450keV$ electron beam, showing a low emittance ($\beta_{\perp} \ll \beta_{z}$) at a beam current of $\sim 1.3kA$, sufficient for excitement of the FEL instability. The propagation of such a beam through an idealised 2D - 1D Bragg cavity was then modelled using the PiC code MAGIC, this is presented in Section 4.3.1.

4.2.1.2 Modelling of the EEE2 2D - 1D Bragg FEM Electron Gun.

Following the completion of the 2D - 1D Bragg FEM experiments using the EEE1 gun, the design was altered to further increase the beam current. This was done for two, related, reasons. Firstly, increasing the beam current was expected to aid in the establishment of the FEL instability earlier in the beam-pulse duration, leading to a more efficient extraction of energy from the electrons to the wave and so increase both the duration and power of the output microwave pulse. This would increase both the power in the output and the overall energy efficiency. Secondly, the power available in the beam would increase, meaning more energy would be available for extraction to the EM wave, again enhancing the potential output power from the FEM. A minimum of a factor of two increase in beam current was set as a target for performance.

While the beam current could be increased by decreasing the axial anode-cathode separation, modelling the gun geometry, with the emitter - anode separation reduced to $4cm$, resulted in an increase in beam current to only $\sim 2.2kA$ for an applied diode voltage of $450kV$, much lower than the $3–3.5kA$ required. Experimentally, axial separations less than $4cm$ had been noted as resulting in E field breakdown, due to excessive field enhancement between the cathode and the tips of the anode, negating this method as a means of increasing beam current further. In contrast, it was found that by decreasing the radial separation between the cathode stalk and the anode-can from $14.5cm$ to $6cm$, keeping all other parameters consistent with the earlier model, the beam current increased to $\sim 3.4kA$, again for a diode potential of $450kV$. This is in keeping with the behaviour expected from equation 4.2, where the reduction in the

ratio of r_a / r_{outer} in the natural log term implies an increase in the space-charge current limit by a factor of ~2.5 .

The resultant model for the EEE2 gun is shown in Figure 4.5:

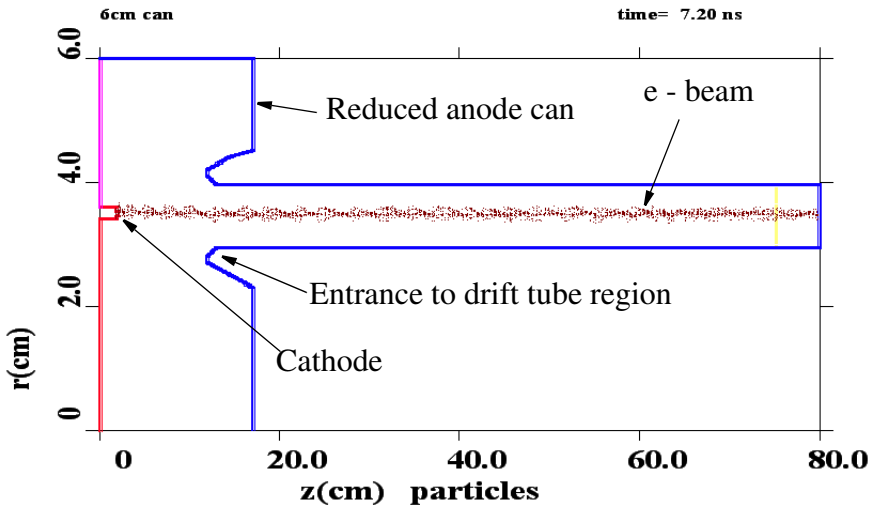

Figure 4.5: Shows the geometry of the FEM plasma-flare gun with the anode can radius reduced to *6cm*. The anode - cathode gap was *10cm*. The beam shown corresponds to an applied voltage of *450kV* with a guide field of *0.64T*.

The effective emitter surface was kept at $2mm$ and the axial electrode separation was maintained at $10cm$. In keeping with the model of the EEE1 gun, the simulations were performed with a radial resolution of $0.4mm$ and an axial resolution of $0.8mm$, for applied diode voltages of $300 - 600kV$, with the simulated beam current measured at a distance of $40cm$ along z. The applied diode potential was kept at $450kV$ with the axial magnetic field set at $0.64T$. As before the space-charge limited current was determined for each diode voltage by increasing the available beam current incrementally until the simulated current reached some steady value. This produced traces similar to those shown in Figure 4.2, resulting in the current to applied voltage relation shown in Figure 4.6.

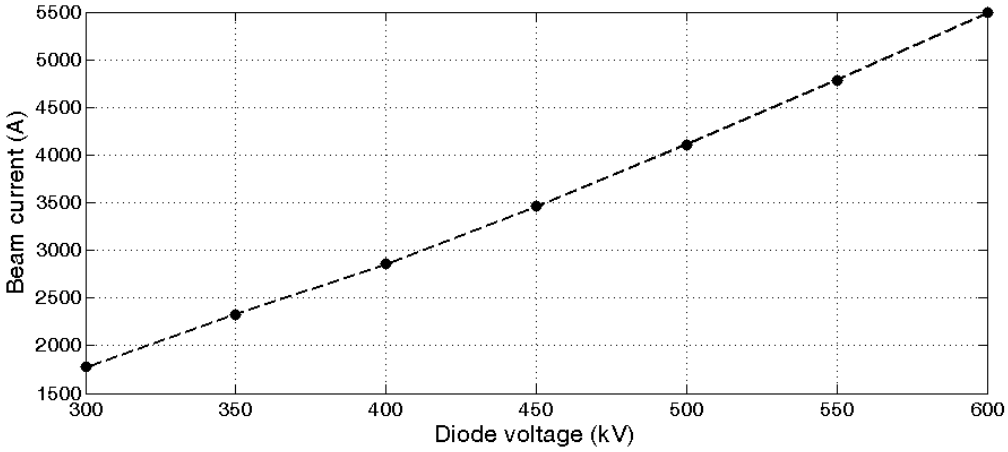

Figure 4.6: Shows the simulated space charge limited beam current for the FEM gun, operating with an anode can of radius *6cm* with an axial electrode gap of *10cm*.

This indicated an increase in the gun perveance to $\sim 11.5(\pm 0.3)\mu P$ for the revised gun geometry, in line with the factor of ~ 2.5 increase in the beam current. Comparing Figures 4.3 and 4.6 it can be seen that the relationship between the diode voltage and beam current behaves in a similar manner, with a slight increase in the non-linearity of the curve in-line with the general trend of equation 4.3 given the reduced anode-can radius.

As before, the quality of the emitted beam was of primary importance. Figure 4.7 shows β_z and γ for the EEE2 gun:

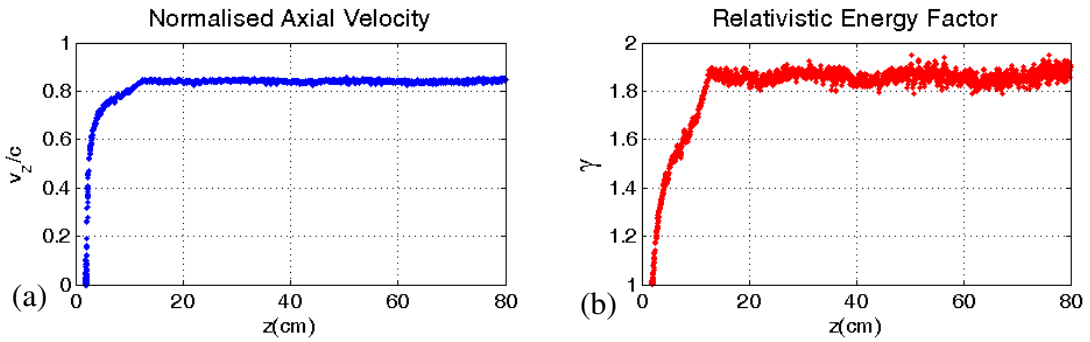

Figure 4.7: (a) Shows β_z for the electrons travelling through the plasma-flare gun. (b) Shows the total relativistic electron energy factor γ.

As with the EEE1 gun simulations, deviation between γ and γ_z was negligible, in the region of $\pm 0.5\%$. Comparing Figure 4.4 (a) and Figure 4.7(a), a modest improvement in the uniformity of β_z through the drift-tube region can be observed:

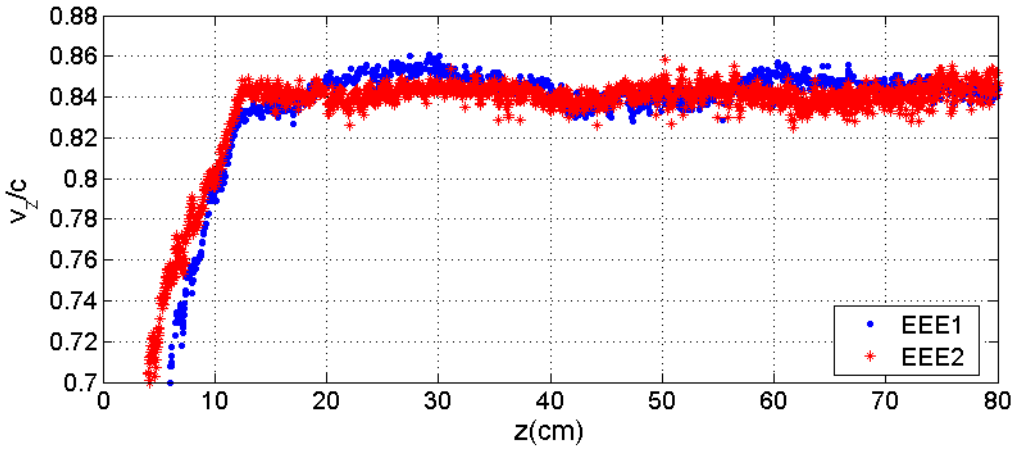

Figure 4.8: Compares β_z for the EEE1 and EEE2 electron guns, i.e. for *1.5kA* and *3.5kA* beam currents respectively.

This is reflected in the more uniform trace of γ in Figure 4.7(b). The spread in electron energies was predicted to be $\sim 445keV(\pm 5\%)$ with $v_z \cong 2.51 \times 10^8 ms^{-1}$ as before. The beam emittance was taken to be on the same order as that of the EEE1 gun due to the similarity in values for $\gamma - \gamma_z$. Modelling of the beam from the EEE2 gun, propagating through the same 2D - 1D Bragg cavity modelled for the EEE1 gun, is presented in Section 4.3.3 for comparison.

4.3 The 2D - 1D Bragg FEM Interaction Region.

The interaction region of the FEM experiment consisted of an azimuthally symmetric undulator, an axial guide magnetic field and a lasing cavity, defined by a 2D Bragg input mirror and a 1D Bragg output mirror, both located on the inner conductor surface. A schematic of such a cavity is given in Figure 4.9.

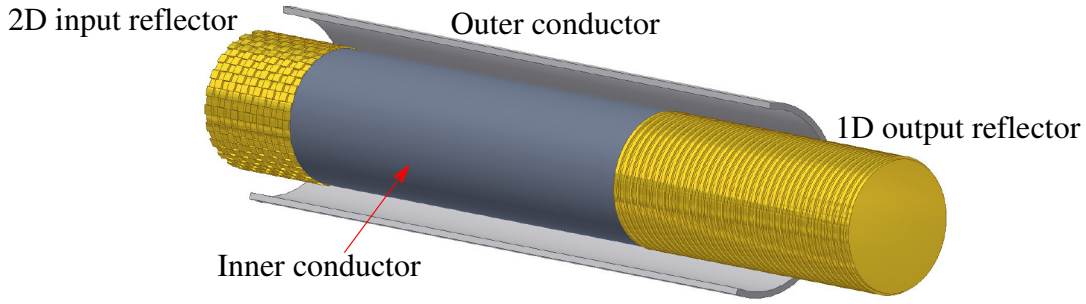

Figure 4.9: Shows a schematic of the 2D - 1D Bragg lasing cavity with the outer conductor surface in cross-section.

The experimental cavity had an inter-reflector separation of $60cm$, formed by a section of smooth co-axial waveguide, with a $10cm$ long input mirror and a $15cm$ long output mirror. This maintained the over-all drift-tube length at $\sim 2m$, in line with the existing experimental infrastructure. Such a cavity was considered acceptable in terms of the proof of principle work undertaken, as the separation between the reflectors should ensure the excitement and growth of the FEL instability in the propagating beam. Modelling of such a cavity, to the degree required for proper comparison with that used in the experiment, was prohibitive, mostly due to the computational power required to accurately model the experiment. This did not, however, preclude modelling of similar cavities and the determination of the likely operation from the FEM, given similar operating parameters. What follows is a discussion of an idealised 2D - 1D Bragg lasing cavity, modelled in conjunction with the magnetic fields presented by the guide and undulator coils. Electron beams synonymous with those produced by the EEE1 and EEE2 gun geometries are considered, with the resultant FEM performances presented in Sections 4.3.2 and 4.3.3 respectively. In both cases the PiC code MAGIC was used in preference to KARAT.

4.3.1 Modelling of the 2D - 1D Bragg Lasing Cavities

The geometry of the 2D - 1D Bragg lasing cavity is inherently non-azimuthally symmetric, due to the azimuthal periodicity of the 2D reflector (see Figure 4.9). This is in contrast to the case of the plasma-flare gun geometries, where the 2.5D operation

of KARAT sufficed in modelling the electron beam production. While KARAT has some functionality in modelling fully 3D geometries, this introduces additional issues, as the over-sized nature of the drift-tube, combined with the high resolution required for accurate modelling, puts simulation of the full cavity geometry beyond the computing capabilities available at the time of this work.

An alternative to KARAT, for modelling the FEM interaction region, was the PiC code MAGIC. Both KARAT and MAGIC work on similar principles, however in addition to 2.5D and fully 3D modelling capabilities, MAGIC offers the additional option of modelling a single azimuthal period, provided that periodicity is reproducible across the azimuth (ATK Mission Systems 2005). In many ways this is similar to the 2.5D operation of KARAT, with a 3D volume, rather than a 2D plane, rotated around the azimuth.

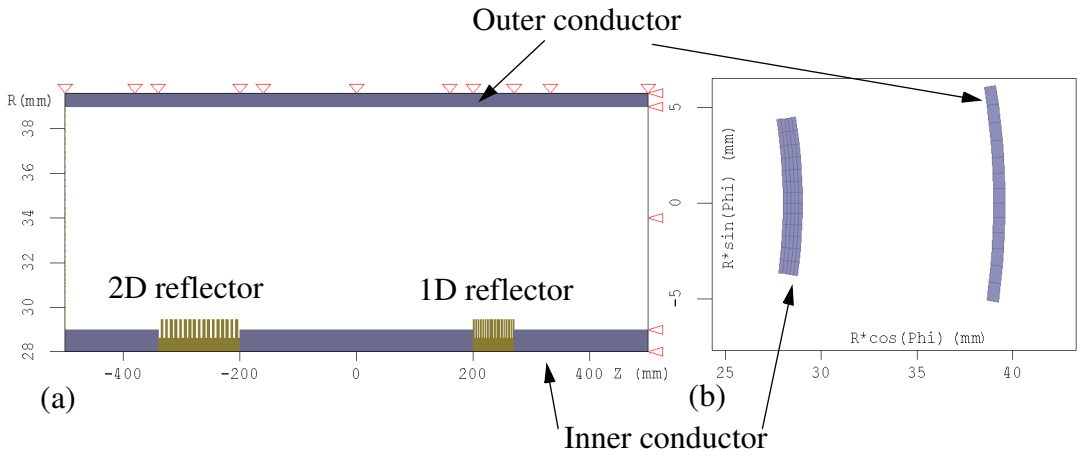

Figure 4.10: Shows the modelled geometry of the 2D - 1D Bragg cavity using the PiC code MAGIC, corresponding to *1/24* of the total geometry. (a) Shows the scaled cross-section in the *r-z* plane (b) Shows the cross-section in the θ-*r* plane.

The geometry of the modelled cavity is shown in Figure 4.10, in longitudinal and transverse cross-section. By modelling such an azimuthal "slice" the computing requirements reduce accordingly, as only $1/24$ th of the number of mesh cells were required, with a similar reduction in the total number of particles. This allowed for the interaction of the electron beam with the undulator field to be modelled in conjunction with the EM interaction with the lasing cavity.

The cavity model was based on the existing experimental parameters for the drift tube, with the mean radius of the inner conductor set at $29mm$ and the radius of the inner surface of the outer conductor set at $39mm$. Optimal performance was noted for a cavity defined by a 17.5 period 2D Bragg input reflector and a 17.5 period 1D Bragg output reflector separated by $40cm$. The 2D reflector had an axial periodicity of $8mm$ and had 24 periodic variations across the azimuth. The 1D reflector had an axial periodicity of $4mm$. Both reflectors had corrugation amplitudes of $\pm 0.4mm$.

The validity of this technique, of modelling a repeating azimuthal slice, in estimating performance from the FEM can be seen in Figure 4.11, which compares the simulation of a 2D reflector over its full geometry, with that of a similar 2D reflector modelled over a single azimuthal period.

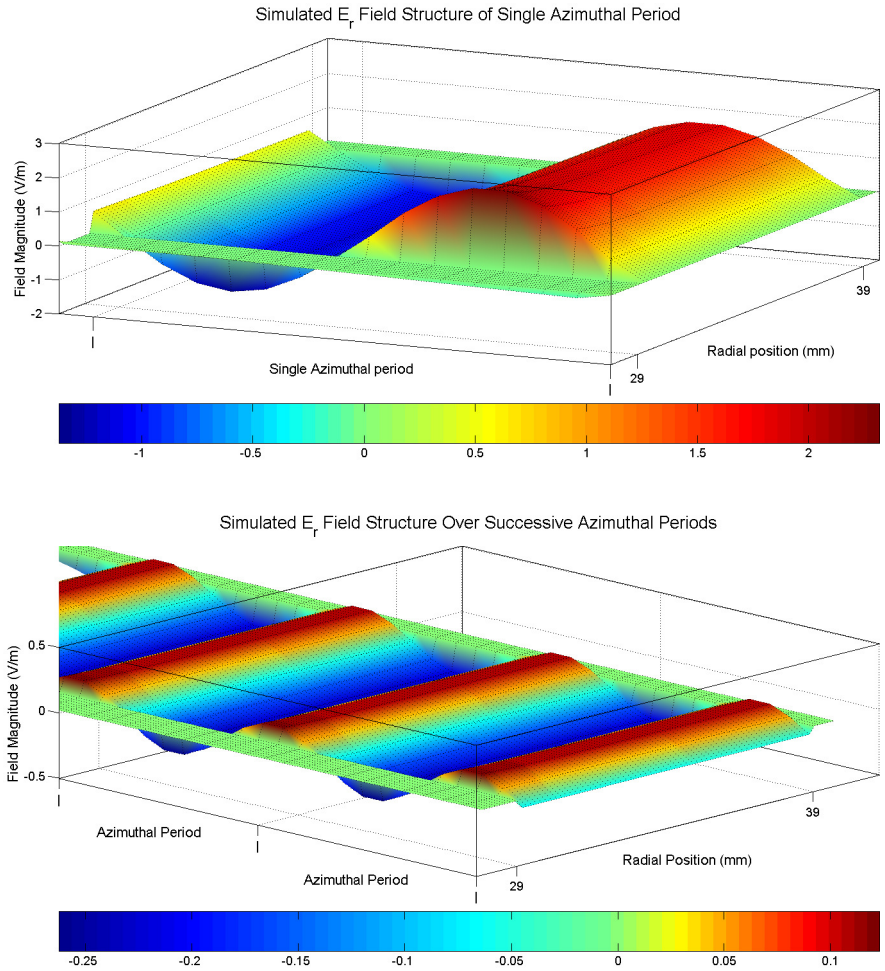

Figure 4.11: Shows the field profile inside a 2D Bragg reflector (a) simulated over a single azimuthal period of a co-axial waveguide. (b) simulated over the full geometry.

As can be seen, the field profile in Figure 4.11 (a) overlays well with that shown in Figure 4.11 (b), implying the same field structures are modelled in both cases over the azimuthal periodicity of the structure. In other words, modelling of a single azimuthal slice of the 2D - 1D Bragg cavity should still provide accurate modelling of the transverse field structure across the azimuth. It should be noted that in both cases the EM field was excited via an oscillating current source at the input port of the structure, as opposed to the insertion of an electron beam. This greatly reduces the computational requirements without adversely affecting the validity of the result.

For the modelled 2D - 1D Bragg FEM, a section of an annular electron beam was injected centred on $r = 33mm$, which took the form of 24 beamlets emitted from adjacent mesh cells. Each individual particle in the simulation corresponded to an electron macro-particle with a charge to mass ratio of $1000 \times e/m_e$. The FEM was driven with beam currents of $70A$ and $120A$ corresponding to $\sim 1.5kA$ and $\sim 3kA$ total beam current respectively (i.e. $1/24$ th of the actual current), to match the expected output from the two plasma-flare gun designs. In both cases the electron energy was set at $460keV$. The undulator field strength was set at $1/10$ th of the guide field strength, with a spike in the magnetic field strength added at $\sim 900mm$ along the z-axis to dump the electron beam to the inner conductor surface.

4.3.2 Modelling of the 2D - 1D Bragg cavity with a 1.5kA beam

The 2D - 1D Bragg cavity is shown in cross-section in Figure 4.12, including the trajectories of two rows of electron beamlets (12 beamlets per row) for an electron energy of $460keV$ and a beam current of $70A$, corresponding to $\sim 1.5kA$ when integrated over the azimuth. The upper and lower beamlets correspond to the boundaries of an electron beam with a finite-thickness, much less than that of the EM wavelength. This allows them to be treated, collectively, as a single electron beam envelope. In this case the axial guide field (B_0) was $0.65T$, setting the undulator field strength (B_u) at $0.065T$.

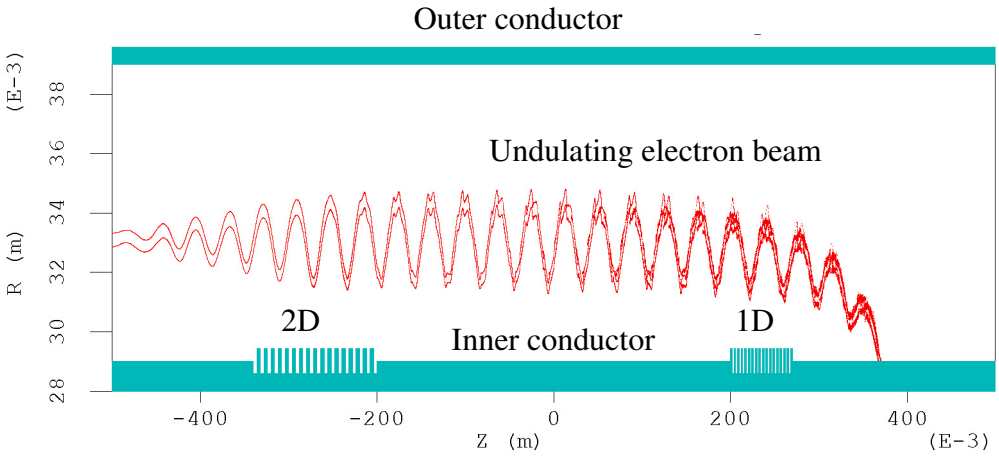

Figure 4.12: Shows the *r-z* cross-sectional geometry of the 2D - 1D Bragg lasing cavity, including the position of the undulating electron beam, modelled using the 3D PiC code MAGIC.

It can be seen that the choice of $B_0 = 0.65T$ and $B_u = 0.065T$, for a beam of $\sim 460keV$ at $\sim 1.5kA$ should be sufficient in establishing the FEL instability, whilst also ensuring the beam is confined enough that the electrons do not impact on either conductor surface. This balance, between ease of electron oscillation and confinement of the radial electron excursion, is intrinsic to the efficient operation of the FEM, as an overly-confined beam would lead to irregularities in the beam oscillations, while an under-confined beam would lead to degradation in the electron beam quality and loss of energy to the drift-tube walls through interception of the outer electrons. Behaviour such as that shown in Figure 4.12 can therefore be seen to be idealised, as the electron trajectories follow well defined sinusoidal paths, whilst maintaining a noticeable separation from either conductor surface.

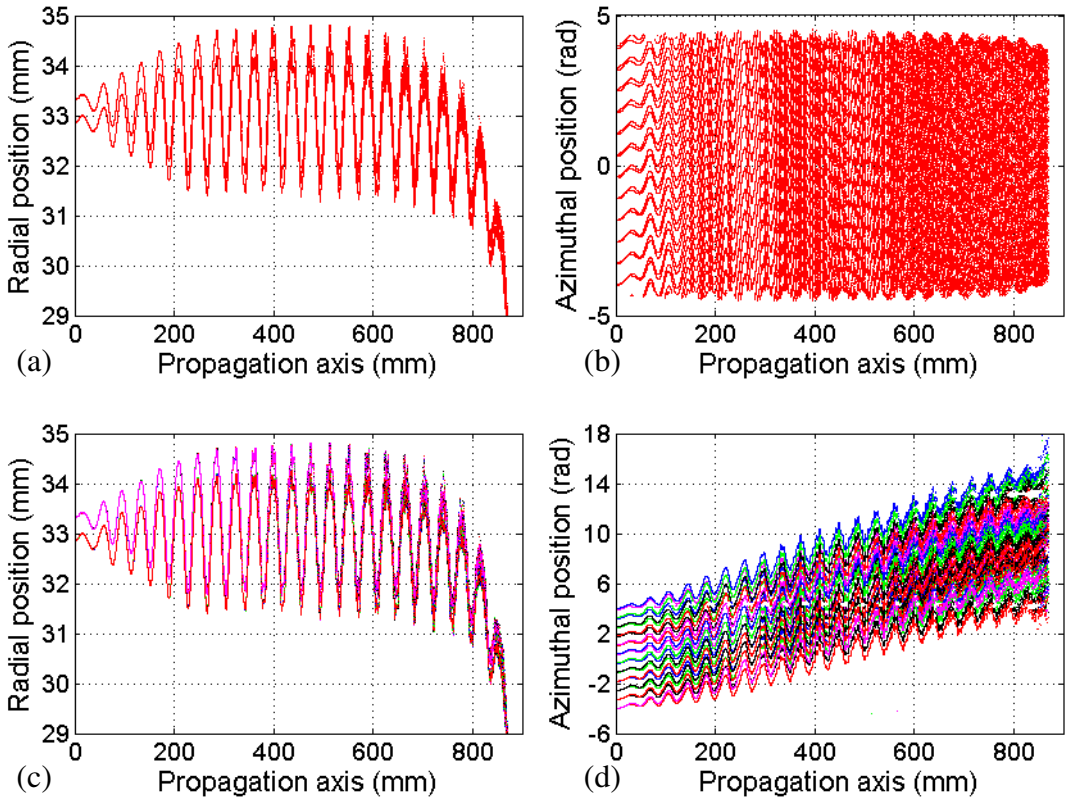

Figure 4.13: (a) Shows the *r*-*z* plane phase-space plot of the beamlet trajectories using raw data from MAGIC. (b) Shows the θ-*z* plane phase-space plot of the same raw data. (c) Shows the *r*-*z* plane phase-space plot of the recovered individual beamlet trajectories from MatLAB. (d) Shows the θ-*z* plane phase-space plot of the corrected azimuthal trajectories of the beamlets.

Examination of individual beamlet evolution along the propagation axis was obtained by extracting 2D phase-space data from MAGIC, i.e. (r, z) and (θ, z), and reconstructing a 3D phase-space plot using the numerical package MatLAB. An example of the recovered trajectory for a single electron beamlet is given in Figure 4.14, while a comparison of the raw data and that recovered after reconstruction of all beamlet trajectories is given in Figure 4.13.

The radial oscillation seen in Figure 4.13(a) and (c) corresponds to the rotation imparted to the electron macro-particles by the periodic $\vec{B}_u(r, z)$ field of the azimuthally symmetric undulator (c.f. Section 2.3.1), as does the azimuthal oscillation

seen in the recovered beamlet trajectories of Figure 4.13(d). Looking at Figure 4.14, the relative magnitude of both the radial and azimuthal oscillation can be seen to be approximately equal, with the electrons initially describing mildly elliptic orbits as they propagate along z. These orbits become more eccentric as the axial bunching mechanism of the FEL instability begins to form:

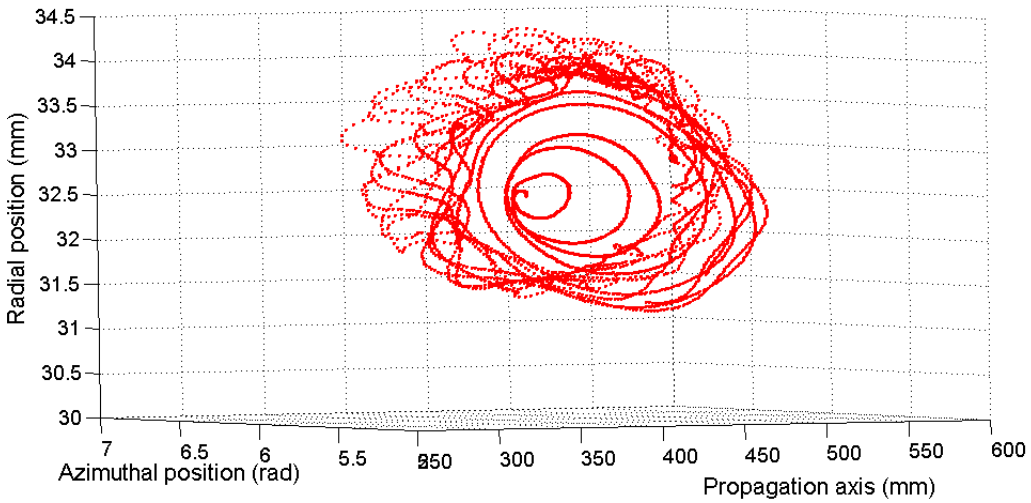

Figure 4.14: Shows a 3D plot of a single electron beamlet, showing the initial uniformity in (r,θ) of the electron oscillations, induced by the periodic undulator magnetic field.

It should be noted that this rotation is not synonymous with Larmor rotation, where electrons rotate around the magnetic field lines of a uniform guide field at a radius of $r_{Larmor} = (mv_{\perp})/(eB_0)$, where $v_{\perp}$ is the transverse velocity of the electrons. In the case of the FEM experiment $v_0 \approx v_z$ (c.f. Section 2.3) indicating the Larmor radius, defined as:

$$r_{Larmor} = \frac{m_e v_{\perp}}{eB_0} \qquad \textbf{4.5}$$

would be small as $v_{\perp} \approx 0$ in the absence of the undulator field.

As will be shown later in this section, no evidence of the cyclotron emission is seen in the output spectra from the modelled cavity, showing a lack of emission at the cyclotron frequency, though some emission at the Weibel frequency can be discerned,

indicating some degree of cyclotron motion in the beam albeit to a much lower degree than that of the FEL motion.

The drift along the azimuth seen in Figure 4.13 (d) is due to the radial dependence of the axial magnetic field strength, both in the axial guide field (B_0) and the axial periodicity of the undulator field (B_u). This results in a "gradient drift" (Jackson 1999) of the electron guiding centres related to the local magnetic field strength, i.e. electrons travelling along a guiding centre radially closer to the undulator coil (where the perturbation in the local magnetic field is stronger) will experience a stronger "drift" than those travelling along guiding centres closer to the axis. This dependence on proximity to the undulator is shown in Figure 4.15, where the trajectories of two electron beamlets are plotted in (θ, z):

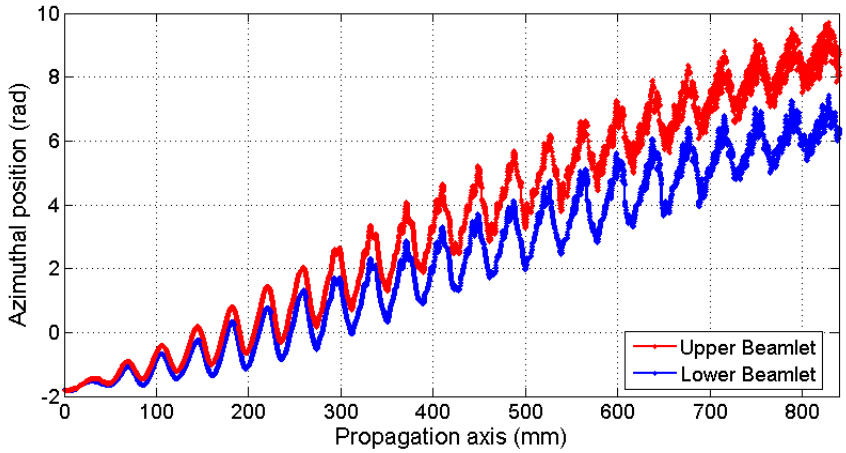

Figure 4.15: Shows the θ-z plane trajectories of an upper and lower beamlet, emitted from adjacent radial mesh cells, with the same initial azimuthal position.

Here the upper and lower beamlets were emitted from radially adjacent mesh-cells, giving them identical θ, z coordinates. The drift can be seen to be reduced in the trajectories of the lower beamlets, as expected due to the decreased gradient of the undulator field closer to the axis.

The "blurring" of the oscillations of the beamlets, seen towards the right in Figure 4.15 results from the formation of electron bunches in the propagating electron beam. In

keeping with the increased local gradient of the undulator field, this blurring can be seen to be stronger in the upper beamlet than the lower beamlet. The nature of the bunching mechanism can be observed readily, across all beamlets, by looking at a 3D cross-section of a small portion of the beam:

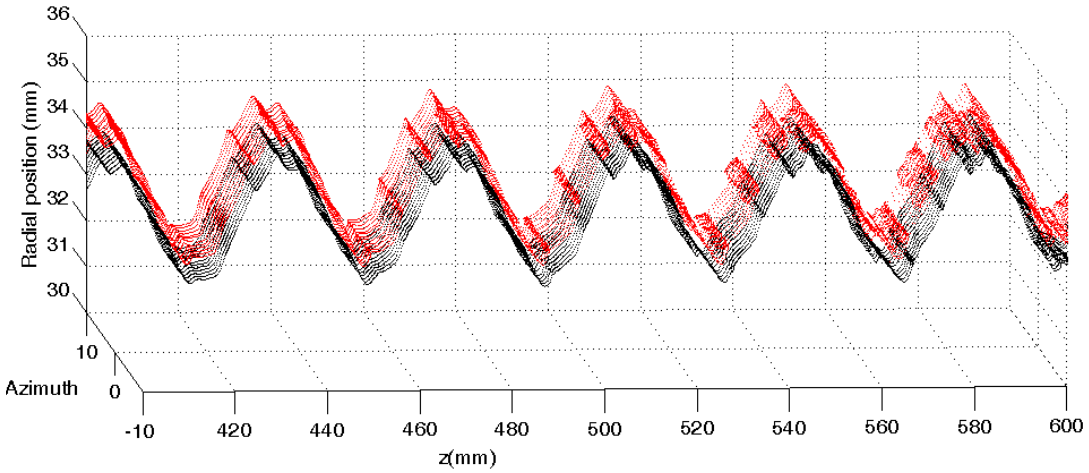

Figure 4.16: Shows the axial bunching along z of the electron beamlets. Uniform bunching across the azimuth was observed.

Examination of Figure 4.16 confirms the formation of axial bunching in the beam; bunches in successive beamlets can be seen to form at identical positions along z. Such bunches were distinguishable in the simulation after $\sim 70 ns$ of run time.

There were two potential beam instabilities which could lead to such bunching, namely the Weibel instability and the FEL instability. The former relies on the Larmor rotation of the electrons, much like the cyclotron instability (which it is associated with), which as stated is small in the FEM experiment. By its nature the Weibel instability requires interaction with an E_θ component, which is absent in the fundamental TEM mode of co-axial waveguide (that which the FEM was designed to operate with). The first mode which would support strong coupling with a Weibel instability in the beam is the $TE_{0,1}$ mode, which would give an expected resonant frequency of $\sim 44 GHz$.

In contrast, if the bunching seen in Figure 4.16 is the result of the establishment of the FEL instability the operating mode would be the fundamental TEM mode, with

resonant coupling, defined by the axial period of the undulator, occurring in the region of $37.5GHz$, with the exact frequency determined by the over-lap of the resonant band-gaps of the input and output mirrors used to define the lasing cavity.

As different modes would be involved in the different axial bunching mechanisms, determination of which bunching mechanism (or indeed mechanisms as may be the case) are present, may in the first instance be made by analysis of the component field profiles. Contour maps of these through the modelled cavity are shown in Figures 4.17 and 4.18 for the $\vec{E}$ and $\vec{B}$ fields respectively.

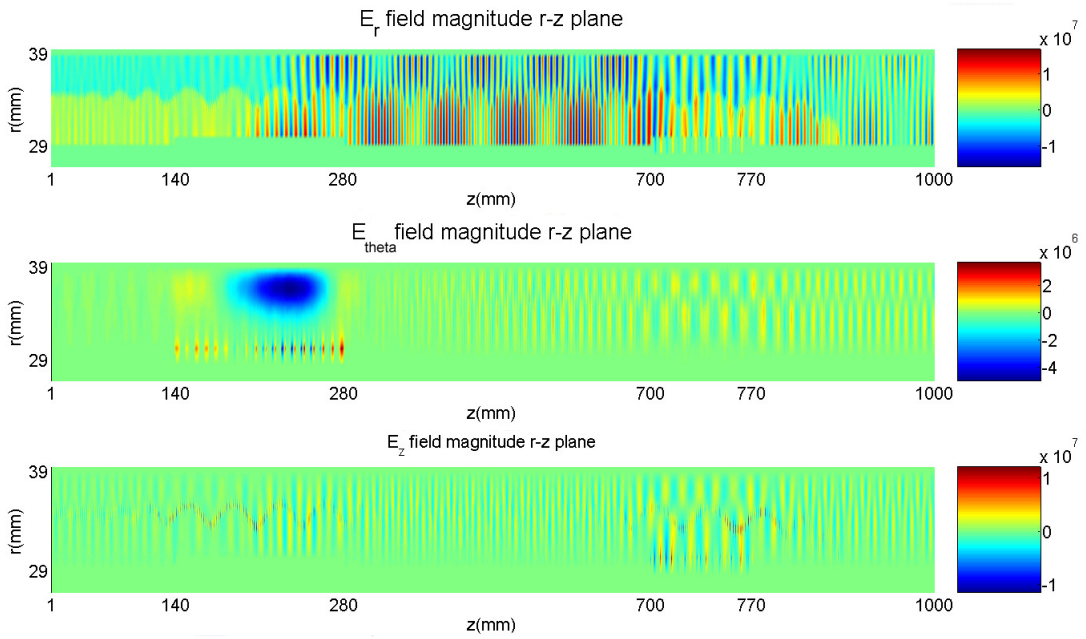

Figure 4.17: Shows the magnitudes of the *E* field components in the *r*-*z* plane, recovered from MAGIC and plotted using MatLAB.

The TEM mode is defined by the E_r and B_θ field components, which can be clearly seen to be the dominant field components both within the cavity and at its output. This indicates that the FEL instability was present and was the dominant bunching mechanism in the beam-wave interaction. Examination of the field profile shows the longitudinal mode of the cavity (that defined between the 2D and 1D Bragg reflectors) to have a longitudinal designation of $p \cong 100$, in line with the TEM_{100} mode expected for a cavity length of $40cm$. No clear evidence of excitement of the Weibel instability

can be discerned, as notable excitement would result in a much higher E_θ and B_z both inside the cavity and at the output.

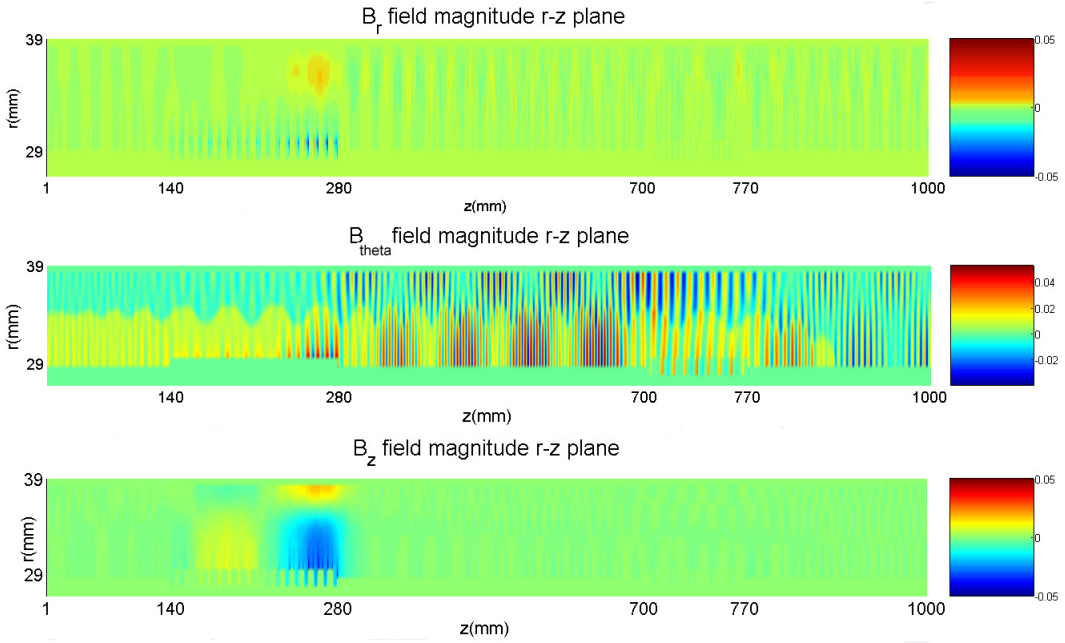

Figure 4.18: Shows the magnitudes of the B field components in the r-z plane recovered from MAGIC and plotted using MatLAB.

The mechanisms which confine the TEM mode within the cavity can also be clearly seen. Looking at E_r and B_θ in the region of the 1D reflector ($700 - 770mm$) direct interaction can be observed; the cross-sectional structure of the 1D reflector is clearly seen (compare with E_θ). In contrast, the coupling mechanism of the 2D mirror ($140 - 280mm$) can be seen to be more complex. While E_r and B_θ both show decaying field amplitudes across the region of the reflector, they also show no interaction with the reflector itself. Rather E_θ, B_r and B_z show localised increases in field amplitudes, confined within the region of the 2D Bragg reflector. This indicates that the TEM mode undergoes some interaction with an intermediate TE mode in the region of the reflector, confirming the four-wave coupling mechanism described in Section 3.3.2. In the general case this refers to coupling between the TEM mode and the $TE_{M,n}$ mode, where M is the number of azimuthal variations of the 2D corrugation and $n = 1, 2\ldots$ is the number of radial variations. For the cavity presented here and that used in the experiment the resonant coupling was taken as occurring between the

TEM mode and the $TE_{24,2}$ near cut-off mode, evidenced by the two radial variations observed in the E_θ and B_z field profiles and the theoretical cut-off frequency of the $TE_{24,2}$ mode lying in the correct region of $\sim 37.5 GHz$ (c.f. Section 3.2.1). The number of variations along the axis was a function of the length of the 2D corrugation

In addition, some information regarding the presence of other modes can also be ascertained. The E_z component, present in the region of the output 1D Bragg reflector, indicates the presence of TM mode coupling at the cavity output. This is in-line with the theoretical predictions of the mirror performance (c.f. Section 3.3.1.2), where a spurious TEM-$TM_{0,1}$ reflection band was expected due to the oversized nature of the cavity. It should be noted however, that the relative magnitude of this interaction, compared to that seen for the pure TEM-TEM operation, indicates only a small fraction of the energy in the TEM mode is lost due to mode conversion.

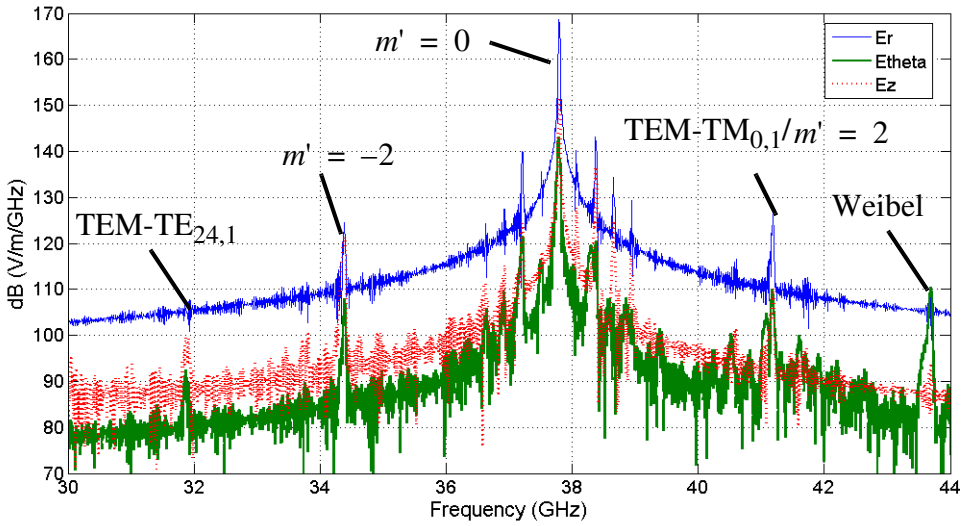

Figure 4.19: Shows the Fourier transform of the *E* field at the output of the lasing cavity.

The spectral content of the output pulse was determined by taking the Fourier transform of the individual field components at the output of the 1D Bragg reflector. Figures 4.19 and 4.20 show the spectral content for the $\hat{E}$ field and $\hat{B}$ field components respectively.

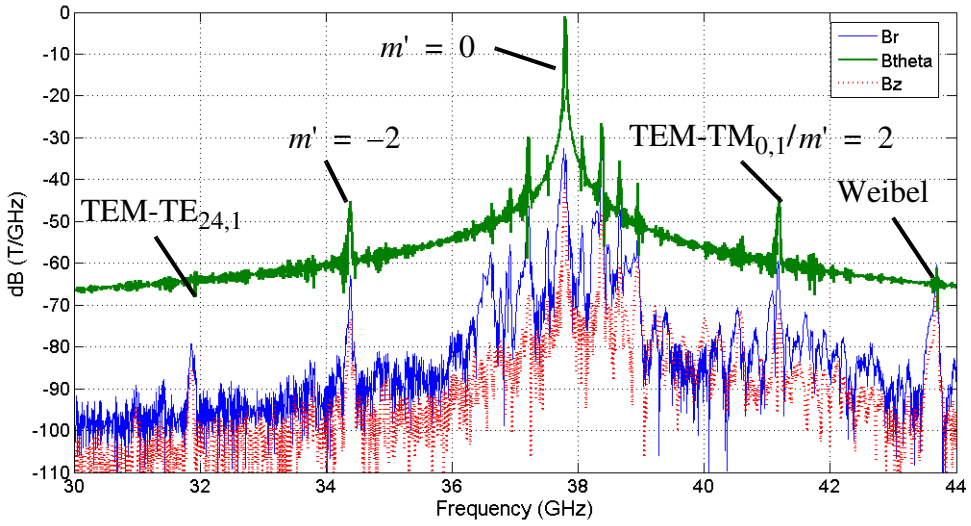

Figure 4.20: Shows the Fourier transforms of the *B* field at the output from the lasing cavity.

From this it can be seen that the E_r and B_θ field components dominate, as expected from Figures 4.17 and 4.18. The spectra can be seen to peak sharply at $\sim 37.8 GHz$, corresponding to the $m' = 0$ eigenmode solution, discussed in Section 3.4, with harmonics, due to the $40cm$ separation of the reflectors, spaced by integer values of $\sim \pm 0.3 GHz$. This agrees well with the expected performance given by analytical theory, which estimated a main resonance between $37.5 - 38 GHz$ for the experimental cavity, with side-lobes located at integer values of $\sim \pm 0.5 GHz$. The $m' = \pm 1$ eigenmode and its harmonics seem dominated by those of the $m' = 0$ eigenmode, however the more pronounced field structure in B_r E_θ and E_z around $36 GHz$ and $39 GHz$ indicate its existence as an EH-like mode.

The spike located at $\sim 43.7 GHz$ in the E_θ, B_r and B_z traces corresponds well with the expected location of radiation generated by the Weibel instability, implying it is present, but as expected from the contour plots is of a much lower amplitude than the dominant FEL mechanism. The spike at $\sim 41 GHz$ in E_θ, E_z and B_r agrees well with both the $m' = 2$ eigenmode (c.f. Figure 3.20) and the parasitic coupling expected between the TEM-$TM_{0,1}$ modes, generated in the region of the 1D reflector; this is

reflected in the slight spikes seen in E_r and B_θ at the same frequency. The spike at $\sim 34.5 GHz$ corresponds well with the expected position of the $m' = -2$ eigenmode while the spike at $\sim 31.9 GHz$ corresponds to spurious coupling of the TEM mode to the lower $TE_{24,1}$ mode. The greatly reduced amplitude of this coupling, when compared to the TEM-$TE_{24,2}$ mode coupling may be explained due to the relatively low number of electrons emitting at the required frequency and a reduced coupling strength due to the miss-match in h_s to $k_{cTE_{24,1}}$.

The estimated power output from this single segment of the optimised lasing cavity was $\sim 6 MW$, giving an estimated total system power in the region of $140 MW$. This can be compared with the results from the experimental cavity, using a comparable electron beam, given in Section 7.3. Some comparison of the measured spectrum and that presented above is provided in Section 7.3, though it should be noted that the experimental measurements were performed using cut-off filters, yielding only a rough guide to the spectral content.

4.3.3 Modelling of the 2D - 1D Bragg Cavity with a 3kA Beam.

Following the successful construction and testing of a FEM based on the EEE1 gun and the proof of principle 2D - 1D Bragg cavity, described in Section 4.3, a move to the implementation of the EEE2 gun (c.f. Section 4.2.1.2) was made, keeping the lasing cavity unchanged. In keeping with this, the simulation presented in Section 4.3.2 was repeated with the beam current increased to $120 A$, corresponding to an increase in total beam current to $\sim 3 kA$. The aim being to examine the suitability of the idealised cavity for use with the higher current electron beam. As the $1.5 kA$ simulation yielded spectral results comparable with the experimental results a similar agreement was expected between the $3 kA$ simulation and experimental results.

From the initial simulation results it was found that keeping the magnetic field at $0.65T$ was insufficient in confining the electron beam once the undulator induced oscillations became established, with the outer electrons impacting on the inner conductor surface. The resultant spectra for the $\vec{E}$ field components are shown in Figure 4.21.

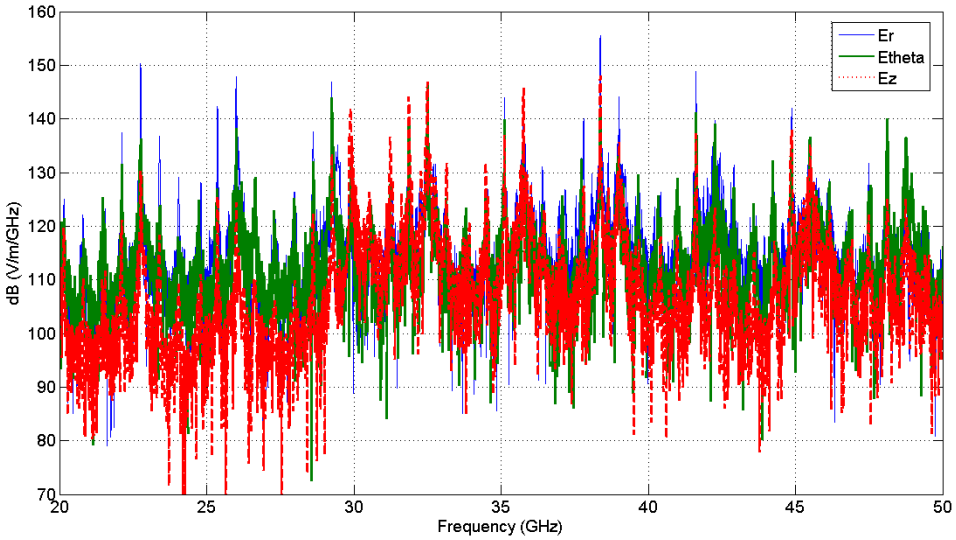

Figure 4.21: Shows the Fourier transform of the *E* field at the output from the lasing cavity, with the guiding magnetic field maintained at *0.65T* and the beam current increased to *3kA*.

As can be seen, simply increasing the beam current, without altering other system parameters, resulted in severe degradation of the cavity performance. One possible solution to this problem would be to reduce the separation between the input and output reflectors, reducing the cavity Q-factor and so reducing the growth rate of the bunching mechanism on the beam. However, as the performance of the cavity modelled for the $1.5kA$ beam was under investigation, to determine its suitability in use with both the EEE1 and EEE2 gun topologies, an alternative solution was taken, that of increasing the magnetic field. This was done to better confine the radial motion of the electrons, and so reduce the risk of exciting the high level of noise seen in Figure 4.21.

Best performance was obtained with the guide field increased to $1.2T$ with the same ratio of B_0/B_u as before. The trajectories of the electron beamlets through the cavity, with the higher beam current and increased magnetic field, are shown in Figure 4.22.

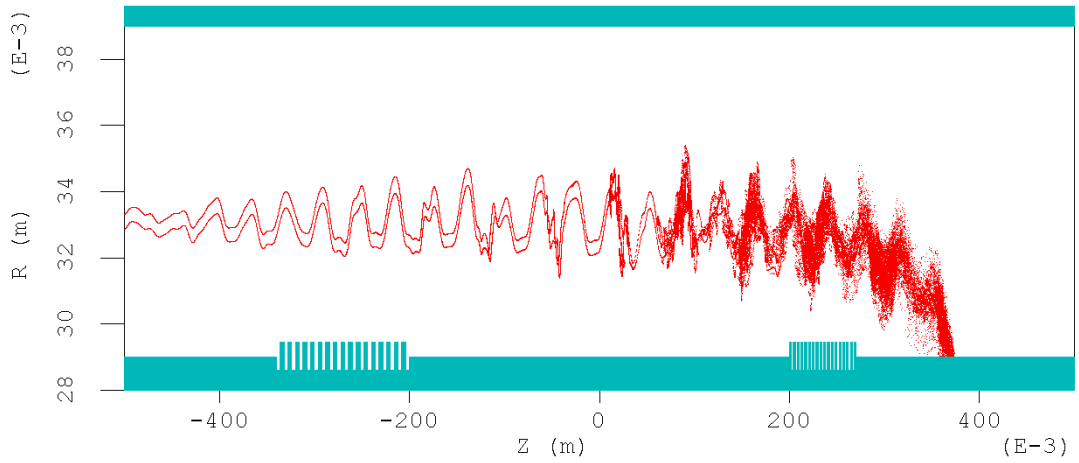

Figure 4.22: Shows the axial bunching of macro-particles in the *120A* beam current simulation of the 2D - 1D Bragg cavity.

Comparing Figure 4.22 with the $1.5kA$ beam case (see Figure 4.12) it can be seen that the spread of the electrons towards the exit of the cavity is much more pronounced, indicating stronger coupling of the beam to the EM field. However it can also be seen that the radial oscillations of the electrons have been constrained by the increased guide field strength, perturbing the electron orbits and leading to the excitement of at least one additional mode in the beam-wave interaction.

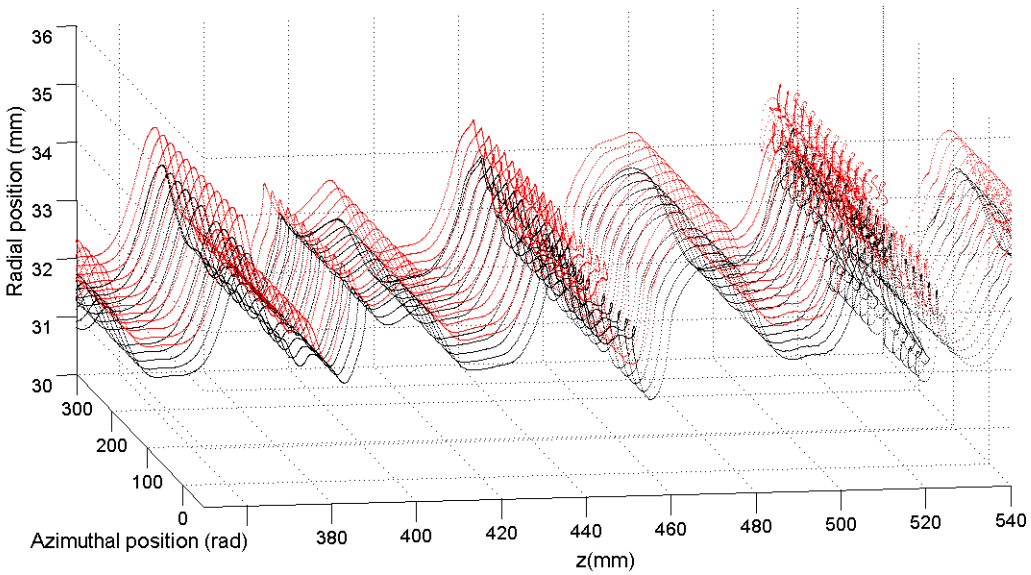

Figure 4.23: Shows the axial bunching along z of the electron beamlets. Uniform bunching was observed across the azimuth.

As with Figure 4.16, looking at a 3D cross-section of the electron beam shows the existence of axial bunching, which occurs uniformly across all bunches, though these appear less well defined than in the $1.5kA$ beam case. The influence of multi-mode operation is most likely the cause for the degradation in the bunching mechanism, as this would reduce the coherence of the electron - TEM mode beam-wave interaction. It is interesting to note, however, that what bunching occurs only does so axially and uniformly across the azimuth. Likewise, all beamlets show the same loss of coherence in the bunching mechanism at the same points along z, which at least indicates the FEL instability is likely to remain the main interaction mechanism.

Some information of the modal content can again be gained from looking at the $\grave{E}$ and $\grave{B}$ field components. Figures 4.24 and 4.25 show the contour plots of the $\grave{E}$ and $\grave{B}$ field components respectively. These can be compared with Figures 4.17 and 4.18.

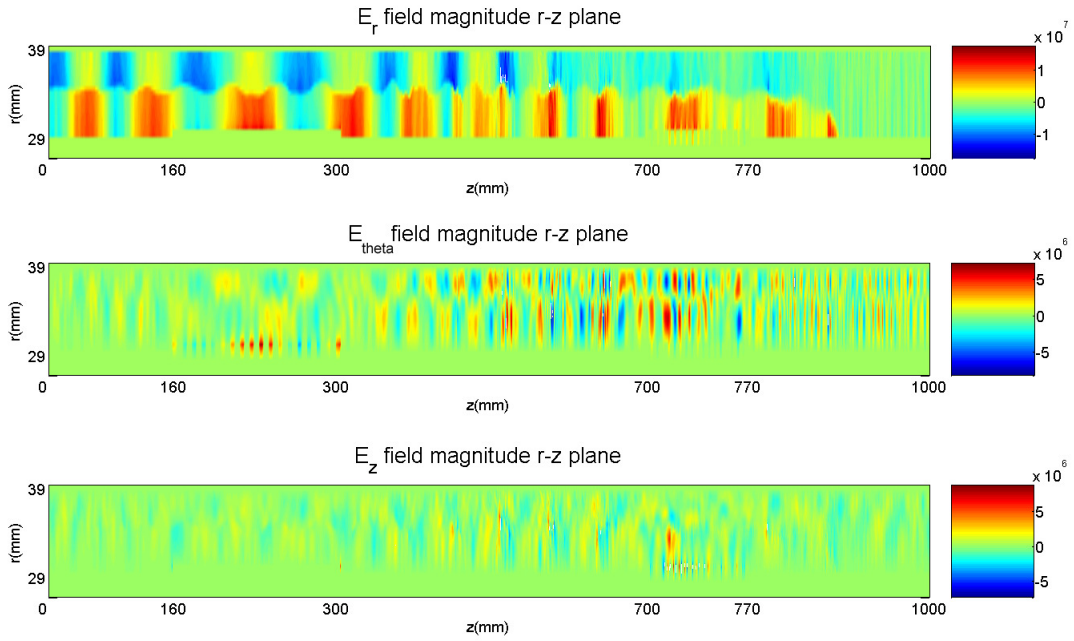

Figure 4.24: Shows the magnitudes of the *E* field components in the *r-z* plane, recovered from MAGIC and plotted using MatLAB.

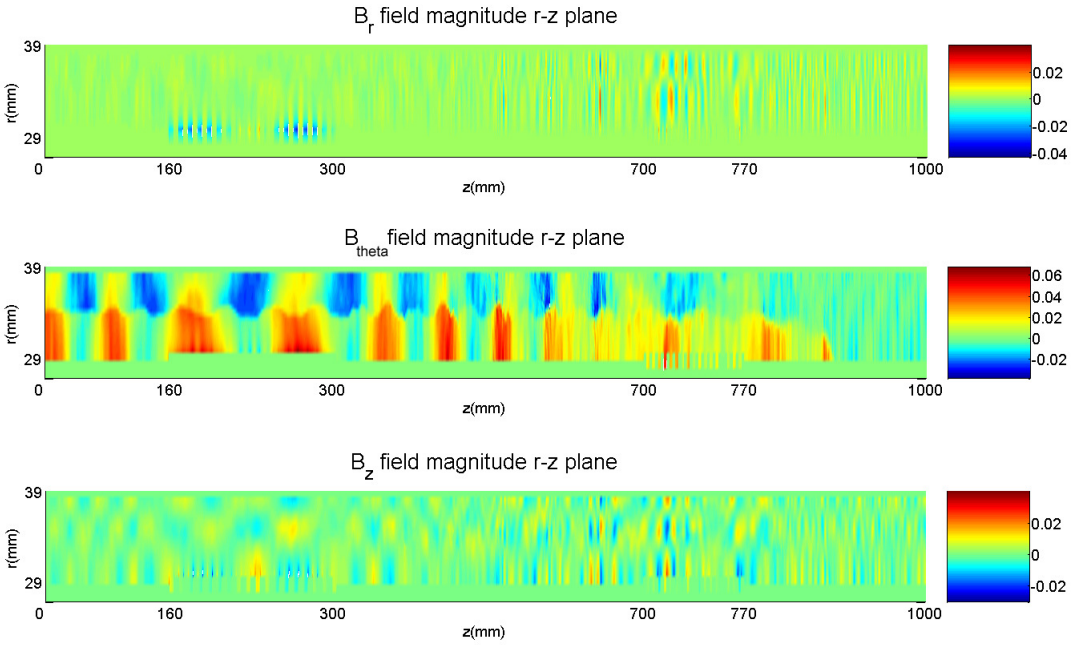

Figure 4.25: Shows the magnitudes of the *B* field components in the *r-z* plane recovered from MAGIC and plotted using MatLAB.

As in the $1.5kA$ case, the dominant field components are E_r and B_θ, which show field profiles distinct from the other field components, indicating growth of the TEM mode. However the presence of another strongly coupled mode can be seen which perturbs the field profiles, most notably in the increased amplitudes of E_θ, B_r and B_z. Looking specifically over the region of the 1D Bragg reflector, the presence of similar field profiles can be observed in both the $1.5kA$ and $3kA$ cases for these field components:

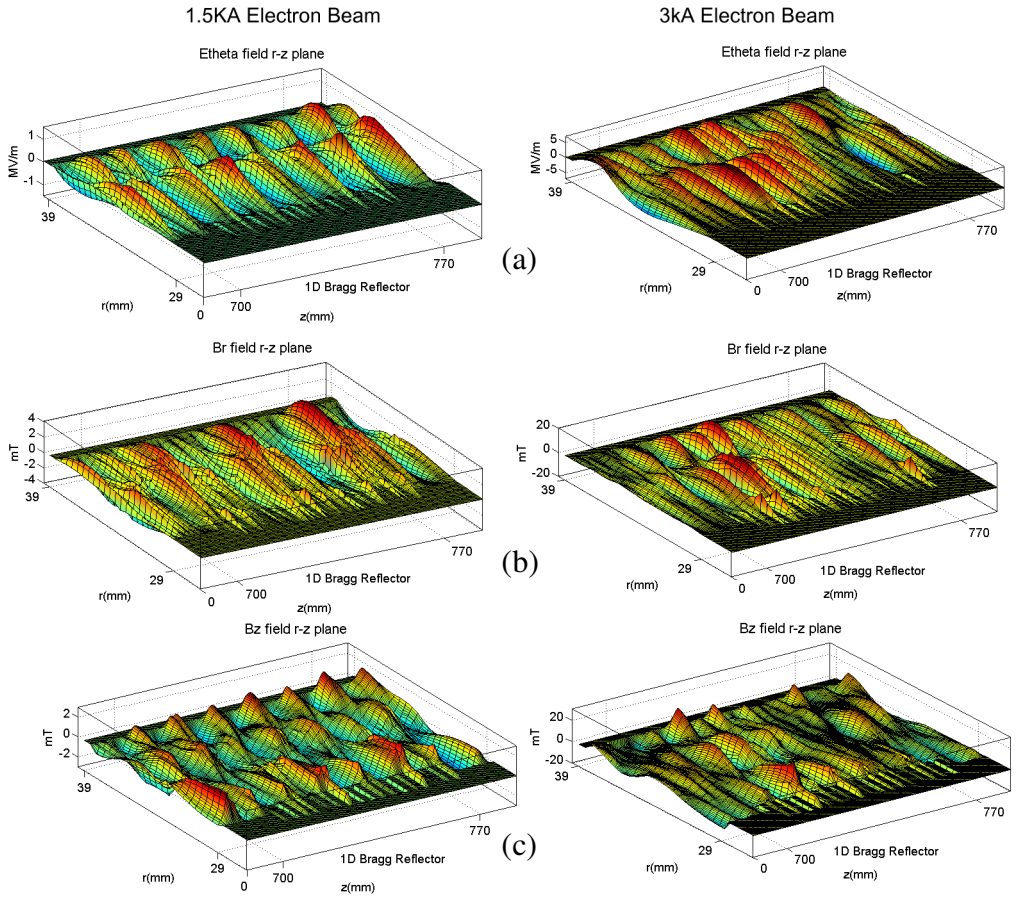

Figure 4.26: Compares the (a) E_θ, (b) B_r and (c) B_z field components for the *1.5kA* and *3kA* simulations.

This indicates that not only was the competing mode present in the $1.5kA$ simulations, but that it was as well defined, albeit at reduced field amplitudes. Comparison of the E_z field components, in Figures 4.17 and 4.24, shows the growth of the competing mode also produces an effect here, indicating it is an HE hybrid mode (c.f. Section 3.2).

Another consequence of increased coupling to the HE mode can be seen in the region of the 2D Bragg reflector. A comparison of all six components of the $\vec{E}$ and $\vec{B}$ fields, in the region of the 2D Bragg reflector, are given in Figures 4.27 and 4.28 respectively:

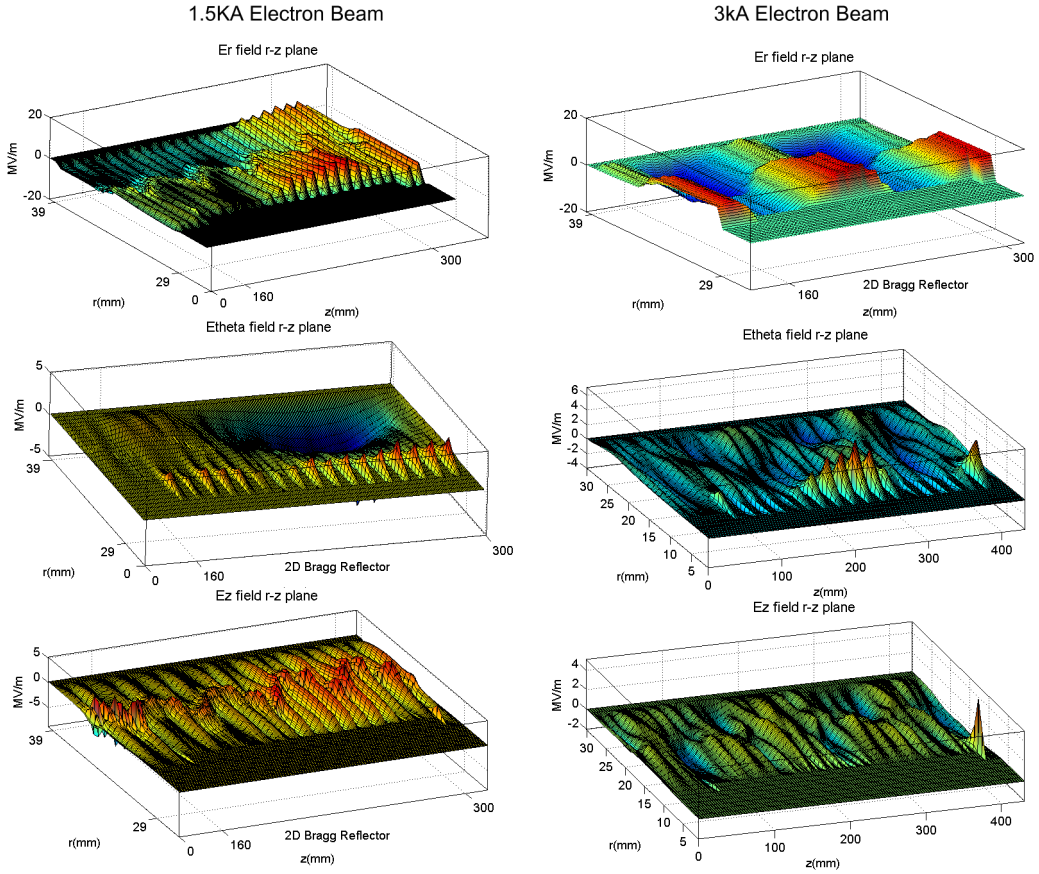

Figure 4.27: Compares the *E* field components for the *1.5kA* and *3kA* simulations, in the region of the 2D Bragg reflector.

Comparing E_θ from the $1.5kA$ and $3kA$ simulations it can be seen that the incidence of the HE mode at the 2D Bragg reflector greatly alters the coupling mechanism, with the competing mode dominating; this is reflected in the field profiles of the E_z, B_r and B_z components which all show modifications which follow that of the E_θ component. This alteration appears to degrade the efficiency of the reflector in containing the TEM mode within the cavity, with the magnitude of the E_r and B_θ components remaining fairly constant from the input of the simulation through to the beginning of the 1D reflector.

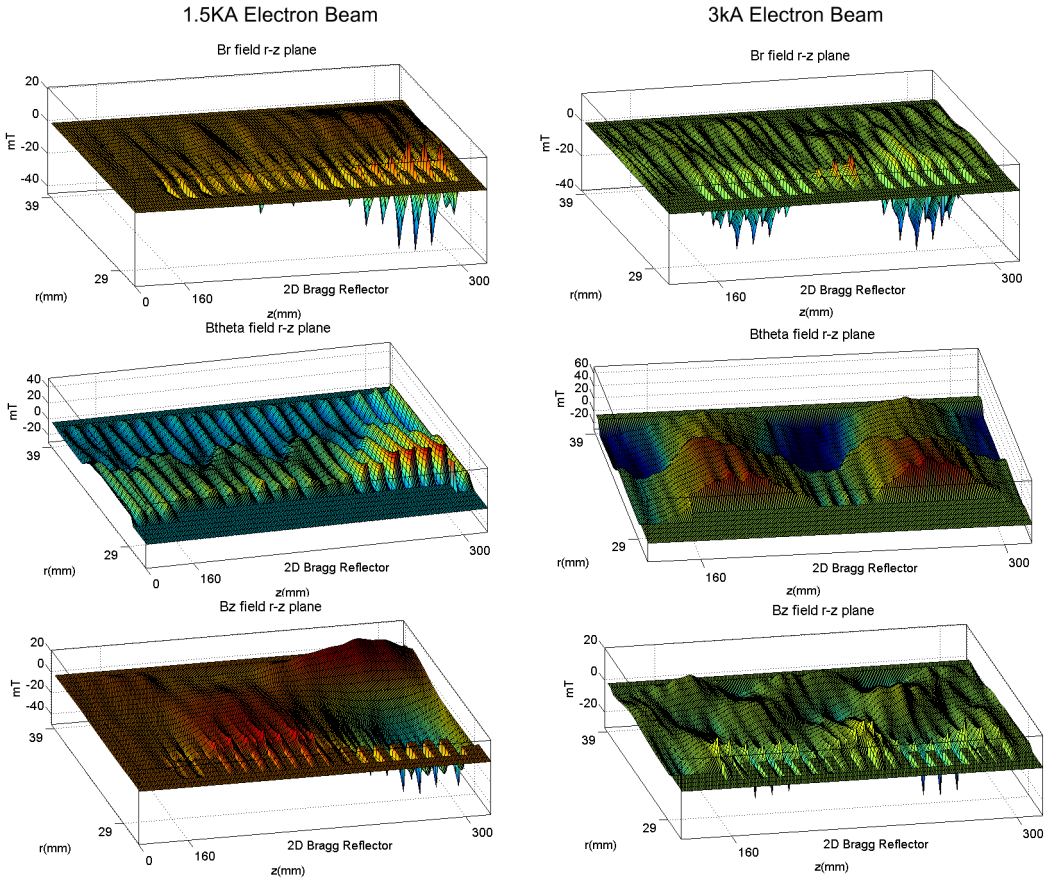

Figure 4.28: Compares the *B* field components, for the *1.5kA* and *3kA* simulations, in the region of the 2D Bragg reflector.

A slight change in the over-all shaping of the E_r and B_z components, in the region of the 2D mirror, may indicate these components are present in the HE mode, though working purely from Figures 4.27 or 4.28, this cannot be clearly ascertained.

Before considering the Fourier transform of the field components, some investigation of the HE mode may be performed by looking at the field contours in the (θ, z) as well as the (r, z), plane. Noting that the E_θ component in the $1.5kA$ simulations, is defined strongly in the region of the 2D Bragg reflector and shows the expected TEM-$TE_{24,2}$ mode coupling, comparison of the azimuthal field profile with that of the $3kA$ case, over this region, allows for a fair approximation of the HE modal designation.

Figure 4.29 compares the (θ, z) and (r, z) E_θ field profiles for the two simulations:

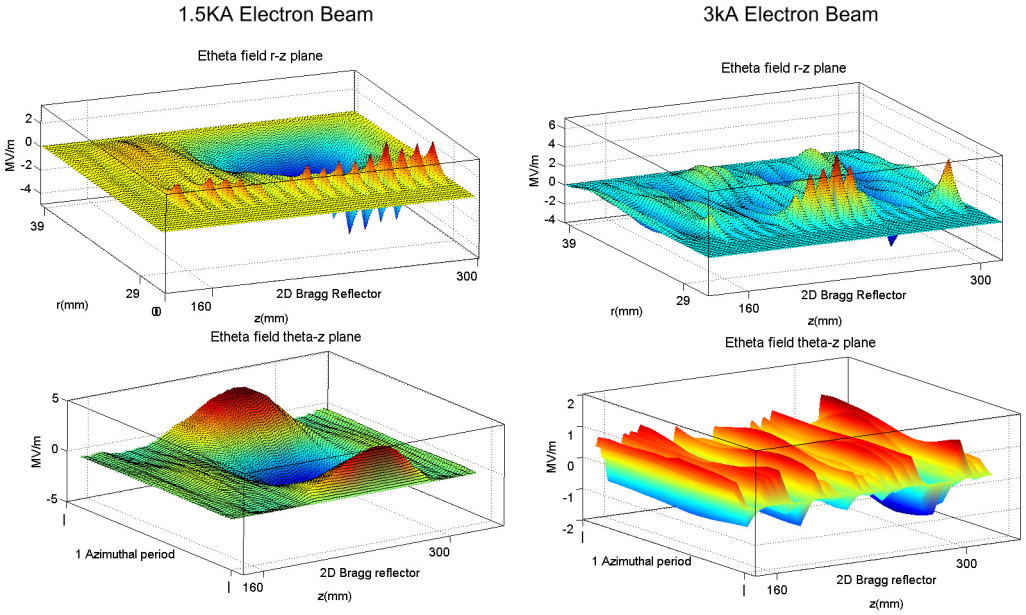

Figure 4.29: Compares the E_θ field components for the *1.5kA* and *3kA* simulations, in the (r,z) and (θ,z) planes.

The transverse profile of the E_θ component in the $1.5kA$ experiment shows a fully periodic field variation over the single azimuthal period of the corrugation, as expected for coupling with a $TE_{24,n}$ mode, with the longitudinal (r,z) cross-section implying $n = 2$, in line with the expected four-wave TEM-$TE_{24,2}$ coupling mechanism. The transverse profile of E_θ in the $3kA$ simulations, however, shows the superposition of the expected $m = 24$ profile with another showing $m \approx 0$ across the azimuth of the single corrugation period modelled. Exact designation of m for this competing mode would require modelling of an increased number of azimuthal periods, putting it beyond the computational resources available at the time of study. It may be assumed, however, that m, for the HE mode, should be low, say $m = 0, 1, 2$, which combined with examination of the longitudinal cross-sections give a tenuous value of $n = 2$, i.e. an $HE_{m,2}$ mode where $m \in (0{:}2)$.

With some description of the operating modes defined, the spectral content generated by the $3kA$ beam, was examined by taking the Fourier transform of the $\vec{E}$ and $\vec{B}$ field components at the output of the 1D Bragg reflector:

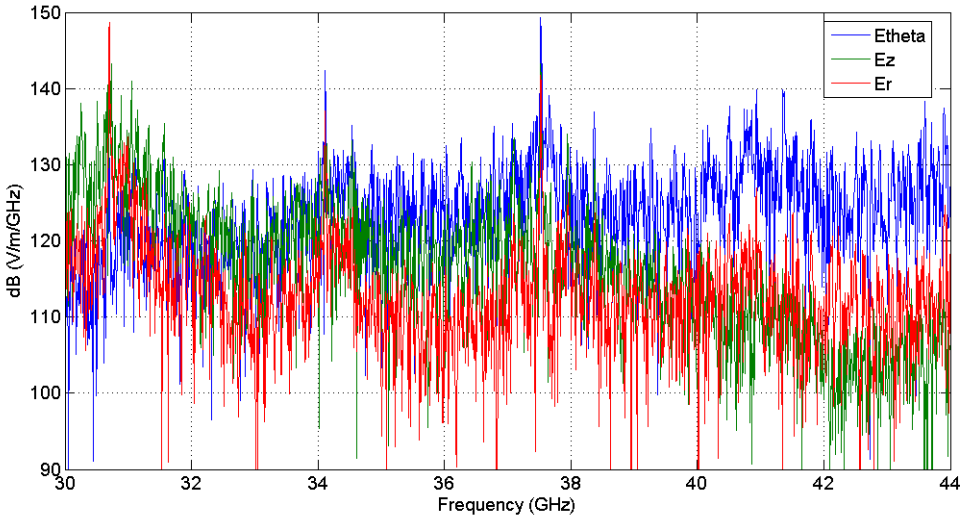

Figure 4.30: Shows the Fourier transforms of the E field components at the output from the lasing cavity.

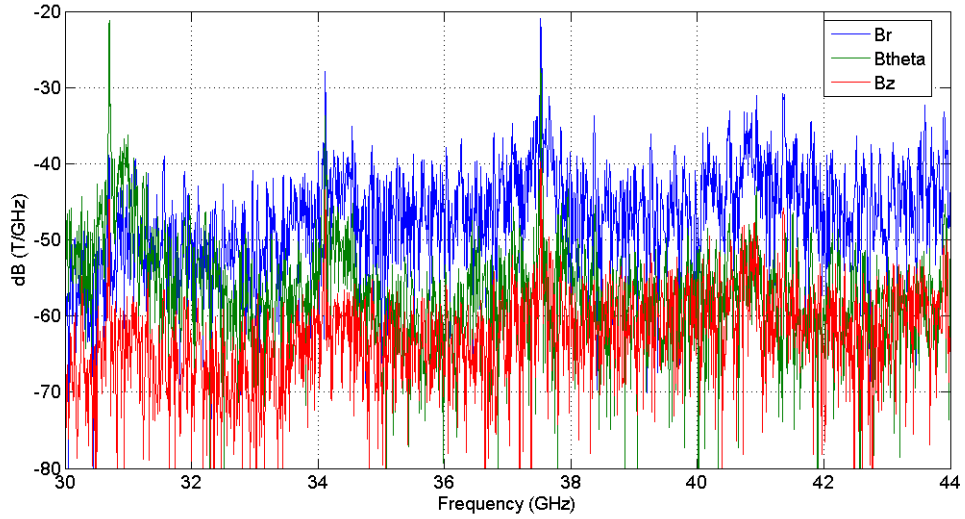

Figure 4.31: Shows the Fourier transforms of the B field components at the output from the lasing cavity.

As expected from Figures 4.24 and 4.25, the spectral content for the $3kA$ case shows a much higher degree of noise than the $1.5kA$ case, though some of the spectral characteristics can still be discerned. The increase in the noise level may be explained by consideration of the Lowbitron interaction discussed in Section 2.3.2; the perturbed electron oscillations seen in Figures 4.22-4.23 leads to an increase in the ratio of $v_\perp / v_z$, reducing the frequency range of the Lowbitron instability such that its operational regime begins to overlap that of the FEM. Clarity of spectral content may be improved by looking at the Fourier transforms of the total E and B fields, as shown in Figure 4.32a and b:

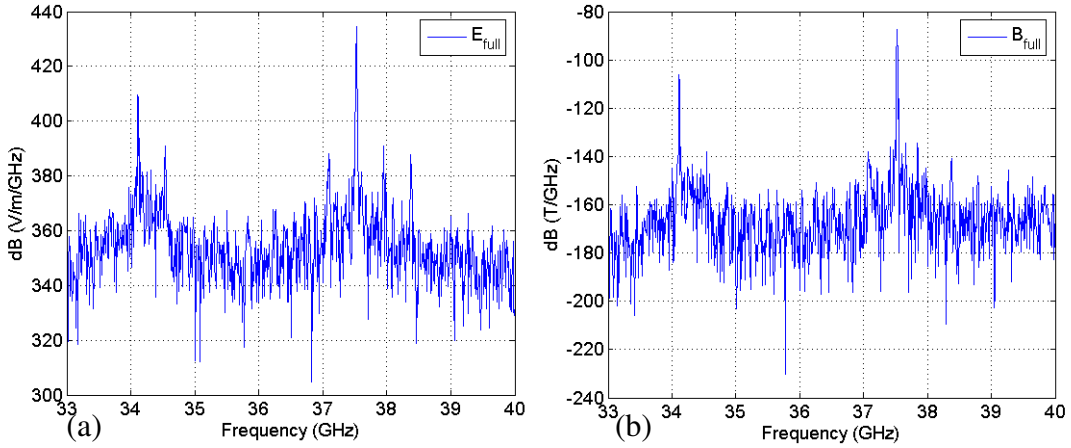

Figure 4.32: (a) Shows the combined E field FFT's and (b) shows the combined B field FFT's for the *3kA* simulations.

In this form the expected operating frequency, from the $m' = 0$ eigenmode, can be clearly seen, with a central frequency of $\sim 37.5GHz$ and longitudinal harmonics separated by $\sim 300MHz$. The lower $m' = -2$ eigenmode can again be seen to be present and to show an increase in both magnitude and spectral width. An equivalence between this eigenmode and the $HE_{m,2}$ mode noted in discussion of the field contour plots is clear, indicating the HE mode designation should be $HE_{2,2}$.

The output power from the segment simulated was $\sim 8MW$, indicating an increase in the expected total output power to $\sim 192MW$ for the cavity, with an associated increase in signal noise. Work on an optimised cavity design for the higher beam current of

$\sim 3kA$ is ongoing at the time of writing this thesis, with the resulting cavity to be measured experimentally. Results obtained using the existing 2D - 1D Bragg cavity, with a $\sim 3 - 4kA$ electron beam, are presented in Section 7.4.3 for comparison.

4.4 Conclusions.

The plasma-flare gun used in the 2D - 1D Bragg FEM experiment was modelled, using the 2.5D PiC code KARAT, for two separate geometries; one with a $14.5cm$ radius anode can and one with a reduced anode can radius of $6cm$. In both cases a magnetic field in the region of $0.65T$ was found adequate to transport a $\sim 450keV$ electron beam across the accelerating gap of the electrodes and into a co-axial drift tube. The initial gun design, with the $14.5cm$ radius can, was estimated to produce beam currents in the range $\sim 1.3 - 1.5kA$ for the given electron energy, while the modified gun design, with the $6cm$ can radius, was estimated to produce beam currents of $\sim 3.3 - 3.5kA$ due to the increased gun perveance.

Simulations of an optimised 2D - 1D Bragg lasing cavity, using injected electron beams of similar parameters to those determined in KARAT, were carried out using the 3D PiC code MAGIC. These showed agreement with the expected operation given by analytical theory, both for the EM interaction with the different reflectors and in the output spectral content. An electron beam current of $\sim 1.5kA$ resulted in the excitation of the expected TEM-$TE_{24,2}$ coupling mechanism in the 2D Bragg reflector and the generation of a $\sim 140MW$ output pulse at the desired frequency of $\sim 37.5GHz$. The excitation of the same cavity by an electron beam of $\sim 3kA$ again resulted in the generation of an operating frequency of $\sim 37.5GHz$ though a marked increase in a parasitic eigenmode was noted along with an increase in the background noise level. This may be due to excitation of a broad-band Lowbitron interaction with the beam, due to the increased $v_{\perp}$ spread, though further investigation, both numerically and experimentally, is required to ascertain if this is the root cause.

For comparison with the experimental cavity, the expected performance of the $1.5kA$ FEM was for the generation of a $\sim 50 - 100MW$ microwave pulse, centred at

$\sim 37.5 GHz$, with potentially some parasitic oscillations observable in the region of $\sim 34 GHz$ and $\sim 44 GHz$. Similar performance was expected using the same experimental cavity with an increased beam current of $3 - 4 kA$, with an expected increase in the output power closer to $100 MW$, though a higher degree of noise in the observed spectrum was expected.

Chapter 5: Construction of the 2D - 1D Bragg Free Electron Maser Experiment.

5.1 Introduction

This chapter presents a discussion of the main components of the 2D - 1D Bragg FEM experiment. A schematic of the experiment is given in Figure 5.1:

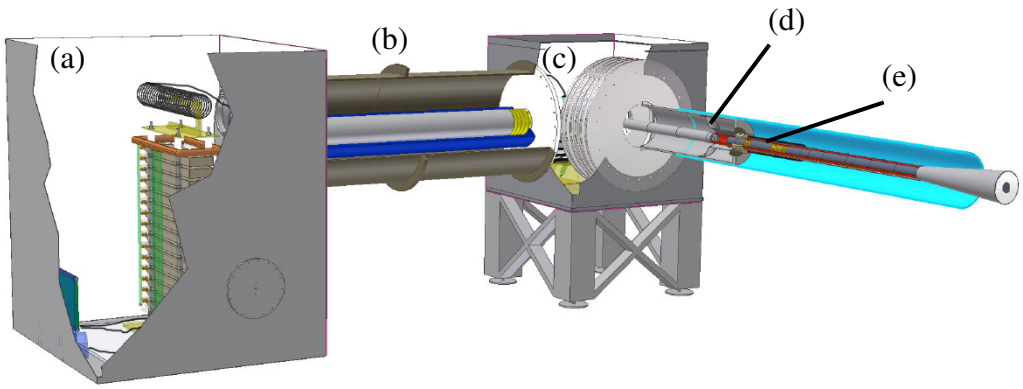

Figure 5.1: Shows a schematic cross-section of the FEM experiment, noting: (a) the Marx-bank power supply, (b) the folded transmission line, (c) the output spark-gap, (d) the plasma-flare electron gun, (e) the FEM interaction region.

Section 5.2 presents the FEM power source, composing of the Marx-bank, transmission line and output spark-gap (Figure 5.1 (a)-(c) respectively). The plasma-flare electron gun (Figure 5.1 (d)) is presented in Section 5.3, along with description of the guide solenoid circuit, used to confine the radial motion of the electrons as they are accelerated into the drift tube region. The FEM interaction region, incorporating the undulator circuit, the 2D - 1D Bragg lasing cavity and the co-axial launching antenna, is described in Section 5.4.

5.2 The 2D - 1D Bragg FEM Power Supply

The pulsed power supply for the FEM experiment can be characterised as a CLC circuit, where the capacitive discharge of the Marx-bank passes through an inductor to a secondary capacitor in the form of the folded transmission line. In such a circuit, the secondary capacitance, presented by the transmission line, is chosen to be greater than that of the Marx-bank to prevent the reflection of energy back through the inductor. The discharge from this secondary capacitor was controlled by a high-voltage spark-gap, in effect producing two stages of development in the shaping of the voltage applied to the electron gun diode. The following section describes the composition and operation of the main components of this power supply, beginning with the Marx-bank and its inductor coil (c.f. Section 5.2.1), followed by the folded transmission line and the high voltage spark-gap forming its output switch (c.f. Section 5.2.2).

5.2.1 The Marx-bank Generator

The Marx-bank pulse generator formed the heart of the FEM power supply:

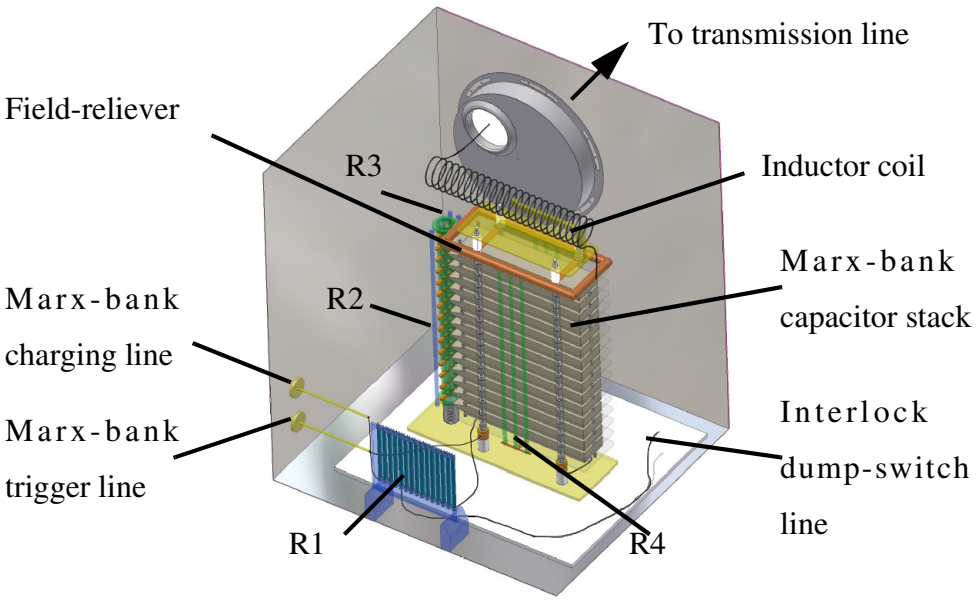

Figure 5.2: Shows the Marx-bank pulse generator in cross-section, noting the main components. The resistors marked R1-4 correspond to those shown in Figure 5.3.

The Marx-bank capacitor stack consisted of fifteen, model 31235, $0.3(\pm 10\%)\mu F$ General Atomic (formerly Maxwell) castor oil capacitors. Each of these was rated to $100kV$ ($< 75kV$ in air), $25kA$, with self-inductances in the region of $0.02\mu H$. This gave a total charging (parallel) capacitance for the stack of $4.5\mu F$ and an inductance of $1.3nH$ with a maximum potential difference of $1.5MV$ achievable, though typically the Marx was charged to between $600 - 900kV$. The capacitors were charged using a Glassman PK100R040 power supply unit (PSU), capable of providing a maximum of $\pm 100kV$ at $40mA$ DC. Typically the capacitors were charged to $40 - 55kV$ each with a charging current in the region of $4 - 8mA$, well within the handling capabilities of both the capacitors and the PSU. The charging circuit for the capacitors is shown in Figure 5.3:

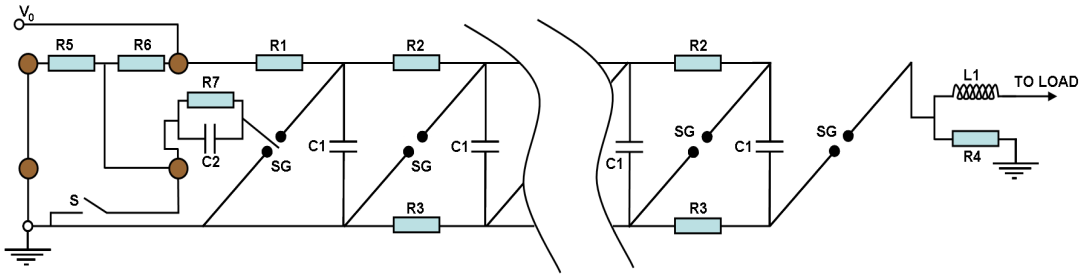

Figure 5.3: Shows the charging circuit for the Marx-bank, noting the connections between the marx-bank support legs (large circles) for the trigger circuit.

Resistor $R1$ corresponds to a set of seventeen $100k\Omega$ wire wound Morganite (latterly Allen-Bradley Electronics) resistors, giving $R1 = 1.7M\Omega$. $R2$ correspond to Copper Sulphate ($CuSO_4$) charging resistors, connected to the positive electrodes of the capacitor stack, while $R3$ refers to a second set of $CuSO_4$ resistors connected across the negative electrodes of the capacitors. The positive electrodes were placed under high tension (HT) while the negative electrodes were tied to ground (GND). Here $R2 \cong 38k\Omega$ and $R3 \cong 76k\Omega$, i.e. $R3 = 2R2$. When the spark-gaps (SG) in the circuit are open, the capacitors are isolated from the load and charge through $R2$ and $R3$, in parallel, to the voltage applied by the PSU. The capacitors do not necessarily charge uniformly, but all will erect to the same final voltage; taken to be when the charging current has reduced to some nominal level, typically $\sim 0.5mA$ in the experiments.

Once fully charged the Marx-bank spark-gaps were closed by triggering a fast thyratron switch, connected to a mid-plane electrode in the first spark-gap. This is initially held at a positive potential by the voltage divider circuit $R5{:}R6$, which applies $\sim 1/4$ of the charging voltage to the mid-plane. This ensures the first spark-gap does not self-close during charging by insulating the HT and GND electrodes from each other. $R5$ and $R6$ were constructed using a series of $100M\Omega$ high voltage resistors, intended to minimise the loss of current from the main charging circuit.

The RC circuit of $R7$ and $C2$ provided an AC filter on the trigger circuit to prevent noise propagating back to the thyratron-switch when the Marx-bank discharge is triggered. $R7 = 23.3k\Omega$ was constructed using high-voltage wire wound resistors while $C2 = 33.6pF$ was constructed using a series of high-voltage ceramic disk capacitors.

When triggered, the circuit for the Marx-bank was significantly altered. Figure 5.4 shows the circuit with the spark-gaps closed, along with a simplified version, removing components not involved in the discharge:

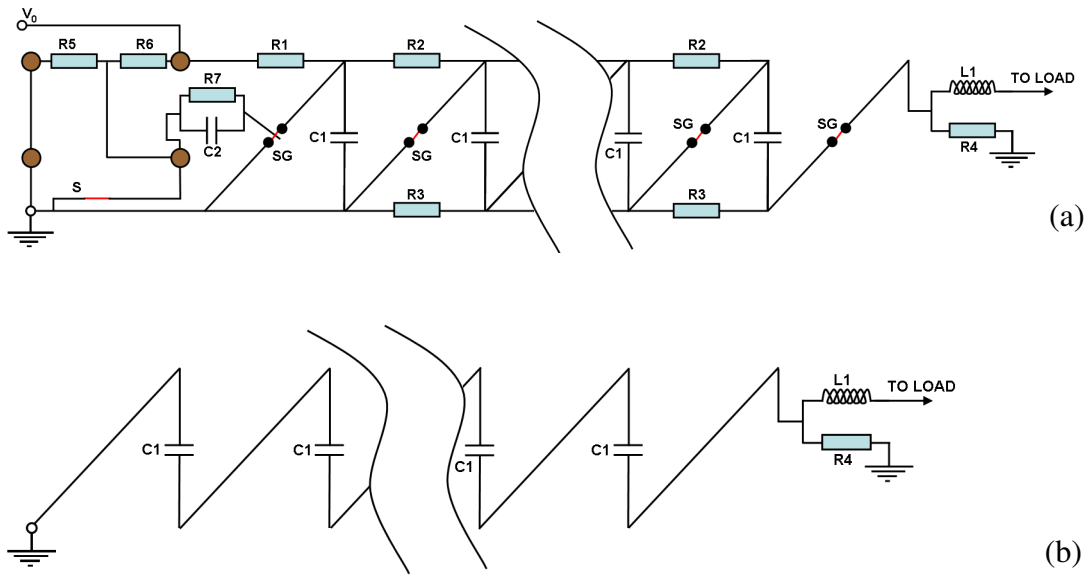

Figure 5.4: (a) Shows the discharge circuit for the Marx-bank, noting the connections between the marx-bank support legs (large circles) for the trigger circuit. (b) Shows a simplified discharge circuit for clarity of operation.

The Marx-bank was triggered using a fast thyratron-switch, connected to a mid-plane electrode, positioned between the first spark-gap electrodes of the capacitor stack. When triggered, this essentially electrically shifts the GND plane of the first spark-gap closer to the HT electrode, instigating breakdown, and producing a potential difference of $-2V_0$ across the second spark-gap, which also breaks, producing a potential difference of $-3V_0$ across the next gap and so on, discharging the capacitors in series. When the Marx-bank is fully erect it can then be considered to function in a similar manner to a single capacitor of $\sim 20nF$.

To reduce the electrical stress imposed by the Marx-bank discharge, a large diameter copper field reliever was placed at the output. In Figures 5.3 and 5.4, $R4$ corresponds to a set of six grounded resistors connected to this field reliever. These were placed in parallel with the inductor coil ($L1$), connecting the output from the Marx-bank to the transmission line, to provide a preferential path for the discharge towards the transmission line, whilst also providing a resistive route to ground, bi-passing the capacitor stack, in the event of a reflected high voltage pulse returning to the power supply. $R4 \approx 7.5k\Omega$.

The Marx-bank described is an "inverting Marx" meaning the capacitors charge at a positive voltage, but the discharge from the Marx-bank is a negative voltage. The Marx-bank erected in $\sim 250ns$, with the maximum voltage applied to the field reliever being in the region of $-800kV$.

Noting that air has a dielectric hold-off of $\sim 30kVcm^{-1}$, such high voltages at the output of the Marx-bank meant it was necessary to immerse it in some form of insulatory medium to ensure safe and proper operation. A common way of addressing this problem is to use the dielectric gas sulphur hexafluride (SF_6), however as this is now classified as a green-house gas (Meurice et al. 2004, Denissov et al. 2005) and can produce the highly toxic bi-product disulphur decafluride (S_2F_{10}) (McCormick & Craggs 1954, DPPEA 2000), the more attractive option of high quality insulator oil was used. Such oil has the advantage of having a dielectric hold-off of $\sim 120kVcm^{-1}$ (EOS 2006) compared to the $\sim 89kVcm^{-1}$ offered by un-pressurised pure SF_6. If this

limit is exceeded the oil simply generates inert carbon particles, which degrade the insulatory properties of the oil but pose no health risk.

In addition to its use in insulating the Marx-bank, insulator oil was also used to insulate the high voltage spark-gap located at the output of the transmission line, hence its placement within a dedicated insulation tank (see Figure 5.1(c)). The rate of particulate build up was minimised by fitting both tanks with removable lids, preventing un-necessary ingress of dust and air born debris from the laboratory into the oil. Figure 5.5 shows the fully constructed Marx-bank within its insulation tank, noting the visible components:

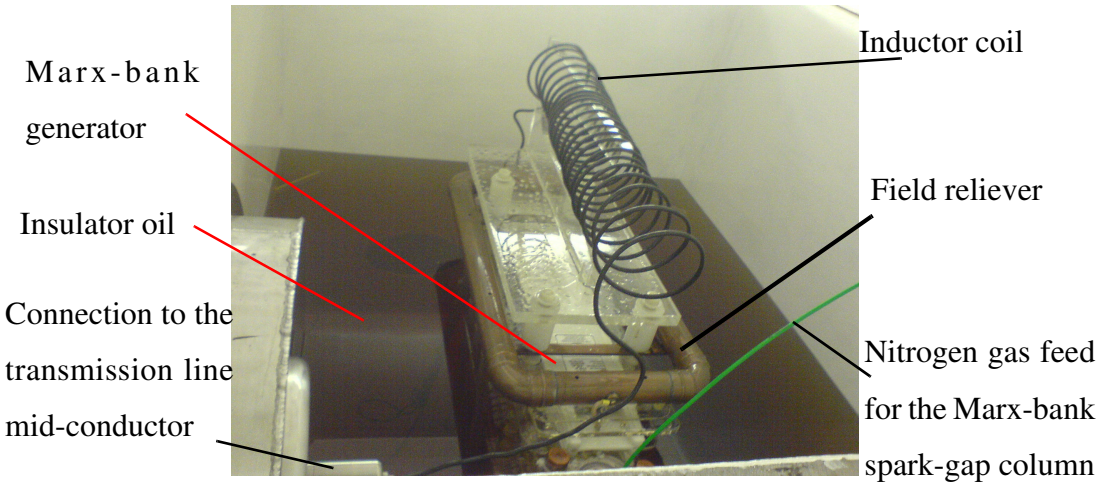

Figure 5.5: Shows the Marx-bank generator in place within its insulation tank, as the insulator oil is being pumped in. The final oil level was *~15cm* above the top of the inductor coil.

The electrodes for the Marx-bank spark-gaps were contained within a sealed perspex column, held at a positive pressure using nitrogen gas. This was done both to negate the ingress of oil into the inter-electrode spacing and to prevent the spark-gaps self closing due to the insufficient hold-off offered by air at charging voltages in excess of $\sim 30kV$; by varying the pressure of the nitrogen accordingly, the charging voltage could be raised to the desired level of $40-60kV$ whilst still allowing for active triggering of the discharge using the thyratron switch. In the experiment the nitrogen

column was pressurised to between $8 - 30 PSI$ (Pounds per Square Inch), though the chamber was tested for positive pressures of up to $12 Bar$.

5.2.1.1 The Inductor Coil.

At the moment the Marx-bank discharge is instigated, the transmission line presents essentially a short circuit. Working from the relation:

$$\frac{dI}{dt} = -\frac{V}{L} \qquad \textbf{5.1}$$

where I is the current, t is time, V is the peak Marx discharge voltage and L is the circuit inductance.

Taking the maximum discharge of the Marx-bank to be in the region of $1 MV$, rising over a time scale of $\sim 250 ns$, the self inductance of the discharging capacitor bank of $\sim 0.02 \mu H$ would be insufficient in preventing the capacitors from exceeding their maximum rated current of $25 kA$. To increase the circuit inductance a 24 turn coil was added between the Marx-bank output and its connection to the transmission line. The coil inductance was calculated using (Lorrain Corsan & Lorrain 1988):

$$L = \frac{\mu n^2 \pi \langle r \rangle^2}{l} \qquad \textbf{5.2}$$

where $\mu = \mu_0 \mu_r$ is the permeability of the medium, $n = 24$ is the number of turns, $l = 1 m$ is the axial length of the coil and $\langle r \rangle = 7.25 cm$ is the coil mean radius.

Taking $\mu_r \approx 1$ for the insulator oil, the inductance of the coil approximates well with the free-space performance of $\sim 12 \mu H$, corresponding to a current flow of $\sim 21 kA$ at $1 MV$ from the Marx-bank, sufficiently below the maximum current rating of the capacitors.

5.2.2 The Pulse-Forming Folded Transmission Line.

The discharge from the Marx-bank exhibited a $1/e$ decay time of $\sim 3 \mu s$ with an associated rise time of $\sim 250 ns$. The direct application of such a pulse across the gun

diode would result in the production of a long electron beam pulse, consisting of highly non-uniform, low energy electrons, making it unsuitable for lasing within the FEM interaction region. Following a similar technique to Spark et al. (1994), the discharge pulse, from the Marx-bank, was "shaped" using the combination of a pulse forming transmission line and a high-voltage output spark-gap. A circuit schematic of the transmission line used is given in Figure 5.6(b), while Figure 5.6(a) shows the schematic of a standard transmission line circuit:

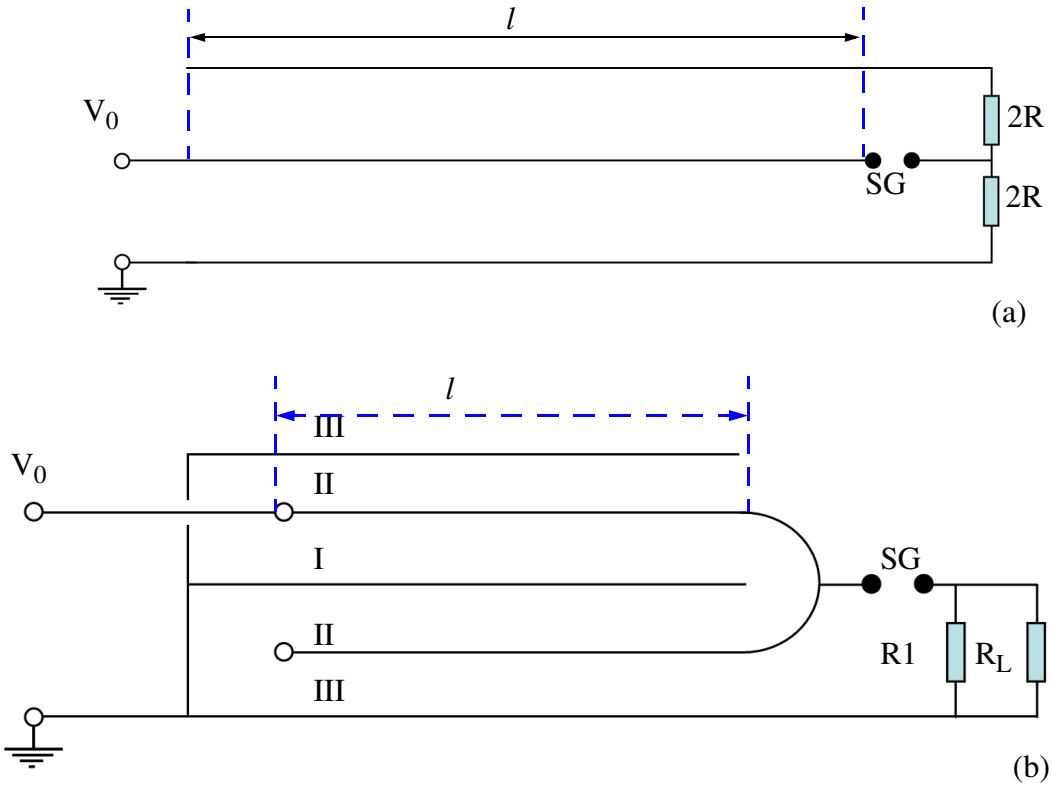

Figure 5.6: (a) Shows the circuit schematic of a standard co-axial transmission line, noting the position of the HT connection point (V_0), the discharge spark-gap (*SG*) and the discharge matching resistors (*R*). (b) Shows the circuit schematic of the folded transmission line, noting the HT connection (V_0), the high voltage spark-gap (*SG*), the discharge matching resistors (*R1*) and the load presented by the gun diode (R_L). *l* is the physical length of the line. and the numerals I, II, III correspond to the central, mid and outer conductors respectively.

Looking initially at the standard transmission line, shown in Figure 5.6(a), this can be characterised as a simple co-axial capacitor, with a capacitance defined by:

$$C = \frac{2\pi l \varepsilon_0 \varepsilon_r}{\ln(r_o / r_i)} \quad \textbf{5.3}$$

where l is the length of the line, r_i and r_o are the radii of the inner and outer conductor surfaces, respectively, and ε_r is the relative permittivity of the medium filling the line.

The capacitance of the line can therefore be adjusted by altering the media between the conductor surfaces, allowing the energy storage capability of the line to be increased by increasing ε_r, as:

$$U = \frac{CV^2}{2} \quad \textbf{5.4}$$

where U is the potential energy storage of the line and V is the applied voltage.

Looking now at the folded transmission line shown in Figure 5.6(b), while this appears, both schematically and physically, to be quite similar to the Blumlein, it operates in a manner identical to that of a standard transmission line of length $2l$. Equations 5.3 and 5.4 therefore hold, under the slight adjustment:

$$C = \frac{4\pi l \varepsilon_0 \varepsilon_r}{\ln(r_o / r_i)} \quad \textbf{5.5}$$

where the ratio r_0 / r_i is taken between either of the two sets of consecutive conductor surfaces (II and I, or III and II in Figure 5.6 (b)).

In addition to the advantages of the increased output pulse length offered by such transmission lines, the fact the structure is co-axial means the line does not suffer from the parasitic inductances experienced by lumped elements. The folded line used in the FEM experiment had a physical length of $l = 2m$, with an outer conductor radius of $70cm$, and a ratio of 2:1 between the radii of the three conductor surfaces ($70cm, 35cm$ and $17.5cm$ for the outer, mid and inner conductors respectively).

The discharge pulse from the Marx-bank (V_0) was applied to the mid-conductor of the folded line, with the line discharge-voltage controlled by the pressure of nitrogen gas in the output spark-gap. This spark-gap was passively switched (i.e. self-closing) making control of the pressure within the gap intrinsic to the proper operation of the experiment; further detail on this can be found in Appendix C.

Assume here that the spark-gap is pressurised such that the full charge from the Marx-bank is passed to the transmission line before the gap closes. Typically the circuit impedances are arranged such that $Z_{source} \gg Z_0 \cong Z_L$, where these terms refer to the impedances of the source, the transmission line and the load respectively.

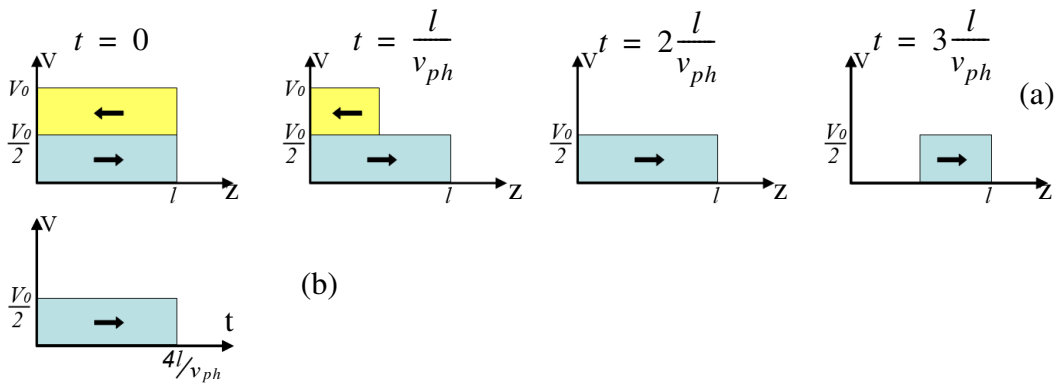

Figure 5.7: (a) Shows the discharge of the transmission line at time steps $t = 0$, $t = l/v_{ph}$, $t = 2(l/v_{ph})$ and $t = 3(l/v_{ph})$. (b) Shows the duration and magnitude of the output pulse from the transmission line.

Assuming the impedance relation given above, the discharge of the folded transmission line follows the cycle shown in Figure 5.7. When the spark-gap closes the stored charge on the transmission line begins to flow, both back towards the Marx-bank and to the load, forming two counter-propagating pulses each with amplitude $V_0/2$. As the impedance presented by the source is typically much higher than that of either the line or the load, the pulse travelling back towards the Marx-bank is reflected back towards the load, allowing the transmission line to continue discharging at $V_0/2$ for a total pulse duration of $4(l/v_{ph})$, where "l" should be noted as being the physical length of the line and $v_{ph} = 1/\sqrt{\mu\varepsilon}$ is the velocity of the pulse in the line. The use of

a standard transmission line, or Blumlein, of the same physical length would give a similar amplitude voltage pulse but with a duration $2(l/v_{ph})$.

In practice the impedance of the load was adjusted such that $Z_L > Z_0$, which provided a peak discharge voltage in the region of $60-70\%$ of V_0, with the voltage pulse applied to the gun diode showing a slightly stepped decay rate. Control of the load impedance was obtained by varying the resistance of a set of matching resistors (R1 in Figure 5.6 (b)) placed in parallel with the gun diode as $Z_L \cong R1$.

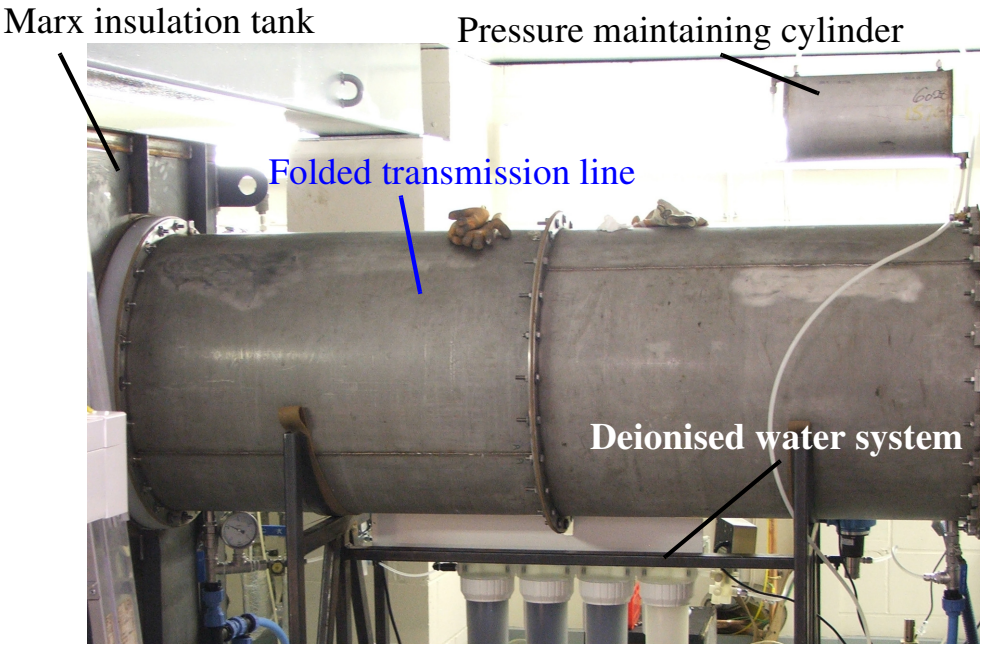

Figure 5.8: Shows the folded transmission line, noting the connection to the Marx-bank insulation tank, the deionised water system and the small cylinder used to maintain a positive pressure on the line.

The filling medium for the line was deionised water, maintained at a resistivity per unit length value of $10-14 M\Omega cm^{-1}$ by a Barnstead E-Pure water purification system (see Figure 5.8) which had a maximum rating of $18 M\Omega cm^{-1}$. Maintenance of the water purity was aided by the use of only stainless steel and polypropylene parts in the construction of the deionised water system, as these do not degrade.

The relatively high dielectric constant of the deionised water, $\varepsilon_r \approx 79$, gave a capacitance of $C \approx 25nF$ for the folded transmission line, sufficiently larger than the $20nF$ of the discharging Marx-bank to prevent reflections of the incident voltage pulse back to the Marx capacitors. The associated energy capacity was $U \approx 6kJ$ for the range of Marx-bank discharge voltages applied. When the high voltage spark-gap at the output of the line is closed, the line impedance $Z_0 = 4.7\Omega$.

5.2.2.1 The High Voltage Spark-Gap.

The discharge from the transmission line was controlled by a passively switched, high voltage, spark-gap located between the output of the transmission line and the connection to the cathode stalk of the electron gun. In this case the breaking voltage of the gap was set by the type of dielectric gas confining it and the pressure that gas was under. The operation of a passively switched spark-gap can be characterised by Paschen's law (also referred to as the Townsend breakdown criterion) (Husain & Nema 1982):

$$V_b = \frac{Bpd_e}{\ln[(Apd)/\ln(1+1/\Gamma)]} \qquad \textbf{5.6}$$

where A and B are constants dependant on the dielectric gas used, p is the gas pressure (in kPa), d_e is the inter-electrode spacing and Γ is the Townsend criterion, where $\Gamma(e^{\alpha d_e} - 1) = 1$ and $\alpha = Ape^{-Bp/E}$ is the primary ionization co-efficient (E is the electric field stress). A useful standard is to consider an inter-electrode spacing of $1cm$, between two perfectly smooth parallel electrode surfaces, with an inter-electrode media of air at room temperature and pressure. In this case the dielectric strength of the gap corresponds to $\sim 30kVcm^{-1}$ (Gilmour 1986).

In practice, estimation of the break-down voltage of a gap using equation 5.6 has some limitations, in that the value of Γ is closely tied to the electrode material, the electrode surface quality and the purity of the gas used. The trend is, however, well known, with the resultant plot known as the Paschen curve (see Figure 5.9) (Bloess et al. 1983).

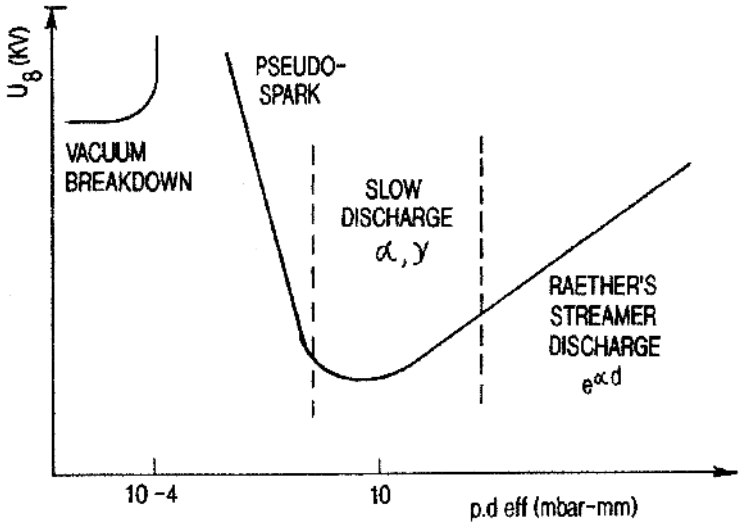

Figure 5.9: Shows a typical Paschen curve, noting the breaking voltage as a function of the gas pressure in the spark-gap for a set electrode separation.

Looking at Figure 5.9, as one moves to lower pressure it can be seen that the sparking voltage reaches a minimum, then begins to increase as, at low pressures, the probability that an electron will strike a molecule travelling between the electrodes is low. This corresponds to the so-called Pseudo-spark discharge region. The vacuum breakdown region results as the assumption of a Poisson distribution in the particles does not hold at very low vacuum, meaning Paschen's law is inapplicable. An example of this region would be the electron gun, described in Section 5.3.1.1, which operated at $\sim 8 \times 10^{-6} mBar$.

The implication of Figure 5.9 is that control of the breakdown voltage can be obtained on either side of the Paschen minimum. For the high voltage spark-gap the choice was made to operate in the Raether's streamer-discharge region, for two reasons; firstly working at a positive pressure would prevent the ingress of insulator oil into the spark-gap, ensuring proper operation and secondly the shallower $V/(pd_e)$ curve allows for more precise control of the breaking voltage.

The spark-gap is shown in cross-section in Figure 5.10 (a):

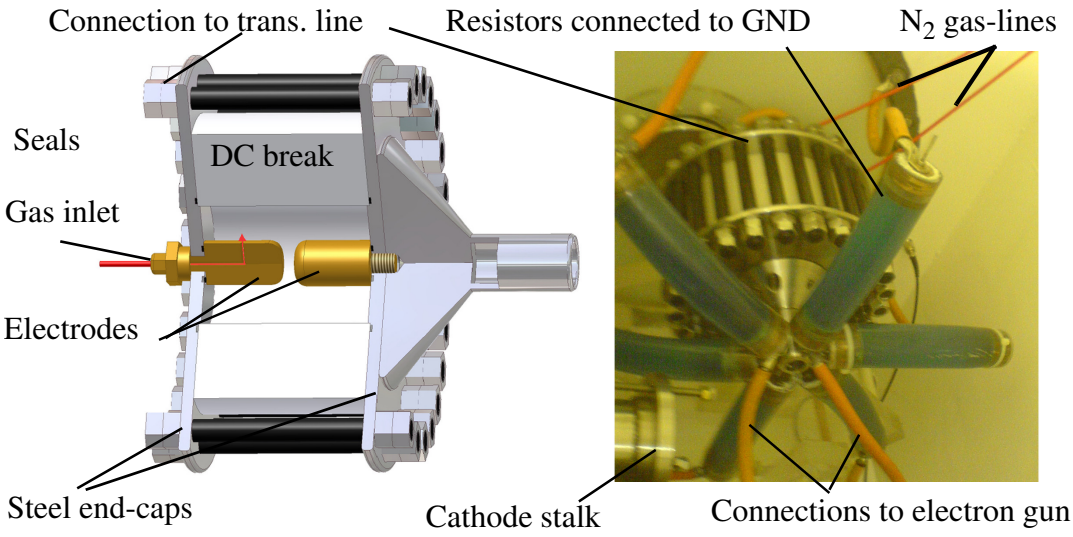

Figure 5.10: (a) Shows a schematic of the output spark-gap, linking the transmission line to the diode. (b) Shows the physical spark-gap in-situ within its insulation tank.

The electrodes were enclosed by two $1cm$ thick stainless steel plates, separated by a thick $15cm$ long nylon cylinder. The electrodes themselves were $6cm$ long with a diameter of $4cm$ and an inter-electrode separation of $1.2cm$. The edges were rounded, with the curvature minimised to maintain a region of uniform field between the facing surfaces. The pressure in the gap was controlled by a gas regulator valve, mounted outside the experimental bay, with a valve positioned in line to allow the gas in the spark-gap to be vented, helping prevent buildup of O-zone and carbon particulates as the number of shots in the experiment progressed.

At the output from the spark-gap a set of six damping resistors, formed using an aqueous solution of copper sulphate, were connected in parallel with the diode (see Figure 5.10 (b)). These were tied to ground on the body of the diode tank, allowing the load impedance (Z_L) to be adjusted by changing the impedance (Z_d) presented by these resistors, as $Z_L \cong Z_d$. The spark-gap was pressure tested up to $18Bar$, however operation was confined to at most $14Bar$. The load impedance could be varied by adjusting both the number of resistors constituting Z_d and by varying the concentration of the copper sulphate solution within the resistors.

5.3 The 2D - 1D Bragg FEM Electron Beam Source.

The electron beam source used in the FEM experiment was based around an annular explosive-electron-emission (EEE), or "plasma-flare" cathode. This was attached to the end of an adjustable cathode stalk, mounted within an evacuated, grounded, anode-can. A tight fitting, single layer, solenoid was placed over the gun-diode region to aid in formation of a uniform electron beam by confining the radial motion of the electrons as they were accelerated between the cathode and the anode. This solenoid continued along the length of the drift-tube, maintaining an axial magnetic field throughout the interaction region of the experiment.

The operation of the plasma-flare cathode is covered in Section 5.3.1, along with description of the two gun geometries employed in the FEM experiment. The guide solenoid circuit is described in Section 5.3.2.

5.3.1 The Plasma-Flare Cathode.

The mechanisms governing the operation of plasma-flare cathodes have been under investigation since the late 1940's, with Rothstein's remark that neither thermionic, nor field-emission, processes can account for the high current densities observed (Rothstein 1948). The explosive vapourisation of the emitter surface was investigated by Nekrashevich & Bakuto (1959 cited in Mesyats 1985) and led to the identification of what would be called the "cathode spot"; localised explosive vaporisation events on the surface of the emitter (Rothstein 1964 cited in Mesyats 1985).

The known contributory processes to cathode spot generation are covered extensively by Mesyats (1983, 1985, 1989, 1991, 1995) and in references (Gilmour 1982, Schrade 1989, Ronald 1996, Ronald et al. 1998). In essence the cathode spot is a small, localised region of plasma, located a short distance from the surface of the cathode emitter. These "spots" arise due to field enhancement around micro-structures and imperfections on the surface of the cathode emitter. An example of such structures are the "whiskers" shown in Figure 5.11 (Gilmour 1982), generated on optically flat

cathode surfaces through the application of electric field stresses in the region of $200kVcm^{-1}$ (Gilmour 1982).

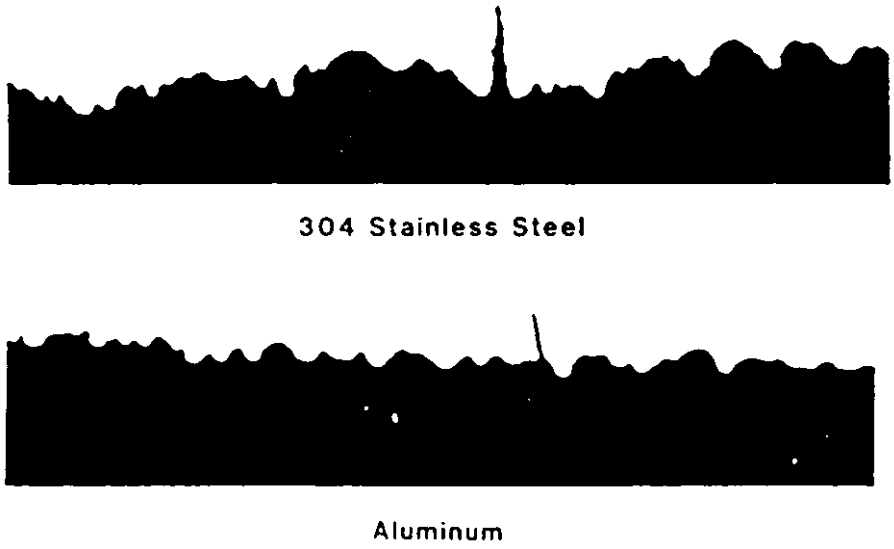

Figure 5.11: Shows whisker micro-structures on stainless steel and aluminium cathode surfaces after the application of a $200kVcm^{-1}$ field.

When an accelerating potential is applied across the electrodes of the diode, the electric field stresses on the micro-structures are greatly enhanced compared to those seen by the bulk of the cathode surface, causing rapid localised heating and explosive sublimation. The ejected material forms a plasma cloud a short distance from the cathode surface (forming the cathode spot), with a molten region directly below. Electrons in the molten region are accelerated towards the plasma cloud by a localised space-charge controlled current of counter-propagating ions. In this way the cathode spot acts as a zero-work function source of electrons as the electrons in the plasma cloud are un-bound and can be accelerated freely by the applied potential.

With the sublimation of the micro structure, the molten region cools, due to the increased thermal conductivity, terminating the flow of electrons to the cathode spot. The electrical field stresses then begin to build and the process repeats. These cyclic explosive emission events are termed “ectons” (Mesyats 1995). Evidence of this cyclic operation can be seen in Figure 5.12, which shows the craters on the surface of a copper cathode after explosive emission has occurred.

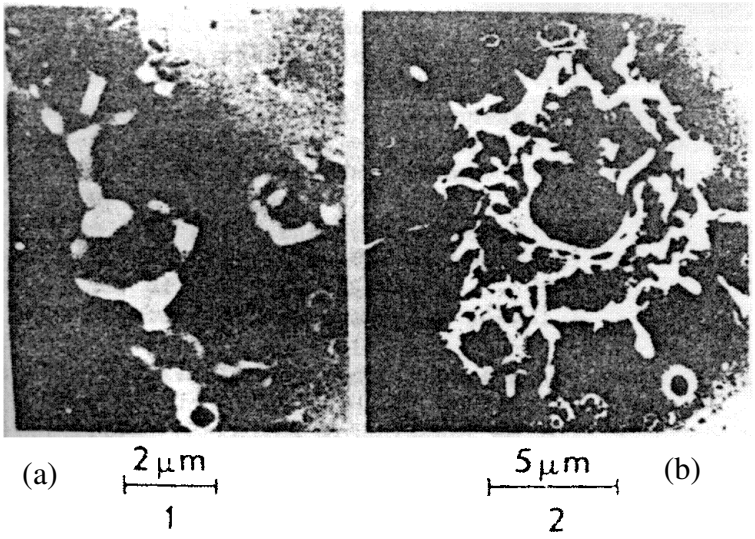

Figure 5.12: Shows craters on the surface of a copper cathode following explosive emission. (a) shows craters after *5ns* (b) shows craters after *20ns* (Gilmour 1982).

When a sufficiently high potential is applied enough cathode spots are produced to form a relatively uniform plasma emitter with similar dimensions to that of the cathode surface. In the case of the annular emitter of the FEM experiment this leads to the production of an annular plasma "flare" between the diode electrodes, hence the name "plasma-flare" electron gun. For complete turn-on of a graphite cathode the applied field should be in excess of $400 kV cm^{-1}$, with the time taken for full activation of the cathode determined both by the applied electric field strength and the cathode material (Bekefi et al. 1987). The velocity of the ejected electrons is determined by the explosive force from the cathode surface and is independent of any external field (Boxman 1983).

Due to the explosive nature of the plasma-flare cathode, the resultant uniformity in the electron beam is typically much lower than that achievable through the use of thermionic, or field emission array cathodes, however these cathodes have a much lower emission current density; in the region of $50 A cm^{-1}$ compared to $\sim 10 kA cm^{-1}$ achievable with plasma-flare cathodes. This factor alone prevents the use of a thermionic or field emission cathode in the FEM experiment, as the required beam

currents lie over a range of values from $1 - 4kA$. Assuming the use of a thermionic or field emission cathode, separate emitter annuli would be required for each beam current, with cross sectional areas covering the range $20 - 80cm^2$. To recover the required beam radius of $r_e \approx 3.5cm$ and a finite width $\Delta r \sim 2mm$ the beams generated would require radial compression, with the degree of compression determined via:

$$n = \sqrt{\frac{S}{\pi\Delta r(\Delta r + 2r_e)}} \qquad \textbf{5.7}$$

where n ranges from $\sim 2 - 4$ across the current range stated and S is the cross-sectional area of the emitter.

In contrast, by choosing a plasma-flare cathode, the emission current is limited by the space-charge limit, determined by the gun perveance (c.f. Section 4.2). For a set gun geometry the current available can be varied, to a degree, simply by increasing the applied potential or by changing the axial anode-cathode separation distance. In this case the mean radius of the cathode (and so the mean radius of the resultant beam) can be constructed to match that of the beam drift-tube, simplifying construction. Some means of recovering higher beam qualities in plasma-flare electron guns can be instituted, these are discussed in Section 5.3.2.

5.3.1.1 Construction of the Plasma-Flare Electron Gun.

The plasma-flare gun used in the 2D - 1D Bragg FEM experiments was based on a design, developed by Konoplev (2001) and implemented by McGrain (2006) for use with a 2D - 2D Bragg FEM. This achieved mean beam currents of $\sim 500A$ for accelerating potentials of $\sim 450kV$, with a guiding magnetic field strength of $\sim 0.6T$.

This was modified in two stages; firstly the emitter geometry was optimised to increase the potential beam current to the $\sim 1.5kA$ range; secondly the radial separation of the anode-can and cathode stalk was reduced, again to increase the potential beam current, in this case to $\sim 3kA$. These two stages correspond to the modelled EEE1 and EEE2 guns presented in Sections 4.2.1.1 and 4.2.1.2 respectively.

A schematic of the EEE2 plasma-flare electron gun is shown in Figure 5.13. The EEE1 gun was identical in its topology, with the exclusion of the anode-reducing insert.

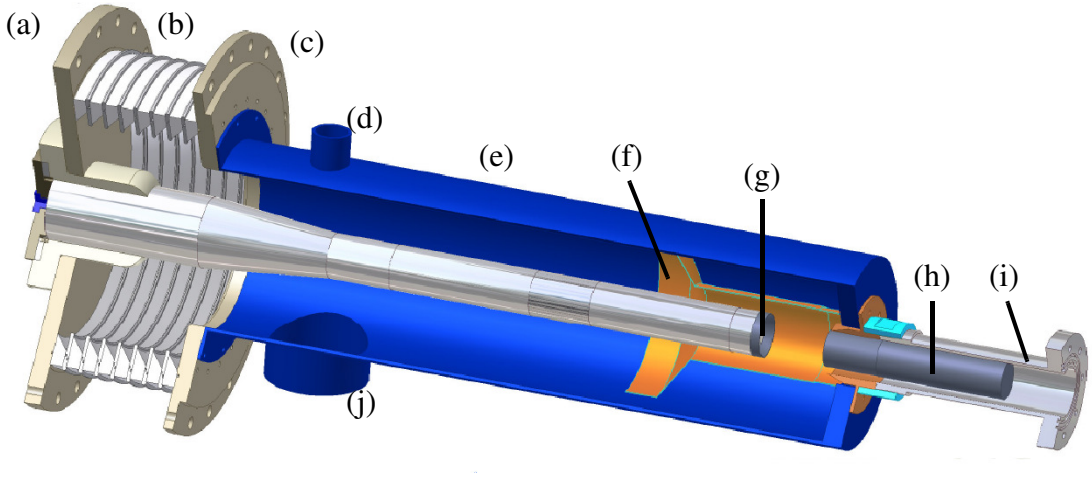

Figure 5.13: Shows the EEE2 gun schematic noting (a) the connecting plate to the power supply (b) the DC break (c) the grounded plate connected to the anode-can (d) the vacuum sensing port (e) the anode-can (f) the anode-reducing insert (g) the cathode emitter (h) the inner-conductor of the drift tube (i) the outer conductor of the drift tube (j) vacuum pumping port.

The cathode stalk was placed at a negative potential by connecting it to the output of the high voltage spark-gap of the transmission-line. The anode-can was held at ground via connection to the grounded body of the insulation tank. Vacuum was afforded by a two stage system, incorporating an Edwards RV12 model roughing pump and a Edwards 100 model Diffstak pump. The vacuum quality was sensed using a BOC Edwards AIGX-8 active ion gauge, monitored using a three channel Edwards active gauge control unit. Using the vacuum system the gun and drift-tube were evacuated to a pressure of $\sim 8 \times 10^{-6} mBar$ for the duration of the experiments. The axial separation of the cathode emitter and the effective anode, formed by the entrance for the drift-tube region, was kept constant at $\sim 10 cm$ throughout the duration of the 2D - 1D Bragg FEM experiments, with the anode-reducing insert (see Figure 5.13) added in the later stages as a means of increasing the beam current. The cathode emitter in all cases was an annular, graphite, knife-edge emitter with a mean radius of $3.5 cm$, matching that of the mean separation between the surfaces of the inner and outer conductors of the drift-tube.

5.3.2 The Guide Solenoid.

As stated in Section 5.3.1, the beam quality of plasma-flare cathodes is limited due to the explosive nature of the beam generation. Two methods of recovering a higher quality beam may be employed. The use of a collimator to scrape the beam edge is common, leaving a high quality beam core at the expense of current. This is often accompanied by the introduction of a guiding axial magnetic field (Gold et al. 1984, Conde & Bekefi 1991), though both collimators and guiding fields may be implemented individually (Fajans et al. 1985, Fajans et al. 1986, Cross et al. 1998). For devices which show an axis-encircling rotation of the electron beam, the reversal of the guide field, relative to the rotation of the electrons, has been shown to further increase energy conversion efficiency (Conde et al. 1991, Kaminsky et al. 1996, Cross et al. 1996, Freund et al. 1999) from one percent to tens of percent, though the advantage of such a field on a beam showing a non-axis-encircling rotation can be considered negligible (Konoplev 2001).

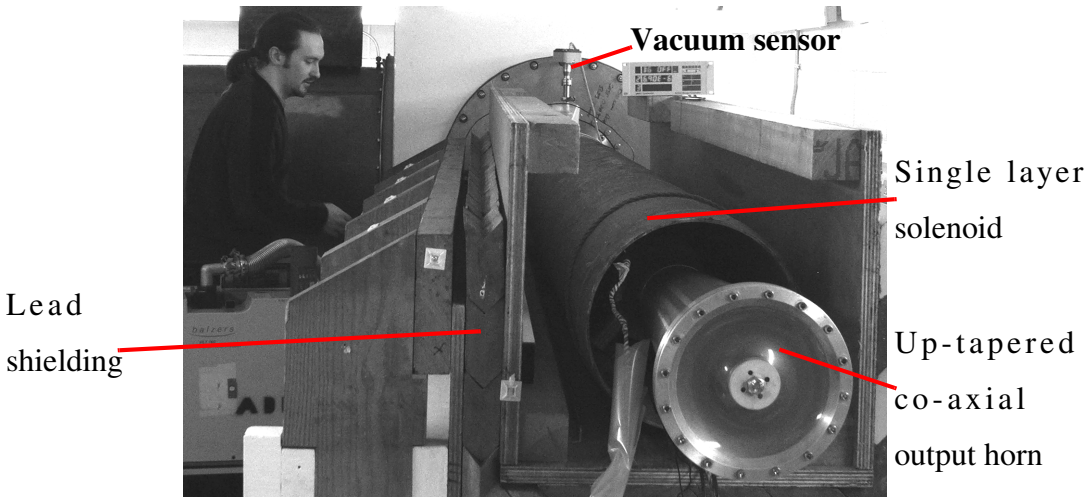

Figure 5.14: Shows the guide solenoid in position on the FEM experiment, noting its proximity to the vacuum port of the anode-can and the co-axial output horn.

In the case of the FEM experiment a collimator was discounted for use, as it would place unreasonable constraints on the alignment of the experiment. Rather a relatively high guiding magnetic field was implemented by the addition of a tight fitting single layer solenoid, beginning close to the vacuum ports of the anode-can and continuing to

the up-tapering co-axial output horn (see Figure 5.14). The solenoid consisted of a 1000 turn $2.55m$ long coil, held rigid by fibre-glass, embedded in epoxy resin.

The addition of a uniform axial magnetic field constrains the radial motion of the electrons. By immersing the inter-electrode region of the electron gun in such a field, the trajectories of the electrons accelerating towards the anode are constrained such that $v_{\perp} \ll v_z$ provided the magnetic field is sufficiently high for the current of the propagating beam (Humphries 2002):

$$\theta_f \leq \tan\left(\frac{\mu_0 I}{2\pi r B_0}\right) \qquad \textbf{5.8}$$

where θ_f is the pitch angle of the electron orbits, r is the radius of the beam envelope and all other parameters have their common meanings. To minimise, or maintain a constant, θ_f it can be seen from equation 5.8 that the guide magnetic field must be increased in-line with the beam current. This agrees with the behaviour noted in modelling of the FEM interaction region at increased beam currents (c.f. Section 4.3.3).

A DC power supply was provided by a set of ten $250\mu F$, $20kV$ capacitors, charged and discharged in parallel. A circuit diagram of the solenoid power supply is given in Figure 5.15:

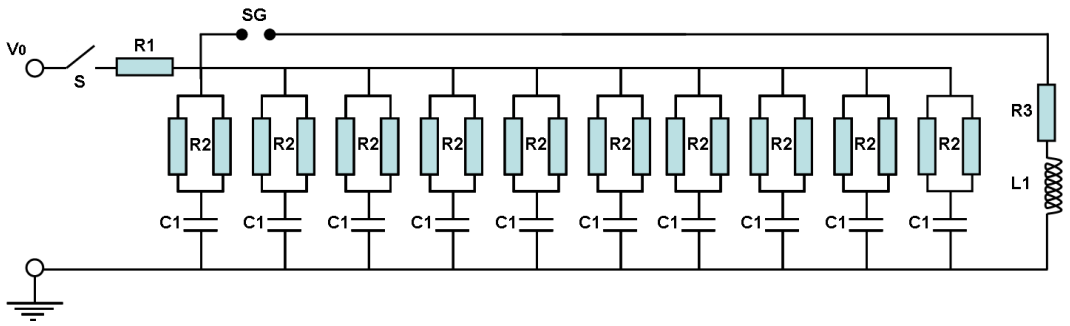

Figure 5.15: Shows the circuit diagram of the solenoid power supply.

In Figure 5.15 $R1 = 500\Omega$ corresponds to a set of charging resistors set in series with the power supply capacitors. $R2$ corresponds to a set of matching resistors with a total

resistance of 46Ω, $R3 = 1.5\Omega$ is the self resistance of the coil, which has inductance $L1 = 0.23\mu H$ and $C1 = 250\mu F$ is the individual capacitance of each capacitor. In this case *SG* corresponds to the spark-gap of a mercury ignitron switch while *S* corresponds to a switch on the charging line of the power supply; *S* is closed during charging. When the required charge is stored in the capacitors *S* is opened and the bank is discharged by a triggered discharge across *SG*. In this way the capacitor bank is charged and discharged in parallel, allowing for summation of the currents from each capacitor at the output to the solenoid coil. This produced a typical LRC discharge curve such as that shown in Figure 5.16:

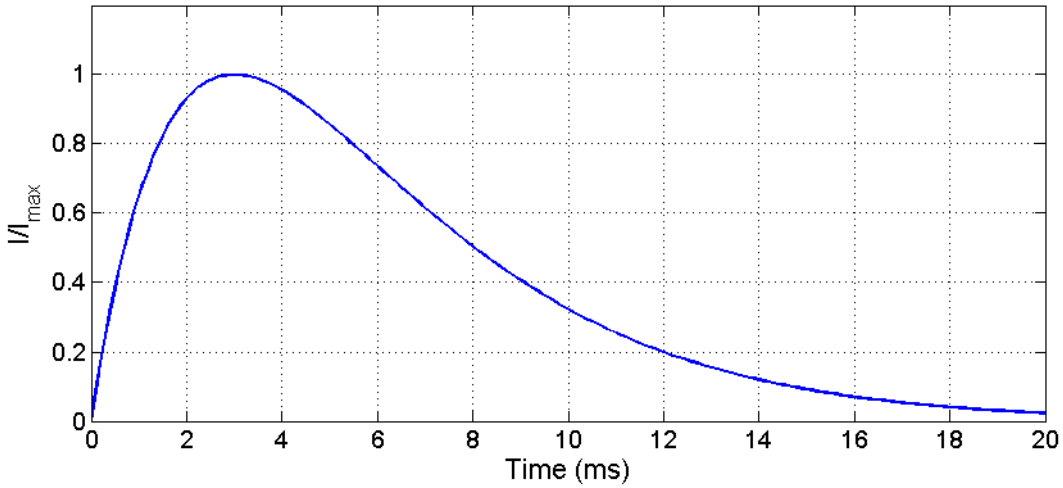

Figure 5.16: Shows the discharge curve of an LRC circuit operating in the critically damped regime.

With the circuit configured such that $\sqrt{L1C1} \cong (R2)/(2L1)$ (the "critically damped" regime), the discharge current from the circuit peaks at a value of:

$$I_{max} = \frac{2}{(\exp)}\frac{V_0}{R2} \qquad \textbf{5.9}$$

where $\exp \cong 2.72$ and the corresponding magnetic field is given by:

$$B(t) = \frac{\mu_0 n_r I(t)}{l} \qquad \textbf{5.10}$$

where $l = 2.55m$ is the axial coil length and $n_r = 1000$ is the number of turns.

The coil current to B_0 relation, for the guide solenoid coil, is presented in Figure 5.17 (a), with the required charging voltage (V_0) to generated the required coil currents, given the circuit parameters, shown in Figure 5.17 (b):

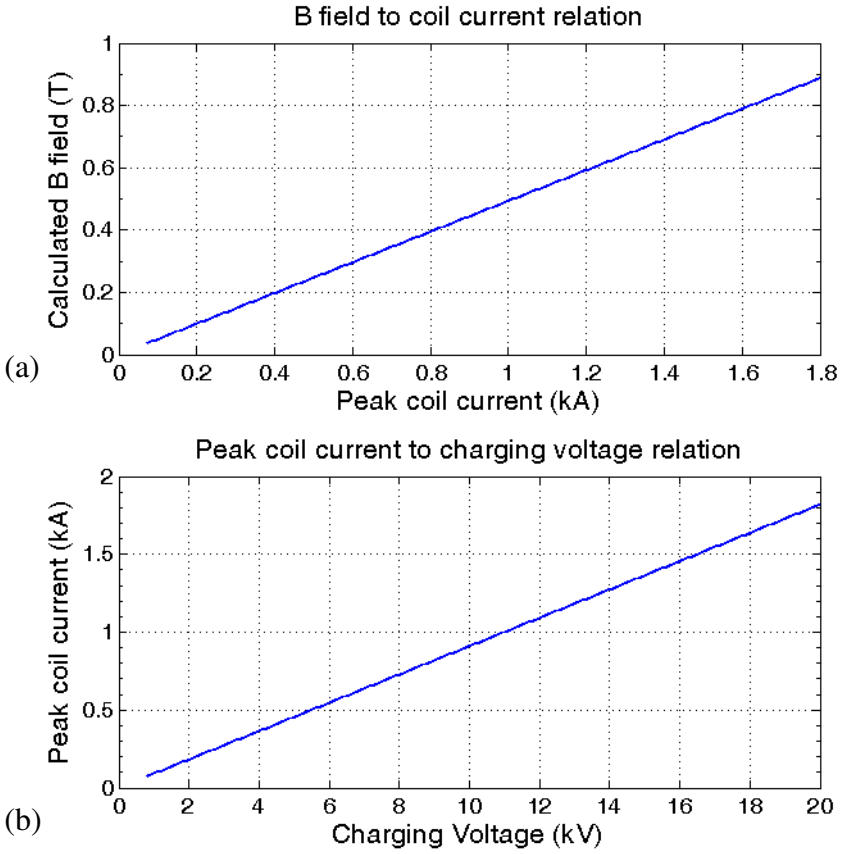

Figure 5.17: (a) Shows the relation between the magnetic field of the guide solenoid and the peak current flowing through the coil (b) shows the relation between the peak coil current and the required charging voltage on the solenoid capacitor bank.

Typically the capacitors were charged in the region of $10 - 14kV$ with resultant circuit currents of $0.9 - 1.3kA$ generating magnetic fields of up to ~ $0.65T$. A theoretical maximum of ~$0.9T$ was achievable with the solenoid circuit configured as described, however this limit was not approached in the experiment as charging voltages above ~$14.5kV$ on the solenoid capacitor bank was found to raise the ground plane of the bay sufficiently to induce early triggering of the Marx-bank discharge.

5.4 The 2D - 1D Bragg FEM Interaction Region

The interaction region for the FEM experiment had three main components; the magneto-optical system of the azimuthally symmetric undulator and guide solenoid fields, the 2D - 1D Bragg co-axial lasing cavity and the tapered, co-axial output horn. A photograph of the experimental components (excluding the guide solenoid) is given in Figure 5.18, showing the interaction region before its attachment to the plasma-flare electron gun.

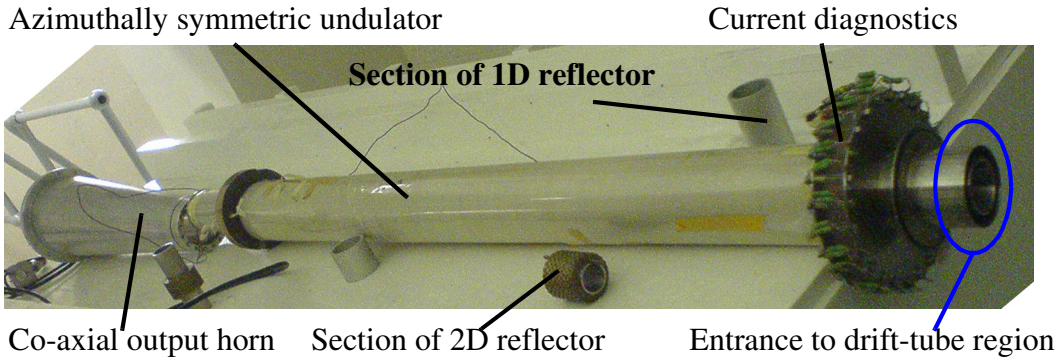

Figure 5.18: Shows the drift-tube of the 2D - 1D FEM experiment, containing the lasing cavity. The azimuthally symmetric undulator is shown wrapped in insulating mylar sheeting. Also shown are some sections of corrugated inner conductor, the up-tapered co-axial output horn and the diagnostics used to monitor the electron beam current.

As the magneto-optics of the interaction region relies on both the undulator and the guide solenoid magnetic fields, the azimuthally symmetric undulator will be discussed first, in Section 5.4.1. The construction of the 2D - 1D Bragg lasing cavity is described in Section 5.4.2, followed by description of the co-axial output horn in Section 5.4.3.

5.4.1 The Azimuthally Symmetric Undulator.

The azimuthally symmetric undulator was formed by a series of two-layer, alternately wound Helmholtz coils. In essence this forms a series of magnetic cusps which induce small orbit rotations in the electron beamlets (c.f. Section 4.3.2). The coils for the solenoid were powered using a similar circuit to that of the guide solenoid, though the number of capacitor stages was reduced. A circuit schematic is given in Figure 5.19:

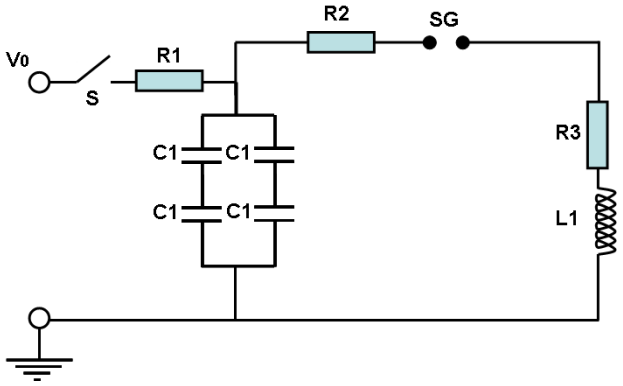

Figure 5.19: Shows the circuit diagram for the undulator power supply.

The symbols in Figure 5.19 share common meanings with those in Figure 5.15. In the case of the undulator power supply $C1=300\mu F$ giving a total capacitance of $1.2mF$, $R1=10k\Omega$, $R2=1\Omega$, $R3=2.3\Omega$ and $L1=1.01\mu H$. The circuit operated in an identical manner to that of the guide solenoid, with the discharges of both circuits and the discharge of the Marx-bank controlled using an adjustable triggered time delay circuit, described in Section 7.2.

The relation between the undulator peak current and the generated B_u field was estimated using KARAT, the resultant curve is plotted in Figure 5.20 (a). The relation between the charging voltage on the capacitors and the resultant peak current, given the circuit parameters, is plotted in Figure 5.20 (b). The charging voltages on the undulator capacitors were typically in the range of $1.5 - 3kV$ giving peak currents of $0.8 - 1.6kA$ and undulator field strengths of $0.035 - 0.065T$. An error of $\pm 5\%$ is noted in these dependence curves due to the expected error in the simulated magnetic field values. These may be compared with the experimentally determined values given in Figure 6.18.

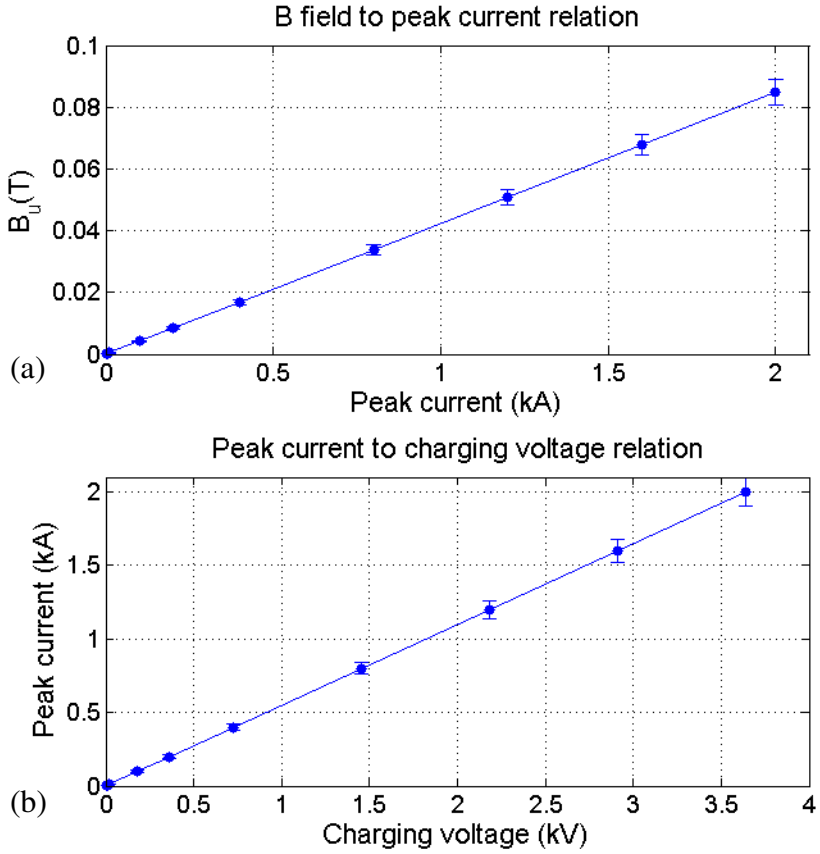

Figure 5.20: (a) Shows the relation between the magnetic field of the undulator and the peak current flowing through the coils (b) shows the relation between the peak current and the required charging voltage on the undulator capacitor bank.

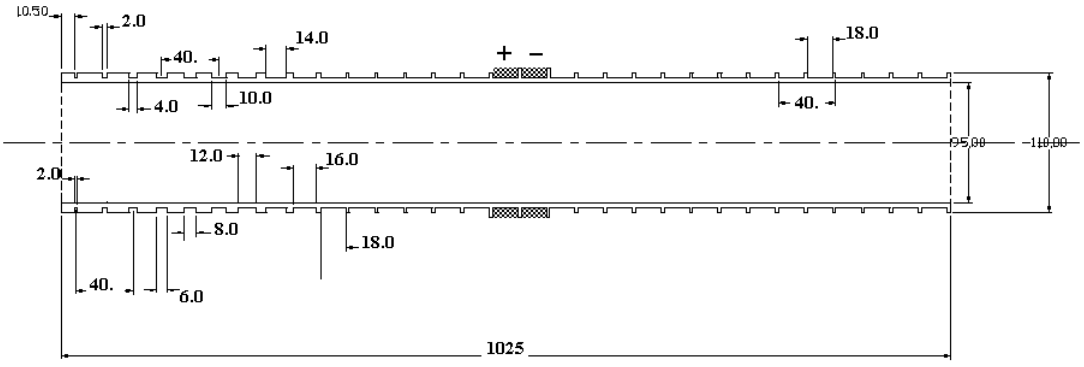

Figure 5.21: Shows a schematic of the former for the azimuthally symmetric undulator noting dimensions in mm.

The Undulator coils themselves were wound on a rigid former to maintain uniform separation of the successive coils (see Figure 5.21). The main body of the undulator consisted of twenty six regular, two-layer coils (13 periods), with each coil wound in alternate directions. Each period consisted of two alternately wound coils, with an axial period length of $4cm$ and an outer diameter of $\sim 9cm$. At the beginning of the undulator a tapered section, consisting of five periods, was used to prevent a sharp transition in the magnetic field seen by the propagating electrons. The magnetic field profile of these coils was measured using a $20A$, low-impedance, amplifier and a magnetic-field pick-up probe (Konoplev 2001):

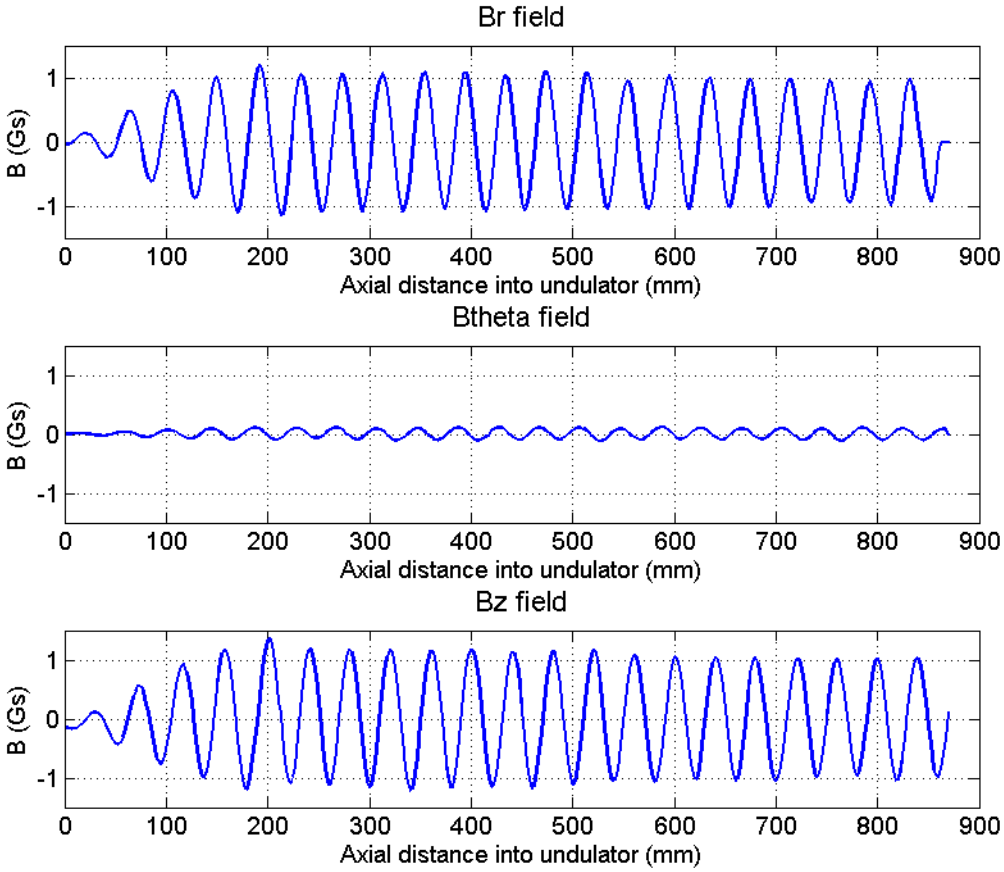

Figure 5.22: Shows the magnetic field profiles of the azimuthally symmetric undulator, measured using a magnetic-field pick-up probe, reported in (Konoplev 2001).

As expected, from the nature of the magnetic field generated by the coils, the static B_z field profile shows the strongest perturbation, though this is closely matched by that seen in B_r, the latter being the result of the "cusp" action between adjacent coils (c.f. Section 2.3.1). The relatively weak B_θ component was measured to be an order of magnitude below the field strengths presented by B_z or B_r and so can be considered to have a negligible effect on the operation of the undulator.

5.4.2 The 2D - 1D Bragg Lasing Cavity.

The drift-tube of the FEM experiment was formed by a vacuum cored co-axial line, with a mean inner conductor radius of $\sim 29.5mm$ and a outer conductor radius of $39.5mm$ (a conductor ratio of ~ 1.3, c.f. Section 3.2.1). The corrugations, which formed the Bragg reflectors of the lasing cavity, were located on the inner conductor surface, with the 2D Bragg input mirror placed in line with the beginning of the uniform region of the undulator coils. The 2D mirror itself was formed by a series of $4mm$ thick half-period cogs ($8mm$ period), with a total length of $10cm$ (12.5 periods). The 1D Bragg output mirror was positioned $60cm$ from the input mirror and was formed by an axial square-wave corrugation with a periodicity of $4mm$. The output mirror was $15cm$ long, i.e. 37.5 periods. Examples of the 2D and 1D Bragg structures are given in Figure 5.23 (a) and (b) respectively.

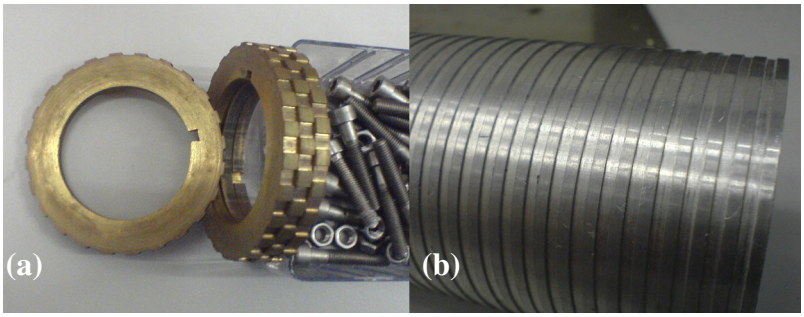

Figure 5.23: Shows examples of the square-wave corrugations used to form the (a) 2D Bragg and (b) 1D Bragg reflectors. (a) Shows the constituent "cogs" used to form 2D structure.

The cogs of the 2D Bragg reflector alternate by $1/2$ period along the azimuth between successive cogs (see Figure 5.23 (a)), producing a 2D periodic structure along both the axial and azimuthal co-ordinates. The "square-wave" profile of the reflectors approximates well with the ideal sinusoidal corrugations assumed in the theory, with the 2D structure in particular proving to be much simpler to manufacture and alter in "cog" form when compared to the production and alteration of a truly double-sinusoidal structure:

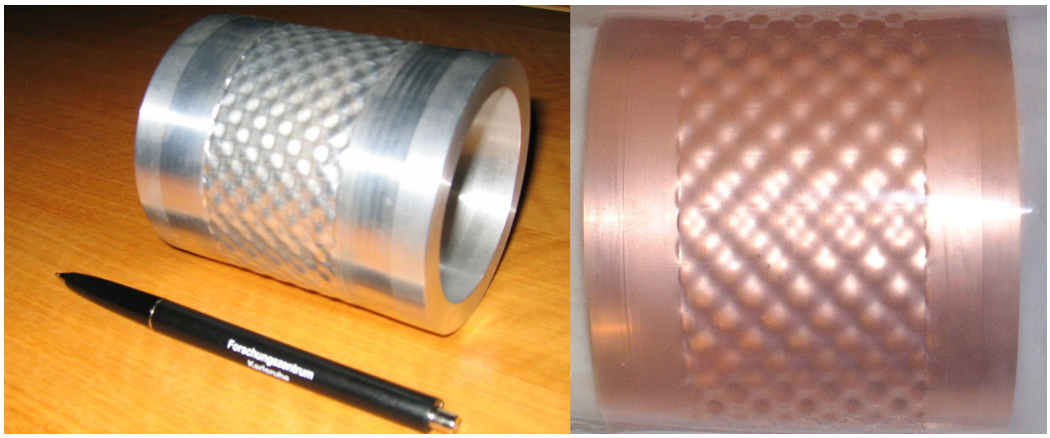

Figure 5.24: Shows the aluminium former for an ideal double-sinusoidal 2D structure and resultant copper 2D Bragg corrugation. This structure was designed to form a 2D reflector on the outer conductor surface of a co-axial waveguide similar to that used on the 2D - 1D Bragg FEM experiment.

While structures such as that shown in Figure 5.24 are certainly more precise in the positioning of the spectral stop and pass bands, they can be seen to be less adjustable than the "cog" like structures used in the experiment, where mirror adjustment can be carried out simply by adding or subtracting cogs.

(a)

(b)

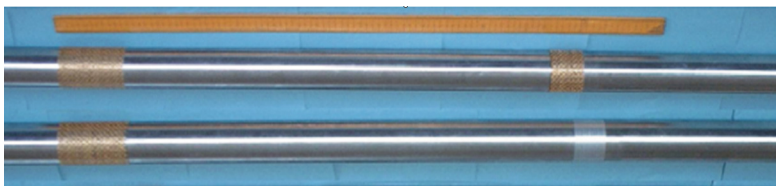

Figure 5.25: Shows inner conductors, incorporating different Bragg structures, for use in forming a two-mirror lasing cavity in a co-axial drift-tube. (a) Shows a 2D - 2D Bragg cavity (b) shows a 2D - 1D Bragg cavity.

The inner conductors for two different, two-mirror, Bragg lasing cavities are shown in Figure 5.25. Figure 5.25 (b) approximates well with the experimental cavity, though the reflector lengths shown differ from those used. The inner conductor stalk was supported at the entrance to the drift tube region by a set of adjustable support pins, with support at the end of the drift-tube region provided by a small dielectric stub and via the connection of the inner conductor to the window of the output horn.

5.4.3 The Microwave Output Horn

The radiation generated by the FEM was coupled to free-space using an up-tapered output horn. The horn was designed to ensure the smooth transition of the EM wave, from the output of the interaction region, to the free-space of the laboratory, essentially allowing for a smooth transition between the impedance of the co-axial line (Z_0) and the impedance of the air in the laboratory (Z_{fs}). The characteristic impedance of the line was calculated as (Pozar 1998):

$$Z_0 = \frac{\sqrt{\mu_0 / \varepsilon}}{2\pi} \ln\left(\frac{b_0}{a_0}\right) \cong 17\Omega \qquad \textbf{5.11}$$

where $\varepsilon \approx \varepsilon_0$ for the line, and b_0 and a_0 are the mean radii of the outer and inner conductor surfaces respectively. Noting the characteristic impedance of free space is:

$$Z_{fs} = \sqrt{\frac{\mu_0}{\varepsilon_0}} \cong 377\Omega \qquad \textbf{5.12}$$

If the impedance of the line was not tapered to match that of free space the sudden transition may have resulted in reflection of the microwave pulse back towards the lasing cavity, essentially forming a secondary cavity at the output of the interaction region and risking auto-modulation of the output signal.

The horn was designed using the PiC code MAGIC, as reported by McGrain (2006); the inner conductor radius was kept constant at $29.5mm$, as in the main drift-tube region, while the outer conductor was tapered adiabatically over a distance of $60cm$ from an initial radius of $39.5mm$ up to $100mm$.

This gave $Z_0 \cong 72\Omega$ at the output of the horn, which using the relation (Pozar 1998):

$$\Gamma_{horn} = \frac{Z_{fs} - Z_{0horn}}{Z_{fs} + Z_{0horn}} \quad \textbf{5.13}$$

estimates the refection coefficient of the horn / free-space boundary (Γ_{horn}) as being ~ 0.7. While not ideal this is an improvement on the ~ 0.9 obtained without the use of the up-tapering of the outer-conductor. A cross-section of the horn is given in Figure 5.26.

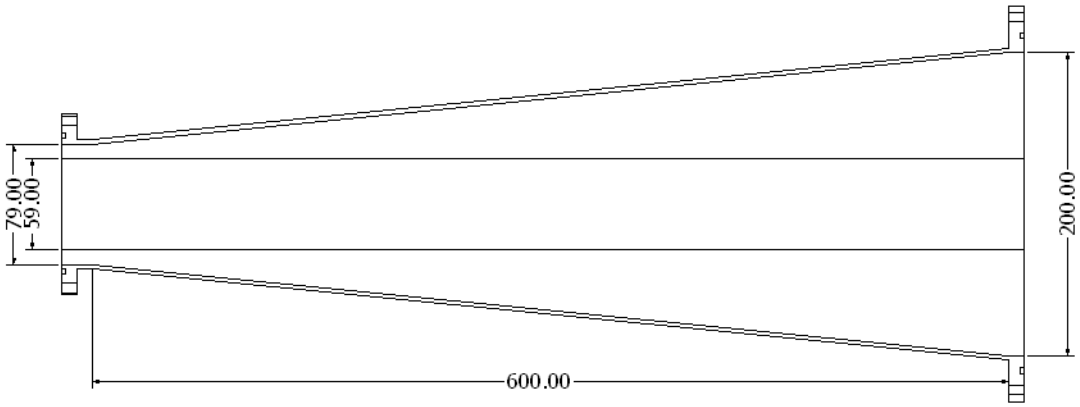

Figure 5.26: Shows a schematic of the co-axial output horn noting the dimensions of the inner conductor and the up-tapered outer conductor. Dimensions are given in mm.

A $0.5mm$ thick mylar window was affixed to the output of the horn, allowing the entire drift-tube and electron gun region to be evacuated. Using the two-stage vacuum system, described in Section 5.3.1.1, this region could be brought down to a pressure of $\sim 8 \times 10^{-6} mbar$. The horn can be seen in-place in Figure 5.14.

The directionality of the emitted microwaves from the horn was measured at a distance of $1.2m$ from the output, using a set of Agilent 8474E crystal detectors (c.f. Section 6.4) configured as in Figure 5.27:

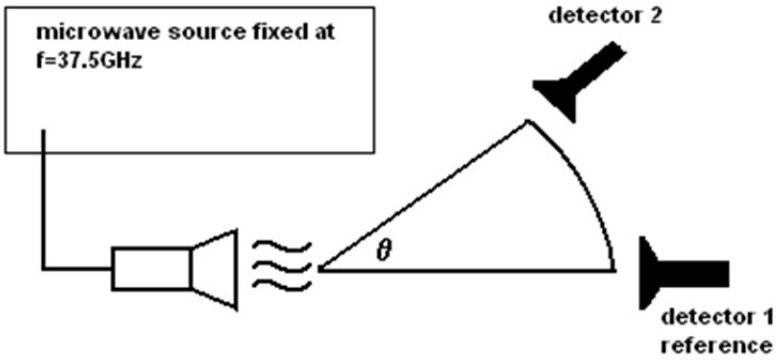

Figure 5.27: Shows a schematic of the experimental setup used to measure the directionality of the EM emitted from the co-axial horn.

The results are plotted in Figure 5.28 against the simulated performance obtained using MAGIC (McGrain 2006):

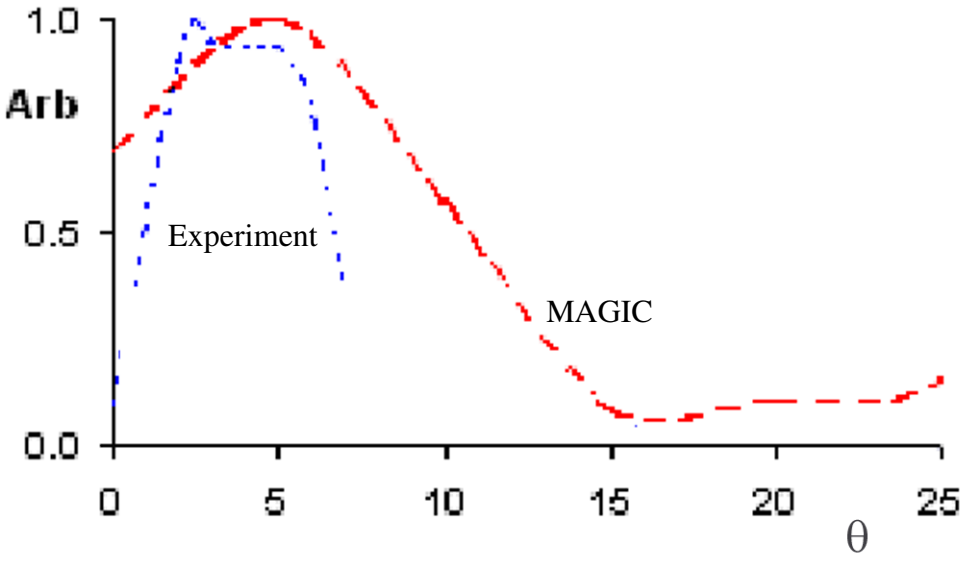

Figure 5.28: Shows the relative microwave power, varying with angle at a fixed distance of *1.2m* from the horn, noting the experimentally measured and numerically simulated performance.

Optimum performance can be seen to occur, for both the simulated and experimentally measured power, in the region of $\theta \approx 5^0$. The rapid decrease seen in the experimentally measured power for values beyond $\sim 6^0$ was the result of the use of a $7dBm$ (max) power source to test the horn directionality. For angles in excess of $\sim 7.5^0$ the microwave signal incident on detector 2 was below the sensitivity threshold of the sensor. While this did not allow for full comparison of radiated output power, it did confirm the angle subtended by the peak output, determining the optimum location for the detectors in sampling the high-power output from the FEM experiment as a whole.

5.5 Summary of Experimental Parameters

The following lists the main operational parameters of the FEM experiment.

Parameter	Value
Marx-Bank Generator:	
Charging Power supply:	Glassman, Model PK100R040
Rating	$\pm 100kV$, $40mA$
Typical charging parameters	$40 - 60kV$, $3 - 8mA$
Marx-Bank Capacitors:	15 x General Atomic Model 31235 (castor oil)
Capacitance	$0.3\mu F(\pm 10\%)$
Self-inductance	$0.02\mu H$
Voltage rating	$100kV$ ($< 75kV$ in air) per cap
Typical charging voltages	$600 - 900kV$
Total charging capacitance	$4.5\mu F$
Total discharging capacitance	$20nF$
Discharge current rating	$25kA$ (max)
Inductor coil:	
Mean radius:	$7.25cm$

Parameter	Value
Self-inductance of coil	~12μH
Transmission Line:	
Physical length	2m
Outer conductor radius	35cm
Mid-conductor radius	17.5cm
Centre conductor radius	9cm
Line Impedance	4.7Ω
Output Spark-Gap	
Pressure Rating	Tested up to ~18bar
Typical operating Pressures	3 – 14bar
Discharge Pulse Duration	~250ns
Plasma-Flare Electron Gun:	
Original Anode-Can Radius (EEE1)	14.5cm
Reduced Anode-Can Radius (EEE2)	6cm
Cathode stalk radius	3cm
Electron Energies	400 – 550keV
Beam Currents	EEE1: 1 – 1.5kA , EEE2: 3 – 3.5kA
Interaction Region:	
Guide Solenoid Field	0.5 – 0.65T
Undulator Field	0.05 – 0.065T
2D Bragg Input Mirror Periodicity	8mm
2D Bragg Mirror length	10cm (12.5 periods)
1D Bragg Mirror Periodicity	4mm
1D Bragg Mirror length	15cm (37.5 periods)
Mirror Separation	60cm

Chapter 6: Experimental Diagnostics

6.1 Introduction

The parameters of the FEM experiment were monitored at various stages throughout its operation. The voltage diagnostics are described in Section 6.2. Resistive divider probes were used to measure the voltage pulses of the Marx-bank and the output spark-gap (taken to be the voltage applied across the electron gun diode), with the potential difference on the transmission line measured using a capacitive divider probe. The current diagnostics are described in Section 6.3. These comprised of current shunts, used to measure the beam current and the current in the solenoid circuit and Rogowski coils, used to measure the current in the undulator circuit and again to monitor the beam current. The microwave pulses generated by the FEM were sampled using broadband ($0.01 - 50GHz$) GaAs rectifying microwave crystal detectors (c.f. Section 6.4). The output power was determined by measuring the power at the crystal detectors and integrating over the measured mode pattern. The spectral content of the pulses was determined using cut-off filters (c.f Section 6.5) and a heterodyne technique (c.f. Section 6.6).

6.2 Voltage Diagnostics.

In total four separate voltage probes were employed in monitoring the performance of the FEM experiment. Of these three were resistive voltage-divider based probes, while the remaining probe was a capacitive voltage-divider, positioned at the end of the transmission line just before the output spark-gap. For the resistive voltage-dividers, theory relevant to all the probes is presented prior to discussion of the individual probes themselves. In the case of the capacitive voltage-divider, as only one such probe was used in the experiment, the theory presented is in terms of the probe used.

6.2.1 Resistive Voltage-divider Probes.

Resistive voltage-divider probes in most cases can be considered to function according to (Horowitz & Hill 1999):

$$V_{out} = \frac{R2}{R1 + R2} V_{in} \qquad \textbf{6.1}$$

where typically $R1 \gg R2$ and the output voltage is taken across $R2$. Successive stages can be added across $R2$ to reduce V_{out} further as required.

For cases where the rise-time of the measured pulse approaches the transit time through the divider elements, the relationship becomes more complex, as each resistor should be more correctly considered as an individual LRC circuit, i.e. a pure resistance in series with a self-inductance (L_s) and in parallel with a self capacitance (C_s):

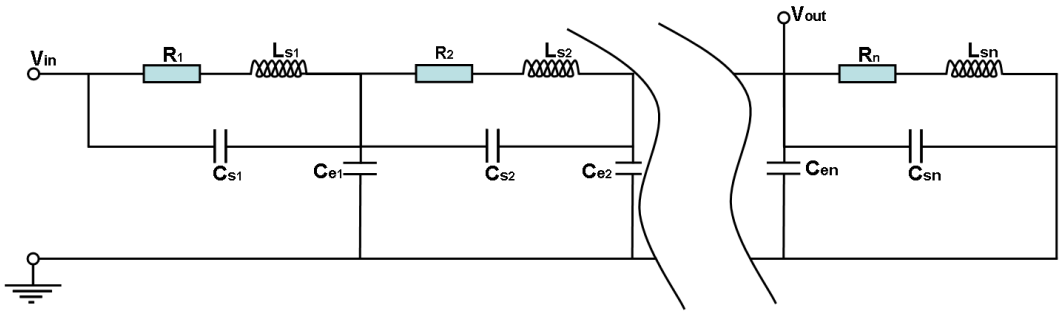

Figure 6.1: Shows the equivalent circuit for a resistive voltage-divider, noting the self inductance (L_s) and self capacitance (C_s). C_e corresponds to the stray capacitance between the resistor and earth.

A series capacitance (C_s) should also be considered, arising due to the stray capacitance between the resistor and ground (He 1995). Here the rise-time of the probe is set by the highest rise-time of the self-inductance, the self-capacitance or the stray capacitance of the probe. These can be investigated by considering each parameter in turn, along with the pure resistance and assuming a zero rise-time for the input pulse.

Under these assumptions the self capacitance gives:

$$V_{out}(t) = \frac{R2V_{in}}{R1+R2}\left[1+\frac{R1C1-R2C2}{R2(C1+C2)}e^{-t/\tau_e}\right] \quad \textbf{6.2}$$

with a rise-time of:

$$t_e = \frac{R1R2(C1+C2)}{(R1+R2)} \quad \textbf{6.3}$$

Again $R1$ corresponds to the resistance of the high voltage arm and $R2$ corresponds the resistance of the low voltage arm. $C1$ and $C2$ corresponds to the total self-capacitance of the high and low voltage arms respectively.

Considering the circuit in terms of the self-inductance, the output voltage is given as:

$$V_{out}(t) = \frac{R2V_{in}}{R1+R2}[1-e^{-(R1+R2)t/nL_s}] \quad \textbf{6.4}$$

where n is the number of resistors and the rise-time of the circuit is:

$$t_L = \frac{2.2nL_s}{R1+R2} \quad \textbf{6.5}$$

resulting from the reduction in the instantaneous current due to L_s. The 2.2 term arises from the exponential term of equation 6.4.

The stray capacitance of the probe corresponds to an output voltage of:

$$V_{out}(t) = \frac{V_{in}R2}{R1+R2}\left[1+2\sum_{k=1}^{\infty}(-1)^n e^{-((n^2\pi^2)/(RC_e))t}\right] \quad \textbf{6.6}$$

where n is an integer (He 1995, Kuffel et al. 2000).

The rise time in this case is given by:

$$t_{Ce} = \frac{(R1 + R2)C_e}{3} \qquad \textbf{6.7}$$

The larger of these rise-times are those due to the self and stray capacitances, indicating these must be minimised in order to obtain the best performance from a resistive divider probe, should fast response times be required.

Both of these effects can be minimised by construction of a probe such as that shown in Figure 6.2. This shows a two stage resistive voltage divider with the initial stage constructed using copper sulphate ($CuSO_4$) solution. The outer column forms a shield against EM noise, whilst also aligning the electric force lines in parallel with the inner $CuSO_4$ column. Such a configuration minimises the stray capacitance between the inner column and ground, and so reduces the effect on the initial stage of the voltage divider circuit (Li 1988).

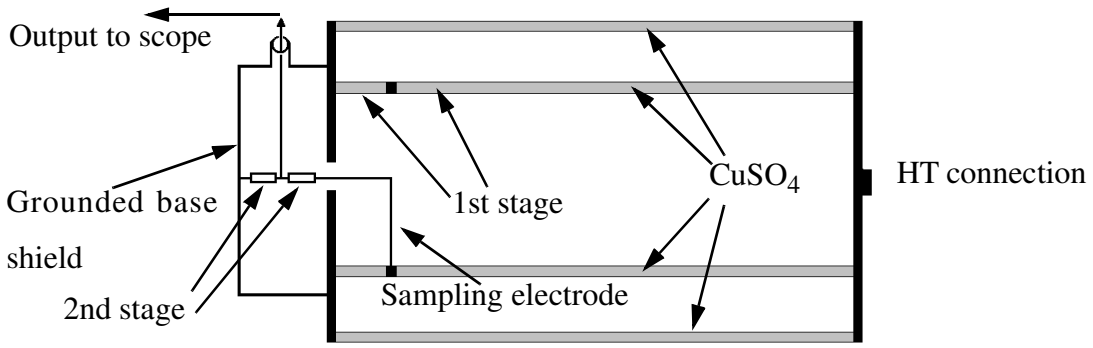

Figure 6.2: Shows a schematic of a two stage shielded resistive-divider voltage probe. Here the upper stage resistance and shielding are provided by a solution of copper sulphate.

In reference to equation 6.3, the effect due to the self-capacitance can be minimised by ensuring the RC time constant of the high and low voltage arms conforms to $R1C1 = R2C2 = R_nC_n$ (where n corresponds to the n^{th} stage of a multi-stage divider). In the initial stage of Figure 6.2 this is achieved by producing both $R1$ and $R2$ from the inner $CuSO_4$ column, where the division is created by introducing a sampling electrode, set at a distance of a few centimetres up from the grounded plate

of the probe. Such dividers have a set resistance ratio, determined by the difference in length of the two sections. Altering the concentration of $CuSO_4$ in the probe will alter the over-all resistance presented by the probe but will not alter the division ratio for sampling. In the second stage the choice of resistors should be made to ensure the RC response is the same through-out the probe.

6.2.1.1 The Marx-Bank Resistive Voltage-Divider Probe.

The voltage probe used to monitor the discharge of the Marx-bank was a simple single stage resistive voltage-divider, characterised by equation 6.1. The relatively high resistance of $R1$ was provided by a weak aqueous solution $CuSO_4$ enclosed by a length of flexible polyurethane tubing, capped at both ends by copper electrodes. Polyurethane was chosen for the main body of the probe as it does not perish in insulator oil (though it loses its elasticity over time). The value of $R1$ was variable by increasing or decreasing the concentration of the $CuSO_4$ solution. In the experiments $R1 = 25.9k\Omega$.

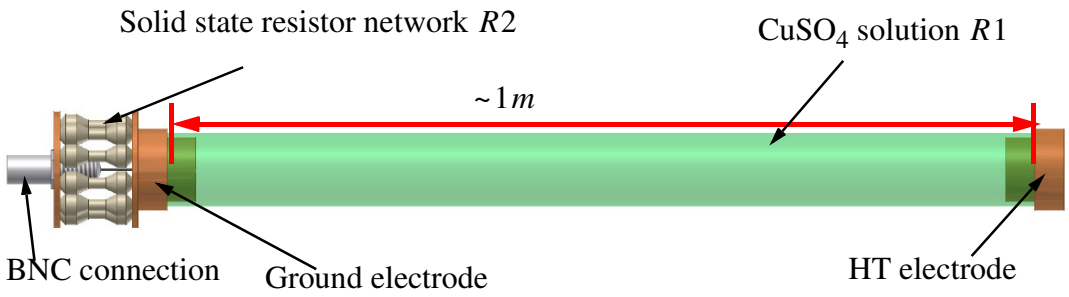

Figure 6.3: Shows a schematic of the voltage probe connected to the Marx-bank to measure the discharge voltage. *R1* was connected to the field reliever at the output of the Marx capacitor bank, with the probe tied to ground through the BNC cable connection to the rear tank.

The use of $CuSO_4$ to form $R1$ has some definite advantages over the use of solid-state resistors. Besides the relative ease with which the resistance offered by $R1$ can be varied, $CuSO_4$ resistors can be considered self-healing in the event of being over-volted, i.e. should an excessive voltage pass through the resistor, causing the solution

to ionise, the resultant ions recover to their initial state, leaving the resistor undamaged. Should such an event occur across a standard solid state (for example a carbon composite) resistor, breakdown may occur across the resistor end-caps, leaving a "track" of embedded carbon on the resistor surface and so reducing its resistance. In the worse case the solid state resistor may fail.

The risk of such failure is also reduced by the use of the flexible polyurethane tubing. An effect of over-volting a resistor, or exposing a resistor to high voltages at a rate faster than it can dissipate any heat generated, is a rapid increase in the temperature of the resistive material. While the $CuSO_4$ solution itself offers enhanced protection from this effect, due to its higher specific heat capacity, should the solution expand, the elasticity of the polyurethane allows for some expansion and contraction of the tubing before failure would occur.

The sampling resistor $R2$ was constructed from a set of ten 220Ω resistors, set in parallel with each other at the base of $R1$, giving $R2 = 22\Omega$. The probe was connected to the field reliever at the Marx-bank output, placing it in parallel with the discharge resistors and in series with the inductor coil connecting the Marx-bank output to the transmission line. A BNC terminal end was connected across the plates of $R2$ (see Figure 6.3), with the outer conductor of a standard ($1.5GHz$ bandwidth) co-axial cable providing the ground connection between the base of the probe and the body of the rear tank, whilst the inner conductor carried the reduced voltage single for measurement on a LeCroy 6200A series $2GHz/5GSs^{-1}$ deep memory digital storage oscilloscope (DSO). Additional attenuation was added to the sampled signal, in the form of a 226kV:1V low-pass filter circuit, used to remove high frequency noise.

6.2.1.2 Shielded, Air-Insulated, Diode Voltage Probe.

The first series of FEM experiments made use of a shielded resistive voltage-divider probe, previously used in the work by He (1995) and McGrain (2006). Its design followed the schematic presented in Figure 6.2, with the best performance noted for a total resistance in the first stage of $8.68k\Omega$ and a total resistance in the second stage

of $1.54k\Omega$. Physically the probe was in the region of $1.5m$ in height, designed to withstand ~$600kV$ without suffering electrical breakdown in air, allowing it to be positioned outside the diode tank. This was accomplished, with connection to the diode provided by an insulated copper rod and a length of co-axial cable (see Figure 6.4). The rise-time of the probe was taken as better than $15ns$, following its use in previous works (He 1995, McGrain 2006).

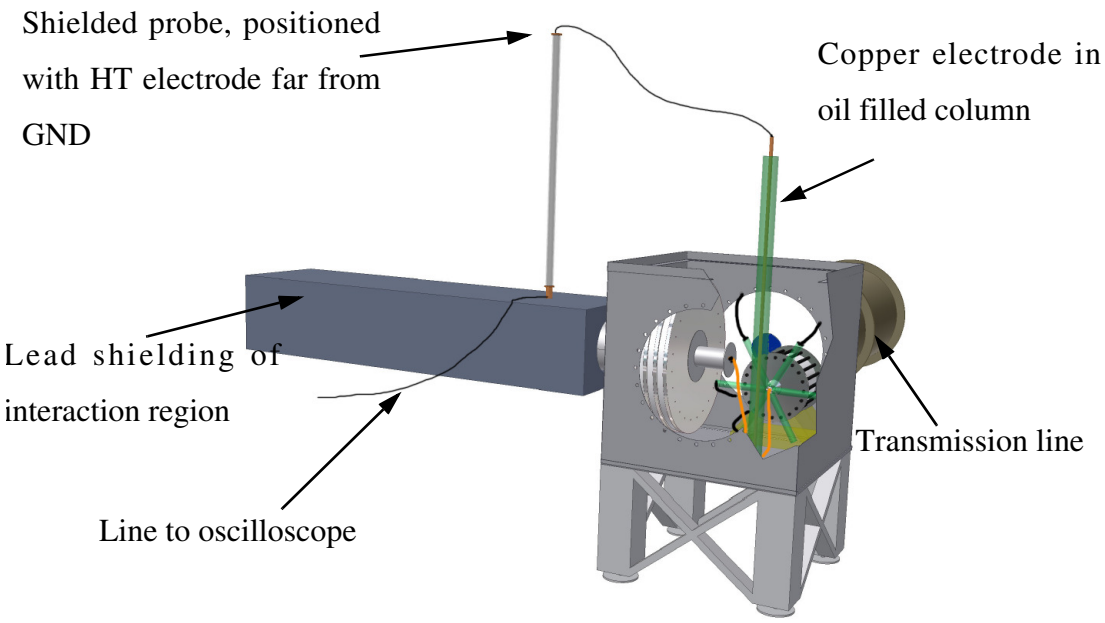

Figure 6.4: Shows the positioning of the shielded gun-diode voltage probe, noting the connection via the insulated copper rod electrode and the separation of the HT electrode on the probe from grounded surfaces.

The rise-time of the diode voltage was typically in the region of $30-50ns$, at least twice the minimum resolvable with the shielded probe. In order to reduce the effects of noise coupled on the co-axial line, from the probe, an attenuator (incorporating a low-pass filter) was included at the connection to a Tektronix TDS640A $500MHz/2GSs^{-1}$ oscilloscope. This gave a total voltage division ratio of 293kV:1V reading on screen. A typical voltage trace is given in Figure 6.5, for a charging voltage of $44kV$ on the Marx-bank capacitors.

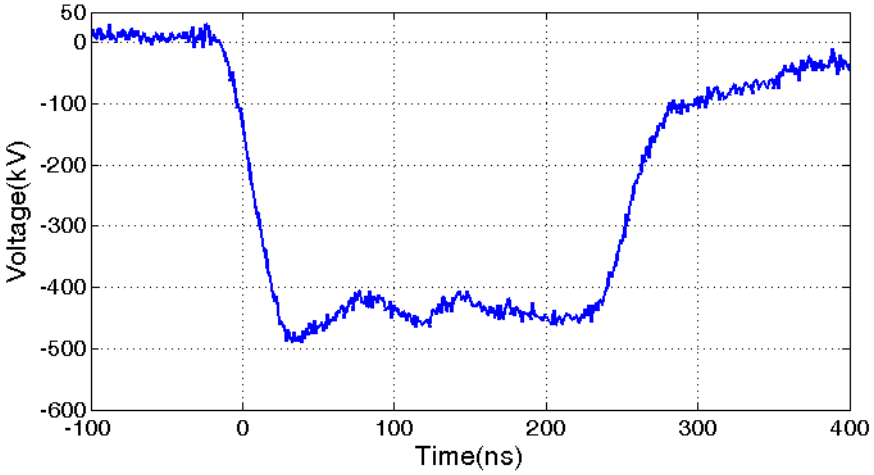

Figure 6.5: Shows the applied diode voltage, for a charging Marx voltage of *44kV*, using the shielded resistive voltage-divider based probe. Recorded using a Tektronix TDS 640A oscilloscope.

6.2.1.3 Non-Shielded, Oil Insulated, Diode Voltage Probe.

In the second set of 2D - 1D FEM experiments the shielded probe was replaced with a much more compact non-shielded probe, capable of being placed within the diode insulating tank. The reasoning behind this change was primarily practical, with the inclusion of a lead roof over the bay preventing the connection of the existing probe to the diode.

The un-shielded probe was designed by Dr. H. Yin and was constructed in a similar fashion to the shielded probe. The resistive divider was constructed in two stages, with the initial stage formed using $CuSO_4$ (Lee 1983, Racz & Patocs 1992). The division of $R1$ and $R2$ in the $CuSO_4$ solution was done, as before, using an electrode placed $\sim 1cm$ from the grounded base plate of the main probe body. This initial sampling electrode was connected to a solid state resistive voltage-divider circuit, with the output taken via standard BNC terminated co-axial cable to a LeCroy 6200A DSO.

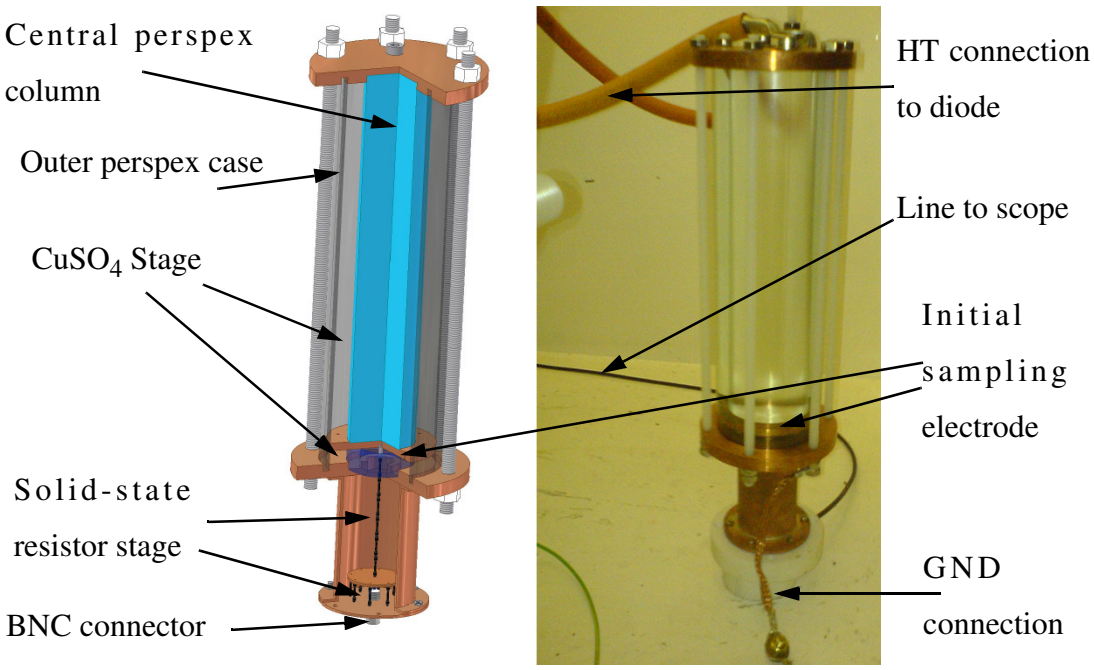

Figure 6.6: (a) Shows the un-shielded probe in cross-section noting main components. (b) Shows the probe in-place in the diode tank, noting the connections to HT and GND.

The un-shielded probe was calibrated by connecting both the shielded and un-shielded probes across the diode and comparing the measured behaviour. A comparison of the different probe responses is given in Figure 6.7 for a charging voltage of $47.9kV$:

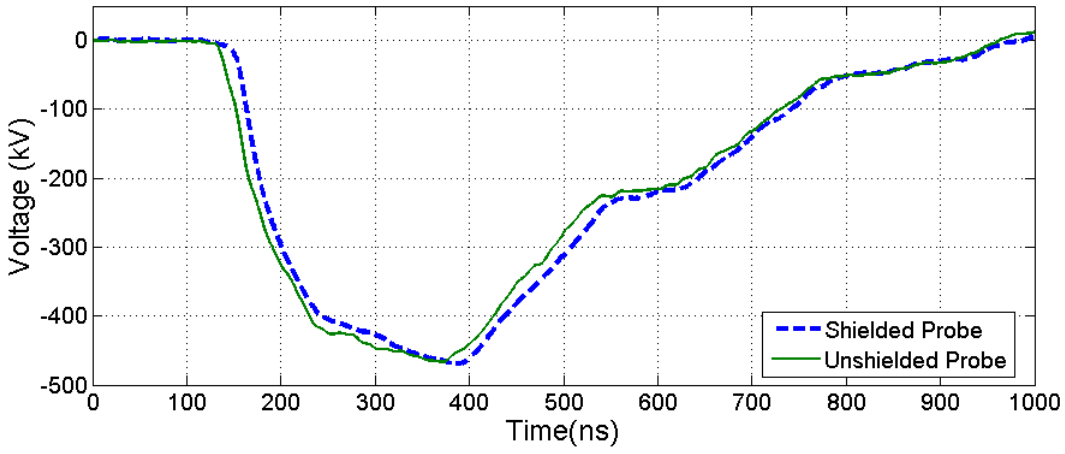

Figure 6.7: Shows a comparison of the voltage traces obtained using the shielded and unshielded voltage probes.

This established a voltage division ratio of 316kV:1V for the unshielded probe, including the attenuation provided by an in line attenuator box (incorporating a low-pass filter) connected between the sensed signal line from the probe and the DSO.

In addition to the reduced size the un-shielded probe showed an improved response to changes in the sensed voltage, as can be seen by the sharper rising edge of the pulse and increased detail in the pulse shape. It should be noted that the pulses shown in Figure 6.7 were recorded using a Tektronix TDS640A series DSO, which had a lower temporal resolution ($500MHz$) than the LeCroy 6200A DSO ($1.5GHz$ single shot bandwidth) used to record the traces shown in Chapter 6. Barring this change in recording equipment the new voltage diagnostic remained unaltered between the time of its calibration and the time of the experiment.

6.2.2 The Capacitive Voltage-Divider Probe.

Capacitive dividers have a number of advantages in sampling high voltages. They can be used to sense DC, frequency modulated CW, long and short pulses and sub-nanosecond rise-time responses (Thomas 1970), without alteration of the device. In addition, provided the probe is placed directly at the measurement sensing location, its input impedance appears to be that of an open circuit, preventing extra loading of the test circuit (Thomas 1967). The equivalent circuit of a single stage capacitive voltage-divider is given in Figure 6.8:

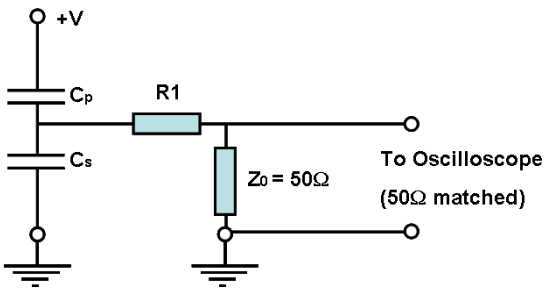

Figure 6.8: Shows the equivalent circuit of a capacitive voltage-divider, noting the secondary resistive voltage-divider circuit.

The value of $C_p \ll C_s$ in order to minimise the rise-time response of the divider (with a lower stable limit on C_p given by Thomas as $\sim 5pF$ (1970)). Calculation of C_p and C_s for the FEM experiment can be determined from the geometry of the probe (see Figure 6.9).

The parallel capacitance (C_p) can be considered as similar to that presented by a parallel plate capacitor, which can be expressed as (Pozar 1998):

$$C_p = \frac{\varepsilon_0 \varepsilon_r S}{d_{sep}} \qquad \textbf{6.8}$$

where S is the surface area of the probe and d_{sep} is the separation between the probe surface and the centre conductor surface of the transmission line. For the FEM capacitive probe $C_p \approx 12pF$, $S \cong 43cm^2$, $d_{sep} \cong 26cm$ and $\varepsilon_r \approx 79$ for the deionised water of the line.

The series capacitance (C_s), taking that both the transmission line and the probe are co-axial, can be given as (Pozar 1998):

$$C_s = \frac{2\pi l \varepsilon_0 \varepsilon_r}{\ln(r_0 / r_i)} \qquad \textbf{6.9}$$

where the dimensions l, r_0 and r_i are noted on Figure 6.9. For the transmission line probe $l = 5cm$, $r_0 = 5cm$ and $r_i = 3.7cm$, giving $C_s \approx 748pF$.

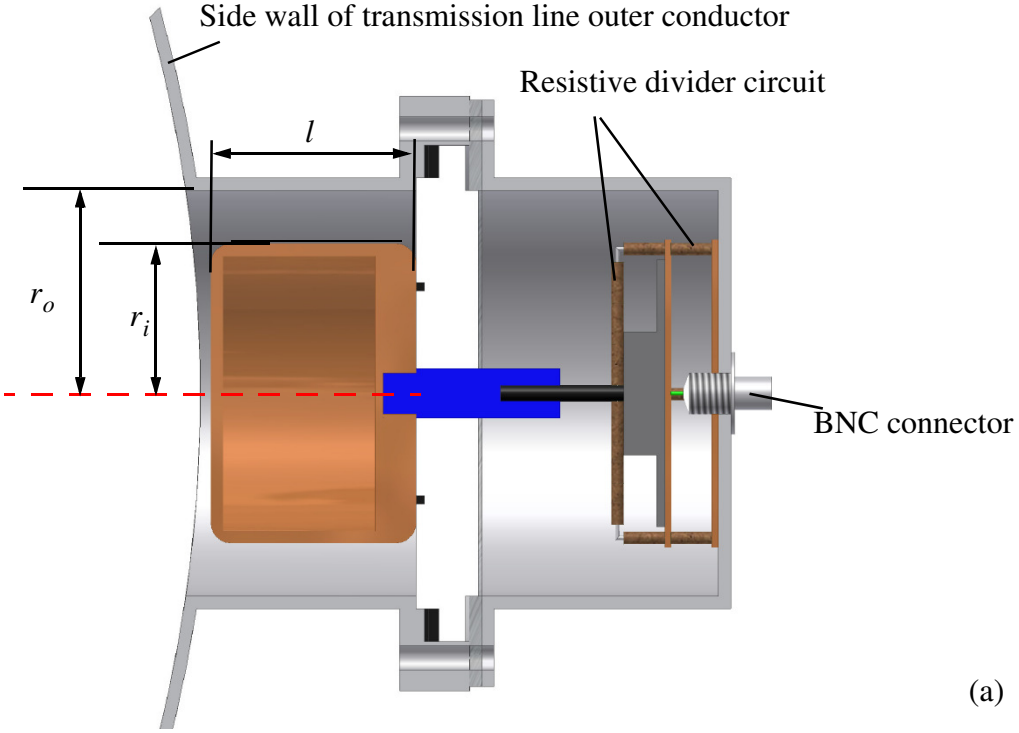

Figure 6.9: Shows a cross-section through the capacitive voltage-divider probe on the FEM transmission line, noting important dimensions and components.

Additional attenuation was added after the capacitive divider stage via the insertion of a resistive divider ($R1 \gg Z_0$). Here $R1$ consisted of three $12k\Omega$ resistive arms, connected in parallel ($R1 = 4k\Omega$) and Z_0 consisted of three 150Ω resistors, also connected in parallel ($Z_0 = 50\Omega$) as shown in Figure 6.8. A BNC terminal was connected across Z_0, with a standard co-axial cable run connecting the probe to a Tektronix TDS640A oscilloscope.

The conversion factor for the probe was calculated as:

$$V_{out} = \frac{Z_0 C_p}{2(C_p + C_s)((Z_0/2) + R1)} V_{in} e^{-i\frac{t_{trans}}{R1(C_p + C_s)}} \qquad \textbf{6.10}$$

where $t_{trans} \cong 250ns$ is the pulse duration of the transmission line discharge.

From the values of $R1$ and C_s it can be seen that the time constant of the divider circuit $R1C_s \gg \tau$, which taken with the relation of $R1$ to Z_0 allows equation 6.10 to be approximated as:

$$V_{out} \approx \frac{C_p Z_0}{2C_s R1} V_{in} \qquad \textbf{6.11}$$

where $(C_p Z_0)/(2C_s R1) \cong 1 \times 10^{-4}$. A reading of $V_{out} = 1V$ therefore corresponds to a voltage on the transmission line output of $V_{in} \cong 10kV$. A typical measurement from the capacitive probe is shown in Figure 6.10. This relates to a pressure on the output spark-gap of $\sim 12Bar$ for a charging voltage of $48kV$ on the Marx capacitors.

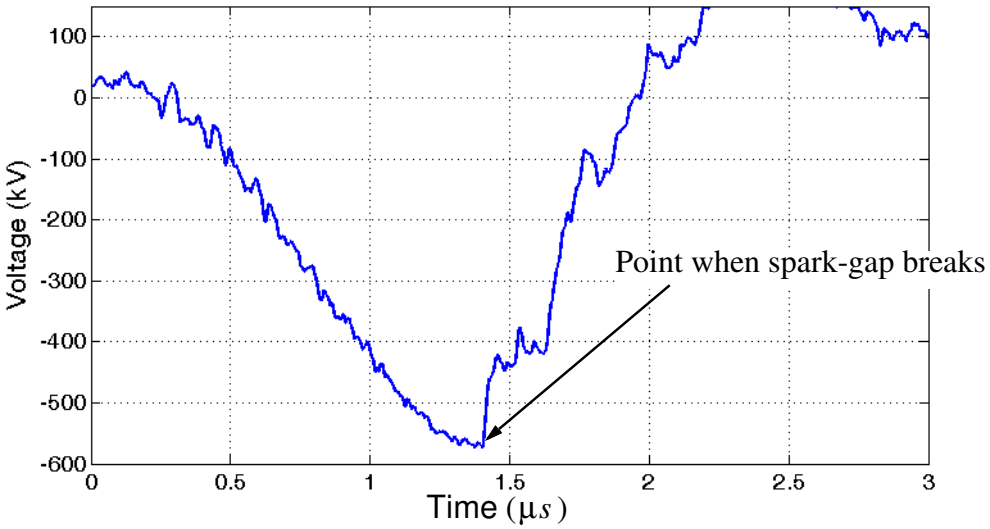

Figure 6.10: Shows a typical voltage measurement from the capacitive probe, located at the output of the transmission line. The drop in voltage at *~1.4μs* corresponds to the closing of the output spark-gap and subsequent rising voltage of the discharge pulse to the diode.

As the potential at the transmission line output was in the range $400 - 600kV$, additional attenuation was required to bring the sampled signal down to a safe level for measurement at the oscilloscope, giving a total conversion ratio of 100kV:1V.

A comparison between the discharge voltage of the transmission line and that measured across the diode is given in Figure 6.11. This shows a high level of agreement in the pulse shaping, with variations in the voltage amplitude clearly visible in both traces.

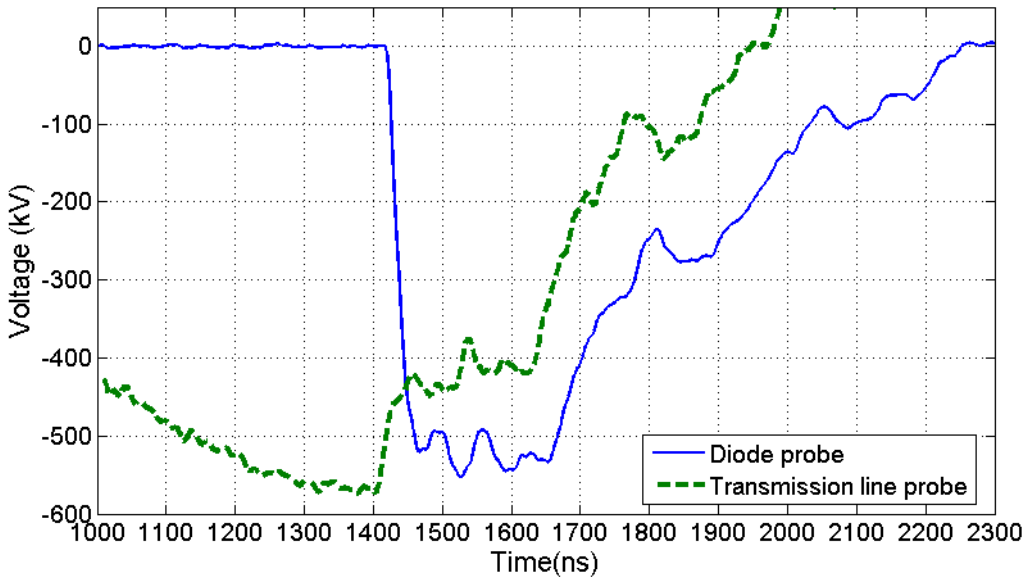

Figure 6.11: Shows a comparison between the voltage pulses of the transmission line and the gun diode, recorded using the capacitive divider and un-shielded resistive divider probes respectively.

The drop in the transmission line voltage occurs due to the breaking of the output spark-gap allowing the flow of current to the diode. It can be seen that the plateau in this discharge coincides with the rising voltage on the diode.

6.3 Current Diagnostics.

The most common means of sensing current flow are through the use of magnetic probes (Phillip & Turner 1965, Thomas 1970, Thornton 1991, He 1995, McGrain 2006) or through the use of low impedance current shunts (Thomas & Hearst 1965, Thomas 1970, Thornton 1991, He 1995, McGrain 2006). The FEM experiment made use of both these methods, in the form of Rogowski coils (c.f.Section 6.3.1) to measure

the beam current and the magnetic field of the wiggler, and current shunts (c.f. Section 6.3.2) to measure the magnetic field of the solenoid and again to measure the current in the electron beam. Both Rogowski coils were formed around perspex cores, giving responses similar to that of vacuum cored coils (as opposed to ferrite cored) and were operated in self-integrating mode (discussed in Section 6.3.1).

6.3.1 Rogowski Coils.

Rogowski coils, or Rogowski belts as they are sometimes more properly regarded, represent a very versatile form of magnetic probe. Qualitatively the action of the Rogowski coil, in which ever form, can be considered by reference to the action of a simple solenoid coil. In the solenoid an applied electromotive force (emf) induces the flow of a current through the windings of the coil, which in turn produces a magnetic field through the centre of the coil. If one considers the Rogowski coil as similar to a solenoid coil, wound in a toroid (see Figure 6.12), then the passage of a time varying current ($I(t)$) through the centre of the toroid can be seen to induce a magnetic field within the centre of the coil. This essentially acts in a reversed manner from the solenoid, with the magnetic field produced in the coil by $I(t)$ induces an emf in the coil winding. Integration of the measured emf therefore allows for calculation of $I(t)$.

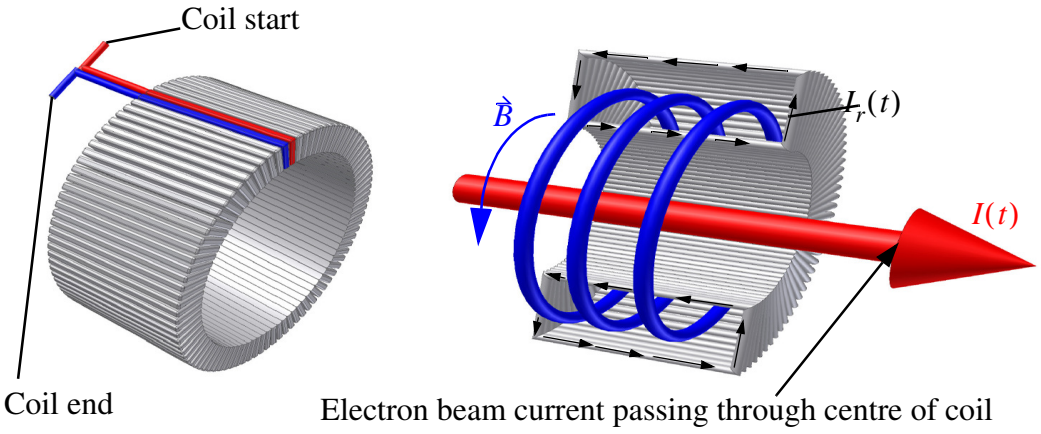

Figure 6.12: Shows the schematic of a toroidal Rogowski coil, noting the relative positioning of the coil ends. In cross-section a representation of the magnetic field lines within the coil are shown, due to the passage of a current through the centre of the coil.

Typically Rogowski coils have the benefit of being electrically isolated from the device under test (DUT), allowing their position to be altered without disturbing the electrical circuit. In terms of physical construction they can take many forms; they may incorporate a magnetic core (He 1995, Jundong et al. 2006), a dielectric core (McGrain 2006) including vacuum or air, or may be wound around lengths of co-axial cable (Murgatroyd et al. 1991) forming a fully flexible Rogowski "belt". In all cases the initial and final turns of the coil are placed closely together to allow for proper measurement of the induced coil emf.

To recover a measurement of $I(t)$ the emf measurement must be integrated over time. This is achieved either through the use of an external integration circuit (a differential Rogowski coil) or through configuring the coil as self-integrating. The circuit diagrams for both forms are given in Figure 6.13a and 6.13b.

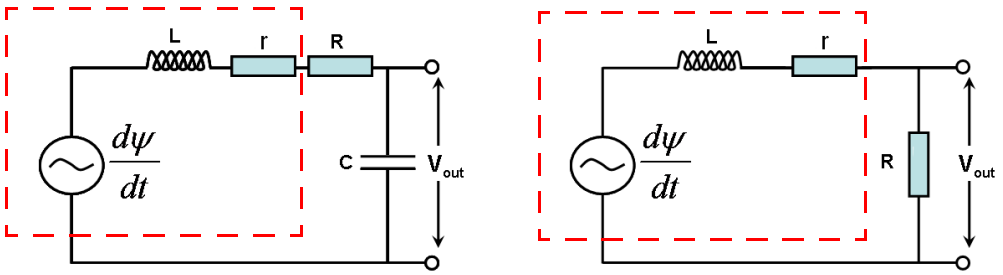

(a) (b)

Figure 6.13: Shows the circuit diagrams for (a) differential and (b) self-integrating Rogowski coils.

Considering the case of the differential Rogowski coil, the emf of the circuit ($d\psi/dt$) may be regarded as the sum of the induced emf of the coil and the potential difference across the integrating RC circuit:

$$\frac{d\psi}{dt} = L\frac{dI_r}{dt} + RI_r + \frac{1}{C}\int_0^{\tau} I_r dt \qquad \textbf{6.12}$$

where the first term relates to the induced coil emf and the latter terms related to the integrator circuit (Benson 1996).

The DC resistance of the coil winding (r) is taken to be negligible compared to the resistance of the integrator circuit (R) (Leonard 1965) and so is neglected. C refers to the integrator capacitance exclusively while L corresponds to the inductance of the Rogowski coil. The initial term in equation 6.12 may be neglected provided $R \gg L\omega$, where ω is the highest significant frequency component of I_r. In addition, if the pulse duration (τ) is significantly less than the RC constant of the integrator ($\tau \ll RC$) the induced current in the coil can be approximated as:

$$I_r \approx \frac{1}{R}\frac{d\psi}{dt} \qquad \textbf{6.13}$$

The voltage measured across C (see Figure6.13a) is then:

$$V(t) = \frac{1}{C}\int_0^{\tau} I_r dt = \frac{1}{RC}\int_0^{\tau} d\psi = \frac{\psi(t)}{RC} \qquad \textbf{6.14}$$

where ψ corresponds to the magnetic flux intercepted over an area $\vec{A}$ ($\psi = \vec{B} \cdot \vec{A}$).

$\psi(t)$ may be expressed in terms of the induced current $I_r(t)$ as (He 1995):

$$\psi(t) = \frac{\mu A n_r I(t)}{l} \qquad \textbf{6.15}$$

where A is the cross-sectional area of the coil, n_r is the number of turns in the coil and l is the coil length.

The measured voltage is therefore related to $I(t)$ by:

$$I(t) = \frac{lRC}{\mu A n_r} V(t) \qquad \textbf{6.16}$$

In cases where $I(t)$ may vary quickly with time the restriction $R \gg L\omega$ limits diagnostic performance of differential Rogowski coils. An alternative configuration is that of the self-integrating coil, which dispenses with the RC integrator circuit, replacing it with a single resistor (see Figure 6.13b). Here the value of the coil resistance (r) is no longer negligible, with the combined resistance chosen such that $R + r \ll L\omega$.

In this case equation 6.12 reduces to:

$$\frac{d\Psi}{dt} \cong L\frac{dI_r}{dt} \qquad \textbf{6.17}$$

where $I_r \approx \frac{\Psi(t)}{L}$.

Noting the coil inductance as:

$$L = \frac{n_r^2 \mu A}{l} \qquad \textbf{6.18}$$

the self-integrating Rogowski coil can be seen to operate as a current transformer with the measured voltage related to $I(t)$ as:

$$I(t) = \frac{n_r}{R}V(t) \qquad \textbf{6.19}$$

with the lower frequency limit for operation set by $R + r \ll L\omega$. This lower limit can usually be taken to have a wavelength on the order of the total length of wire used to wind the coil (Leonard 1965).

Both Rogowski coils used in the FEM experiment were self-integrating, wound on dielectric (perspex) cores. This gave performance similar to that of vacuum cored coils with the advantage of rigidity in the coil structure.

6.3.1.1 The Electron Beam Rogowski Coil.

The coil used to measure the electron beam current formed an integral part of a DC break between the anode of the gun-diode and the outer conductor of the drift tube, with the coil situated within a perspex casing which formed the DC break. The coil itself consisted of 200 turns of $2mm$ diameter varnished copper wire, with a total wire length of $\sim 27.2m$.

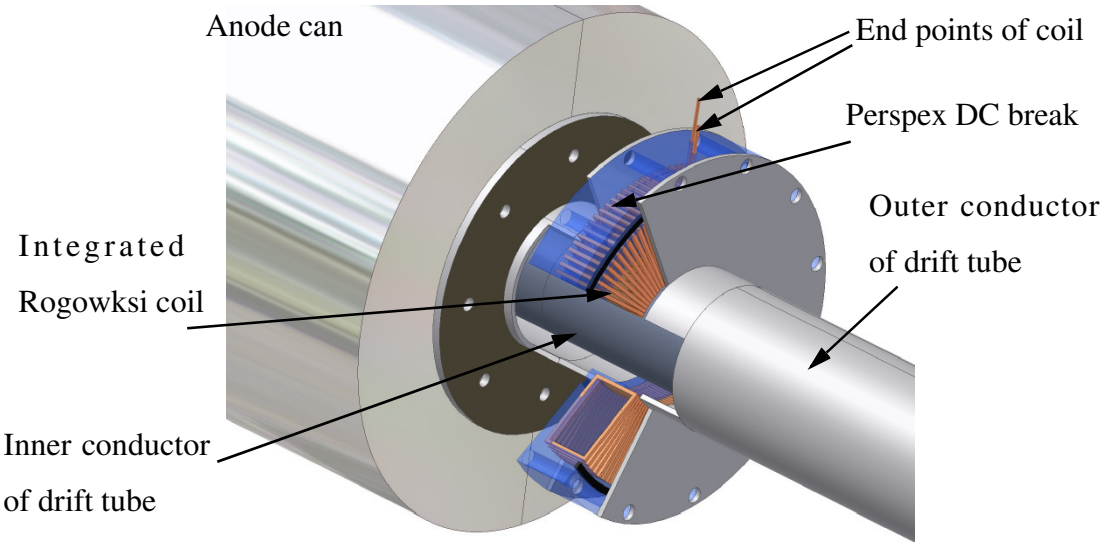

Figure 6.14: Shows a schematic of the electron beam Rogowski coil, noting its position within the perspex DC break between the anode can of the gun-diode and the outer conductor of the drift tube.

The resistor R was provided by a 50Ω matched load attached at the input to a Tektronix TDS640A oscilloscope, connected to the probe via standard, BNC terminated, co-axial cable. A typical pulse recorded using the Rogowski coil is given in Figure 6.15. The charging voltage on the Marx-bank capacitors for the pulse shown in Figure 6.15 was $40kV$, with the output spark-gap pressure set at $8bar$. It should be noted that the Rogowski coil was only used in the $1.5kA$ 2D - 1D Bragg experiment. In the $3kA$ experiments an alternative, current shunt diagnostic was employed (c.f. Section 6.3.2.2).

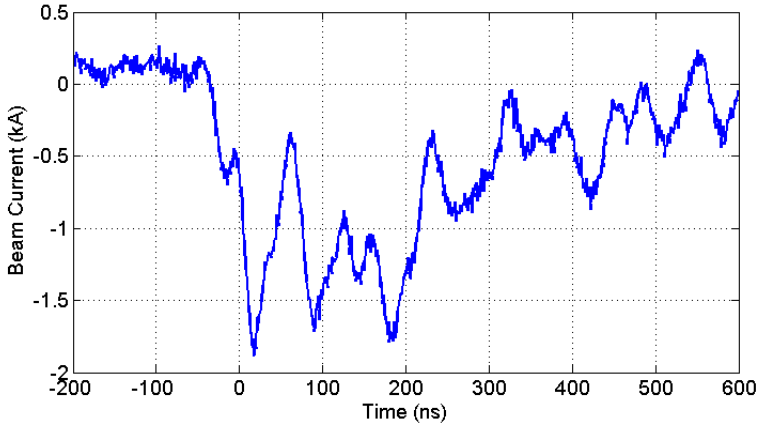

Figure 6.15: Shows an electron-beam current pulse recorded using the integrated Rogowski coil.

The large ripple noted on the pulse was due to the presence of a large AC noise signal incident on the probe. The relative magnitude of this signal was estimated by repeating the experimental run as before, minus the magnetic focusing of the guide solenoid field, essentially dumping the electron beam to the anode can wall. The trace produced is given in Figure 6.16 along with the recovered beam current obtained after subtraction of the background noise signal.

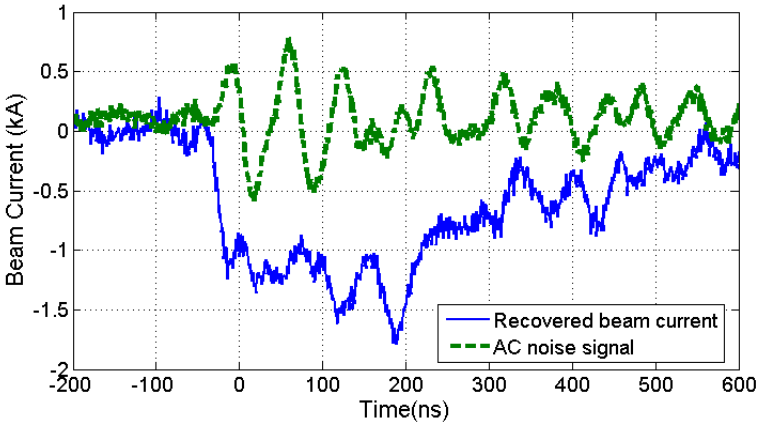

Figure 6.16: Shows the AC signal generated by the electron beam impacting on the anode can wall along with the electron-beam current measurement recovered after removal of the noise signal.

6.3.1.2 The Undulator Rogowski Coil.

The Rogowski coil, used to measure the current flow in the undulator circuit, was positioned on the line leading from the undulator power supply (c.f. Section 5.4.1) to the undulator coil itself. The coil consisted of ~ 280 turns with a total wire length of $\sim 93m$. Anodised copper wire was used to form the coil, with a mean wire diameter of $\sim 0.8mm$. As before the resistor R was provided by a 50Ω matched load connected at the oscilloscope, in this case a Tektronix TDS640A.

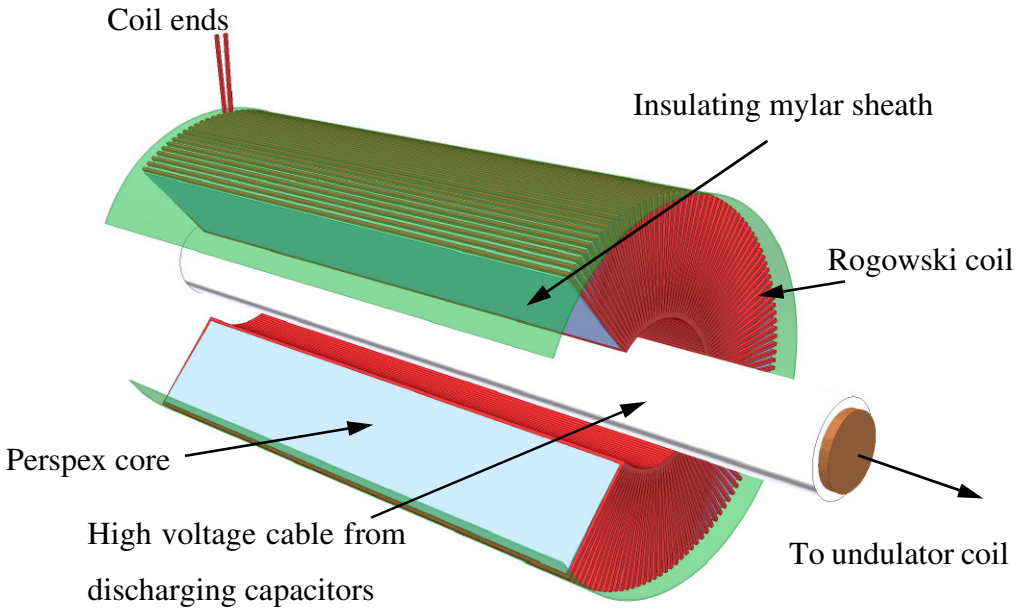

Figure 6.17: Shows a schematic of the Rogowski coil placed in the undulator circuit. The coil was positioned, as indicated in Figure 5.19, on the line leading from the output from the capacitors to the undulator coils.

Taking values for $I(t)$, calculated from the measured pulse amplitude on the DSO, the magnetic field generated for a given charging voltage was compared. Plots of the expected and experimentally determined responses are given in Figure 6.18.

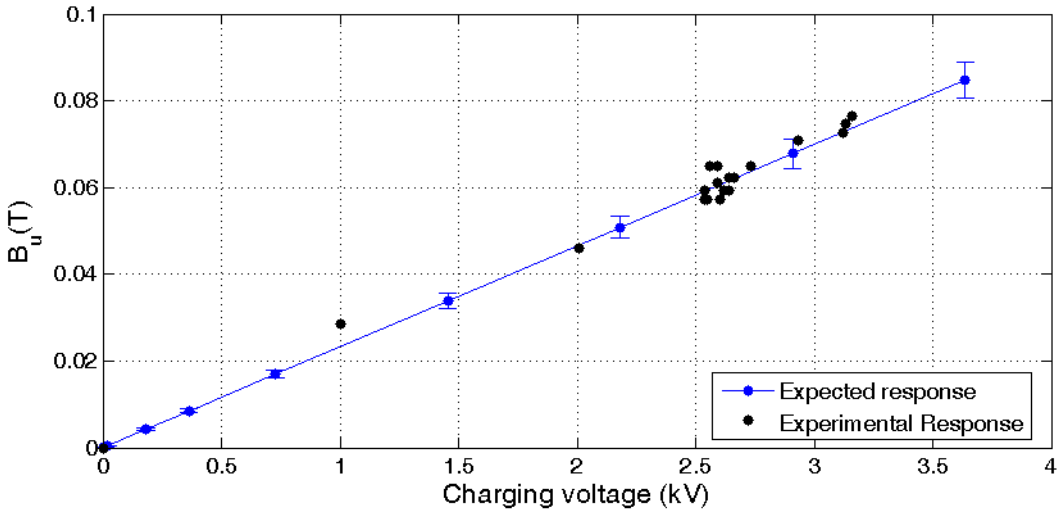

Figure 6.18: Shows the peak magnetic field, in the regular section of the undulator coil, for a range of applied charging voltages.

This shows that the undulator performed as expected, with shot to shot variation of $\sim 10\%$, corresponding to the margin for error in the diagnostic.

6.3.2 Current Shunt Diagnostics.

Current shuts can reach sub-nanosecond rise-times with a high degree of sensitivity; they are typically employed for sampling low frequency, high amplitude currents showing a fast rise-time (Thornton 1975). The idealised current shunt acts as a pure resistance of low value compared to that of the device under test (DUT) ($R_{shunt} \ll R_{DUT}$). Shunts are integrated in series with the DUT with the voltage drop across the shunt giving a direct correlation with the current flowing in the circuit through Ohm's law.

As discussed in Section 6.2.1, no resistor shows a truly "pure" resistance, devoid of self-capacitance (C_s) or self-inductance (L_s), with the effects of both becoming more pronounced as the required response time of the diagnostic approaches the transit time of the pulse through the shunt.

6.3.2.1 Current Shunt Operation

A current shunt can approach a purely resistive response provided C_s and L_s obey the relation (Leonard 1965):

$$\omega L_s \ll R \ll \frac{1}{\omega C_s} \qquad \textbf{6.21}$$

where $\omega \cong 0.35(2\pi / t_r)$ is the highest significant frequency component of the current and t_r is the current rise-time (He 1995).

A potential error arises due to an increase in shunt resistance due to the skin effect. This can be mitigated by ensuring the diameter of the shunt (D) satisfies:

$$D = \sqrt{\frac{2}{\omega_h \sigma \mu}} \qquad \textbf{6.22}$$

where σ is the conductivity of the resistive material and μ is the permeability. For shunts consisting of multiple resistive components equation 6.22 relates to each component individually.

Under the assumption that all of the energy lost from the circuit to the shunt is absorbed by the shunt material, in the limit where the current rise-time is much shorter than the pulse duration ($t_r \ll \tau$), the shunt undergoes a change in temperature corresponding to:

$$\Delta T = \frac{I^2 R \tau}{c_m m} \qquad \textbf{6.23}$$

where c_m corresponds to the specific heat capacity of the shunt material and m corresponds to the shunt mass. In order for the change in resistance, due to the change in temperature, to be considered negligible:

$$\frac{I^2 R \tau}{c_m m} \alpha_T \ll 1 \qquad \textbf{6.24}$$

where α_T is a co-efficient of the shunt's resistivity.

Current shunts should be located as close to the ground plane as possible, preferably directly connected to ground, to minimise noise coupling on the diagnostic and to ensure the measurement is not taken across a floating potential (He 1995).

Provided these criteria are met the current determined using Ohm's law, calculated using the measured potential difference across the resistive shunt, gives a good approximation of the circuit current.

6.3.2.2 The Electron Beam Current-Shunt.

In the $3kA$ 2D - 1D FEM experiments, the Rogowski coil diagnostic was replaced with a current shunt, constructed using twenty-four sets of four parallel 10Ω carbon resistors, giving a total shunt resistance of $R \approx 0.1\Omega$.

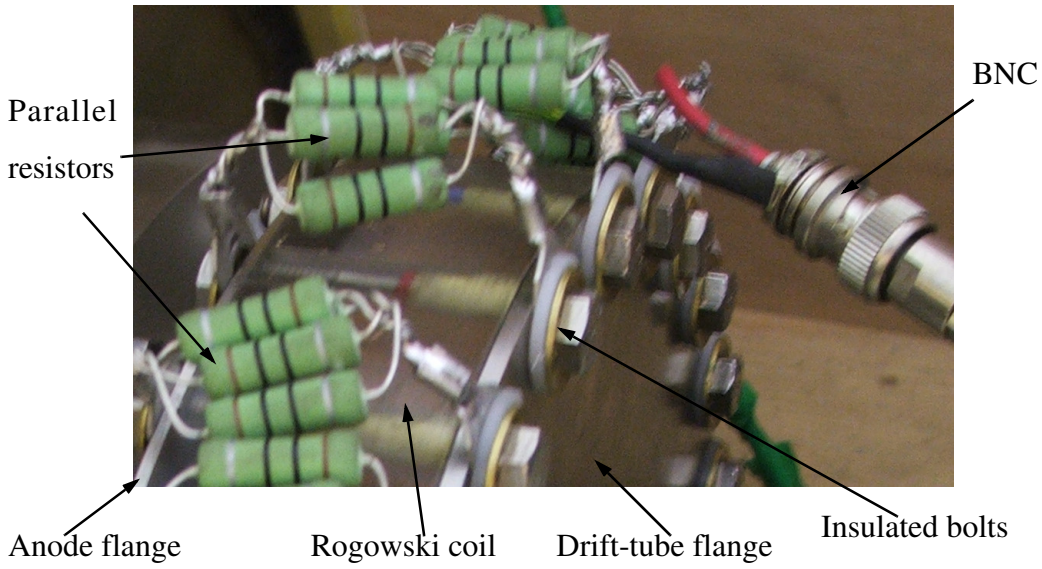

Figure 6.19: Shows the current shunt constructed across the fixing plates of the Rogowski coil, used to measure the beam current.

A typical trace of the electron beam current, measured using the current shunt, is given in Figure 6.20, corresponding to a charging voltage of $40kV$ on the Marx-bank capacitors with the output spark-gap pressure set at $9Bar$. The trace was recorded using a Tektronix TDS6124C DSO.

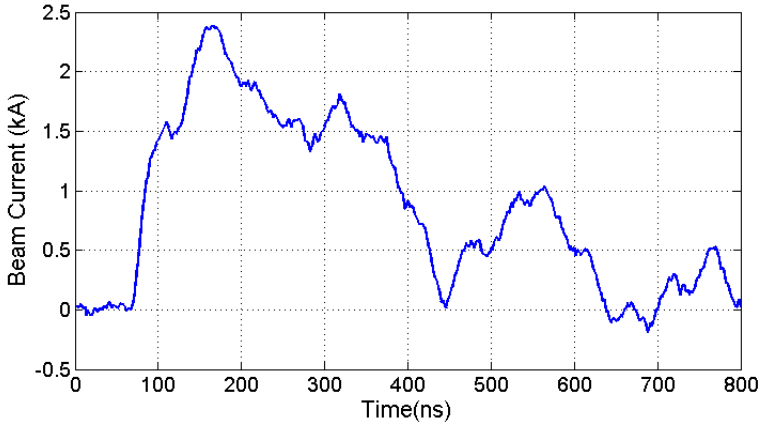

Figure 6.20: Shows the electron beam current measured, using the current shunt diagnostic, for a charging voltage of *40kV* on the Marx-bank capacitors.

In comparison with Figure 6.16, it should be noted that the increased beam current in Figure 6.20 was due to the reduced anode radius (c.f. Section 5.3) in the electron gun diode, which increased the space charge current limit. Another notable change is the elongated discharge time. This can be attributed primarily to the low energy tail of the electron beam, though some effects from stray capacitance may be inferred from the decaying AC behaviour observable towards the end of the pulse. The reversal in the sign of the current, between Figures 6.16 and 6.20, arises from a change in the polarity of the co-axial cable connection to the diagnostics, it does not correspond to a change in the direction of current flow.

6.3.2.3 The Solenoid Current-Shunt.

The current shunt used to monitor the current flow in the solenoid circuit was constructed from 270 metal-film high precision 3Ω resistors, set in parallel in a tightly packed toroid. The shunt resistance was checked using a Keithly 2700 multi-meter, operating as a four-wire voltmeter, giving a reading of $R \approx 0.011\Omega$. This was confirmed using a Thurlby-Thandar PL154 $15V$, $4A$ supply, set at ~$0.1V_{max}$. This produced a current reading of $341mA$ on the Thurlby, with a voltage-drop of $3.53mV$

across the coil measured using the Keithly 2700 multi-meter, operating as a high precision voltmeter (i.e. $R \approx 0.01\Omega$).

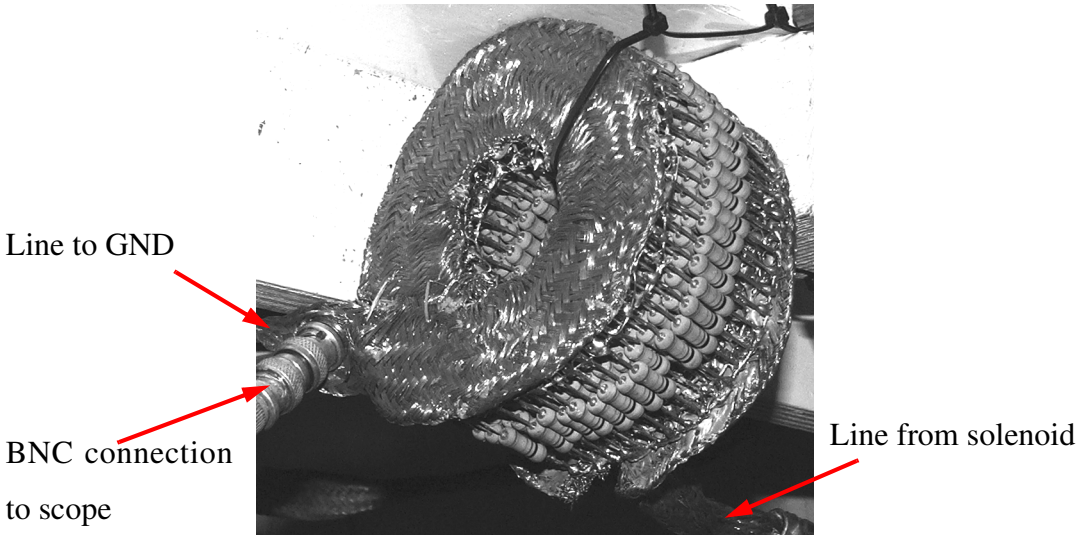

Figure 6.21: Shows the current shunt connected in-line with the solenoid coil, positioned close to the ground plane of the circuit.

Taking that the peak B field for a long solenoid can be calculated as:

$$B = \frac{\mu_0 n_r V(t)}{lR} \qquad \textbf{6.25}$$

where the number of turns $n_r = 1000$, $l = 2.55m$ and $R = 0.011\Omega$, the magnetic field generated for a given charging voltage could be determined. A comparison between the expected performance (given the circuit parameters) and the experimental observed performance is given in Figure 6.22. Note that the diagnostic was taken to have an error of $\sim 10\%$ over the range shown, given the pulsed nature of the circuit and the change of resistance with temperature of the shunt ($\sim 50 ppm/K$ for the metal-film resistors used).

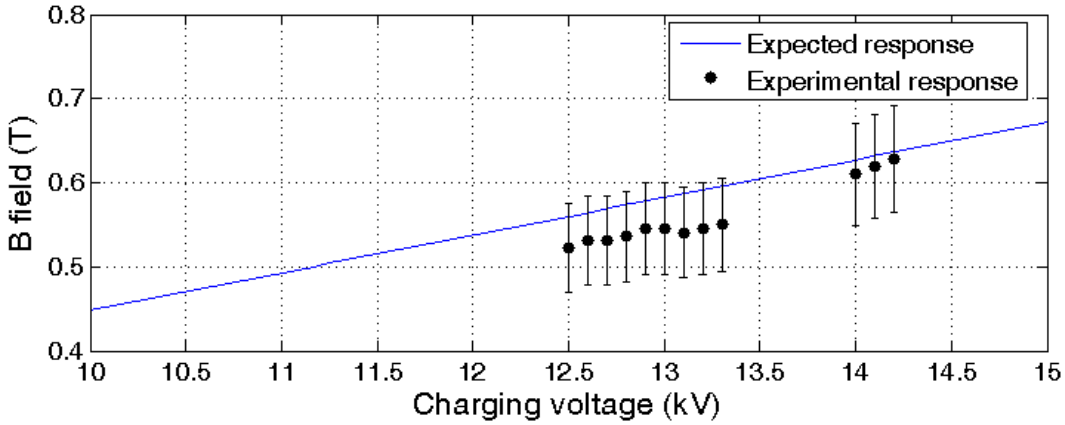

Figure 6.22: Shows the peak *B* field generated in the solenoid coil, for charging voltages on the solenoid capacitors in the range of *12.5 - 14.2kV*.

Looking at Figure 6.22 it can be seen that the expected *B* field, for a given charging voltage, falls within the range of that measured using the current shunt. The deviation in this result was non-critical, as the strength of the guiding field simply had to be sufficient to constrain the electron beam and maintain the cyclotron frequency far from the operating frequency of the FEM.

Recalling that the guide solenoid and undulator systems were independently tunable, resonance between the electron beam and the magneto-optical systems could be found by setting a value for the charging voltage of the guide solenoid and tuning the undulator charging voltage over a series of shots. An example of this is given in Section 7.4.3.

6.4 Microwave Pulse Power Measurement.

The microwave output from the FEM experiment was sampled using a set of two broadband Agilent 8474E series ($0.01 - 50GHz$) co-axial microwave detectors, serial numbers 01027 and 01030. The internal circuit of the detectors is shown in Figure 6.23 (Agilent Technologies 2002).

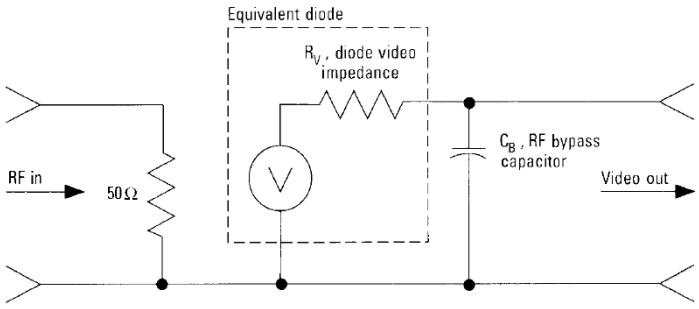

Figure 6.23: Shows the circuit for the Agilent 8474 series co-axial microwave detectors, noting the equivalent diode presented by the PDB GaAs detector crystal.

The equivalent diode of the microwave detector was formed by a planar doped barrier (PDB) Gallium Arsenide (GaAs) semiconductor diode structure. These were quoted as having superior temperature stability characteristics compared to either point-contact or Schottky diode based detectors. (Agilent Technologies 2002). The detectors were rated up to a maximum input of $200mW$, though the frequency response rating of $\pm 0.6dB$ from $26.5 - 40GHz$ was quoted for $\leq 20dBm$ $(100mW)$.

The detectors crystals were calibrated, in two stages, at $1GHz$ intervals between $35 - 40GHz$. In the first stage the voltage response of each crystal was measured for input powers ranging from $-10dBm$ to $12dBm$. The input signal was provided by a HP 83752B synthesised sweeper set in CW mode, while the voltage response was measured on a Keithly 2700 high precision multi-meter. In the second stage the actual power output from the source was measured by connecting the source output to an Anritsu CW MA2474D probe, connected to an Anritsu ML2496A high-frequency $(300MHz)$ pulsed power meter. The calibrated responses for the 01027 crystal are given in Figure 6.24 with the responses for the 01030 crystal given in Figure 6.25.

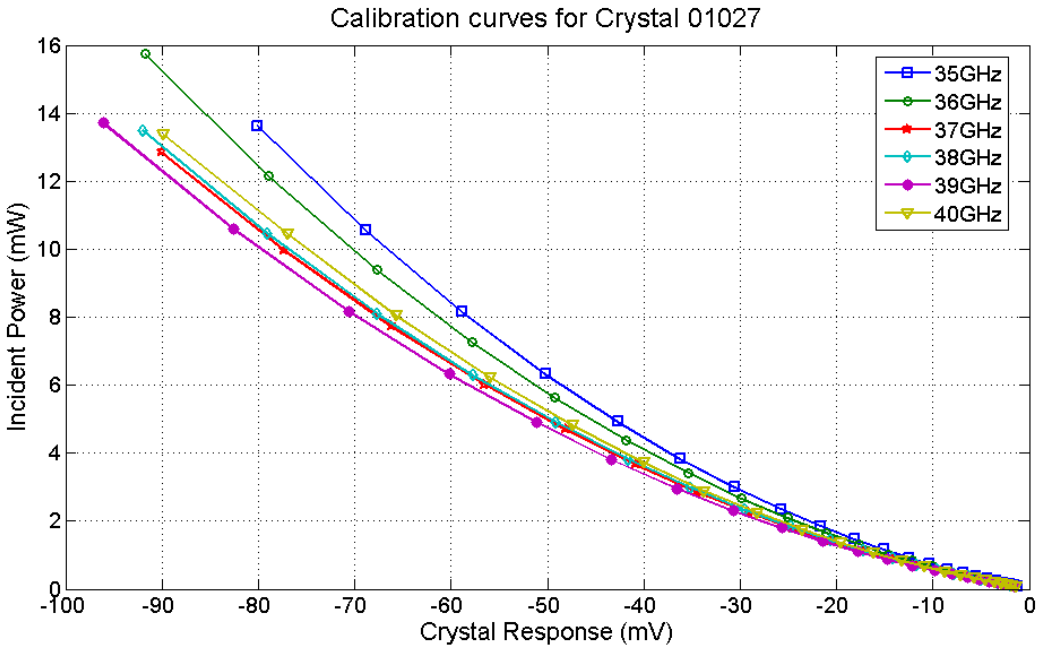

Figure 6.24: Shows the calibration curves, for crystal detector 01027, for the frequency range *35 - 40GHz*.

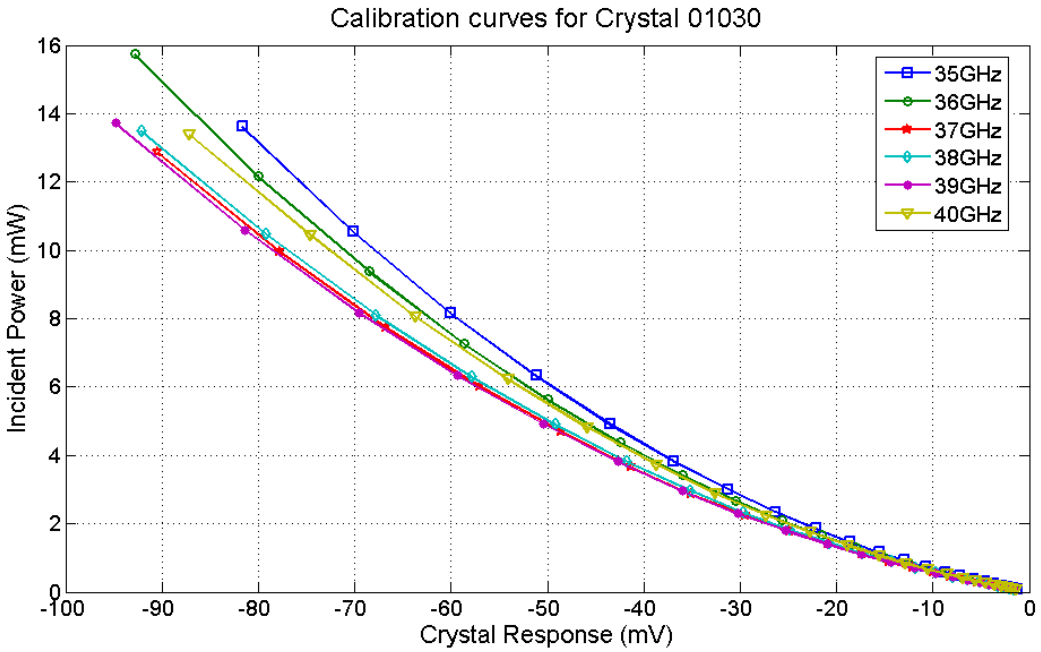

Figure 6.25: Shows the calibration curve for Crystal 01030, for the frequency range *35 - 40GHz*.

The output power from the FEM was derived by measuring the power at the receiving horn of the crystal detector, taking into account any added attenuation used to bring the sampled signal down to a safe level. This gave a measure of the power over the angle subtended by the receiver horn, which could then be integrated over the measured mode pattern to obtain the total output power.

6.5 Spectral Measurement Using Cut-Off Filters.

The FEM experiment sampled the output microwave pulses using detector horns, connected to lengths of standard circular and rectangular Ka-band ($26.4 - 40GHz$) hollow metallic waveguide, terminated in rectangular to co-axial adaptors, connected to the microwave detector crystals discussed in Section 6.4. As a preliminary means of determining spectral content one of waveguide lines incorporated an additional section allowing the insertion of a length of tapered circular waveguide with a reduced mean inner radius. The introduction of such a waveguide section acted as a high-pass filter, attenuating those portions of the sampled microwave spectrum with a wavelength greater than the cut-off wavelength of the filter.

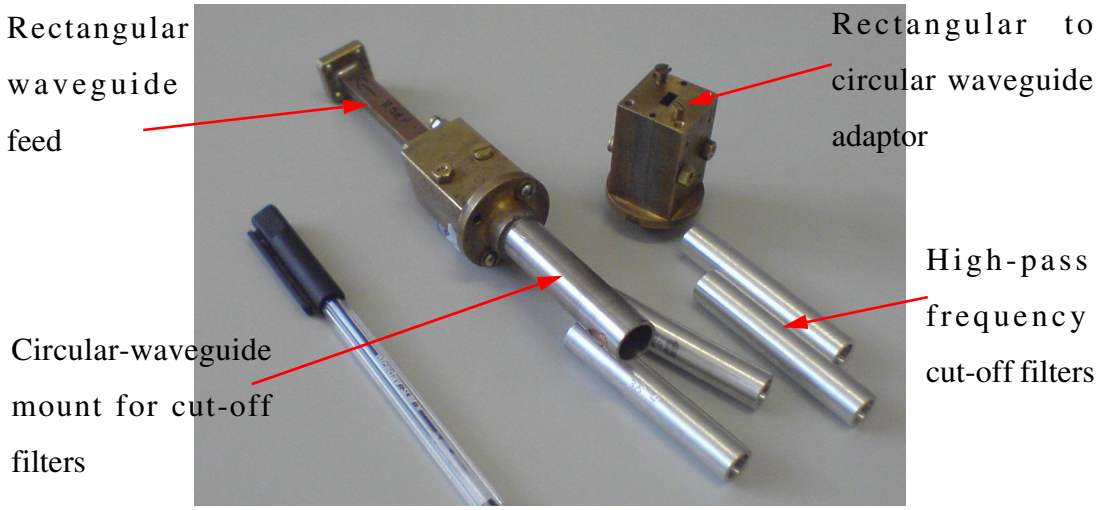

Figure 6.26: Shows the waveguide mount for the high-pass filters, along with a selection of filter inserts. Note the conversion from rectangular to circular waveguide performed at either side of the filter mount.

The cut-off frequency of the filter inserts was determined using a HP8757D scalar network analyser (SNA), with the calibration signal provided by an HP83752B synthesized sweeper. The measured performance for each filter is given in Figure 6.27.

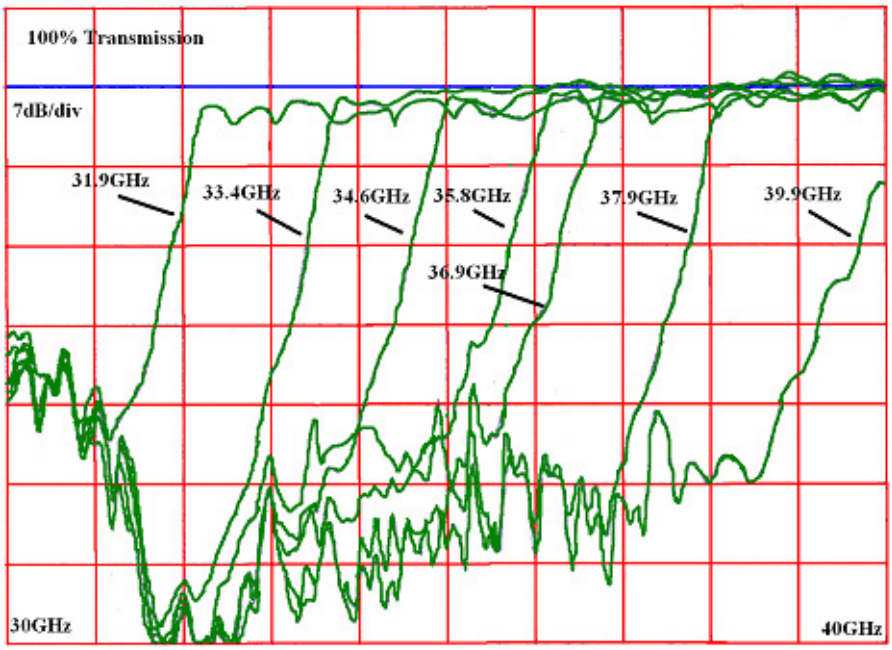

Figure 6.27: Shows the transmission profiles of the high-pass frequency cut-off filters used in the FEM experiments.

6.6 Spectral Measurement using a Frequency Mixing Technique.

A more accurate method of determining the spectral content of a microwave pulse is to measure the spectrum directly. This method is limited by the frequency bandwidth of the oscilloscope used to record the measurement, determined by the scope's maximum temporal resolution. In other words, an oscilloscope can only resolve signals with frequencies at or below the limit set by its minimum time step, giving:

$$f_{max} = 1/t_{min} \qquad \textbf{6.25}$$

For signals suspected of having spectral content in excess of this limit, a useful means of recovering this information is to use a heterodyne technique. In this case the sampled signal is "mixed" with a local oscillator (LO) signal, producing signals with

frequencies corresponding to the sum and difference of the sampled and LO signals. The "difference" signal, termed the intermediate frequency (IF) signal, is then recorded on the oscilloscope, while the "sum" signal is filtered out by the mixer circuit.

The FEM experiment made use of a BMC-28B Farran-Technology Ka-band frequency mixer ($26.4 - 40GHz$), consisting of a GaAs (Gallium Arsenide) Schottky diode mixer crystal. The mixer was subject to a DC bias of $\sim 9V$ provided by a standard $12V, 7Ah$ battery. For calibration, the HP83752B synthesized sweeper, set in CW mode, was used to provide the LO signal, with an Anritsu E8267D, $250kHz - 44GHz$, Vector Signal Generator (VSG) providing $100 - 300ns$ long single frequency pulses at the RF input, essentially mimicing the operation of the FEM. A circuit schematic is given in Figure 6.28:

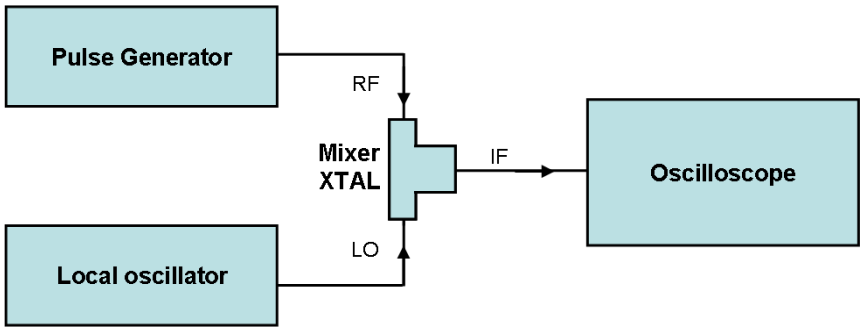

Figure 6.28: Shows the schematic of the test circuit used to determine the performance of the Ka-band mixer crystal.

A Tektronix TDS6124C DSO was used to record the IF signal, both in the calibration of the crystal and in the experiment. This was capable of detecting $100ns$ pulses over a bandwidth of $\pm 7GHz$ from an LO frequency of $35GHz$, however in the experiments the effective bandwidth of the heterodyne measurement was reduced to $\pm 2.5GHz$ from the LO frequency, due to aliasing in the Fourier transform algorithm beyond this range. As the output from the FEM experiment was expected to be in the region of $37GHz$, the LO frequencies used were typically in the range of $36 - 38GHz$.

6.7 Summary of Diagnostic Parameters

The following lists the main diagnostic parameters of the FEM experiment:

Parameter	Value
Voltage Diagnostics:	
Marx-Bank Voltage Probe:	*Single-stage, unshielded Resistive Divider*
Conversion Factor:	$226kV$:$1V$ on DSO
Transmission Line Probe:	*Single-stage Capacitive Divider*
Conversion Factor:	$100kV$:$1V$
Shielded Diode-Voltage Probe:	*Two-stage, Shielded Resistive Divider*
Conversion Factor:	$293kV$:$1V$ on DSO
Unshielded Diode-Voltage Probe:	*Two-stage Unshielded Resistive Divider*
Conversion Factor:	$316kV$:$1V$ on DSO
Current Diagnostics:	
Beam-Current Rogowski Coil:	$n_r = 200turns$, *perspex cored.*
Conversion Factor:	$I_{peak} = n_r \times$ DSO reading$/(50\Omega)$
Beam-Current Current Shunt:	$R \cong 0.1\Omega$
Conversion Factor:	$I \cong$ DSO reading$/R$
Solenoid Current Current Shunt:	$R \cong 0.011\Omega$
Conversion Factor	$I \cong$ DSO reading$/R$
Undulator-Current Rogowski Coil:	$n_r = 280turns$, *perspex cored*
Conversion Factor:	$I_{peak} = n_r \times$ DSO reading$/(50\Omega)$
Microwave Power Diagnostics:	
Detector Crystals:	Agilent 8474E series $(0.01 – 50GHz)$

Parameter	Value
Microwave Spectral Content diagnostics:	
High-Pass Cut-Off Filters:	*Filters for:* $31.9GHz$, $33.4GHz$, $34.6GHz$, $35.8GHz$, $36.9GHz$, $37.9GHz$, $39.9GHz$.
Ka-Band Heterodyne Mixer Crystal:	*Farran-Technologies model BMC-28B*
DC Bias:	Provided by $12V$, $7Ah$ battery with a $5.6k\Omega$ resistor in-line (+)
Operating range:	$\pm 7GHz$ from LO frequency, within Ka-band $(26.4 - 40GHz)$
Effective range in Experiment:	$\pm 2.5GHz$ from LO frequency

Chapter 7: Experimental Results of the 2D - 1D Bragg Free Electron Maser

7.1 Introduction.

The results of the 2D - 1D Bragg FEM experiments are presented, beginning with a discussion of the triggered discharge circuit (c.f. Section 7.2) common to both the $1.5kA$ and $3kA$ beam current experiments. This is followed by the results obtained using the $1.5kA$ EEE gun, as presented in Section 7.3. The accelerating potential imposed across the gun electrodes was monitored using a shielded resistive divider probe (c.f. Section 7.3.1). The resultant beam current was monitored using a Rogowski coil, integrated with the DC break between the anode can and the drift-tube outer conductor (c.f. Section 7.3.2). The output microwave spectral content was estimated using a series of high-pass cut-off filters (c.f. Section 7.3.3), with the microwave power measured using Agilent 8474E series ($0.01 - 50GHz$) co-axial microwave detectors (c.f. Section 7.3.4).

The results from the 2D - 1D Bragg FEM, incorporating the reduced anode can geometry EEE gun (c.f. Sections 4.2.1.2 & 5.3) are presented in Section 7.4. The voltage diagnostics were expanded to include monitoring of the discharge from the Marx-bank and the transmission line, in addition to the voltage applied across the diode (c.f. Section 7.4.1). The beam current measurement was obtained using a current shunt connected across the outer-conductor DC break (c.f. Section 7.4.2). The microwave power output was determined as before using the Agilent 8474E crystal detectors (c.f. Section 7.4.3), with the spectral content of the pulses examined more closely using a heterodyne mixer crystal to measure the wave-form (c.f. Sections 7.4.3 & 7.4.3.1).

7.2 The Triggered Discharge Circuit.

The guide solenoid and undulator were powered by single-shot capacitive discharge power supplies, as opposed to running CW. This had an important consequence, in regards to the operation of the FEM, as the electron beam, generated by the EEE gun, must show a relatively small initial transverse velocity spread and must be capable of transportation through the drift tube region without incidence on the drift tube walls. The performance of the undulator and guide solenoid circuits were monitored using a differentiating Rogowski coil (c.f. Section 6.3.1.2) and a current shunt (c.f. Section 6.3.2.3) respectively.

The solenoid was triggered using a mercury filled ignitron switch, with the undulator circuit triggered in a similar manner after a preset time delay. This allowed for alignment of the undulator discharge with the peak magnetic field of the solenoid. The Marx-bank discharge was time-correlated with the peaks of the undulator and solenoid fields using the same delay circuitry, with the discharge itself instigated using a fast thyratron switch. The evolution of the magnetic fields are shown in Figure 7.1, along with a line denoting the triggering of the Marx-bank:

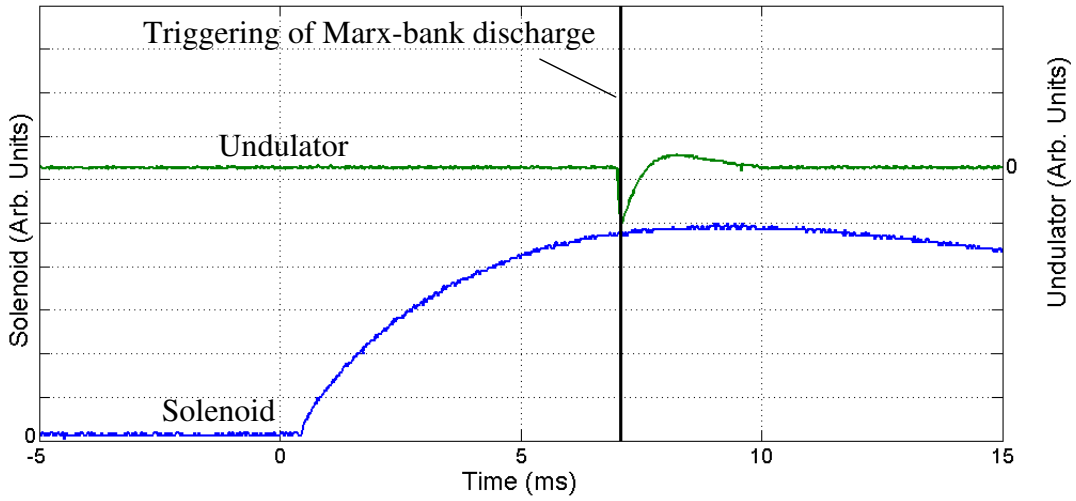

Figure 7.1: Shows the timing of the solenoid and undulator magnetic field profiles. The vertical line denotes the timing of the Marx-bank discharge. Trace amplitudes have been normalised and adjusted for clarity.

As can be seen in Figure 7.1 the discharge time of the solenoid magnetic field is on the order of milliseconds, with the undulator discharge on the order on tens of microseconds. These are both substantially longer than the time scale of the diode voltage pulse, which was on the order of hundreds of nanoseconds. While the magnetic field profiles of the undulator and the guide solenoid show defined regions of rising and decaying field strength, quasi-CW operation can be approached, provided the peak discharges of the magnetic fields overlap with the Marx-bank discharge time and are of substantially longer duration than the resultant electron beam.

Looking more closely at the region of Figure 7.1 associated with the discharge of the Marx-bank, the uniformity of the undulator and guide solenoid fields are clearly observed:

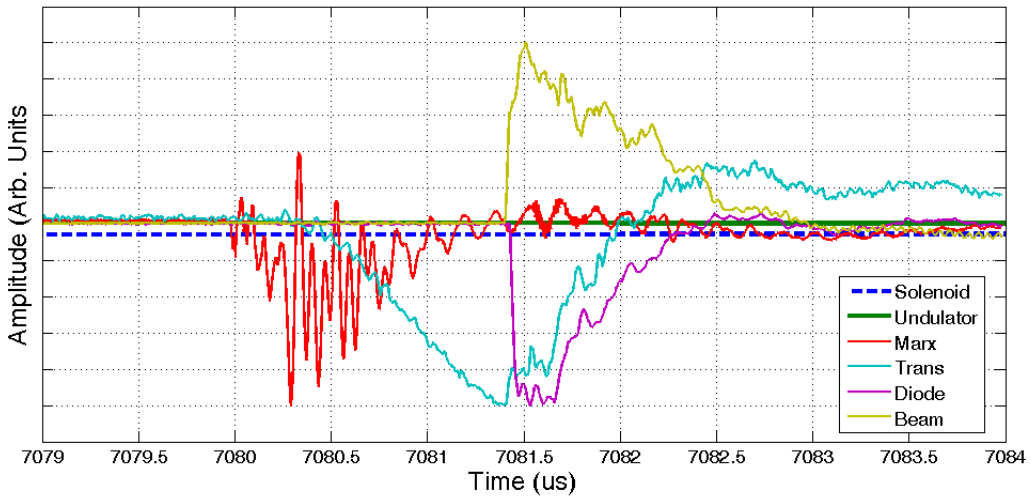

Figure 7.2: Shows a close-up, of the region of Figure 7.1, corresponding to the operational pulse from the FEM. The amplitudes of all traces are in arbitrary units for ease of display.

Neither magnetic field shows appreciable change for the duration of the FEM experimental operation (from the triggered discharge of the Marx-bank through to the termination of the electron beam current), confirming quasi-CW operation. The time correlation, of the solenoid and undulator magnetic fields to the electron beam pulse, was monitored for each experimental run throughout both stages of the experiment.

7.3 2D - 1D Bragg FEM Experiment Utilising a 1.5kA Beam.

The following section describes the results of the 2D - 1D Bragg FEM experiment, carried out using the EEE gun, described in Section 4.2.1.1, to generate a $\sim 1.5kA$, $450keV$ electron beam. This was confined by an axial magnetic field of $\sim 0.6T$, with the undulator strength varied, until resonance was found in the region of $0.06 - 0.063T$. The lasing cavity was defined by a $10cm$ long, $8mm$ period, 2D input reflector and a $15cm$ long, $4mm$ period, 1D output reflector, with a separation of $60cm$.

7.3.1 Measurement of the Electron Accelerating Potential.

For the FEM experiment to operate efficiently a mono-energetic electron beam, with low velocity spread, is required. The energy in the beam is set by the accelerating potential across the electron gun-diode, provided by the shaped discharge of the transmission line, with the total electron energy taken to be synonymous with the applied diode voltage, i.e. an applied voltage of $440kV$ corresponds to a total electron energy of $440keV$.

In order for an appropriate electron beam to be generated the applied voltage pulse should display a "flat-top", with well defined rising and decaying edges. Noting the KARAT simulations of the EEE gun diode (c.f. Section 4.2.1.1) and the explosive nature of the EEE cathode, a portion of the electron's energy lies in transverse, as opposed to the desired axial, momentum. From the simulations, in conjunction with equation 2.4, it was estimated that an accelerating voltage of $\sim 430keV$ was required to deliver sufficient axial momentum to properly couple the electrons to the undulator field at $\sim 37.5GHz$ (the expected resonant frequency of the 2D - 1D Bragg cavity).

The applied diode potential was determined by a combination of factors. The initial discharge from the Marx-bank under-went pulse shaping via the action of the transmission line and output spark-gap, with the breaking voltage of the spark-gap and the value of the matching resistor network determining the discharge profile of the voltage pulse; experimental investigation of this process is presented in Section 7.4.1.

The voltages applied across the gun diode, for the $1.5kA$ 2D - 1D FEM experiments, were measured using the shielded resistive divider probe described in Section 6.2.1.2:

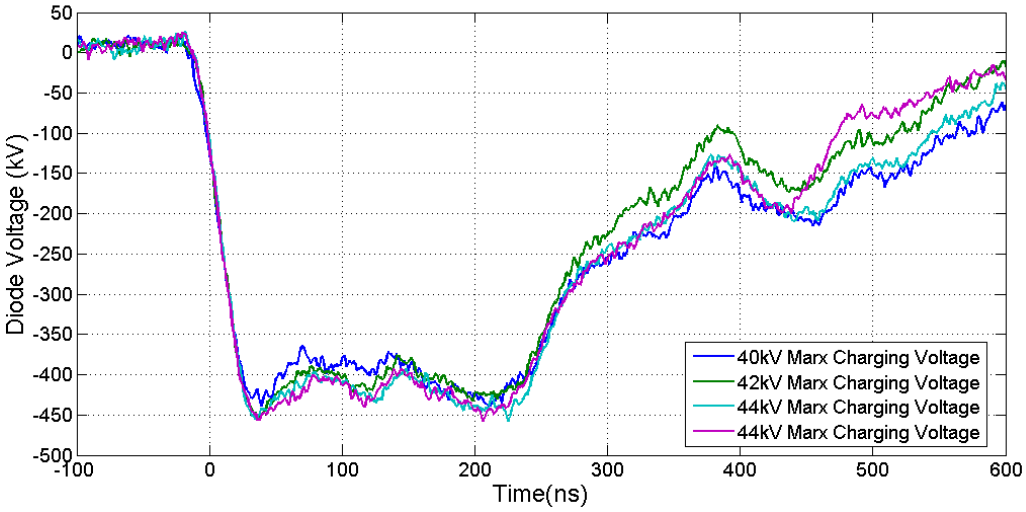

Figure 7.3: Shows a selection of voltage traces, measured across the gun diode, for charging voltages on the Marx-bank capacitors of *40 - 44kV*.

The extended decay exhibited by the voltage traces of Figure 7.3 shows the output spark-gap matching resistors were configured to be slightly mismatched with the load seen by the transmission line, leading to a diode voltage of $\sim 2/3$ that of the discharge voltage from the Marx-bank. For a perfectly matched load $1/2$ of the Marx-bank output voltage would have been applied across the electron gun, however a move to such exact matching of the load to line impedance would have necessitated a marked increase in the charging voltage on the Marx-capacitors to $\sim 60kV$ in order to achieve the required electron energy. This would result in increased electrical stress on the insulating dielectric oil, whilst also necessitating increases in the pressure of the Nitrogen gas used in the Marx-bank spark-gap column and the output spark-gap.

While the mismatched load results in a stepped decay of the diode voltage, leading to the creation of a lower energy "tail" forming at the end of the electron beam pulse, the reduced electrical and mechanical stresses on the experimental apparatus were preferable for proof of principle experiments.

It can be readily seen that the profile of the voltage pulse remains constant regardless of the initial charging voltage, with similar rise times noted and similar decay rates. For a Marx-bank charging voltage of $44kV$ the resultant voltage traces peak at $\sim 430kV(\pm 5\%)$, corresponding to electron energies of $\sim 430keV$, in the region required for interaction with the undulator magnetic field as predicted by KARAT. The spread in total electron energy of $\sim 10\%$ can be considered acceptable, given the explosive nature of the electron beam generation process (c.f. Section 5.3).

7.3.2 Measurement of the Electron Beam Current.

For the FEM experiment to generate microwave pulses of any notable magnitude the current of the electron beam must be sufficiently above the start-up current for the resonance of interest, this was estimated to be in the region of $0.5kA$ for the cavity configuration used. In reference to the simulations of the EEE gun, giving the estimated gun perveance as being $\sim 4.3(\pm 0.1)\mu P$, the measured diode potential of $\sim 430 - 450keV$ was expected to generate beam currents in the region of $1.5kA$. Figure 7.4 show the current pulses, corresponding to the applied diode voltages shown in Figure 7.3.

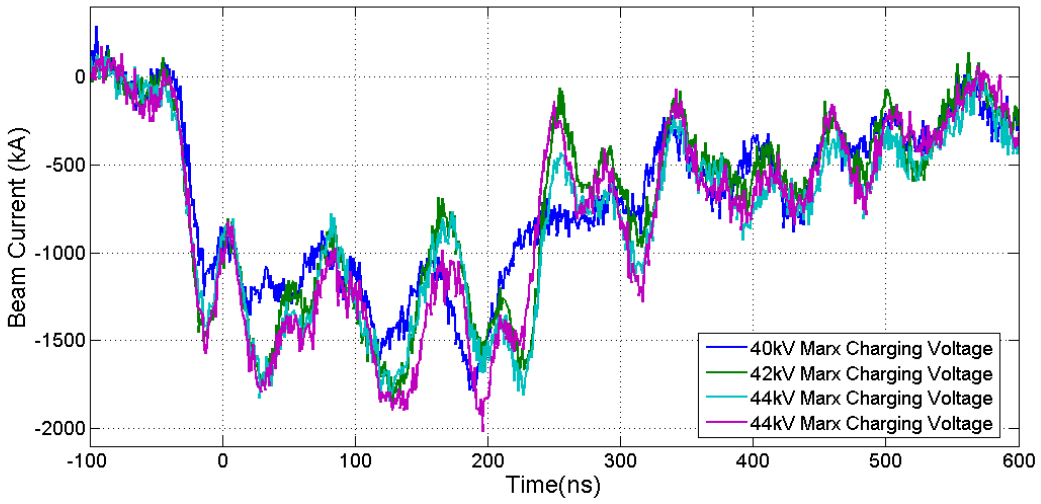

Figure 7.4: Shows the electron beam current traces corresponding to the applied diode voltage traces shown in Figure 7.3.

Experimentally this current was measured using a self-integrating Rogowski coil, permanently positioned inside a DC break between the anode-can and the outer conductor of the drift-tube (c.f. Section 6.3.1.1). Again a high degree of reproducibility can be seen in the pulse shapes between different shots, with varying electron energies determining the magnitude of the beam current, as expected. From these the gun perveance can be estimated to be $\sim 4.6(\pm 0.3)\mu P$, agreeing well with the value determined using KARAT given the explosive nature of the beam generation.

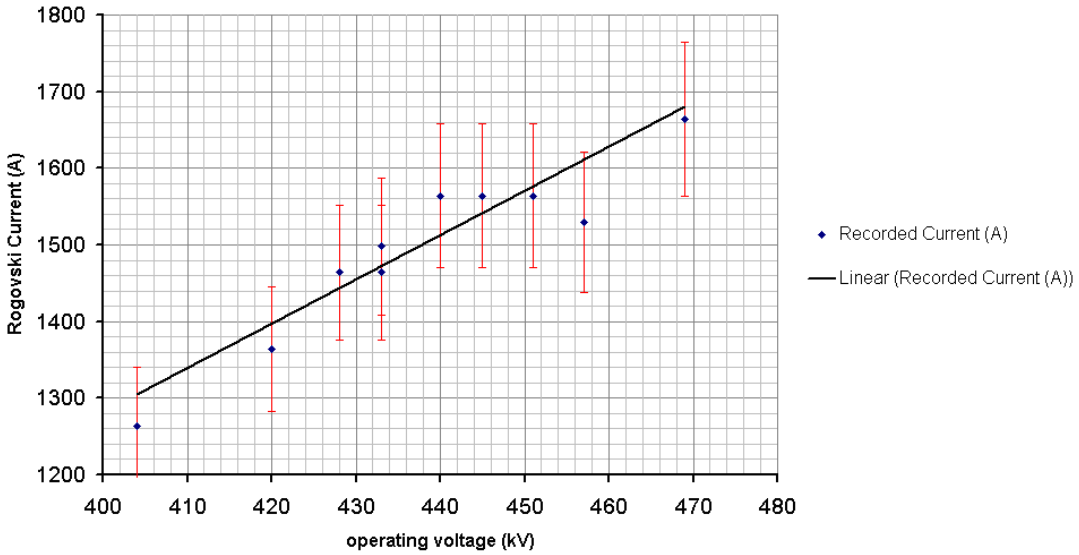

Figure 7.5: Shows the dependence of the electron beam current versus the applied diode voltage. The error bars correspond to *6%* of the measured value.

As Rogowski coils operate through magnetic induction of a secondary current, proportional to the current passing axially through the centre of the coil torus, it can be inferred that the transverse spread in particle energies of the physical electron beam is on the order of that simulated using KARAT, indicating a negligible spread in the initial transverse particle momentum.

7.3.3 Measurement of the Output Microwave Spectral Content.

Via the introduction of high-pass cut-off filters in-line with the microwave power diagnostic (c.f. Section 6.5) it was possible to narrow down the operating frequency of the FEM as shown in Figure 7.6. For the pulses shown the axial magnetic field strength was $\sim 0.6T$, with the undulator magnetic field being $\sim 0.06T$. The accelerating potential on the gun diode was kept in the range $430 - 460kV$ with associated beam currents of $1.4 - 1.7kA$.

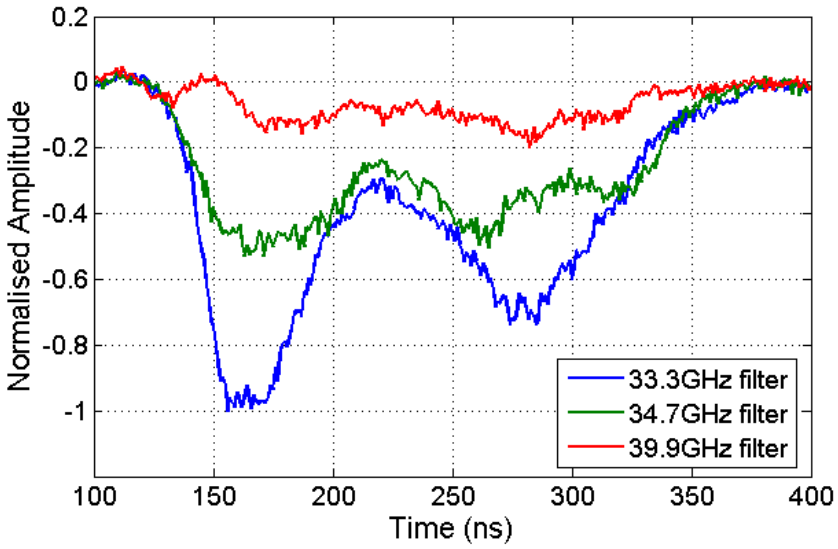

Figure 7.6: Shows normalised traces of the microwave pulses recorded using different high-pass cut-off filters.

From Figure 7.6 it can be seen that the majority of the energy in the microwave pulse was concentrated in the band between $34.7 - 40GHz$, agreeing well with the expected resonant frequency for the 2D - 1D Bragg cavity of $37.5GHz$.

The main concentration of energy in the output spectra was attributed to the dominant resonance of the 2D Bragg reflector, occurring between the fundamental TEM mode of the co-axial drift-tube and the higher order $TE_{24,2}$ mode present in the region of the 2D corrugation. The lower frequency portion of the pulse, shown to be attenuated between the pulses measured using the $33.3GHz$ and $34.69GHz$ filters corresponds well to the position of the $m' = -2$ eigenmode predicted by analytical theory (c.f.

Section 3.4) and found to correspond to a $HE_{2,2}$ mode through numerical simulation (c.f. Sections 4.3.2-4.3.3).

Subtracting the trace obtained using the $34.7GHz$ filter from that obtained using the $33.3GHz$ filter, it can be readily observed that the parasitic lower-frequency resonance only shows an appreciable amplitude at the beginning and end of the pulse. In regards to the growth seen at the beginning of the pulse, this indicates that both resonances are initially excited within the cavity, with the desired resonance (with the TEM mode) dominating after approximately $50ns$:

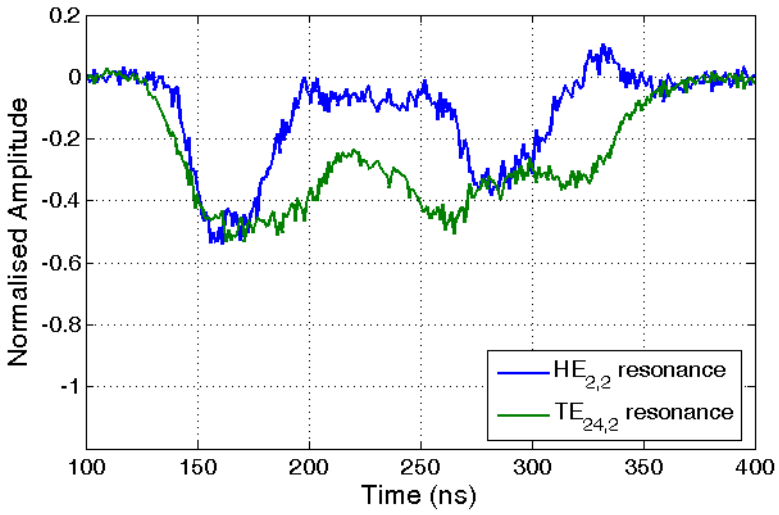

Figure 7.7: Shows the relative magnitudes of the resonances attributed to the $HE_{2,2}$ and $TE_{24,2}$ resonances calculated using the difference between the two similar pulses recorded using the *34.7GHz* and *33.3GHz* filters.

The growth of the parasitic resonance toward the end of the pulse may result from the increased number of electrons decelerated electrons (lower energy) generated by the interaction with the TEM resonance. In contrast the resonant transfer of energy from the electron beam to the TEM mode can be seen to remain relatively constant in magnitude throughout the pulse duration.

While this only serves as a rough guide to the spectral content of the FEM output microwave pulses it does indicate the presence of a dominant resonance in the region

of the expected resonant output frequency for the 2D - 1D Bragg lasing cavity. The reduced efficiency of the spurious resonance may be due to its likely association with a Lowbitron-like interaction. This may initially compete with the FEL instability before being dominated by the more stable FEL beam-wave interaction. Towards the end of the pulse, when the electron bunches are well established and the beam has gained a significant $v_{\perp}$ component, a Lowbitron-like interaction would see preferential coupling, resulting in the later peak in the HE resonance.

7.3.4 Determination of the Output Power in the Microwave Pulses.

The function of the output horn of the FEM experiment was to produce a highly directional, focused radiation pulse. As both the drift-tube and the horn itself are co-axial this output radiation is confined by a slowly expanding cone:

Figure 7.8: Shows a picture of the output radiation impacting on a neon bulb panel. The resultant pattern of lit bulbs shows the conical nature of the radiation pulse.

The output microwave cone subtended an angle of $\sim 5^0$ with the centre of the horn over an axial length of $60cm$. Figure 7.8 shows the impact of this conical radiation pulse on a neon bulb panel, with the "hole" in the centre of the radiation pattern clearly visible. The horns used to pick up the output microwaves from the FEM and channel them to the Agilent detector crystals only sample a portion of the total output microwave power. In order to get a true representation of the microwave output it was necessary

to take measurements of the output at different polarisations and different angles from the centre of the horn and integrated the power measured at the detectors over the measured radiation pattern. The total radiated power (P_{tot}) conforms to the equation:

$$P_{tot} = 2\left(l_{det}^2 \frac{P_0}{360 S_0} 4\pi^2 \Delta\psi \sum f_i \sin(\psi_i)\right) \quad \textbf{7.1}$$

where $l_{det} \cong 1.2m$ is the separation from the output horn to the detector horn, P_0 is the detected microwave power, $S_0 = 4 \times 10^{-4} m^2$ is the surface area of the horn aperture, ψ_i is the angle of the measurement in radians, $\Delta\psi \cong 0.087 rad$ and f_i is a weighting factor dependant on the polarisation of the detector horn. This can be simplified as:

$$P_{tot} = 4\pi\Delta\psi l_{det}^2 \frac{P_0}{S_0} (\sum B_{i1} + B_{i2}) \quad \textbf{7.2}$$

where $B_{i1,2} = f_{i1,2}\left(\sin\left(\frac{2\pi\psi_i}{360}\right)\right)$. The $1, 2$ subscripts correspond to the two transverse polarisations. The summation term corresponded to ~1.31 .

Using the experimentally determined preferential values of $0.063T$ for the undulator field and $0.56T$ for the guide solenoid field, the applied diode voltage was adjusted until a maximum output-pulse amplitude was obtained. The corresponding pulse is shown in Figure 7.9 plotted in terms of the total microwave output power.

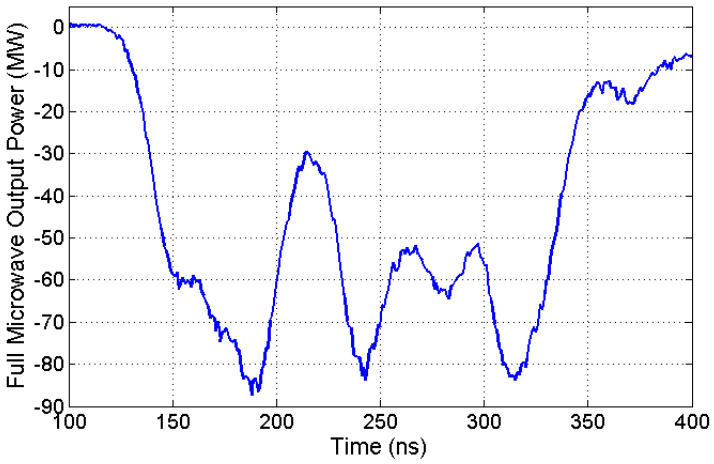

Figure 7.9: Shows the maximum output power from the 2D - 1D FEM experiment, expressed in terms of the total system power.

This resulted in the measurement of a $\sim 200ns$ long microwave pulse with a mean power of $\sim 60MW(\pm 10\%)$, giving an energy efficiency of $\sim 10\%$. The spectral content was estimated as lying between $34.7 - 39.9GHz$.

7.4 Second Stage of the 2D - 1D Bragg FEM Experiment.

The second stage of the 2D - 1D Bragg FEM experiment involved the use of the EEE gun, described in Section 4.2.1.2, to generate a $\sim 3.4kA$, $450keV$ electron beam, confined by an axial magnetic field of $\sim 0.62T$. The undulator strength was varied, until resonance was found, in the region of $0.05 - 0.052T$. The lasing cavity was altered slightly, with the addition of $1/2$ period $(4mm)$ to the length of the input mirror and the removal of 1 period $(4mm)$ from the output mirror. The input and output corrugation amplitudes remained constant at $\pm 0.8mm$ and $\pm 0.5mm$ respectively, with the reflector separation maintained at $60cm$ as before.

7.4.1 Measurement of the Electron Accelerating Potential.

The inclusion of additional diagnostics, for the secondary experimental run, allowed for monitoring of the electron accelerating potential at three key stages as it evolved through the FEM power supply. A simple resistive divider probe monitored the discharge voltage from the Marx-bank (c.f. Section 6.2.1.1) while the potential of the transmission line was monitored using a capacitive divider probe located just before the connection to the output spark-gap (c.f. Section 6.2.2). The shaped voltage pulse, applied across the diode by the transmission line, was monitored using a purpose built non-shielded resistive divider probe (c.f. Section 6.2.1.3), replacing the large shielded probe used in the $1.5kA$ FEM experiments. The traces recorded for a typical voltage pulse, as it evolved through the power supply, are given in Figure 7.10 The charging voltage on the Marx-bank capacitors was $50kV$.

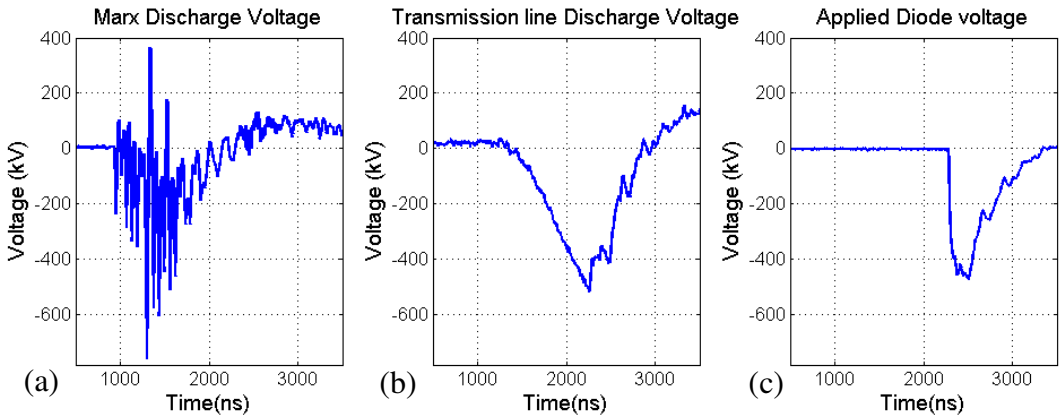

Figure 7.10: Shows (a) the output voltage from the Marx-bank (b) the voltage discharge from the transmission line (c) the voltage applied to the gun diode for a charging voltage of *50kV* per capacitor on the Marx-bank.

The distortion seen in Figure 7.10a was most likely due to coupling between the diagnostic and the noise signal of the closing spark-gaps of the Marx-bank. While this prevents determination of the exact magnitude and shape of the discharge pulse from the Marx-bank the diagnostic retains some merit (c.f. Appendix C). The most important consequence of these additional voltage diagnostics was the ability to fully monitor the evolution of the voltage pulse through the power supply, allowing for optimisation of the applied diode pulse for a range of different charging voltages on the Marx-bank capacitors. This is covered in detail in Appendix C.

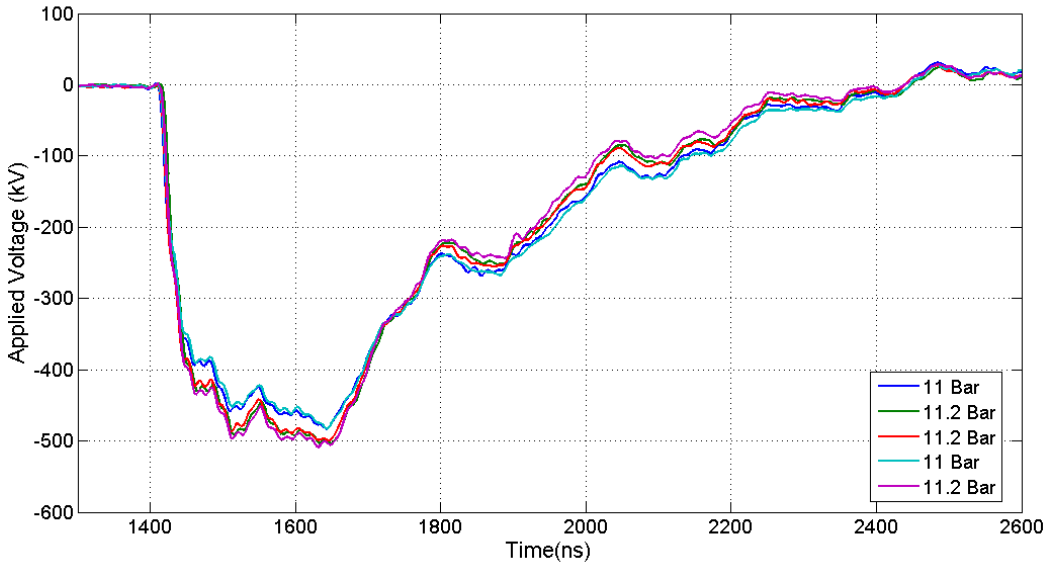

Figure 7.11: Shows the measured applied diode potentials for a set of four shots, with *50kV* charging voltage on the Marx-bank capacitors and *11-11.2bar* of pressure on the output spark-gap.

Figure 7.11 gives a sample of traces for a set of pulses with near identical operating parameters, the most notable variation being in the pressure of Nitrogen gas in the output spark-gap of the transmission line. From this a high degree of reproducibility between shots can be observed, with a slight increase in spark-gap pressure resulting in higher peak and average pulse voltages.

By monitoring the power supply performance on a pulse by pulse basis and following the procedures presented in Appendix C, the optimum diode voltage pulse, for a given Marx charging voltage, could be obtained.

7.4.2 Measurement of the Beam Current.

The electron beam current was measured using a current shunt, constructed across the plates of the integrated Rogowski coil on the drift tube outer conductor (c.f. Section 6.3.2.2.). As in the initial experiments a fair degree of reproducibility between shots was observed:

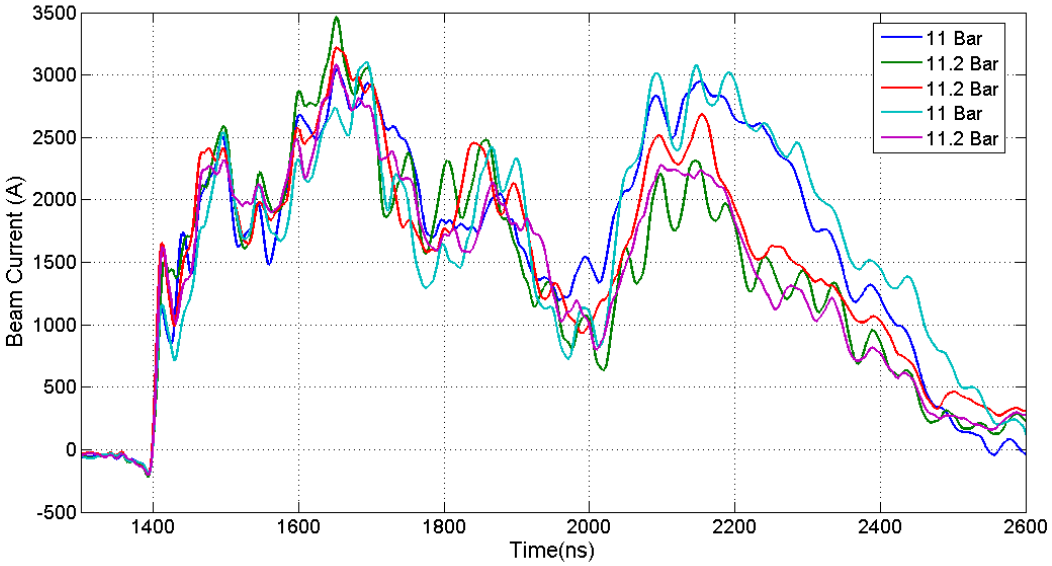

Figure 7.12: Shows the beam current traces, corresponding to the applied diode voltage traces shown in Figure 7.11.

Comparing the traces shown in Figures 7.3.2 and 7.4.2, the introduction of the anode insert, within the EEE gun diode, can be seen to have had the desired result of increasing the electron beam current, though to a slightly lower value than that predicted by KARAT (c.f. Section 4.2.1.2). This was attributed in part to an increased spread in $v_{\perp}$ of the beam electrons, resulting in a lower bulk v_z streaming velocity and so in the measured current. In line with this, an increased spread in $v_{\perp}$ could result in beam scrapping; incidence of the beam electrons on the conductor surface. As will be explained in Section 7.4.3 this was expected to occur, due to constraints placed on the maximum achievable B_0, and is likely to be the cause of the sustained high current observed throughout the duration of the current pulse, as the current measurement towards the end of the pulse would contain components from both the beam passing

through the current shunt diagnostic and from currents on the surface of the conductor surfaces caused by beam scrapping. It should be noted, that the change in sign of the measured signal, was the result of a change in the polarity of the terminals of the diagnostic between the two sets of experiments and does not indicate the presence of an ion, as opposed to electron, beam.

7.4.3 Measurement of the Output spectral Content and Pulse Power.

Through experimental investigation it was found that an applied diode voltage in the range $500–550kV$ was required to obtain proper coupling with the undulator field. This increase from the $\sim 450kV$, of the $1.5kA$ experiments, was attributed to a higher degree of electron transverse velocity spread, due to the increased beam current of $\sim 3kA$.

Under such conditions the action of the guiding magnetic field, in constraining the oscillating electrons, becomes of paramount importance in achieving efficient energy conversion between the electrons and the EM wave. The elongation of the high current region of the pulses shown in Figure 7.12 correspond to applied diode voltages in the region of $480kV$, indicated the requirement of a much stronger magnetic field for operation at the increased voltage of $550kV$. The maximum achievable guide magnetic field was found to be $\sim 0.62T$, limited by the maximum stable discharge of the guide solenoid's power supply ($\sim 14kV$ per capacitor).

While sufficient to provide transport of the electron beam into the interaction region, from the electron gun-diode (c.f. Section 4.2.1.2), this was expected to be insufficient to confine the radial motion imparted to the beam electrons by the undulator, resulting in a degree of incidence of the electron beam on the conductor surfaces (c.f. Section 4.3.3). With this in mind, the expected conversion efficiency (and so output power) from the FEM experiment was expected to show decreased performance when compared to the lower ($1.5kA$) beam current experiments. Investigation of the spectral content of the output microwave pulses was still however of interest, as even with a marked reduction in conversion efficiency, the FEL instability should still be

discernible as should excitement of parasitic modes within the cavity.Working with the guide solenoid field set close to is maximum value, with the charging voltage on the Marx-bank capacitors set at $55kV$ (required for ~$550kV$ on the diode) and the output spark-gap pressure set at $13.5\pm0.1Bar$, the undulator field was varied from 0 – $0.06T$, with the spectral content of the resultant pulses determined through the use of a heterodyne mixer crystal as opposed to the cut-off filter's used in the initial experiments.

Determination of the microwave pulse power was done concurrently with the measurement of the pulse spectrum, using the same Agilent 8474E detector crystals as in the initial experiments, with the total system power determined as in Section 7.3.4. Figures 7.13 - 7.16 show the detected microwave pulses for undulator fields of $0T$, $0.045T$, $0.05T$ and $0.052T$, respectively, giving the pulses in terms of the total output power. Figures 7.13 - 7.16 also show the "mixed" frequency signals and the recovered pulse spectra.

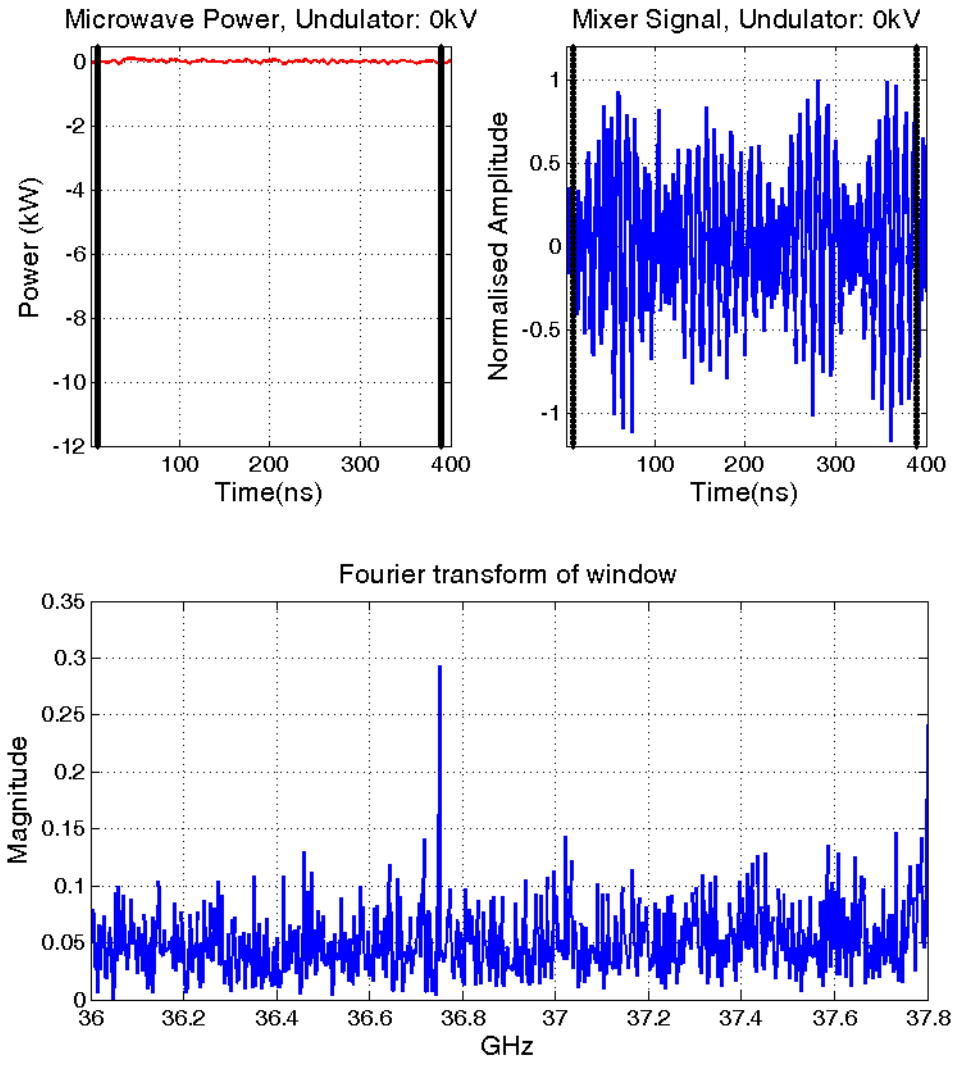

Figure 7.13: Shows the microwave pulse, mixer signal and resultant pulse spectrum for the 2D - 1D FEM operating with a guide magnetic field of *~0.62T* and an undulator field of *0T*. The applied diode voltage was *~550kV*, with the output spark-gap pressure set at *~13.5bar*. The vertical bars denote the window used in the Fourier analysis of the mixer signal.

It should be noted that the magnitude of the microwave pulse here lay close to the lower limit of that measurable by the detector crystal, hence the near flat response seen in Figure 7.13. The signal observed by the mixer crystal was subject to less attenuation, allowing for proper mixing of the RF and LO signals.

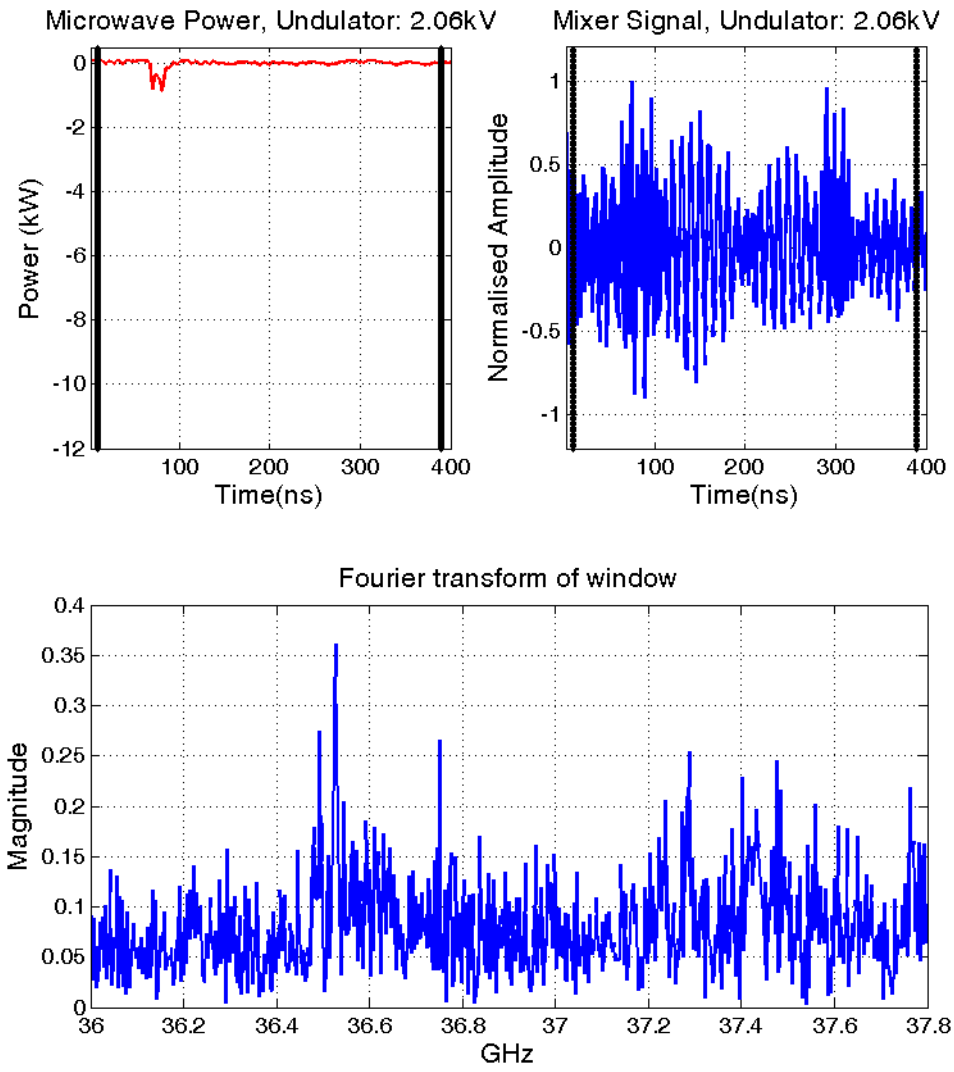

Figure 7.14: Shows the microwave pulse, mixed signal and resultant pulse spectrum for the 2D - 1D FEM operating with a guide magnetic field of *~0.62T* and an undulator field of *~0.045T*. The applied diode voltage was *~550kV*, with the output spark-gap pressure set at *~13.6bar*. The vertical bars denote the window used in the Fourier analysis of the mixer signal.

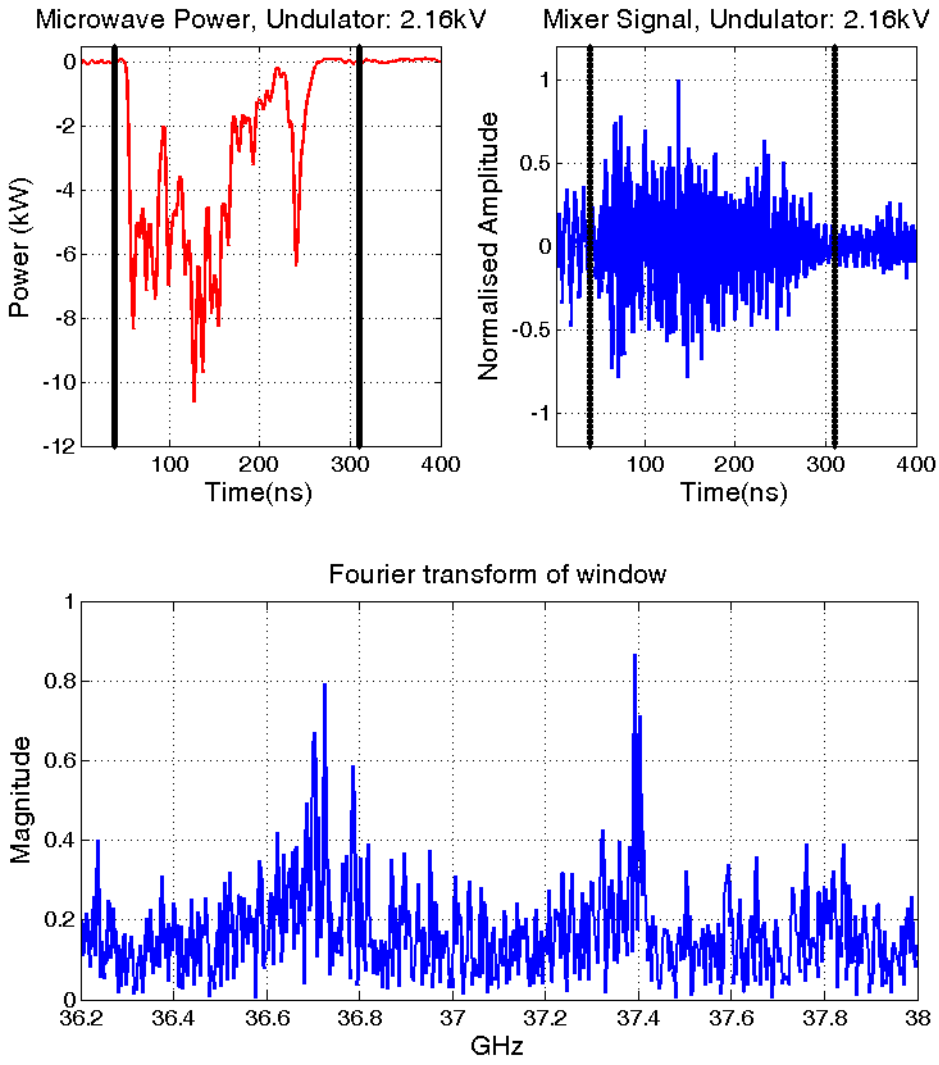

Figure 7.15: Shows the microwave pulse, mixed signal and resultant pulse spectrum for the 2D - 1D FEM operating with a guide magnetic field of *~0.62T* and an undulator field of *~0.05T*. The applied diode voltage was *~550kV*, with the output spark-gap pressure set at *~13.5bar*. The vertical bars denote the window used in the Fourier analysis of the mixer signal.

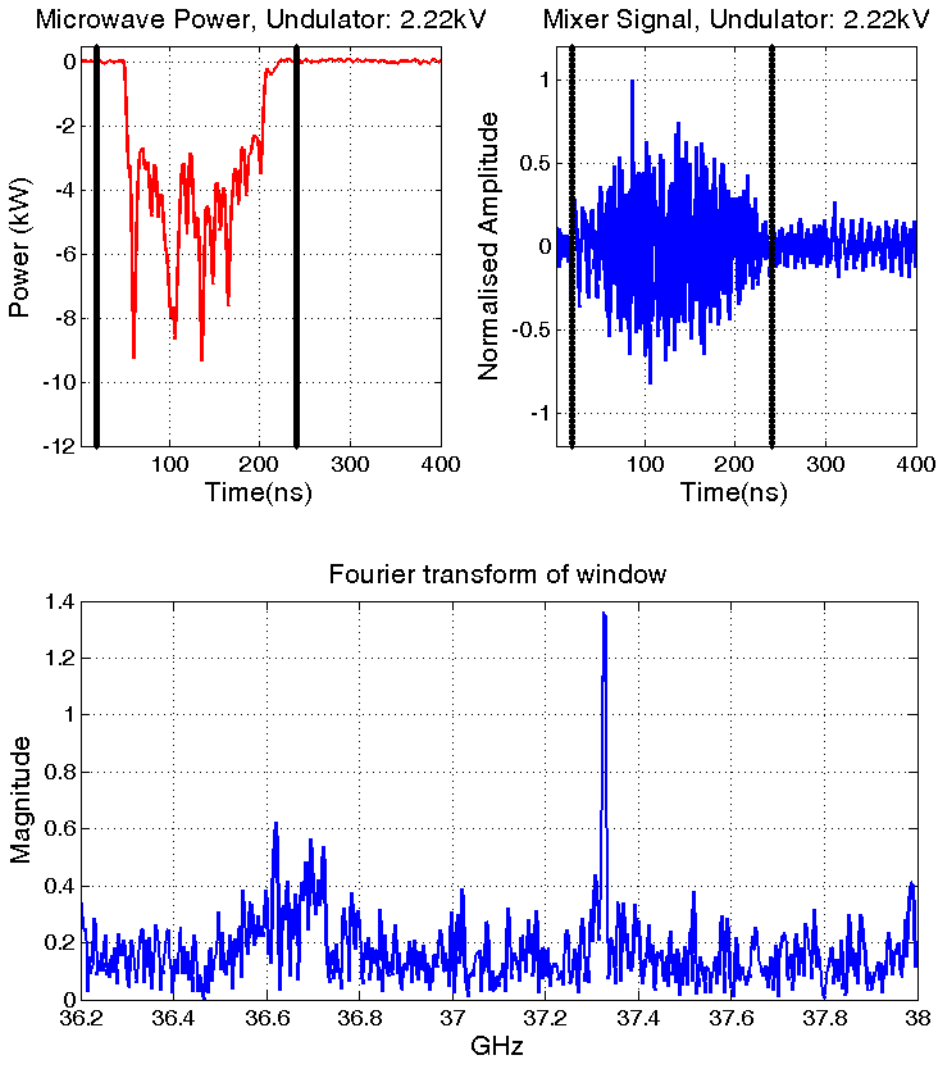

Figure 7.16: Shows the microwave pulse, mixed signal and resultant pulse spectrum for the 2D - 1D FEM operating with a guide magnetic field of *~0.62T* and an undulator field of *~0.052T*. The applied diode voltage was *~520kV*, with the output spark-gap pressure set at *~13.4bar*. The vertical bars denote the window used in the Fourier analysis of the mixer signal.

Looking at Figures 7.13 - 7.16 it can be seen that excitement of the FEL instability within the lasing cavity began for an undulator field strength of $\sim 0.045T$ and achieved resonance at a field strength of $\sim 0.052T$. For undulator field strengths in excess of $\sim 0.052T$ pulses such as those shown in Figure 7.13 were observed, indicating the undulator had moved out of resonance with the electron beam.

The maximum output power was measured to be in the region of $\sim 5-6kW$, as expected due to the reduced achievable guiding magnetic field strength. However it can be seen that, even with such a marked decrease in conversion efficiency, sufficient resonant coupling occurred to generate well defined spikes in the spectral content. At resonance (see Figures 7.15 & 7.16) the main resonant frequency, in the region of $37.4GHz$ coincides well with the expected output frequency of $37.5GHz$ for the 2D - 1D Bragg cavity, i.e. it corresponds to the resonant frequency of the 2D reflector for proper TEM - $TE_{24,2}$ operation. The spurious resonance at $\sim 36.7GHz$ shows some interesting behaviour and will be discussed below. Due to limitations on the bandwidth offered by the heterodyne measurement of the spectral content (c.f. Section 6.6), the excitement of the $HE_{2,2}$ eigenmode could not ascertained, however it's existence is expected and should lie in the region of $34GHz$ as in the $1.5kA$ experiments.

An interesting aspect to the lower resonance, at $36.7GHz$, is its presence when no undulator field is applied (see Figure 7.13). Typically this would indicate the excitement of a CARM interaction in the beam, however for a guide field strength of $\sim 0.62T$ and electron energies of $550keV$, the cyclotron frequency is $\sim 8.3GHz$. A more likely explanation for the presence of this resonance can be seen in relation to the theory presented in Section 3.3.1.2, where an overall deviation in the 1D periodicity of just $-0.06mm$ would be sufficient to place the first lower eigenmode solution at the frequency shown in Figure 7.13. If one assumes some degree of interaction between the EM noise generated by the electron beam (due to the increased transverse energy spread present in the higher current beam) and the lasing cavity, any enhanced region of the spectrum which lies close to one of the eigenmode solutions should appear defined above noise in the Fourier transform of the mixer signal.

As this resonance can be seen in each of Figures 7.13 - 7.16, with its magnitude growing as the undulator field strength is increased, this indicates further, that its presence is not due to a cyclotron interaction, as such a beam - wave interaction would not be enhanced by the lasing cavity and so would have a uniform (or degraded) magnitude as the dominant FEL beam-wave interaction became resonant.

If one now recalls the Fourier transforms of the output from the MAGIC simulations of the $1.5kA$ FEM (see Figures 4.19 - 4.20), resonant frequencies at integer values of $\pm 0.3GHz$ around the central Bragg resonance were observed, with those at $\pm 0.6GHz$ showing the greatest magnitude. For the experimental cavity the lower of these harmonics also falls in the region of the $\sim 36.7GHz$ resonance seen in Figures 7.13 - 7.16, which offers some explanation why the lower resonance is less well defined than the main resonance, as the undulator field is increased; it may be the result of two or more resonant processes operating at similar frequencies within the lasing cavity, such as interaction with the parasitic $m' = -1$ eigenmode of the 2D Bragg reflector (c.f. Section 3.4).

7.4.3.1 Spectral Evolution in the Microwave Pulses

In addition to offering precise measurement of the overall spectral content of the EM pulses, the use of a mixer crystal to resolve the wave-form of the microwave pulses, also allows for the temporal evolution of the pulse's spectral content to be analysed. Focusing on the pulses shown in Figures 7.15 and 7.16, changes in the spectral content were determined by reducing the analysis window to $\sim 50ns$ and stepping through the duration of the pulse, performing a Fourier analysis of the signal at each stage.

Detailed analysis of the pulse shown in Figure 7.15 is given in Figure 7.17. Here competition between the two resonant frequencies of $\sim 36.7GHz$ and $37.4GHz$ can be seen to favour the lower frequency resonance for the majority of the pulse, with the upper resonance only gaining dominance towards the end of the pulse, with the overall magnitude of both resonances summing to near equal magnitude (see Figure 7.15). This indicates that, while an undulator field strength of $0.05T$ was sufficient to engage

lasing in the 2D - 1D Bragg cavity, the intended, upper, cavity resonance was not preferentially coupled to, with mode competition clearly evident across the pulse.

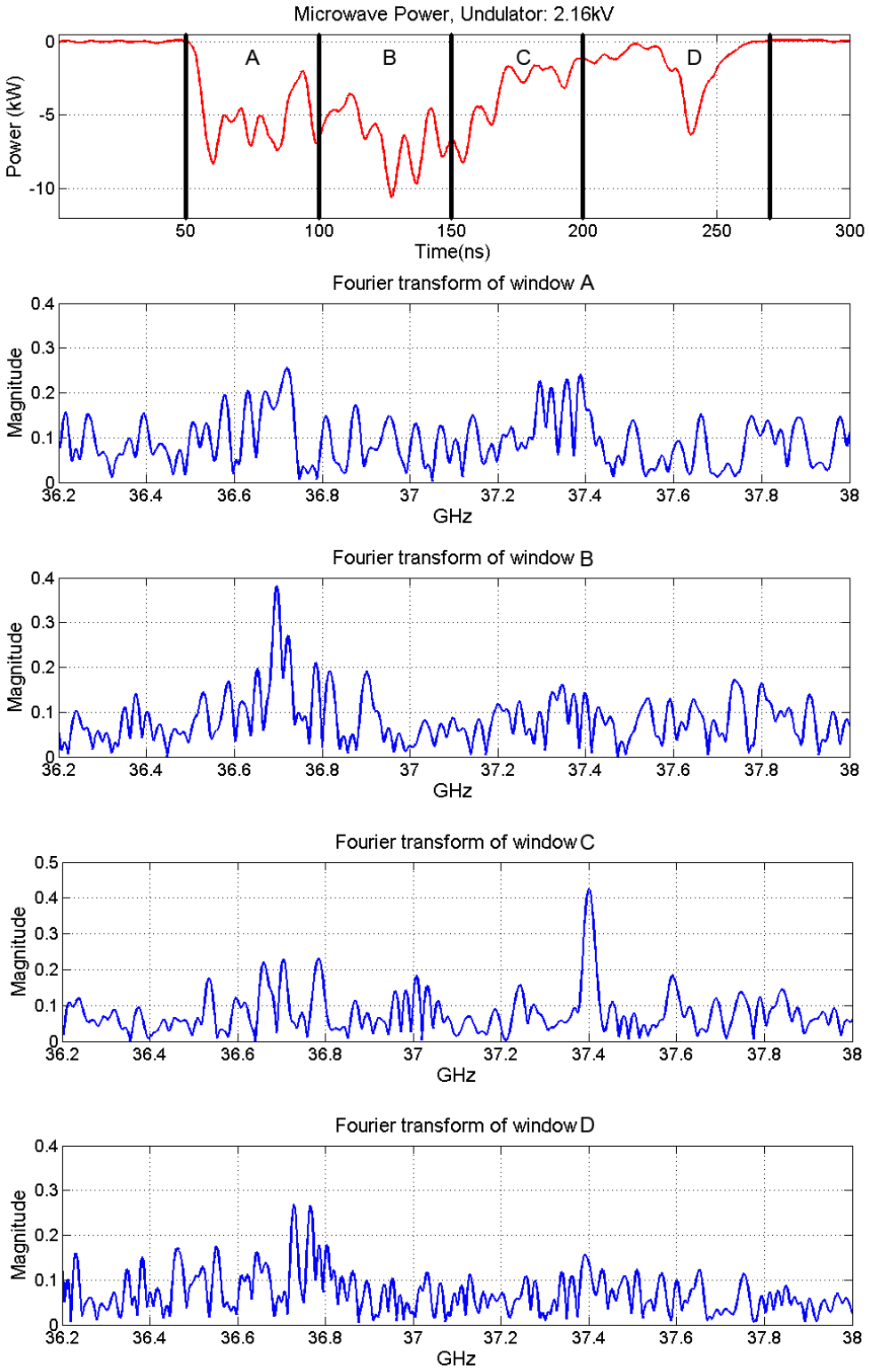

Figure 7.17: Shows the temporal evolution of the spectral content in the pulse shown in Figure 7.15.

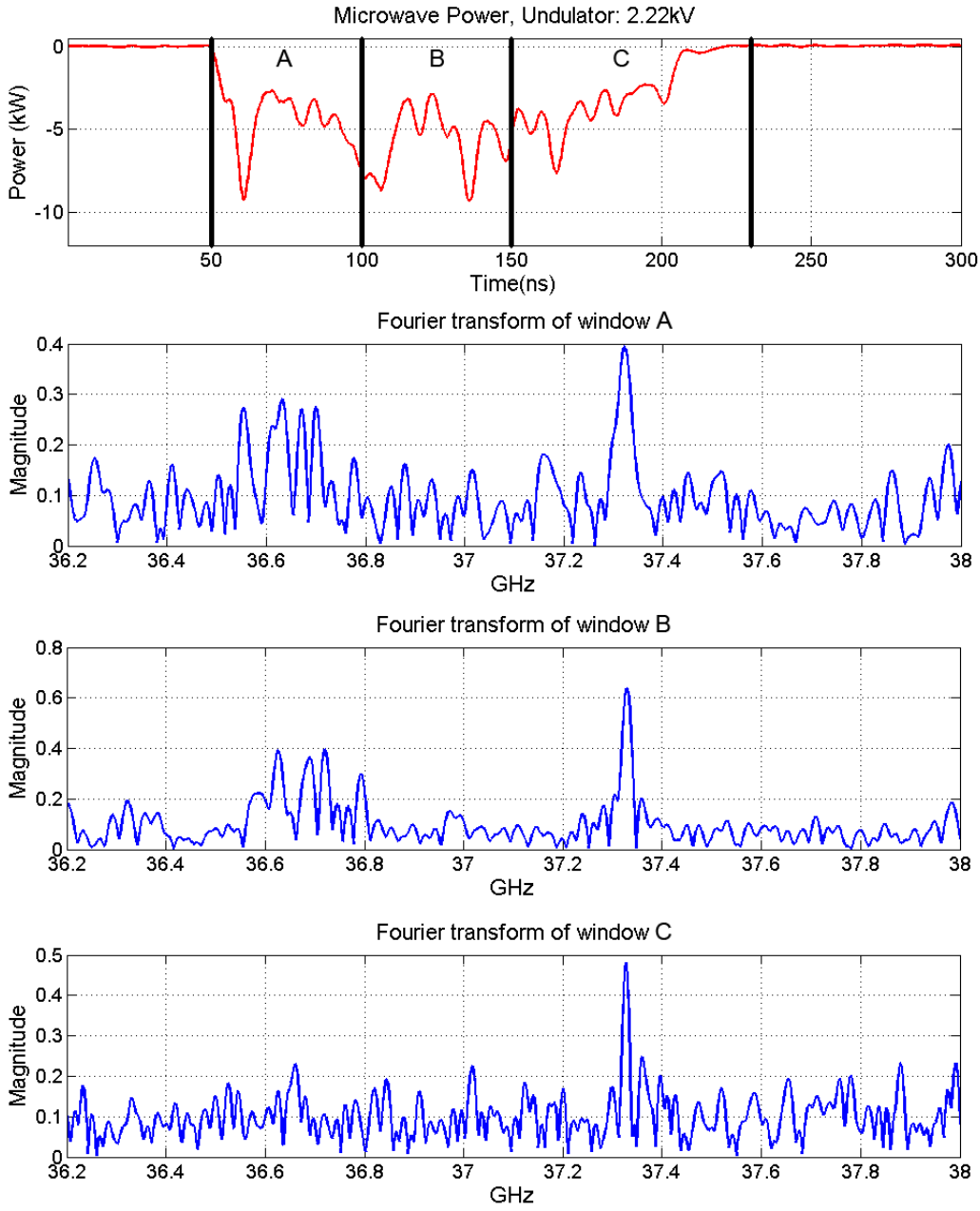

Figure 7.18: Shows the temporal evolution of the spectral content of the pulse shown in Figure 7.16.

Detailed analysis of the pulse shown in Figure 7.16 is given in Figure 7.18. Here the undulator field was increased slightly to $0.052T$, with the resultant microwave pulse showing a more defined shape of slightly shorter duration. It is clear, in this case, that the higher frequency resonance dominates throughout the pulse. As in Figure 7.17 both

the upper and lower resonances are present, to some degree, at the beginning of the pulse, however the upper resonance quickly shows preferential coupling with the electron beam as its magnitude grows throughout the pulse, while the magnitude of the lower resonance stays relatively constant. The slight reduction in the resonant frequencies from $37.4GHz$ and $36.7GHz$ to $37.4GHz$ and $36.6GHz$ was a consequence of the slight increase in the undulator field intensity, introducing a slight decrease in the beam - wave resonant wave-number.

7.5 Discussion of Results

The power supply of the 2D - 1D Bragg FEM experiment was shown to operate in a highly reproducible manner in both stages of the experiment, in terms of the capability of generating a known response at the output of the transmission line, for a given charging voltage on the Marx-bank capacitors. The Marx-bank and transmission-line diagnostics were used to optimise voltage pulse applied across the electron gun-diode, achieving an output power of $60MW(\pm 10\%)$ in the $1.5kA$ experiments. Such optimisation of the power supply, using these diagnostics, had the added advantage of reducing the risks of reflected pulses from the transmission line damaging the Marx-bank.

In the $1.5kA$ experiments, the Rogowski coil diagnostic used to measure the electron beam current resulted in a relatively uniform value for the calculated gun perveance, indicating both the validity of the diagnostic and the uniformity of the axial electron energy across the beam (i.e. the measured current agrees well with that of the relatively mono-energetic electron beam simulated using KARAT). In the $3kA$ experiments an insufficiently strong guiding magnetic field may have contributed to a distortion between the expected beam current performance and that measured in the experiment. The high current noted in what would correspond to the low energy tail of the microwave pulse (compare Figures 7.3 & 7.4 with Figures 7.11 and 7.12) may result from a sizable portion of the electron beam impacting on the outer drift tube wall, causing an erroneous rise in the measured current. Should this prove to be the case, the

reduced beam current propagating through the drift tube may be the cause for the reduced output power observed in the $3kA$ experiments.

Experimentally this issue should be resolvable. The maximum magnetic field obtainable from the guide solenoid was limited to ~$0.62T$ by the requirement to keep the charging voltage on the capacitive power supply $\leq 14kV$. This constraint was the result of a "rise" observed in the ground plane when the solenoid circuit was discharged, which was sufficient to trigger the Marx-bank trigger circuit, discharging the Marx out-of-synch with the timing circuit and preventing proper operation of the experiment. With suitable isolation between the two circuits the guide solenoid should be able to operate up to ~$0.8 - 1T$ (Konoplev 2001), which may prove sufficient to confine the higher current ($3kA$) electron beam.

Alternatively, the introduction of the anode reducing insert in the EEE gun may have introduced instabilities in the electron beam, due to the increased risk of self-field effects in what is essentially an increased density plasma. In this case the removal of the reducing bull, coupled with the improved optimization techniques used on the power supply, should result in the recovery of microwave output powers in excess of $100MW$. Improvement beyond the $60MW$ output power of the $1.5kA$ experiments should be readily achievable in either case.

In regards to the spectral content of the microwave pulses, it is reasonable to regard the two resonances observed in the $1.5kA$ experiments as being associated with the cavity resonances generated by the TEM - $TE_{24,2}$ ($m' = 0$) and parasitic $HE_{2,2}$ ($m' = -2$) eigenmodes of the 2D Bragg reflector, for the upper and lower frequency resonance respectively; the relative separation between the two resonances corresponds well with the expected separation of $3 - 4GHz$ between these two potential resonances.

Looking at the spectral content of the microwave pulses in the $3kA$ experiments, the proximity of the two resonant frequencies indicates that while the upper resonance at ~$37.4GHz$ is most likely due to the TEM-$TE_{24,2}$ operation in the 2D reflector (corresponding well with the estimated $37.5GHz$), the lower resonance is most likely

the result of emission from the first, lower, eigenmode solution of the $m' = 0$ eigenmode of the 2D Bragg reflector, coupled with some degree of excitation of the parasitic $m' = -1$ eigenmode of the reflector. The roots of this spurious resonance may prove inconsequential in future work, as it can be seen in Figures 7.16 and 7.18 that the intended resonance at $\sim 37.5 GHz$ can be preferentially coupled to the electron beam with proper selection of the guide and undulator field strengths.

Chapter 8: Conclusions and Future Work.

8.1 Introduction.

The work presented in this thesis described the theoretical basis for, and numerical modelling of, a high-power co-axial FEM experiment based on a novel 2D - 1D Bragg lasing cavity. This was followed by the construction and experimental investigation of such an FEM, utilising two different electron beam sources to drive the FEM interaction. This chapter brings together the results of the theoretical (c.f. Section 8.1.1), numerical (c.f. Section 8.1.2) and experimental (c.f. Section 8.1.3) investigations, drawing comparisons and conclusions between all three. The chapter concludes with a look to future work, both for the 2D - 1D Bragg FEM experiment and to work utilising the novel aspects offered by 2D Bragg structures in general (c.f. Section 8.2).

8.1.1 Model and Basic Equations.

The aim of the preceding work was to design, build and experimentally measure the performance of a FEM based on a high-current electron beam and a 2D - 1D Bragg lasing cavity. From previous work on purely 2D Bragg lasing cavities it was expected that the fundamental resonant frequency of the 2D reflector would set the operating frequency of the 2D - 1D Bragg lasing cavity, enabling the generation of monochromatic, high power microwave pulses in the region of $\sim 37.5 GHz$.

From previous simulation work it was known that the existing electron gun geometry could, potentially, produce beam currents in the region of $\sim 1.5 kA$ (Konoplev 2001) with modifications to the cathode geometry, though only $0.5 kA$ had been achieved (McGrain 2006). Beam currents of $\sim 1.5 kA$ from a modified EEE electron gun were achieved experimentally for the first time in this thesis. Taking an initial estimate of the beam density of $\sim 300 A/cm$, in line with Konoplev (2001), and using equations 2.11 and 2.12 the electron source was expected to place the operation of the FEM in the High-Gain Compton regime, allowing its description to follow similar theory to that of the Low-Gain Compton regime. An increase in the beam current by roughly a factor of two ($\sim 3 kA$) was expected to result in a corresponding increase in the beam current density to $600 - 700 A/cm$, assuming a similar degree of radial spread in the beam (Δr). This was considered sufficiently low to maintain the assumption of High-Gain Compton operation, with any increased spread in Δr resulting in a decrease in the density.

For emission at the desired frequency of $\sim 37.5 GHz$ ($\lambda = 8 mm$), from the fundamental TEM mode of the co-axial drift-tube, a bulk streaming velocity of $\beta_z \approx 0.8$ was estimated, corresponding to electron energies of $\sim 450 keV$. This gave the initial design parameters for the FEM current source; that it should provide a highly mono-energetic (low spread in β_z) $\sim 450 keV$ electron beam with beam currents of $\sim 1.5 kA$ and $\sim 3 - 4 kA$ for the different stages of the 2D - 1D Bragg FEM experiment.

Confinement of such high current electron beams, even with the reduced beam densities offered by the over-sized nature of the FEM experiment, requires the

inclusion of an axial guiding magnetic field, to constrain the radial movement of the electrons and so prevent incidence of the beam on the conductor surfaces. The magnitude of this axial field was set such that both the resultant cyclotron and Weibel frequencies were far removed from the operating FEM frequency, to reduce the likelihood of competition between the respective beam instabilities. A guide magnetic field strength of $\sim 0.6T$ was selected, as this provides sufficient constraints to the radial electron motions while placing the spectral locations of the cyclotron and Weibel instabilities as distinctly separate from the FEL instability. With B_0 set at $0.6T$ equation 2.7 was used to estimate the required undulator field strength to induce the FEL instability in the region of $\sim 37.5GHz$. This was determined to occur in the region of $0.06 - 0.067T$, roughly 10% of the guiding magnetic field strength.

The existence of an additional beam instability, the Lowbitron instability, was considered due to the similarity between the undulator employed here and that theorised in the Lowbitron design. Interference from Lowbitron-driven emission in the electron beam was considered to be unlikely due to the low spread expected in $v_\perp$ placing the Lowbitron frequency at the relatively high frequency range of $80 - 90GHz$, well above the operational range of the FEM.

In estimating the parameters for the lasing cavity the main points considered were:

- The mean dimensions of the co-axial drift-tube (waveguide)
- The corrugation parameters of the 1D and 2D Bragg reflectors (corrugation amplitude and axial / azimuthal periodicity).
- The possible excitement of parasitic resonances due to the oversized nature of the interaction region.

Using equations 3.16a-3.16b - 3.19 it was determined that an oversized co-axial waveguide with mean radii of $a_0 = 30mm$ and $b_0 = 40mm$ (for the inner and outer conductor surfaces respectively) would result in the positioning of the cut-off frequency of the $TE_{24,2}$ mode at $\sim 37.5GHz$, with a variation of $\pm 2\%$ in this value for $a_0, b_0 \pm 0.5mm$. This modal cut-off was important, as the operating frequency of the FEM depends not only on proper matching of the electron beam-energy to the

undulator field strength, but also to the correct matching of the operating TEM mode ($m_a = 0$) to a higher-order mode satisfying the Bragg resonance conditions within the 2D Bragg reflector. Given that the axial periodicity of the 2D Bragg reflector was to be $8mm$ and for proper operation $h_z \approx h_s$ (where $h_s = M/r_0$ is the azimuthal wave-number) the 2D corrugation should have $M = 24$ when positioned on the inner conductor surface, as would be the case in the physical experiment (if positioned on the outer conductor surface, to maintain $h_z \approx h_s$, $M = 28$).

For operation with the TEM mode this sets the required higher-order mode as requiring $m_b = 24$, which is satisfied by the $TE_{24,2}$ mode. As this mode coupling occurs at (or near) $k_{cTE_{24,2}}$ back-scattering would occur from the higher-order mode at ~90^0 to the incidence angle, allowing for the production of a phase-locked-loop across the azimuth of the Bragg lattice, producing a phase-stable reflected wave back into the interaction region. In the ideal case this should allow for enhancement of the phase stability of the oscillator and so in the resultant microwave pulse.

Due to the over-sized nature of the interaction region, the possible excitement of nearby parasitic cavity resonances was also considered, specifically those generated by the TEM-$TM_{0,1}$ eigenmode of the 1D-Bragg reflector and the $m' = \pm 1, \pm 2$ eigenmodes of the 2D Bragg reflector. It was considered likely that some degree of parasitic excitation would occur, given the relatively high-order longitudinal mode of the desired cavity resonance (~TEM_{150}), however preferential coupling to the operating mode should be achievable via proper matching of the magneto-optics to the bulk streaming velocity of the electron beam (i.e. the mean electron energy).

8.1.2 Numerical Modelling of the FEM.

Numerical modelling of the 2D - 1D Bragg FEM experiment was used to design and estimate the performance of two separate electron-gun geometries and a single 2D - 1D Bragg lasing cavity. The gun geometries were modelled using the 2.5D PiC code KARAT, while the interaction of the resultant electron beams with a 2D - 1D Bragg lasing cavity were modelled using the fully 3D PiC code MAGIC.

Working from the analytic estimations, two electron gun geometries were modelled with the aim of creating current sources of $\sim 1.5kA$ and $\sim 3.5kA$, both with $\beta_z \approx \beta \approx 0.8$, i.e. electron energies of $450keV$ with a low velocity spread. A $\sim 1.3kA$ beam was achieved by constructing a model of the existing electron gun and optimising the cathode geometry. An axial magnetic field strength of $0.6T$ was determined to be sufficient to constrain radial spread in the electron beam to $\sim 2mm$ with no incidence of the beam on either conductor surface of the drift-tube. For an applied diode potential of $450kV$ the resultant electron energies were $450keV(\pm 7\%)$ with $\beta \cong \beta_z \cong 0.8$ and a diode perveance of $4.3(\pm 0.1)\mu P$.

Increasing the beam current by decreasing the axial separation of the diode electrodes was discounted, as previous experimental experience had shown this to provide a maximum achievable beam current of $\sim 2.2kA$, below the target value of $3-4kA$. Rather the radial separation between the cathode stalk and the anode-can was varied, with the required performance observed with the anode-can radius reduced to $6cm$ (down from $14.5cm$). An axial guide magnetic field of $0.6T$ was again found to be sufficient to confine the electron beam at a radial thickness of $\sim 2mm$ with $\beta_z \approx \beta \approx 0.8$ albeit at a slightly depressed potential of $445keV(\pm 5\%)$. The gun perveance was estimated to have increased to $\sim 11.5(\pm 0.3)\mu P$.

The 2D - 1D Bragg lasing cavity was then simulated using the FDTD PiC code MAGIC, using identical cavity geometries for simulations of $\sim 1.5kA$ and $\sim 3kA$ driving currents in the FEM. Due to the constraints imposed by the available computational hardware, at the time of this work, modelling of the full geometry of the 2D - 1D Bragg cavity was not achievable. However, under the assumption of azimuthal symmetry in the resonant mode profiles, the ability of MAGIC to model a 3D cross-section of a single azimuthal period's width of the lasing cavity was exploited in order to obtain estimates of the full cavity performance. Such quasi-2.5D simulations could be completed in $\sim 10-15$ days.

In the case of the $1.5kA$ simulations a guide magnetic field strength of $0.6T$ was found to be sufficient to prevent radial spread of the undulating electrons causing incidence

on the conductor surfaces, without causing distortion to the undulations of the beam. The insertion of an electron beam with energies of $\sim 460keV$ through an undulator field of 10% of B_0 ($B_u = 0.06T$) was found to result in the generation of a strong resonance with the TEM_{100} cavity mode, as expected for the modelled cavity length of $40cm$ and an operating resonance of $\sim 37.5GHz$. The output power was estimated to be $\sim 140MW$ with the desired operating mode, dominating the emission spectra. Some excitation of the Weibel instability and an $HE_{2,2}$ eigenmode were ascertained, but both were at sufficiently low amplitudes to be considered as negligible when compared to the operating mode.

In the case of the $\sim 3kA$ simulations B_0 had to be increased to $1.2T$ to prevent impact of the undulating electron beam on the conductor surfaces. Maintaining the B_0/B_u relation of $B_u = 0.1B_0$, best performance was observed for an electron beam with energies of $\sim 460keV$, with an increase in the output power to $\sim 190MW$. There was however an increase in the noise level, attributed in part to the excitement of a broad-band Lowbitron-like interaction, resulting from the increased spread in $v_\perp$ and to the perturbed oscillations of the electron-beam due to the increased B_0 field. Investigation of the emission spectra show increased competition between the fundamental cavity resonance at $\sim 37.5GHz$ and the parasitic $HE_{2,2}$ mode, with both showing relatively similar amplitudes.

Through the course of these numerical investigations it was ascertained that quasi-single mode operation should be achievable at least in the case of the $1.5kA$ FEM, provided proper selection of operating parameters. The higher current FEM was expected to show mode competition with the lower frequency HE2,2 eigenmode, generated in the 2D Bragg reflector, however it was expected that some degree of preferential coupling to the desired TEM operating mode should be achievable with careful control of B_u. Direct competition between the FEL, lowbitron, Weibel and cyclotron instabilities was considered unlikely due to the relative spectral position of each, though the generation of an increased level of noise in the $\sim 3kA$ FEM was expected. The modelled energy extraction efficiencies were $\sim 20\%$ and $\sim 14\%$ for the $1.5kA$ and $3kA$ FEM's respectively. The experimental values were expected to be

approximately $50-60\%$ of that simulated in each case, indicating efficiencies of $\sim 10\%$ for the $1.5kA$ FEM and $\sim 7\%$ for the $3kA$ FEM.

8.1.3 Experimental Results from the 2D - 1D Bragg FEM.

The 2D - 1D Bragg FEM experiments were carried out in two stages, the first using an electron beam source which provided $\sim 1.4-1.7kA$ and electron energies in the range $430-450keV$. The second current source provided $\sim 2-3kA$ at electron energies of $440-500keV$. In both cases a high degree of reproducibility between shots was observed, with variation being on the order of a few percent.

The experimental lasing cavity parameters remained largely unchanged throughout the course of 2D-1D Bragg experiments. The $1.5kA$ lasing cavity was defined by a $10cm$ long ($8mm$ period) 2D Bragg reflector and a $15cm$ long ($4mm$ period) 1D Bragg reflector, separated by a $60cm$ long section of smooth co-axial waveguide. For the $\sim 2-3kA$ FEM the 1D mirror was shortened by $4mm$ (1 period) while the 2D mirror length was increased by $4mm$ ($1/2$ period), with the reflector separation (and over-all system length) left unchanged. In all cases the corrugation amplitudes were $\pm 0.8mm$ for the 2D Bragg reflector and $\pm 0.5mm$ for the 1D Bragg reflector.

For the $\sim 1.5kA$ FEM, best performance was observed for an electron beam with energies of $\sim 440keV$ (and a beam current of $\sim 1.5kA$), propagating in a combined magnetic field of $B_0 \cong 0.56T$ and a $B_u \cong 0.063T$. This generated a $\sim 150ns$ long microwave pulse at $60MW(\pm 10\%)$ corresponding to a conversion efficiency of $\sim 10\%$, or $\sim 10J$ of energy in the pulse. The spectral content was determined to lie between $34.7-39.9GHz$ using high-pass cut-off filters. When this experiment was repeated with a similar value electron beam, but with $B_0 = 0.6T$ and $B_u = 0.06T$, it was shown that the $HE_{2,2}$ mode was excited, along with the fundamental operating mode, resulting in a degree of mode competition at the beginning and end of the microwave pulse. The fundamental operating mode was, however, seen to dominate for the bulk duration of the pulse.

In the higher $\sim 2-3kA$ experiments, proper confinement of the electron beam was unattainable due to restrictions imposed on the operation of the guide-solenoid circuit, limiting the maximum achievable magnetic field strength to $\sim 0.62T$. This resulted in a marked decrease in the conversion efficiency and so in the output microwave power, as the majority of the beam was suspected to have impacted on the conductor surfaces. A sufficient portion remained, however, to excite the FEL instability within the interaction region, as evidenced by the results obtained using the heterodyne measurement technique (described in Section 6.6 and applied in Section 7.4.3). From these the expected resonance at $\sim 37.5GHz$ was clearly observed, along with a parasitic resonance at $\sim 36.7GHz$, corresponding well with the position of the $m' = -1$ eigenmode of the 2D Bragg reflector and the first, lower pass-band, of the 1D Bragg reflector assuming a slight detuning of $\sim 0.1mm$ (see Figure 3.11). This would allow for the almost delta-function like spike seen in Figure 7.13 and the obvious resonant behaviour seen in Figures 7.14-7.16. The fixed relative position of this spike to the operating mode, as one varies the undulator field strength, lends weight to the conclusion that the spikes are related and that the lower frequency spike is not associated with the Weibel instability, as this would tune with B_0 rather than B_u.

Investigation of the influences of the undulator field, on the excitement of these two modes, show that the fundamental mode can be preferentially coupled, with tight control of the operating parameters. Best performance in this case was measured for $B_0 \cong 0.62T$, $B_u \cong 0.052T$, $V \cong 520keV$ and $I \cong 2.5kA$. This produced a $\sim 130ns$ microwave pulse at $\sim 6kW$.

While this is notably lower than the $60MW$ measured for the $1.5kA$ FEM experiments, this should be viewed in context with the reduced magnetic field confinement from that estimated as required for proper operation of the high-current experiment. High power outputs of $\geq 60MW$ are expected to be recovered in future experiments, via increased isolation of the solenoid supply from the Marx-bank circuit, allowing the full $1T$ of the guide field to be employed.

8.2 Future work.

8.2.1 Future of the 2D - 1D Bragg FEM Experiment.

The future investigation of the 2D - 1D Bragg FEM experiment can be summarised in the following stages:

Firstly the anode insert, used to boost the electron beam-current, should be removed from the electron gun, allowing the recovery of high power operation within the limits imposed by the maximum axial guide-field strength. The spectral content of these higher power microwave pulses should then be investigated using the heterodyne technique employed in the $2 - 3kA$ FEM experiments, allowing characterization of the spectral evolution of pulses with time. This should allow for tighter analysis of the modal content and determination of the correct operational parameters to achieve single mode operation and so higher conversion efficiencies, leading to increases in the output power.

With this achieved the next step would be to modify the 2D - 1D Bragg lasing cavity to more correctly approximate that modelled for the optimised case presented in Section 4.3.2. Improved isolation of the guide solenoid and Marx-bank circuits would be implemented at this stage. The $1.5kA$ experiment would then be repeated with the expectation of further improved conversion efficiencies $(15 - 20\%)$ and output powers in excess of $100MW$.

The anode insert would then be replaced and the $2 - 3kA$ experiment repeated with the new 2D - 1D Bragg cavity and a more appropriate axial magnetic field strength $(0.8 - 1T)$. This should allow for sufficient beam confinement to generate high power microwave pulses from the lasing cavity, though the conversion efficiency would be likely to be on the order of $5 - 10\%$. The 2D - 1D Bragg cavity would then be altered to reflect that of an optimised cavity, modelled using the PiC code MAGIC. Initial results from simulation show that a reduction of the reflector separation to $20cm$ should allow for the excitation of the FEL instability within the lasing cavity, with the

spectral content of the output pulse shown to be monochromatic, albeit at a slightly upshifted frequency of $\sim 39 GHz$ (See Figure 8.1).

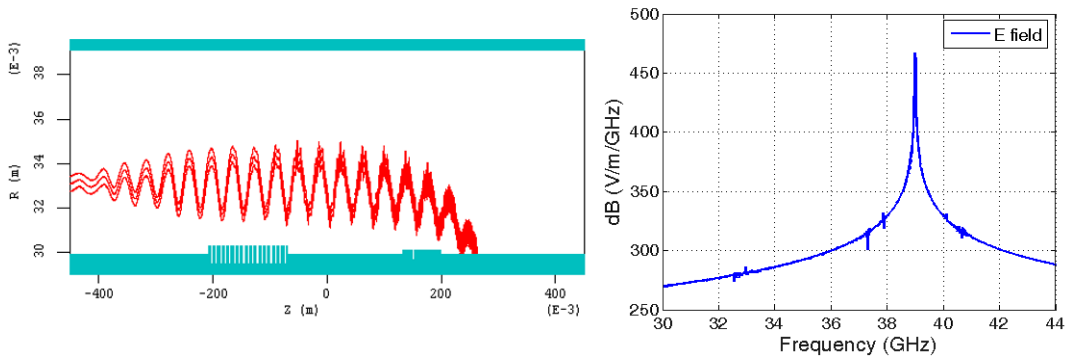

Figure 8.1: Shows a cross-section of a 2D - 1D Bragg lasing cavity with the reflector separation reduced to *20cm*. The Fourier transform of the output microwave pulse is provided.

The mechanism resulting in this spectral shift is under investigation, though resonance with the 2D and 1D Bragg reflectors appears self-evident. The expected conversion efficiency for the case shown is $\sim 8\,\%$, with output powers expected in the region of $120 MW$.

8.2.2 Further Applications for 2D Bragg Resonant Structures

In addition to their application as finite bandwidth reflectors, 2D Bragg structures may also be used as resonant cavities in their own right, with the boundary conditions of the cavity ascribed to either end of the corrugation. Such, relatively simple, structures are easily scalable in size (and so frequency) allowing their application into the so-called Terahertz-gap ($\sim 0.1 - 10 THz$) where few sources of EM generation exist. Due to the phase stability and mode selectivity, offered by 2D Bragg structures, even when over-sized, high power ($> 100 kW$) EM sources should be achievable in the range of $100 - 200 GHz$, with $> 10 MW$ estimated at frequencies of $\sim 80 GHz$.

References

Agafonov M. A., Arzhannikov A. V., Ginzburg N. S., Inanenko V. G., Kalinin P. V., Kuznetsov S. A., Peskov N. Yu., Sinitsky S. L., 1998. Generation of Hundred Joules Pulses at 4-mm Wavelength by FEM with Sheet Electron Beam. *IEEE. Trans. on Plasma Sci.*, **26**(3), pp.531-535.

Agafonov M. A., Arzhannikov A. V., Ivanenko V. G., Kalinin P. V., Kuznetsov S. A., Sinitsky S. L., Ginzburg N. S., Peskov N. Yu., 1997. Super-power Generator of mm-Waves Driven By Microsecond Sheet Beam. *11th IEEE International Pulsed Power Conference - Digest of Technical Papers*, **vol1-2**, pp.121-126

AgarinN., V., Arzhannikov A. V., Bobylev V. B., Ginzburg N. S., Ivanenko V. G., Kalinin P. V., Kuznetsov S. A., Peskov N. Yu., Sergeev A. S., Sinitsky S. L., Stepanov V. D., 2000. First Operation of a Powerful FEL with Two-Dimensional Distributed Feedback. *Nuclear Instruments and Methods in Physics Research A,* **445**, pp. 222-229.

Agilent Technologies, 2002. *Coaxial GaAs Microwave Detectors - 0.01 to 50GHz Data Sheet.* Available online at: http://cp.literature.agilent.com/litweb/pdf/5952-0801.pdf

Aitken P., McNeil B. W. J., Robb G. R. M., Phelps A. D. R., 1998. A Comparison of the FEL and CRM Operating Simultaneously at Two Resonant Frequencies. *Nuclear Instruments and Methods in Physics Research A*, **407**, pp. 136-140.

Anritsu 1996. *Series 373XXA Vector Network Analyser Operations Manual*. Distributed by Anritsu with VNA.

Antonsen T. M. Jr., Levush B., 1989. Mode competition and Suppression in Free-Electron Laser Oscillators. *Phys. Fluids B,* **1**(5), pp.1097-1106.

Arzhannikov A. V., Bobylev V. B., Sinitsky S. L., Tatasov A. V., Ginzburg N. S., Peskov N. Yu., 1995. Ribbon-FEL Experiments at One-Dimension Distributed Feedback. *Nuclear Instruments and Methods in Physics Research A*, **358**, pp.112-113.

ATK Mission Systems, 2004. *MAGIC User's Manual*. Available online: http:// www.mrcwdc.com/magic/FormsPDF/MagicManual.pdf

Balkcum A. J., McDermott D. B., Phillips R. M., Lin A. T., Luhmann N. C. Jr., 1996. 250-MW X-Band TE01 Ubitron Using a Coaxial PPM Wiggler. *IEEE Trans. on Plasma Sci.*, **24**(3), pp.802-807.

Balkcum A. J., McDermott D. B., Phillips R. M., Lin A. T., Luhmann N. C. Jr., 1998. High-Power Coaxial Ubitron Oscillator: Theory and Design. *IEEE Trans. on Plasma Sci.*, **26**(3), pp.548-555.

Barker R. J. & Schamiloglu E., 2001. *High-Power Microwave Sources and Technologies*. New York: IEEE Press.

Bekefi G., Fajans J., 1985. Comments on "Study of Gain Bandwidth and Tunability of a Millimeter-Wave Free Electron Laser Operating in the Collective Regime" [Phys. of Fluids, 26, 1683, 1985]. *Phys. of Fluids*, **28**(10), p. 3177.

Bekefi G., Hartemann F., Kirkpatrick D. A., 1987. Temporal evolution of beam emittance from a field-emission electron gun. *J. Appl. Phys.*, **62**(5), p.1564.

Benford J., Swegle J. A., 1992. *High-Power Microwaves*. Norwood (MA): Artech House Inc.

Benson H., 1996. *University Physics Revised Edition.* USA: John Wiley & Sons.

Billardon M., Elleaume P., Ortega J. M., Bazin C., Bergher M., Velghe M., Deacon D. A. G., Petroff Y., 1985. Free Electron Laser Experiment as ORSAY - A Review. *IEEE Journal of Quantum Electronics*, **21**(7), p.805.

Birdsall C. K., Brewere G. R., Haeff A. V., 1953. The Resistive-Wall Amplifier. *Proceedings of the I.R.E 1953*, pp. 865 - 875.

Bloess D., Kamber I., Riege H., Bittner G., Bruckner V., Christiansen J., Frank K., Hartmann W., Lieser N., Schultheiss Ch., Seebock R., Steudtner W., 1983. The Triggered Pseudo-Spark Chamber as a Fast Switch and as a High-Intensity Beam Source. *Nuclear Instruments and Methods in Physics Research*, **205**(1-2), pp. 173-184.

Bonifacio R., 1997. High Gain Free Electron Laser with Waveguide. In Cairns R. A. (ed.) & Phelps A. D. R. (ed.) *Generation and Application of High Power Microwaves*. London: SUSSP Publications, IOP Publishing. pp 29 - 56.

Boxman R. L., 1983. A Model of the Multicathode-Spot Vacuum Arc. *IEEE Trans. Plasma Sci.*, **PS-11**(3), p. 138.

Bracewell R. N., 1947. Charts for Resonant Frequencies of Cavities. *Proc. of the IRE*, **35**(8), pp. 830-841.

Bratman V. L., Denisov G. G., Ginzburg N. S., Petelin M. I., 1983. FEL's with Bragg Reflection Resonators: Cyclotron Auto-resonance Masers Versus Ubitrons. *IEEE Journal of Quantum Electronics*, **QE19**(3), p.282.

Bratman V. L., Denisov G. G., Kol'chugin B. D., Samsonov S. V., Volkov A. B., 1996. High Efficiency CARM. *Nuclear Instruments and Methods n Physics Research A*, **375,** p. 360.

Bratman V. L., Denisov G. G., Ofitserov M. M., Samsonov S. V., Arkipov O. V., Kazacha V. I., Krasnykh A. K., Perelstein E. A., Zamril A. V., 1992. Cyclotron Autoresonance Maser with High Doppler Frequency Up-Conversion. *International Journal of Infrared and Millimeter Waves*, **13**(12), p. 1857.

Burt G., 2004. *Sweep-Frequency Microwave Pulse Compression Using a Helically Corrugated Waveguide*. University of Strathclyde, Ph. D. thesis.

Burt G., Samsonov S. V., Ronald K., Denisov G. G., Young A. R., Bratman V. L., Phelps A. D. R., Cross A. W., Konoplev I. V., He W., Thomson J., Whyte C. G., 2004. Dispersion of Helically Corrugated Waveguides: analytical, numerical and Experimental Study. *Phys. Rev. E*, **70**(4), article: 046402.

Chu T. S., Hartemann F. V., Danly B. G., Temkin R. J., 1994. Single-Mode operation of a Bragg Free-Electron Maser Oscillator. *Phys. Rev. Lett.*, **72**(15), pp.2391-2394

Colson W. B., 1977. One-body Electron Dynamics in a Free Electron Laser. *Phys. Lett. A*, **64**, pg. 190.

Colson W. B., 1981. The Nonlinear Wave Equation for Higher Harmonics in Free-Electron Lasers. *IEEE Journal of Quantum Electronics*, **QE17**(8), pp.1417-1427.

Colson W. B., 1997. Short Wavelength Free-Electron Lasers in 1997. *Nuclear Instruments and Methods in Physics Research A* **407**, pp. 26 - 29.

Conde M. E., Bekefi G., 1991. Experimental Study of a 33.3GHz Free-Electron-Laser Amplifier with a Reversed Axial Guide Magnetic Field. *Phys. Rev. Lett.*, **67**(22), p.3082.

Cross A. W., 1993. *Electron Cyclotron Maser Experiments Using Cold and Thermionic Cathodes*. University of Strathclyde, Ph. D. Thesis

Cross A. W., Ginzburg N. S., He W., Jaroszynski D. A., Peskov N. Yu., Phelps A. D. R., Whyte C. G., 1998. A 32GHz Bragg Free-Electron Maser (FEM) Oscillator with Axial Guide Magnetic Field. *Nuclear Instruments and Methods in Physics Research A*, **407**(1998), p.181.

Cross A. W., He W., Konoplev I. V., Phelps A. D. R., Ronald K., Robb G. R. M., Whyte C. G., Ginzburg N. S., Peskov N. Yu., Sergeev A. S., 2001. Experimental and Theoretical Studies of 2D Bragg Structures for a Coaxial Free Electron Maser. *Nuclear Instruments and Methods in Physics Research A*, **475**(2001), pp. 167-172.

Cross A. W., Konoplev I. V., Phelps A. D. R., Ronald K., 2003. Studies of Surface Two-Dimensional Photonic Band-Gap Structures. *Journal of Applied Physics*, **93**(4), pp. 2208-2218.

Danilov Yu. Yu., Kuzikov S. V., Petelin M. I., 2000. Theory of a Microwave-Pulse Compressor Based on a Barrel-Shaped Cavity with Helical-Corrugated Surface. *Technical Physics*, **45**(1), pp. 63-65. Translated from *Zhurnal Tekhnicheskoi Fiziki*, **70**(1), 2000, pp.65-67.

Davidson R. C., McMullin W. A., 1982. Intense Free Electron Laser Harmonic Generation in a Longitudinal Magnetic Wiggler. *Phys. of Fluids*, **26**(3), p. 840.

Deacon D. A. G., Elias L. R., Madey J. M. J., Ramian G. J., Schwettman H. A., Smith T. L., 1977. First Operation of a Free Electron Laser. *Phys. Rev. Lett.*, **38**(16), p. 892.

Denisov G. G., Bratman V. L., Cross A. W., He. W., Phelps A. D. R., Ronald K., Samsonov S. V., Whyte C. G., 1998. Gyrotron Traveling Wave Amplifier with a Helical Interaction Waveguide. *Phys. Rev. Lett.*, **81**(25),p. 5680.

Denisov G. G., Resnikov M. G., 1982. Corrugated Cylindrical Resonators for Short-Wavelength Relativistic Microwave Oscillators. *Radio Physics and Quantum Electronics*, **25**(5), p. 407. Translated from *Izcestiya Vysshikh Uchebnykh Zavedenii, Radiofizika*, **25**(5), p.562.

Denissov D., Rebholz H., Kohler W., Tenbohlen S., 2005. *Dielectric Strength of Different Gases in GIS*, University of Stuttgart.

DPPEA, 2000. *SF_6 Safe Handling Procedures.* North Carolina Department of Environment and Natural Resources. Available online: http://www.p2pays.org/ref/22/21612.pdf

Edinghoffer J. A., Neil G. R., Hess C. E., Smith T. I., Fornaca S. W., Schwettman H. A., 1984. Variable-Wiggler Free-Electron-Laser Oscillations. *Phys. Rev. Lett.* **52**(5), p.344.

Efthimion P. C., Schlesinger S. P., 1977. Stimulated Raman Scattering by an Intense Relativistic Electron Beam in a Long Rippled Magnetic Field. *Phys. Rev. A*, **16**(2), pp.633-639.

Elias L. R., Fairbank W. M., Madey J. M. J., Schwettman H. A., Smith T. L., 1976. Observation of Stimulated Emission of Radiation by Relativistic Electrons in a Spatially Periodic Transverse Magnetic Field. *Phys. Rev. Lett.,* **36**(13), p.717.

Elias L. R., Ramian G., Hu J., Amir A., 1986. Observation of Single-Mode Operation in a Free Electron Laser. *Phys. Rev. Lett.*, **57**(4), pp.424-427.

EOS (Electrical Oil Services) 2006. [Discussion of dielectric properties of unused insulator oil] (Personal communication, 2006). Contact number: 0845 602 1003

Fajans J., Bekefi G., Yin Y. Z., Lax B., 1985. Microwave Studies of a Tunable Free-Electron Laser in Combined Axial and Wiggler Magnetic Fields. *Physics of Fluids* **28**(6), p.1995.

Fajans J., Wurtele J. S., Bekefi G., Knowles D. S., Xu K., 1986. Nonlinear Power Saturation and Phase (Wave Refractive Index) in a Collective Free-Electron Laser Amplifier. *Phys. Rev. Lett.* **57**(5), p.579.

Farokhi B., Maraghechi B., 2005. Boundary Effects on Raman Free-Electron Laser with Coaxial Wiggler. *Phys. of Plasmas*, **12**(2), article:023105.

Freund H. P., Anotonsen T. M. Jr., 1996. *Principles of Free-Electron Lasers 2nd Edition.* London (UK): Chapman & Hall.

Freund H. P., Gold S. H., 1984. Efficiency Enhancement in Free-Electron Lasers Using a Tapered Axial Guide Field. *Phys. Rev. Lett.*, **52**(11), pp.926-929.

Freund H. P., Granatstein V. L., 1997. Long Wavelength Free-Electron Lasers in 1997. *Nuclear Instruments and Methods in Physics Research A* **407**, pp. 30 - 33.

Freund H. P., Jackson R. H., Danly B. G., Levush B., 1999. Power and Bandwidth Studies for W-Band Free-Electron Masers. *Nuclear Instruments and Methods in Physics Research A,* **429** (1999) p. 70.

Freund H. P., Jackson R. H., Pershing D. E., Taccetti J. M., 1993. Nonlinear Theory of the Free-Electron Laser Based Upon a Coaxial Hybrid Wiggler. *Phys. Plasmas*, **1**(4) pp.1046-1059.

Freund H. P., Nguyen K., Pershing D. E., 1997. Theory of a Ubitron in a Corrugated Waveguide. *Nuclear Instruments and Methods in Physics Research A*, **393**, pp.304-307.

Friedman M., Herndon M., 1972a, Microwave Emission Produced by the Interaction of an Intense Relativistic Electron Beam with a Spatially Modulated Magnetic Field. *Phys. Rev. Lett.*, **28**(4), p. 210.

Friedman M., Herndon M., 1972b. Emission of Coherent Microwave Radiation from a Relativistic Electron Beam Propagating in a Spatially Modulated Field. *Phys. Rev. Lett.*, **29**(1), p. 55.

Fuks M. I., Goikhman M. B., Kovalev N. F., Palitsin A. V., Schamiloglu E., 2004. Waveguide Resonators with Combined Bragg Reflectors. *IEEE Trans. on Plasma Sci.*, **32**(3), p.1323.

Gallagher D. A., Barsanti M., Scafuri F., Armstrong C., 2000. High-Power Cusp Gun for Harmonic Gyro-Device Applications. *IEEE Trans. on Plasma Sci.*, **28**(3), pp.695-699.

Gilmour A. S. Jr., 1986. *Microwave Tubes*, Dedham MA: Artech House Inc.

Ginzburg N. S., Kaminsky A. K., Kaminski A. A., Peskov N. Yu., Sedykh S. N., Sergeev A. P., Sergeev A. S., 1998a. Theoretical and Experimental Comparison of FEL-Oscillators with Conventional and Reversed Guide Field. *IEEE Trans. on Plasma Sci.*, **26**(3), pp.536-541.

Ginzburg N. S., Kaminsky A. K., Kaminski A. A., Peskov N. Yu., Sedykh S. N., Sergeev A. P., Sergeev A. S., 1998b. Single-Mode and Multimode Operation Conditions in JINR0IAP Millimeter-Wave FEL-Oscillator. *IEEE Trans. on Plasma Sci.*, **26**(3), pp.542-547.

Ginzburg N. S., Kaminsky A. K., Kuzikov S. V., Perel'shtein E. A., Peskov N. Yu., Sedykh S. N., Sergeev A. P., Sergeev A. S., 2006. Feasibility of Using a Free-Electron Maser with a Bragg Resonator for Testing High-Q Resonant Structures. *Technical Physics,* **51**(7), p.887. Translated from *Zhurnal Tekhnichaskol Fiziki*, **76**(7), p. 69.

Ginzburg N. S., Peskov N. Yu., Sergeev A. S., Konoplev I. V., Ronald K., Phelps A. D. R., Cross A. W., 2004. On the Mechanism of High Selectivity of Two-Dimensional Coaxial Bragg Resonators. *Nuclear Instruments and Methods in Physics Research A*, **528**, pp.78-82.

Ginzburg N. S., Peskov N. Yu., Sergeev A. S., Phelps A. D. R., Konoplev I. V., Robb G. R. M., Cross A. W., Arzhannikov A. V., Sinitsky S. L., 1999. Theory and Design on a Free-Electron Maser with Two-Dimensional Feedback Driven by a Sheet Electron Beam. *Phys. Rev. E*, **60**(1), pp.935-945.

Ginzburg N. S., Sergeev A. S., Peskov N. Yu., Konoplev I,. V., Robb G. R. M., Phelps A. D. R., 1996. Mode Competition and Control in Free Electron Lasers With One and Two Dimensional Bragg Resonators. *Nuclear Instruments and Methods in Physics Research A*, **357**, pp.202-206.

Glyavin M. Yu., Goldberg A. L., Kuftin A. N., Lygin V. K., Postnikova A. S., Zapevalov V. E., 1999. Experimental Studies of Gyrotron Electron Beam Systems. *IEEE Trans. on Plasma Sci.,* **PS-27**(2), p. 474

Gold S. H., Black W.M., Freund H. P., Granatstein V. L., Jackson R. H., Efthimion P. C., Kinkead A. K., 1983. Study of Gain, Bandwidth and Tunability of a Millimeter Wave Free Electron Laser Operating in the Collective Regime. *Physics of Fluids* **26** (9), pp. 2683 - 2688.

Gold S. H., Black W.M., Freund H. P., Granatstein V. L., Jackson R. H., Efthimion P. C., Kinkead A. K., 1985. Reply to Comments of Bekefi & Fajans [Study of Gain, Bandwidth and Tunability of a Millimeter Wave Free Electron Laser Operating in the Collective Regime]. *Physics of Fluids* **28** (10), p. 3179.

Gold S. H., Fliflet A. W., Manheimer W. M., McCowan R. B., Lee R. C., Granatstein V. L. Hardesty D. L., Kinkead A. K., Sucy M., 1988. High Power Ka-Band Gyrotron Oscillator Experiments with Slotted and Unslotted Cavities. *IEEE Trans. on Plasma Sci.* **PS-16**(2), p. 142.

Gold S. H., Haresty D. L., Kinkead A. K., Barnett L. R., Granatstein V. L., 1984. High-Gain 35GHz Free-Electron Laser-Amplifier Experiment. *Phys. Rev. Lett*. **52**(14), p.1218.

Gorn E. J., 1952. Traveling-Wave Electron Reaction Device. *United States Patent Office*. **Patent No. 2,591,350**.

Grant I. S., Phillips W. R., 1990. *Electromagnetism 2nd Edition.* Chichester, England: John Wiley & Sons Ltd.

Greiner W., 1998. *Classical Electrodynamics*. New York, USA: Springer-Verlag New York Inc.

Grover L. K., Pantell R. H., 1985. Simplified Analysis of Free-Electron Lasers Using Madey's Theorem. *IEEE Journal of Quantum Electronics*, **QE21**(7), pp.944-951.

Harris L. P., 1983. Transverse Forces and Motions at Cathode Spots in Vacuum Arcs. *IEEE Trans. on Plasma Sci.* **PS-11**(3), p. 94

Harvey A. F., 1963. *Microwave Engineering*. New York: Academic Press Inc. NY

He W., 1995. *Electron Beam Production, Diagnoses and CARM Experiments.* University of Strathclyde, Ph D. Thesis.

Hecht E., 2001. *Optics International (4th) Edition*. Publisher: Addison-Wesley.

Horowitz P., Hill W., 1999. *The Art of Electronics 2nd Edition*. Printed in USA: Cambridge University Press.

HP, 1992. 8757D *Scalar Network Analyser, Operations Manual*. Distributed by HP with SNA.

Humphries S. Jr., 2002. *Charged Particle Beams Electronic Edition.* Available at: http://www.fieldp.com/cpb.html

Husain E., Nema R. S., 1982. Analysis of Paschen Curves for Air, N_2 and SF_6 Using the Townsend Breakdown Equation. *IEEE Trans. on Electrical Insulation*, **EI-17**(4), pp. 350-353.

Ioannidis Z. C., Latsas G. P., Tigelis I. G., Dumbrajs O., 2008. TM Modes in Coaxial Cavities with Inner Surface Corrugations. *IEEE Trans. on Plasma Sci.*, **36**(5), p. 2613.

Jackson R. H., Gold S. H. Parker R. K., Freund H. P., Efthimion P. C., Granatstein V. L., Herndon M., Kinkead A. K., Kosakowski J. E., Kwan J. T., 1983. Design and operation of a Collective Millimeter-Wave Free-Electron Laser. *IEEE Journal of Quantum Electronics*, **19**(3), pp. 346 - 356.

Jackson J. D., 1999. *Classical Electrodynamics 3rd Edition.* NJ, USA: John Wiley & Sons. Inc.

Jacobs K. D., Bekefi G., Freeman, J. R., 1981. The Diffusive Wiggler- A Spatially Periodic Magnetic Pump for Free-Electron Lasers. *J. Appl. Phys.*, **52**(8),pp.4977-4981

Jecko F., Papiernik A., 1983. Helically Corrugated Circular Waveguides as Antenna Feeders. *Electronics Letters*, **19**(14), pp.555 - 557.

Jundong Z., Qiaogen Z., Jiangbo J., Fengbo T., Lianddian Y., Lanjun Y., 2006. Design of a Rogowski Coil with a Magnetic Core Used for Measurements of Nanosecond Current Pulses. *Plasma Science and Technology*, **8**(4), p.457

Kaminsky A. K., Kaminsky A. A., Sarantsev V. P., Sedykh S. N., Sergeev A. P., Ginzburg N. S., Peskov N. Yu., Sergeev A. S., Bogachenkov V. A., 1996. High Efficiency FEL-Oscillator with Bragg Resonator Operated in the Reverse Guide Field Regime. *Nuclear Instruments and Methods in Physics Research A,* **357**. pp.215-218.

Kapitza P. L., Dirac P. A. M., 1933. The Reflection of Electrons from Standing Light Waves. *Proc. Cambridge Phys. Soc.*, **vol 29**(3), pp. 297-300.
Kitchen R., 2001. *RF and Microwave Radiation Safety Handbook 2nd Edition.* Printed in UK: Butterworth-Heinemann.

Kirkman R. A., Kline M., 1946. The Transverse Electric Modes in Co-axial Cavities. *Proceedings of the IRE*, **34**(1), pp.14-17.

Kirkpartick D. A., Bekefi G., DiRienzo A. C., Freund H. P., Ganguly A. K., 1989. A Millimeter and Submillimeter Wavelength Free-Electron Laser. *Phys. Fluids B*, **1**(7), pp.1511-1518.

Kononenko O, Gandel Y., 2006. Standing Waves in a Coaxial Cavity Gyrotron with a Corrugated Insert. *Microwave Conference 2006, APMC 2006, Asia-Pacific*, pp. 1300-1303.

Konoplev I. V., 2001. *Free-Electron Maser with Two Dimensional Distributed Feedback.* University of Strathclyde, Ph. D. Thesis.

Konoplev I. V., 2007. Private discussion regarding the design and operation of the EEE gun.

Konoplev Iv. V., Cross A. W., He W., Phelps A. D. R., Ponald K., Robb G. R. M., Whyte C. G., Ginzburg N. S., Peskov N. Yu., A. S. Sergeev, 2000. Progress of the Strathclyde Free Electron Maser Experiment Using a 2D Bragg Structure. *Nuclear Instruments and Methods in Physics Research A*, **445**, pp.236-240.

Konoplev I. V., Cross A. W., MacInnes P., He W., Phelps A. D. R., Whyte C. G., Ronald K., Robertson C. W., 2008. Free-Electron Maser Based on a Cavity with Two- and One-Dimensional Distributed Feedback. *Appl. Phys. Lett.,* **92**(21), article:211501.

Konoplev I. V., Cross A. W., MacInnes P., He W., Whyte C. G., Phelps A. D. R., Robertson C. W. Ronald K., Young A. R., 2006a. High-current Oversized Annular Electron Beam Formation for High-Power Microwave Research. *Appl. Phys. Lett.*, **89**(17), Article: 171503.

Konoplev I. V., Cross A. W., Phelps A. D. R., He W., Ronald K., Whyte C. G., Robertson C. W., MacInnes P., 2007. Experimental and Theoretical Studies of a Coaxial Free-Electron Maser Based on Two-Dimensional Distributed Feedback. *Phys. Rev. E*, **76**(5), article: 056406.

Konoplev I. V., McGrain P., Cross A. W., Ronald K., Phelps A. D. R., 2005. Wave Interference and Band Gap Control in Multiconductor One-Dimensional Bragg Structures. *Journal of Applied Physics*, **97**(7), article: 073101.

Konoplev I. V., McGrain P., He W., Cross A. W., Phelps A. D. R., Whyte C. G., Ronald K., Robertson C. W., 2006b. Experimental Study of Co-axial Free Electron Maser Based on 2D Distributed Feedback. *Phys. Rev. Lett.*, **96**(3), article: 035002.

Konoplev I. V., Phelps A. D. R., Cross A. W., Ronald K., 2003. Experimental Studies of the Influence of Distributed Power Losses on the Transparency of Two-dimensional Surface Photonic Band-Gap Structures. *Phys. Rev. E* **68**(6), article: 066613.

Kroll N. M., Morton P. L., Rosenbluth M. N., 1981. Free-Electron Lasers with Variable Parameter Wigglers. *IEEE Journal of Quantum Electronics*, **QE17**(8), pp.1436-1468.

Kuffel E., Zaengl W. S., Kuffel J., 2000. *High Voltage Engineering Fundamentals 2nd Edition.* UK: Butterwoth-Heinemann.

Lee Z. Y., 1983. Subnanosecond High-Voltage Two-Stage Resistive Divider. *Rev. Sci. Instrm.*, **54**(8), p. 1080.

Leonard S. L., 1965. Basic Macroscopic Measurements. In Huddlestone R. H. & Leonard S. L., ed. *Plasma Diagnostic Techniques*. London: Academic Press Inc. (London) Ltd. Ch. 2.

Li Z. Y., 1988. Improved $CuSO_4$ HV Pulse Divider. *Rev. Sci. Instrum.*, **59**(7), p. 1244

Lingwood C., Carter R. G., Burt G., 2009. High Efficiency Multiple Beam Klystron (MBK) Stability. *Proceedings of International Vacuum Electronics Conference 2009*, pp. 241 - 242.

Lorrain P., Corsan D.R., Lorrain, F., 1988. *Electromagnetic Fields and Waves 3rd Edition.* USA: W.H.Freeman & Co Ltd.

Luchini P., Motz H., 1990. *Undulators and Free-Electron Lasers.* Oxford: Clarendon Press.

Luchini P., Solimeno S., 1985. Gain and Mode Coupling in a Three-Dimensional Free-Electron Laser: A Generalization of Madey's Theorem. *IEEE Journal of Quantum Electronics*, **QE21**(7), pp.952-965.

Madey J. M. J., 1971. Stimulated Emission of Bremsstrahlung in a Periodic Magnetic Field. *J. Appl. Phys.*, **42**(5), p. 1906.

Maraghechi B., Sepehri Javan N., 2001. Raman Free-Electron Laser with Longitudinal Electrostatic Wiggler and Annular Electron Beam. *Phys. of Plasmas*, **8**(9), pp.4193-4201.

Marcuvitz N., 1986. *Waveguide Handbook*, *New Edition*.Published by the IET.

Mathew J., Pasour J. A., 1986. High-Gain, Long-Pulse Free-Electron-Laser Oscillator. *Phys. Rev. Lett.*, **56**(17), pp.1805-1808.

McCormick N. R., Craggs J. D., 1954. Some Measurements of the Relative Dielectric Strength of Gases. *J. Appl. Phys.*, **5**, pp.171-173.

McDermott D. B., Balkcum A. J., Luhmann N. C., 1996. 35-GHz 25-kW CW Low-Voltage Third-Harmonic Gyrotron. *IEEE Trans. on Plasma Sci.*, **24**(3), pp.613 - 619.

McDermott D. B., Balkcum A. J., Phillips R. M., Luhmann N. C. Jr., 1995. Periodic Permanent Magnet Focusing of an Annular Electron Beam and its Application to a 250MW Ubitron Free-Electron Maser. *Phys. Plasmas*, **2**(11), pp.4332-4337.

McDermott D. B., Marshall T. C., Schlesinger S. P., Parker R. K., Granatstein V. L., 1978. High-Power Free-Electron Laser Based on Stimulated Raman Backscattering. *Phys. Rev. Lett.*, **41**(20), pp. 1368-1371.

McGrane P., 2006. *Computation and Experimental Studies of Distributed Bragg Feedback for Use in a High-Power Free-Electron Maser.* University of Strathclyde, Ph. D. Thesis.

McMullin W. A., Bekefi G., 1981. Coherent Radiation From a Relativistic Electron Beam in a Longitudinal, Periodic Magnetic Field. Appl. Phys. Lett., **39**(10), pp.845-847.

McMullin W. A., Bekefi G., 1982. Stimulated Emission From Relativistic Electrons Passing Through a Spatially Periodic Longitudinal Magnetic Field. *Phys. Rev. A*, **25**(4), article 1836.

McMullin W. A., Davidson R. C., Johnson G. L., 1983. Stimulated Emission From a Relativistic Electron Beam in a Variable-Parameter Longitudinal Magnetic Wiggler. *Phys. Rev A*, **28**(2), p. 517.

Mesyats G. A., 1983. Explosive Processes on the Cathode in a Vacuum Discharge. *IEEE Trans. on Elec. Insul.*, **EI-18**(3), p. 218.

Mesyats G. A., 1985. A Cyclical Explosive Model of the Cathode Spot. *IEEE Trans. on Elec. Insul.,* **EI-20**(4), p. 729.

Mesyats G. A., 1991. Vacuum Discharge Effects in the Diodes of High-Current Electron Accelerators. *IEEE Trans. on Plasma Sci.* **19**(5), p. 683.

Mesyats G. A., 1995. Ecton Mechanism of the Vacuum Arc Cathode Spot. *IEEE Trans. on Plasma Sci.*, **23**(6), p. 879.

Mesyats G. A., Proskurovsky D. I., 1989. *Pulse Electrical Discharge in Vacuum. Springer Series on Atoms and Plasmas.* New York: Springer-Verlag Berlin Heidelberg New York.

Meurice N., Sandre E., Aslanides A., Vercauteren D. P., 2004. Simple Theoretical Estimation of the Dielectric Strength of Gases. *IEEE Trans. on Dielectrics and Electrical Insulation*, **11**(6), p 946.

Milton O., 1974. Electrical Breakdown in a Cold Cathode Vacuum Diode. *IEE Trans. on Electrical Insulation*, **EI-9**(2), p. 68.

Motz H., 1951. Applications of the Radiation from Fast Electron Beams. *Journal of Applied Physics*, **22**(5), pp. 527 - 535.

Motz H., Thon W., Whitehurst R. N., 1953. Experiments on Radiation by Fast Electron beams. *Journal of Applied Physics*, **24**(7), p. 826.

Murgatroyd P. N., Chu A. K. Y., Richardson G. K., West D., Yearley G. A., Spencer A. J., 1991. Design Note: Making Rogowski Coils. *Meas. Sci. Thechnol.* **2**(1991) p. 1218.

Ortega J. M., Glotin F., Prazeres R., 2006. Extension in Far-Infrared of the CLIO Free-Electron Laser. *Infrared Physics & Technology*, **49**(2006), p. 133-138

Orzechowski T. J., Anderson B. R., Clark J. C., Fawley W. M., Paul A. C., Prosnitz D., Scharlemann E. T., Yarema S. M., Hopkins D. B., Sessler A. M., Wurtele J. S., 1986. High-Efficiency Extraction of Microwave Radiation from a Tapered-Wiggler Free-Electron Laser. *Phys. Rev. Lett.*, **57**(17), pp.2172-2175.

O'Shea P. G., Freund H. P., 2001. Free-Electron Lasers: Status and Applications. *Science*, **vol 292**, pp. 1853 - 1858.

Pantell R. H., Soncini G., Puthoff H. E., 1968. Stimulated Photon-Electron Scattering. *IEEE Journal of Quantum Electronics*, **QE-4**(11), pp. 905-907.

Parker R. K., Jackson R. H., Gold S. H., Freund H. P., Granatstein V. L., Efthimion P. C., Herndon M., Kinkead A. K., 1982. Axial Magnetic-Field Effects in a Collective-Interaction Free-Electron Laser at Millimeter Wavelengths. *Phys. Rev. Lett.*, **48**(4), pp.238-242.

Pasour J. A., 1987. Free-Electron Lasers. In Granatstein V. L. (ed.) & Alexeff I. (ed.) *High-Power Microwave Sources*. London: Artec House Inc. Ch. 6.

Pasour J. A., Gold S. H., 1985. Free-Electron Laser Experiments With and Without a Guide Magnetic Field: A review of Millimeter-Wave Free-Electron Laser Research at the Naval Research Laboratory. *IEEE Journal of Quantum Electronics*, **21**(7), pp.845-859.

Phillips R. C., Turner E. B., 1965. Construction and Calibration Techniques of High Frequency Magnetic Probes. *The Review of Scientific Instruments*, **36**(12), p. 1822.

Phillips R. M., 1960. The Ubitron, a High-Power Traveling-Wave Tube Based on a Periodic Beam Interaction in Unloaded Waveguide. *IRE Trans. Electron Dev*., **7**(4), p. 231.

Pierce J. R., 1954. *Theory and Design of Electron Beams 2nd Edition*. New York, Van Nostrad.

Poole M., 2000. Storage ring-based fels: 4th generation performance at long wavelengths from present rings-present capabilities and future possibilities. *Synchrotron Radiation News*, **13**(1), pp. 4-17.

Pozar D. M., 1998. *Microwave Engineering 2nd Edition.* USA. John Wiley & Sons.

Racs B., Patocs A., 1992. Fast High-Voltage Resistive Pulse Divider. *Meas. Sci. Technol.*, **3** (1992), pp. 926 - 928.

Rhee M. J., Destler W. W., 1974. Relativistic Electron Dynamics in a Cusped Magnetic Field. *Phys. of Fluids*, **17**(8), pp.1574-1581.

Robertson C. W., Sprangle P., 1989. A Review of Free-Electron Lasers. *Phys. Fluids B*, **1**(1), pp.3-42.

Ronald K., 1996. *Gyrotron experiments using explosive emission cathodes*. Ph. D. University of Strathclyde.

Ronald K., Cross A. W., Phelps A. D. R., He W., Yin H., Spark S. N., 1998. Explosive Cathode Gyrotron Experiments. *IEEE Trans. on Plasma Sci,* **26**(3), p. 375.

Rothstein J., 1948. On the Mechanism of Electron Emission at the Cathode Spot of an Arc. *Phys. Rev. Lett*. April 1948, p. 1214.

Samsonov S. V., Phelps A. D. R., Bratman V. L., Burt G., Denisov G. G., Cross A. W., Ronald K., He W., Yin H., 2004. Compression of Frequency-Modulated Pulses using Helically Corrugated Waveguides and Its Potential for Generating Multigigawatt RF Radiation. *Phys. Rev. Lett.*, **92**(11), article: 118301.

Schrade H. O., 1989. Arc Cathode Spots: Their Mechanism and Motion. *IEEE Trans. on Plasma Sci.* **17**(5), p.635.

Shaw E. D., Chichester R. J., Chen S. C., 1986. Microtron Accelerator for a Free Electron Laser. *Nuclear Instruments and Methods in Physics Research Section A*, **250**(1-2), pp. 44-48.

Sheffield R. L., Stein W. E., Warren R. W., Fraser J. S., Lumpkin A. H., 1985. Electron-Beam Diagnostics and Results for the Los Alamos Free-Electron Laser. *IEEE Journal of Quantum Electronics*, **21**(7), pp.895-903.

Shi-Chang Z., Xiao-Hui C., Ying-Xin L., 2007. Effect of Eccentricity on Transmission in a Coaxial Bragg Structure. *Int. J. Infrared Milli. Waves*, **28**, pp.1043-1050.

Shraga I. Goren Y., Leibovitch C., Eckhouse S., 1986. Experimental Demonstration of Longitudinal Wiggler Free-Electron Laser. *Appl. Phys. Lett.*, **49**(21), pp.141-1414.

Sinnis J., Schmidt G., 1963. Experimental Trajectory Analysis of Charged Particles in a Cusped Geometry. *Phys. of Fluids*, **6**(6), pp.841-845.

Spark S. N., Cross A. W., Phelps A. D. R., Ronald K., 1994. Megawatt, 330 Hz PRF Tunable Gyrotron Experiments. *International Journal of Infrared and Millimeter Waves*, **15**(12), p.2003.

Sprangle P., Smith R. A., 1980. Theory of Free-Electron Lasers. *Phys. Rev. A*, **21**(1), pp.293-301.

Sprangle P., Tang Cha-Mei, Manheimer W. M., 1979. Nonlinear Formulation and Efficiency Enhancement of Free-Electron Lasers. *Phys. Rev. Lett.,* **43**(26), pp.1932-1936.

Swegle J. A., Poukey J. W., Leifeste G. T., 1985. Backward-wave Oscillators with Rippled Wall Resonators: Analytic Theory and Numerical Simulation. *Phys. Fluids*, **28**(9), p. 2882.

Tang Chai-Mei, Sprangle P. A., 1985. Three-Dimensional Numerical Simulations of FEL's by the Transverse Mode Spectral Method. *IEEE Journal of Quantum Electronics*, **QE21**(7), pp.970-978.

Tarakanov V. P, 1997. *User's Manual for Code KARAT Ver. 7.03 May 97.* Springfield VA: Distributed by Berkely Research Associates Inc.

Thomas R. J., 1967. Response of capacitive voltage dividers. *Microwaves*, **vol.6** pp. 50-53, August 1967

Thomas R. J., 1970. High-Impulse Current and Voltage Measurement. *IEEE Trans. on Instrumentation and Measurement.* **IM-19**(2), p. 102

Thomas R. J., Hearst J. R., 1965. *An Electronic Scheme for Measurement of Exploding Wire Energy.* Technical Report No. 14170. Livermore CA: University of California Ernest O. Lawrence Radiation Laboratory.

Thornton E. 1975. Subnanosecond Risetimes in Metal Foil Coaxial Shunts. *Journal of Physics E: Scientific Instruments*, **8**, p. 1052.

Thornton E., 1991. Voltage and Current Measurement in Pulsed Power Circuits. In IEE (Institute of Electrical Engineers) *Colloquium of Measurement Techniques for Power Electronics*. London UK 16 December 1991. IEE: London.

Thumm M., 1997. Modes and Mode Conversion in Microwave Devices. In Cairns R. A. (ed.) & Phelps A. D. R. (ed.) *Generation and Application of High Power Microwaves*. London: SUSSP Publications, IOP Publishing. pp 121 - 171

Vanderlinde J., 2004. *Classical Electromagnetic Theory 2nd Edition*. Drodrecht, The Netherlands: Springer Publishing.

Waldron R. A., 1969. *Theory of Guided Electromagnetic Waves*. Printed in Great Britain: Butler & Tanner Ltd. Frome and London.

Wang M. C., Granatstein V. L., Kehs R. A., 1986. Design of a Bragg Cavity for a Millimeter Wave Free-Electron Laser. *Appl. Phys. Lett.* **48**(13), pp.817-819.

Wei Y., Park G., Joo Y., Yu G., Wang W., Liu S., Uhm H. S., 2002. Theory of High-Power Wide-Band Traveling-Wave Tube Using Coaxial Inverted Helical Groove Slow-Wave Structure. *IEEE Trans. on Plasma Sci.*, **30**(5), p.2010.

Yariv A., Nakamura M., 1977. Periodic structures for integrated optics. *IEEE Journal of Quantum Electronics*, **QE13**(4), p.233.

Yariv A., Yeh P., 2006. *Photonics, Optical Electronics in Modern Communications 6th Edition.* NY: Oxford University Press New York.

Yin Y. Z., Bekefi G., 1983. Dispersion Characteristics of a Free-Electron Laser with a Linearly Polarized Wiggler and Axial Guide Field. *J. Appl. Phys.*, **55**(1), pp.33-41.

Ying-Xin L., Shi-Chang Z., 2007. Multiwave Interaction Formulation on a Coaxial Bragg Structure and its Experimental Verification. *Phys. of Plasmas.*, **14**(11), article:113301.

Ying-Xin L., Shi-Chang Z., 2008. Separation of Band-Gap Overlap in a Coaxial Bragg Structure Operating in Higher-Order Mode at Terahertz Frequency. *Phys. of Plasmas.*, **15**(3),article:033301.

Appendix A: 1D Bragg Derivations

A.1 Derivation of the Coupled Wave Equations for 1D Reflectors.

Starting from the base version of the Helmholtz equation for the $\vec{E}$ field in smooth co-axial waveguide, assuming operation in the fundamental TEM mode:

$$\nabla^2 E + \omega^2 \mu \varepsilon E = 0 \qquad \textbf{A.1}$$

where the wave impedance for the TEM mode is defined as:

$$Z_w = \frac{\omega\mu}{k_z} = \frac{2\pi Z_0}{\ln(b_0/a_0)} = \sqrt{\frac{\mu}{\varepsilon}} \qquad \textbf{A.2}$$

where a_0 and b_0 are the unpertubed radii of the inner and outer conductors respectively, $Z_0 = V_0/I_0$ is the characteristic impedance of the line (V_0 and I_0 are the voltage and current incident on the line respectively) and all other quantites have their common meanings.

Equation A.2 becomes:

$$\nabla^2 E + \frac{\omega^2 \mu^2}{4\pi^2 Z_0^2} \ln^2\left(\frac{b_0}{a_0}\right) E = 0 \qquad \textbf{A.3}$$

The introduction of a periodic corrugation on either the inner or outer conductor surface in a co-axial waveguide can be represented by a sinusoidal perturbation in the radius of the relevent conductor surface:

$$r(\theta, z) = r_0 \pm r_1 \cos(M\theta + h_z z) \qquad \textbf{A.4}$$

where r_0 is the mean radius of the corrugation (equal to the radius of the smooth waveguide) and r_1 corresponds to the corrugation amplitude, with the sign for the periodic term determining whether the corrugation begins at a maxima or a minima. The relation between the sign of the periodic term and the resultant extrema will be discussed later in the derivation. M is the number of variations across the azimuth and

corresponds to the azimuthal wave-number expressed in radians ($h_s = M/r_0$), while h_z denotes the axial wave-number.

In the first instance, assuming a corrugation on the outer conductor surface, with the inital extrema of the corrugation chosen to be a maxima, equation A.4 corresponds to a modification in the natural log term of equation A.3 as:

$$\ln^2\left(\frac{b_0}{a_0} + \frac{r_1}{a_0}\cos(M\theta + h_z z)\right) \qquad \textbf{A.5}$$

where r_1 corresponds to the amplitude of the corrugation.

Equation A.5 expands as:

$$\ln^2\left(\frac{b_0}{a_0}\left(1 + \frac{r_1}{b_0}\cos(M\theta + h_z z)\right)\right) = \left(\ln\left(\frac{b_0}{a_0}\right) + \ln\left(1 + \frac{r_1}{b_0}\cos(M\theta + h_z z)\right)\right)^2$$
$$= \ln^2\left(\frac{b_0}{a_0}\right) + 2\ln\left(\frac{b_0}{a_0}\right)\ln\left(1 + \frac{r_1}{b_0}\cos(M\theta + h_z z)\right) + \ln^2\left(1 + \frac{r_1}{b_0}\cos(M\theta + h_z z)\right)$$

where $2\ln\left(\frac{b_0}{a_0}\right)\ln\left(1 + \frac{r_1}{b_0}\cos(M\theta + h_z z)\right) \gg \ln^2\left(1 + \frac{r_1}{b_0}\cos(M\theta + h_z z)\right)$.

giving equation A.3 as:

$$\nabla^2 E + \frac{\omega^2\mu^2}{4\pi^2 Z_0^2}\ln^2\left(\frac{b_0}{a_0}\right)E + \frac{\omega^2\mu^2}{2\pi^2 Z_0^2}\ln\left(\frac{b_0}{a_0}\right)\ln\left(1 + \frac{r_1}{b_0}\cos(M\theta + h_z z)\right)E = 0 \qquad \textbf{A.6}$$

Noting the relationship given in equation A.2 this reduces to:

$$\nabla^2 E + k_z^2 E + \frac{2k_z^2}{\ln(b_0/a_0)}\ln\left(1 + \frac{r_1}{b_0}\cos(M\theta + h_z z)\right)E = 0 \qquad \textbf{A.7}$$

Using the Taylor expansion $\ln(1 + A) = A - \frac{A^2}{2} + \frac{A^3}{3} - \ldots$ where $A \gg \frac{A^2}{2}$ implies:

$$\nabla^2 E + k_z^2 E + \frac{2k_z^2}{\ln(b_0/a_0)}\frac{r_1}{b_0}\cos(M\theta + h_z z)E = 0 \qquad \textbf{A.8}$$

If we now go back to equation A.3 and consider the case of a corrugation presented on the inner conductor surface, if the same choice of sign for the periodic term is made the natural log term of equation A.3 would now be expressed as:

$$\ln^2\left(\frac{b_0}{a_0 + r_1\cos(M\theta + h_z z)}\right) \tag{A.9}$$

which expands as:

$$\begin{aligned}\ln^2\left(\frac{b_0}{a_0 + r_1\cos(M\theta + h_z z)}\right) &= \ln^2\left(\frac{b_0}{a_0}\left(\frac{1}{1 + r_1\cos(M\theta + h_z z)}\right)\right)\\ &= \ln^2\left(\frac{b_0}{a_0}\left(1 - \frac{r_1}{a_0}\cos(M\theta + h_z z)\right)\right)\\ &= \left(\ln\left(\frac{b_0}{a_0}\right) + \ln\left(1 - \frac{r_1}{a_0}\cos(M\theta + h_z z)\right)\right)^2\\ = \ln^2\left(\frac{b_0}{a_0}\right) + 2\ln\left(\frac{b_0}{a_0}\right)\ln\left(1 - \frac{r_1}{a_0}\cos(M\theta + h_z z)\right) &+ \ln^2\left(1 - \frac{r_1}{a_0}\cos(M\theta + h_z z)\right)\end{aligned} \tag{A.10}$$

under the assumptions $1 \gg \frac{r_1}{a_0}\cos(M\theta + h_z z)$ and

$$2\ln\left(\frac{b_0}{a_0}\right)\ln\left(1 - \frac{r_1}{a_0}\cos(M\theta + h_z z)\right) \gg \ln^2\left(1 - \frac{r_1}{a_0}\cos(M\theta + h_z z)\right),$$

equation A.3 therefore takes the form:

$$\nabla^2 E + k_z^2 E + \frac{2k_z^2}{\ln(b_0/a_0)}\ln\left(1 - \frac{r_1}{a_0}\cos(M\theta + h_z z)\right)E = 0 \tag{A.11}$$

which through the same Taylor expansion yields:

$$\nabla^2 E + k_z^2 E - \frac{2k_z^2 r_1}{a_0\ln(b_0/a_0)}\cos(M\theta + h_z z)E = 0 \tag{A.12}$$

Regarding equations A.8 and A.12 it can be seen that moving the corrugation from the outer to the inner conductor surface introduces a switch in sign of the final term. In other words the relation between the sign of the periodic term and the initial condition of the corrugation inverts when moving between corrugations on the inner and outer

conductor surfaces. For simplicity equations A.8 and A.12 may be expressed in a generalised form, substituting $\chi = (\pm r_1)/r_0$, where in this case $+r_1$ corresponds to an initial maxiam and $-r_1$ corresponds to an inital minima, for both conductors:

$$\nabla^2 E + k_z^2 E + \frac{2\chi {k_z}^2}{\ln(b_0/a_0)} \cos(M\theta + h_z z) E = 0 \qquad \textbf{A.13}$$

Considering the first term in equation A.13, the magnitude of the E field can be regarded as:

$$E(z) = Re(A_+ e^{-ik_{z+}z} + A_- e^{ik_{z-}z}) e^{-i\omega t} \qquad \textbf{A.14}$$

where in this case the field profile is taken to be time invariant, allowing the common $e^{-i\omega t}$ term to be suppressed. The $A_{+,-}$ terms correspond to the amplitudes of incident and scattered partial waves, travelling in the $+z$ and $-z$ directions respectively. $k_{z+,-}$ corresponds to the range of axial wave-numbers of the incident and scattered waves, respectively, which (assuming a lossless system) are related to the axial wave-number of the corrugation by:

$$h_z = (k_{z+} - (\delta_{z+} - i\sigma_z)) + (k_{z-} - (\delta_{z-} - i\sigma_z)) \qquad \textbf{A.15}$$

where $\delta_{z+,-}$ are the loss-less deviations of $k_{z+,-}$ from h_z and $i\sigma_z$ corresponds to the ohmic losses incurred along z. Here the axial wave-numbers of the incident and scattered waves are taken to be sinonymous, giving $k_{z+} = k_{z-} = k_z$ and

$$\delta_z - i\sigma_z = k_z - (h_z/2) - i\sigma z \qquad \textbf{A.16}$$

where $\delta_z \ll h_z$.

This implies:

$$\nabla^2 E = -k_z^2 (A_+ e^{-ik_z z} + A_- e^{ik_z z}) - 2ik_z \left(\frac{dA_+}{dz} e^{-k_z z} - \frac{dA_-}{dz} e^{ik_z z} \right) \qquad \textbf{A.17}$$

where the higher order differential terms are disgarded $\left(\frac{d^2 A_\pm}{dz^2} \ll 2ik_z \frac{dA_\pm}{dz} \right)$.

Substitution into equation A.13 and dividing through by $-2ik_z$ yields:

$$\frac{dA_+}{dz}e^{-k_z z} - \frac{dA_-}{dz}e^{ik_z z} + i\frac{\chi k_z}{\ln(b_0/a_0)}\cos(M\theta + h_z z)E = 0 \qquad \textbf{A.18}$$

Noting that for the 1D Bragg reflector $M = 0$, the cosine term reduces to $\cos(h_z z)E$, which can be expanded as:

$$\cos(h_z z)E = \frac{1}{2}(e^{ih_z z} + e^{-ih_z z})(A_+ e^{-ik_z z} + A_- e^{ik_z z}) \qquad \textbf{A.19}$$

giving:

$$\frac{dA_+}{dz}e^{-k_z z} - \frac{dA_-}{dz}e^{ik_z z} + i\kappa k_z\begin{pmatrix} A_+(e^{-i(k_z - h_z)z} + e^{-i(k_z + h_z)z}) \\ + A_-(e^{i(k_z + h_z)z} + e^{i(k_z - h_z)z}) \end{pmatrix} = 0 \qquad \textbf{A.20}$$

where κ is the coupling coefficient:

$$\kappa = \frac{\chi}{2\ln(b_0/a_0)} \qquad \textbf{A.21}$$

Multiplying equation A.20 by $e^{ik_z z}$:

$$\frac{dA_+}{dz} - \frac{dA_-}{dz}e^{2ik_z z} + i\kappa k_z[A_+(e^{ih_z z} + e^{-ih_z z}) + A_-(e^{i(2k_z + h_z)z} + e^{i(2k_z - h_z)z})] = 0 \qquad \textbf{A.22}$$

and recalling the relation given in equation A.16, taking the Slow Varying Wave Approximation (SVWA) of equation A.22 all terms varying faster than $2(\delta_z - i\sigma_z)z$ average to zero, leaving:

$$\frac{dA_+}{dz} + i\kappa k_z A_- e^{2i(\delta_z - i\sigma_z)z} = 0 \qquad \textbf{A.23a}$$

A similar procedure can be carried out multiplying equation A.20 by $e^{-ik_z z}$, yielding:

$$\frac{dA_-}{dz} - i\kappa k_z A_+ e^{-2i(\delta_z - i\sigma_z)z} = 0 \qquad \textbf{A.23b}$$

Considering the amplitudes of the waves to be functions of the detuning δ; $A_+(z) = A'_+(z)e^{i(\delta_z - i\sigma_z)z}$, $A_-(z) = A'_-(z)e^{-i(\delta_z - i\sigma_z)z}$, equations A.23a and A.23b become:

$$\frac{dA'_+}{dz} + i(\delta_z - i\sigma_z)A'_+ + i\kappa k_z A'_- = 0 \qquad \textbf{A.24a}$$

$$\frac{dA'_-}{dz} - i(\delta_z - i\sigma_z)A'_- - i\kappa k_z A'_+ = 0 \qquad \textbf{A.24b}$$

These constitute the wave propagation equations for the incident (equation A.24a) and scattered (equation A.24b) partial waves as they proagate through the corrugation.

A.2 Calculation of the Dispersion Curve .

The amplitudes of the partial waves can be considered as functions of the eigen-modes of the perturbed waveguide:

$$A'_\pm(z) = a_\pm e^{\Lambda z} \qquad \textbf{A.25}$$

where Λ is unknown and considered to be complex.
Substitution of equation A.25 into equations A.24a and A.24b yields:

$$\Lambda a_+ + i(\delta_z - i\sigma_z)a_+ + i\kappa k_z a_- = 0 \qquad \textbf{A.26a}$$

$$\Lambda a_- - i(\delta_z - i\sigma_z)a_- - i\kappa k_z a_+ = 0 \qquad \textbf{A.26b}$$

which can be re-arranged to give:

$$a_+ = -\left(\frac{i\kappa k_z}{(\Lambda + i(\delta_z - i\sigma_z))}\right)a_- \qquad \textbf{A.27a}$$

and

$$a_{-} = \left(\frac{i\kappa k_z}{(\Lambda - i(\delta_z - i\sigma_z))}\right)a_{+} \qquad \textbf{A.27b}$$

This implies:

$$\pm\Lambda = \pm\sqrt{\kappa^2 k_z^2 - (\delta_z - i\sigma_z)^2} \qquad \textbf{A.28}$$

For a propagating wave Λ is imaginary, i.e. $\Lambda = \pm ik'_z$ where k'_z is the perturbed wave-number of the propagating wave. Substituting into equation A.28 and re-arranging for δ_z:

$$(\delta_z - i\sigma_z) = \pm\sqrt{\kappa^2 k_z^2 + k'^2_z} \qquad \textbf{A.29}$$

Recalling equation A.16:

$$k_z^2 - k_z h_z + \frac{h_z^2}{4} - i\sigma_z(2k_z + h_z) - \sigma_z^2 = \kappa^2 k_z^2 + k'^2_z \qquad \textbf{A.30}$$

$$\Rightarrow k_z^2(1-\kappa^2) - k_z h_z + \frac{h_z^2}{4} - k'^2_z - \sigma_z^2 - i\sigma_z(2k_z + h_z) = 0$$

$$\Rightarrow k_z^2 - \frac{h_z + 2i\sigma_z}{1-\kappa^2}k_z + \frac{h_z^2}{4(1-\kappa^2)}\left(1 - \frac{4[k'^2_z + \sigma_z^2 + i\sigma_z h_z]}{h_z^2}\right) = 0$$

which has solutions of the form:

$$k_z = \frac{h_z + 2i\sigma_z}{2(1-\kappa^2)} \pm \sqrt{\frac{(h_z + 2i\sigma_z)^2}{4(1-\kappa^2)^2} - \frac{h_z^2}{4(1-\kappa^2)} + \frac{[k'^2_z + \sigma_z^2 + i\sigma_z h_z]}{(1-\kappa^2)}} \qquad \textbf{A.31}$$

This can be further simplifed as:

$$k_z = \frac{h_z + 2i\sigma_z}{2(1-\kappa^2)} \pm h_z \sqrt{\frac{1 + 2i\sigma_z h_z - \sigma_z^2}{4(1-\kappa^2)^2} - \frac{1}{4(1-\kappa^2)} + \frac{[k'^2_z + \sigma_z^2 + i\sigma_z h_z]}{h_z^2(1-\kappa^2)}}$$

$$= \frac{h_z}{2(1-\kappa^2)} \pm h_z \sqrt{\frac{2i\sigma_z h_z - \sigma_z^2 + \kappa^2}{4(1-\kappa^2)^2} + \frac{[k'^2_z + \sigma_z^2 + i\sigma_z h_z]}{h_z^2(1-\kappa^2)}}$$

$$\frac{h_z}{2(1-\kappa^2)} \pm \frac{h_z}{2(1-k^2)} \sqrt{\kappa^2 + \frac{4[k'^2_z + \sigma_z^2 + i\sigma_z h_z](1-\kappa^2)}{h_z^2}}$$

Taking into account the presence of successive spatial harmonics, this may be substituted into the dispersion relation ($\omega^2 = k^2c^2$) as:

$$\omega_{1,2} = \frac{h_z}{2}\left(n + \frac{1}{1-\kappa^2}\left[1 \pm \sqrt{\kappa^2 + \frac{4[k'^2_z + \sigma_z^2 + i\sigma_z h_z](1-\kappa^2)}{h_z^2}}\right]\right)c \qquad \textbf{A.32}$$

where $n = 0, 1, 2, \ldots$ is an integer representing the order of the spatial harmonic.

A.3 Reflection Co-efficient in 1D Bragg Reflectors.

Considering the wave amplitudes of equations A.24a and A.24b to be functions of the solutions of Λ (equation A.28), they take the form:

$$A'_+(z) = a_{+1}e^{\Lambda z} + a_{+2}e^{-\Lambda z} \qquad \textbf{A.33a}$$

$$A'_-(z) = a_{-1}e^{\Lambda z} + a_{-2}e^{-\Lambda z} \qquad \textbf{A.33b}$$

where the 1 and 2 subscripts denote the first and second roots of Λ respectively and the amplitudes $a_\pm$ are functions of the corrugation length (l_{1D}), independant of z. This implies:

$$\frac{dA'_\pm}{dz} = \Lambda a_{\pm 1}e^{\Lambda z} - \Lambda a_{\pm 2}e^{-\Lambda z} \qquad \textbf{A.34}$$

Substitution into equations A.24a and A.24b gives:

$$e^{\Lambda z}(a_{+1}(\Lambda + i(\delta_z - i\sigma_z)) + i\kappa k_z a_{-1}) = e^{-\Lambda z}(a_{+2}(\Lambda - i(\delta_z - i\sigma_z)) - i\kappa k_z a_{-2}) \quad \textbf{A.35a}$$

$$e^{\Lambda z}(a_{-1}(\Lambda - i(\delta_z - \sigma_z)) - i\kappa k_z a_{+1}) = e^{-\Lambda z}(a_{-2}(\Lambda + i(\delta_z - i\sigma_z)) + i\kappa k_z a_{+2}) \quad \textbf{A.35b}$$

which has solutions:

$$a_{+1}(\Lambda + i(\delta_z - i\sigma_z)) + i\kappa k_z a_{-1} = 0 \quad \textbf{A.36a}$$

$$a_{+2}(\Lambda - i(\delta_z - i\sigma_z)) - i\kappa k_z a_{-2} = 0 \quad \textbf{A.36b}$$

$$a_{-1}(\Lambda - i(\delta_z - i\sigma_z)) - i\kappa k_z a_{+1} = 0 \quad \textbf{A.36c}$$

$$a_{-2}(\Lambda + i(\delta_z - i\sigma_z)) + i\kappa k_z a_{+2} = 0 \quad \textbf{A.36d}$$

re-arranging and substituting for $a_{-1,2}$ in equation A.34 yields:

$$A'_{+} = -\frac{i\kappa k_z}{\Lambda + i(\delta_z - i\sigma_z)} a_{-1} e^{\Lambda z} + \frac{i\kappa k_z}{\Lambda - i(\delta_z - i\sigma_z)} a_{-2} e^{-\Lambda z} \quad \textbf{A.37a}$$

$$A'_{-} = a_{-1} e^{\Lambda z} + a_{-2} e^{-\Lambda z} \quad \textbf{A.37b}$$

The boundary conditions for the incident A'_{+} and scattered A'_{-} waves correspond to $A'_{+}(z)\big|_{z=0} = 1$ and $A'_{-}(z)\big|_{z=l_{1D}} = 0$, which implies $a_{-1} = -a_{-2} e^{-2\Lambda l_{1D}}$ and so:

$$A'_{+} = a_{-2} i\kappa k_z \left(\frac{e^{\Lambda(z-2l_{1D})}}{\Lambda + i(\delta_z - i\sigma_z)} + \frac{e^{-\Lambda z}}{\Lambda - i(\delta_z - i\sigma_z)} \right) \quad \textbf{A.38a}$$

$$A'_{-} = -a_{-2}(e^{\Lambda(z-2l_{1D})} - e^{-\Lambda z}) \quad \textbf{A.38b}$$

Recalling equation A.28, equation A.38a can be simplified to:

$$A'_{+} = i a_{-2} \left(\frac{(\Lambda - i(\delta_z - i\sigma_z)) e^{\Lambda(z-2l_{1D})} + (\Lambda + i(\delta_z - i\sigma_z)) e^{-\Lambda z}}{\kappa k_z} \right) \quad \textbf{A.39}$$

The reflection co-efficient can now be calculated as:

$$|R(z)| = \left|\frac{A'_-(z)}{A'_+(z)}\right| = \left|i\kappa k_z\left(\frac{e^{\Lambda(z-2l_{1D})} - e^{-\Lambda z}}{(\Lambda - i(\delta_z - i\sigma_z))e^{\Lambda(z-2l_{1D})} + (\Lambda + i(\delta_z - i\sigma_z))e^{-\Lambda z}}\right)\right| \quad \textbf{A.40}$$

multiplying through by $e^{\Lambda l_{1D}}/e^{\Lambda l_{1D}}$:

$$|R(z)| = \left|i\kappa k_z\left(\frac{e^{\Lambda(z-l_{1D})} - e^{-\Lambda(z-l_{1D})}}{(\Lambda - i(\delta_z - i\sigma_z))e^{\Lambda(z-l_{1D})} + (\Lambda + i(\delta_z - i\sigma_z))e^{-\Lambda(z-l_{1D})}}\right)\right|$$

$$= \left|i\kappa k_z\left(\frac{e^{\Lambda(z-L_{1D})} - e^{-\Lambda(z-L_{1D})}}{\Lambda(e^{\Lambda(z-l_{1D})} + e^{-\Lambda(z-l_{1D})}) - i(\delta_z - i\sigma_z)(e^{\Lambda(z-l_{1D})} - e^{-\Lambda(z-l_{1D})})}\right)\right|$$

which implies:

$$|R(z)| = \left|i\kappa k_z\left[\frac{\sinh(\Lambda(z-l_{1D}))}{\Lambda\cosh(\Lambda(z-l_{1D})) - i(\delta_z - i\sigma_z)\sinh(\Lambda(z-l_{1D}))}\right]\right| \quad \textbf{A.41}$$

Noting $R(z)$ has its maximum value at $z = 0$:

$$|R(z)|\big|_{z=0} = \left|\frac{i\kappa k_z}{\Lambda\coth(\Lambda l_{1D}) - i(\delta_z - i\sigma_z)}\right| \quad \textbf{A.42}$$

The magnitude of the transmission co-efficient ($|T(z)|$) can be obtained via:

$$|T|^2 = 1 - |R|^2 - |\Omega|^2 \quad \textbf{A.43}$$

where Ω is the total system losses.

Appendix B: 2D Bragg Derivations

B.1 Derivation of the Coupled Wave Equations for 2D Reflectors

A 2D Bragg reflector, formed by a corrugation on either surface of a co-axial waveguide, can be described in the quasi-cartesian co-ordinates (r, s, z) by:

$$r(s, z) = r_0 + 2r_1 \cos(h_s s)\cos(h_z z) \qquad \textbf{B.1}$$

where r_0 is the mean radius of the conductor suface, r_1 is the corrugation amplitude and $h_{s,z}$ are the azimuthal and axial wave-numbers of the corrugation respectively. The azimuthal period is taken along the conductor surface ($s = \theta r_0$) with a periodicity $d_s = (2\pi r_0)/M$, where M is the number of azimuthal variations, giving $h_s = M/r_0$.

In terms of resonance between the structure and an incident EM field, it should be noted that the radial wave-number of the Bragg is undefined here, i.e. $h_r = 0$, as $d_r = \infty$. With this in mind one makes the assumption:

$$h_\tau = \sqrt{h_s^2 + h_r^2} = h_s \qquad \textbf{B.2}$$

where h_τ is the combined transverse Bragg vector.

As in the 1D Bragg reflector, the corrugation induces a perturbation in the natural log term of the Helmholtz equation, giving it the form:

$$\nabla^2 E + \frac{\omega^2\mu^2}{4\pi^2 Z_0^2}\ln^2\left(\frac{b_0}{a_0}(1 + 2\chi\cos(h_\tau\tau)\cos(h_z z))\right)E = 0 \qquad \textbf{B.3}$$

where b_0 and a_0 are the radii of the unperturbed outer and inner conductor sufaces respectively. $\chi = \pm r_1/r_0$ is the ratio of the deviation in the radius of the conductor surface to the mean radius, where the sign of χ determines the initial extrema of the corrugation.

The natural log term is expanded as in Section A.1, giving equation B.3 the form:

$$\nabla^2 E + k^2 E + \frac{4k^2\chi}{\ln(b_0/a_0)}\cos(h_\tau\tau)\cos(h_z z)E = 0 \qquad \textbf{B.4}$$

where the magnitude of the E field is composed of the parital waves:

$$\begin{aligned} E(z,\tau) &= (A_+ e^{-ik_{zA}z} + A_- e^{ik_{zA}z})e^{\pm ik_{cA}\tau} + (B_+ e^{-ik_{zB}z} + B_- e^{ik_{zB}z})e^{\pm ik_{cB}\tau} \\ &= \left[\begin{array}{l} (A_{+\mathrm{R}} e^{-ik_{cA}\tau} + A_{+\mathrm{L}} e^{ik_{cA}\tau})e^{-ik_{zA}z} + (A_{-\mathrm{R}} e^{-ik_{cA}\tau} + A_{-\mathrm{L}} e^{ik_{cA}\tau})e^{ik_{zA}z} \\ + (B_{+\mathrm{R}} e^{-ik_{cB}\tau} + B_{+\mathrm{L}} e^{ik_{cB}\tau})e^{-ik_{zB}z} + (B_{-\mathrm{R}} e^{-ik_{cB}\tau} + B_{-\mathrm{L}} e^{ik_{cB}\tau})e^{ik_{zB}z} \end{array}\right] \end{aligned} \qquad \textbf{B.5}$$

where τ denotes the transverse wave-vector, as the cut-off frequency in co-axial waveguide depends on both r and θ. The subscripts R, L denote the right and left hand polarisations of the partial waves that make up the linearly polarised $A_\pm$ and $B_\pm$ modes.

From this we set the wave-vector (k) in equation B.4 to be:

$$k = \sqrt{k_z^2 + k_c^2} = \sqrt{k_{zA}^2 + k_{cA}^2} \cong \sqrt{k_{zB}^2 + k_{cB}^2} \qquad \textbf{B.6}$$

The $\frac{4k^2\chi}{\ln(b_0/a_0)}\cos(h_\tau\tau)\cos(h_z z)E$ term in equation B.4 expands as:

$$\frac{k^2\chi}{\ln(b_0/a_0)}\left[\begin{array}{l} A_{+\mathrm{R}}(e^{-i(k_{cA}-h_\tau)\tau} + e^{-i(k_{cA}+h_\tau)\tau})(e^{-i(k_{zA}-h_z)z} + e^{-i(k_{zA}+h_z)z}) \\ + A_{+\mathrm{L}}(e^{i(k_{cA}+h_\tau)\tau} + e^{i(k_{cA}-h_\tau)\tau})(e^{-i(k_{zA}-h_z)z} + e^{-i(k_{zA}+h_z)z}) \\ + A_{-\mathrm{R}}(e^{-i(k_{cA}-h_\tau)\tau} + e^{-i(k_{cA}+h_\tau)\tau})(e^{i(k_{zA}+h_z)z} + e^{i(k_{zA}-h_z)z}) \\ + A_{-\mathrm{L}}(e^{i(k_{cA}+h_\tau)\tau} + e^{i(k_{cA}-h_\tau)\tau})(e^{i(k_{zA}+h_z)z} + e^{i(k_{zA}-h_z)z}) \\ + B_{+\mathrm{R}}(e^{-i(k_{cB}-h_\tau)\tau} + e^{-i(k_{cB}+h_\tau)\tau})(e^{-i(k_{zB}-h_z)z} + e^{-i(k_{zB}+h_z)z}) \\ + B_{+\mathrm{L}}(e^{i(k_{cB}+h_\tau)\tau} + e^{i(k_{cB}-h_\tau)\tau})(e^{-i(k_{zB}-h_z)z} + e^{-i(k_{zB}+h_z)z}) \\ + B_{-R}(e^{-i(k_{cB}-h_\tau)\tau} + e^{-i(k_{cB}+h_\tau)\tau})(e^{i(k_{zB}+h_z)z} + e^{i(k_{zB}-h_z)z}) \\ + B_{-L}(e^{i(k_{cB}+h_\tau)\tau} + e^{i(k_{cB}-h_\tau)\tau})(e^{i(k_{zB}+h_z)z} + e^{i(k_{zB}-h_z)z}) \end{array}\right] \qquad \textbf{B.7}$$

while the $\nabla^2 E = \dfrac{\partial^2 E}{\partial z^2} + \dfrac{\partial^2 E}{\partial \tau^2}$ term expands as:

$$\frac{\partial^2 E}{\partial z^2} = \begin{bmatrix} -k_{zA}^2[(A_{+\mathrm{R}}e^{-ik_{cA}\tau} + A_{+\mathrm{L}}e^{ik_{cA}\tau})e^{-ik_{zA}z} + (A_{-\mathrm{R}}e^{-ik_{cA}\tau} + A_{-\mathrm{L}}e^{ik_{cA}\tau})e^{ik_{zA}z}] \\ -k_{zB}^2[(B_{+\mathrm{R}}e^{-ik_{cB}\tau} + B_{+\mathrm{L}}e^{ik_{cB}\tau})e^{-ik_{zB}z} + (B_{-\mathrm{R}}e^{-ik_{cB}\tau} + B_{-\mathrm{L}}e^{ik_{cB}\tau})e^{ik_{zB}z}] \\ -2ik_{zA}\left(\dfrac{\partial A_{+\mathrm{R}}}{\partial z}e^{-ik_{cA}\tau} + \dfrac{\partial A_{+\mathrm{L}}}{\partial z}e^{ik_{cA}\tau}\right)e^{-ik_{zA}z} \\ +2ik_{zA}\left(\dfrac{\partial A_{-\mathrm{R}}}{\partial z}e^{-ik_{cA}\tau} + \dfrac{\partial A_{-\mathrm{L}}}{\partial z}e^{ik_{cA}\tau}\right)e^{ik_{zA}z} \\ -2ik_{zB}\left(\dfrac{\partial B_{+\mathrm{R}}}{\partial z}e^{-ik_{cB}\tau} + \dfrac{\partial B_{+\mathrm{L}}}{\partial z}e^{ik_{cB}\tau}\right)e^{-ik_{zB}z} \\ +2ik_{zB}\left(\dfrac{\partial B_{-\mathrm{R}}}{\partial z}e^{-ik_{cB}\tau} + \dfrac{\partial B_{-\mathrm{L}}}{\partial z}e^{ik_{cB}\tau}\right)e^{ik_{zB}z} \\ +\left(\dfrac{\partial^2 A_{+\mathrm{R}}}{\partial z^2}e^{-ik_{cA}\tau} + \dfrac{\partial^2 A_{+\mathrm{L}}}{\partial z^2}e^{ik_{cA}\tau}\right)e^{-ik_{zA}z} \\ +\left(\dfrac{\partial^2 A_{-\mathrm{R}}}{\partial z^2}e^{-ik_{cA}\tau} + \dfrac{\partial^2 A_{-\mathrm{L}}}{\partial z^2}e^{ik_{cA}\tau}\right)e^{ik_{zA}z} \\ +\left(\dfrac{\partial^2 B_{+\mathrm{R}}}{\partial z^2}e^{-ik_{cB}\tau} + \dfrac{\partial^2 B_{+\mathrm{L}}}{\partial z^2}e^{ik_{cB}\tau}\right)e^{-ik_{zB}z} \\ +\left(\dfrac{\partial^2 B_{-\mathrm{R}}}{\partial z^2}e^{-ik_{cB}\tau} + \dfrac{\partial^2 B_{-\mathrm{L}}}{\partial z^2}e^{ik_{cB}\tau}\right)e^{ik_{zB}z} \end{bmatrix} \quad \textbf{B.8}$$

and:

$$\frac{\partial^2 E}{\partial \tau^2} = \begin{bmatrix} -k_{cA}^2[(A_{+\mathrm{R}}e^{-ik_{cA}\tau} + A_{+\mathrm{L}}e^{ik_{cA}\tau})e^{-ik_{zA}z} + (A_{-\mathrm{R}}e^{-ik_{cA}\tau} + A_{-\mathrm{L}}e^{ik_{cA}\tau})e^{ik_{zA}z}] \\ -k_{cB}^2[(B_{+\mathrm{R}}e^{-ik_{cB}\tau} + B_{+\mathrm{L}}e^{ik_{cB}\tau})e^{-ik_{zB}z} + (B_{-\mathrm{R}}e^{-ik_{cB}\tau} + B_{-\mathrm{L}}e^{ik_{cB}\tau})e^{ik_{zB}z}] \\ -2ik_{cA}\left(\frac{\partial A_{+\mathrm{R}}}{\partial \tau}e^{-ik_{cA}\tau} - \frac{\partial A_{+\mathrm{L}}}{\partial \tau}e^{ik_{cA}\tau}\right)e^{-ik_{zA}z} \\ -2ik_{cA}\left(\frac{\partial A_{-\mathrm{R}}}{\partial \tau}e^{-ik_{cA}\tau} - \frac{\partial A_{-\mathrm{L}}}{\partial \tau}e^{ik_{cA}\tau}\right)e^{ik_{zA}z} \\ -2ik_{cB}\left(\frac{\partial B_{+\mathrm{R}}}{\partial \tau}e^{-ik_{cB}\tau} - \frac{\partial B_{+\mathrm{L}}}{\partial \tau}e^{ik_{cB}\tau}\right)e^{-ik_{zB}z} \\ -2ik_{cB}\left(\frac{\partial B_{-\mathrm{R}}}{\partial \tau}e^{-ik_{cB}\tau} - \frac{\partial B_{-\mathrm{L}}}{\partial \tau}e^{ik_{cB}\tau}\right)e^{ik_{zB}z} \\ +\left(\frac{\partial^2 A_{+\mathrm{R}}}{\partial \tau^2}e^{-ik_{cA}\tau} + \frac{\partial^2 A_{+\mathrm{L}}}{\partial \tau^2}e^{ik_{cA}\tau}\right)e^{-ik_{zA}z} \\ +\left(\frac{\partial^2 A_{-\mathrm{R}}}{\partial \tau^2}e^{-ik_{cA}\tau} + \frac{\partial^2 A_{-\mathrm{L}}}{\partial \tau^2}e^{ik_{cA}\tau}\right)e^{ik_{zA}z} \\ +\left(\frac{\partial^2 B_{+\mathrm{R}}}{\partial \tau^2}e^{-ik_{cB}\tau} + \frac{\partial^2 B_{+\mathrm{L}}}{\partial \tau^2}e^{ik_{cB}\tau}\right)e^{-ik_{zB}z} \\ +\left(\frac{\partial^2 B_{-\mathrm{R}}}{\partial \tau^2}e^{-ik_{cB}\tau} + \frac{\partial^2 B_{-\mathrm{L}}}{\partial \tau^2}e^{ik_{cB}\tau}\right)e^{ik_{zB}z} \end{bmatrix} \quad \textbf{B.9}$$

which, taking:

$$-\begin{pmatrix} (k_{zA}^2 + k_{cA}^2)[A_{+\mathrm{R,L}}e^{\mp ik_{cA}\tau}e^{-ik_{zA}z} + A_{-\mathrm{R,L}}e^{\mp ik_{cA}\tau}e^{ik_{zA}z}] \\ +(k_{zB}^2 + k_{cB}^2)[B_{+\mathrm{R,L}}e^{\mp ik_{cB}\tau}e^{-ik_{zB}z} + B_{-\mathrm{R,L}}e^{\mp ik_{cB}\tau}e^{ik_{zB}z}] \end{pmatrix} = -k^2 E \quad \textbf{B.10a}$$

with:

$$2ik_{zA}\left(\frac{\partial A_{+\mathrm{R,L}}}{\partial z}e^{-ik_{zA}z} + \frac{\partial A_{-\mathrm{R,L}}}{\partial z}e^{ik_{zA}z}\right) \gg \left(\frac{\partial^2 A_{+\mathrm{R,L}}}{\partial z^2}e^{-ik_{zA}z} + \frac{\partial^2 A_{-\mathrm{R,L}}}{\partial z^2}e^{ik_{zA}z}\right) \quad \textbf{B.10b}$$

and

$$2ik_{cB}\left(\frac{\partial B_{+\mathrm{R,L}}}{\partial \tau}e^{-ik_{zB}z} - \frac{\partial B_{-\mathrm{R,L}}}{\partial \tau}e^{ik_{zB}z}\right) \gg \left(\frac{\partial^2 B_{+\mathrm{R,L}}}{\partial \tau^2}e^{-ik_{zB}z} + \frac{\partial^2 B_{-\mathrm{R,L}}}{\partial \tau^2}e^{ik_{zB}z}\right) \quad \textbf{B.10c}$$

gives $\nabla^2 E$ as:

$$
\begin{aligned}
\nabla^2 E = \; & -k^2 E \\
& -2i\left[\left(\frac{\partial A_{+\mathrm{R}}}{\partial z}k_{zA} + \frac{\partial A_{+\mathrm{R}}}{\partial \tau}k_{cA}\right)e^{-ik_{cA}\tau} + \left(\frac{\partial A_{+\mathrm{L}}}{\partial z}k_{zA} - \frac{\partial A_{+\mathrm{L}}}{\partial \tau}k_{cA}\right)e^{ik_{cA}\tau}\right]e^{-ik_{zA}z} \\
& +2i\left[\left(\frac{\partial A_{-\mathrm{R}}}{\partial z}k_{zA} - \frac{\partial A_{-\mathrm{R}}}{\partial \tau}k_{cA}\right)e^{-ik_{cA}\tau} + \left(\frac{\partial A_{-\mathrm{L}}}{\partial z}k_{zA} + \frac{\partial A_{-\mathrm{L}}}{\partial \tau}k_{cA}\right)e^{ik_{cA}\tau}\right]e^{ik_{zA}z} \\
& -2i\left[\left(\frac{\partial B_{+\mathrm{R}}}{\partial z}k_{zB} + \frac{\partial B_{+\mathrm{R}}}{\partial \tau}k_{cB}\right)e^{-ik_{cB}\tau} + \left(\frac{\partial B_{+\mathrm{L}}}{\partial z}k_{zB} - \frac{\partial B_{+\mathrm{L}}}{\partial \tau}k_{cB}\right)e^{ik_{cB}\tau}\right]e^{-ik_{zB}z} \\
& +2i\left[\left(\frac{\partial B_{-\mathrm{R}}}{\partial z}k_{zB} - \frac{\partial B_{-\mathrm{R}}}{\partial \tau}k_{cB}\right)e^{-ik_{cB}\tau} + \left(\frac{\partial B_{-\mathrm{L}}}{\partial z}k_{zB} + \frac{\partial B_{-\mathrm{L}}}{\partial z}k_{cB}\right)e^{ik_{cB}\tau}\right]e^{ik_{zB}z} \\
& +\left(\frac{\partial^2 A_{+\mathrm{R}}}{\partial \tau^2}e^{-ik_{cA}\tau} + \frac{\partial^2 A_{+\mathrm{L}}}{\partial \tau^2}e^{ik_{cA}\tau}\right)e^{-ik_{zA}z} \\
& +\left(\frac{\partial^2 A_{-\mathrm{R}}}{\partial \tau^2}e^{-ik_{cA}\tau} + \frac{\partial^2 A_{-\mathrm{L}}}{\partial \tau^2}e^{ik_{cA}\tau}\right)e^{ik_{zA}z} \\
& +\left(\frac{\partial^2 B_{+\mathrm{R}}}{\partial z^2}e^{-ik_{cB}\tau} + \frac{\partial^2 B_{+\mathrm{L}}}{\partial z^2}e^{ik_{cB}\tau}\right)e^{-ik_{zB}z} \\
& +\left(\frac{\partial^2 B_{-\mathrm{R}}}{\partial z^2}e^{-ik_{cB}\tau} + \frac{\partial^2 B_{-\mathrm{L}}}{\partial z^2}e^{ik_{cB}\tau}\right)e^{ik_{zB}z}
\end{aligned}
\qquad \textbf{B.11}
$$

Here the remaining second order terms account for diffractive effects between the longitudinaly propagating $A_{\pm}$ and close to cut-off $B_{\pm}$ partial waves.

Substituting equations B.11 & B.7 into equation B.4 gives the Helmholtz equation the form:

$$
\begin{aligned}
&-2i\left[\left(\frac{\partial A_{+\mathrm{R}}}{\partial z}k_{zA}+\frac{\partial A_{+\mathrm{R}}}{\partial \tau}k_{cA}\right)e^{-ik_{cA}\tau}+\left(\frac{\partial A_{+\mathrm{L}}}{\partial z}k_{zA}-\frac{\partial A_{+\mathrm{L}}}{\partial \tau}k_{cA}\right)e^{ik_{cA}\tau}\right]e^{-ik_{zA}z}\\
&+2i\left[\left(\frac{\partial A_{-\mathrm{R}}}{\partial z}k_{zA}-\frac{\partial A_{-\mathrm{R}}}{\partial \tau}k_{cA}\right)e^{-ik_{cA}\tau}+\left(\frac{\partial A_{-\mathrm{L}}}{\partial z}k_{zA}+\frac{\partial A_{-\mathrm{L}}}{\partial \tau}k_{cA}\right)e^{ik_{cA}\tau}\right]e^{ik_{zA}z}\\
&-2i\left[\left(\frac{\partial B_{+\mathrm{R}}}{\partial z}k_{zB}+\frac{\partial B_{+\mathrm{R}}}{\partial \tau}k_{cB}\right)e^{-ik_{cB}\tau}+\left(\frac{\partial B_{+\mathrm{L}}}{\partial z}k_{zB}-\frac{\partial B_{+\mathrm{L}}}{\partial \tau}k_{cB}\right)e^{ik_{cB}\tau}\right]e^{-ik_{zB}z}\\
&+2i\left[\left(\frac{\partial B_{-\mathrm{R}}}{\partial z}k_{zB}-\frac{\partial B_{-\mathrm{R}}}{\partial \tau}k_{cB}\right)e^{-ik_{cB}\tau}+\left(\frac{\partial B_{-\mathrm{L}}}{\partial z}k_{zB}+\frac{\partial B_{-\mathrm{L}}}{\partial z}k_{cB}\right)e^{ik_{cB}\tau}\right]e^{ik_{zB}z}\\
&+\left(\frac{\partial^2 A_{+\mathrm{R}}}{\partial \tau^2}e^{-ik_{cA}\tau}+\frac{\partial^2 A_{+\mathrm{L}}}{\partial \tau^2}e^{ik_{cA}\tau}\right)e^{-ik_{zA}z}\\
&+\left(\frac{\partial^2 A_{-\mathrm{R}}}{\partial \tau^2}e^{-ik_{cA}\tau}+\frac{\partial^2 A_{-\mathrm{L}}}{\partial \tau^2}e^{ik_{cA}\tau}\right)e^{ik_{zA}z}\\
&+\left(\frac{\partial^2 B_{+\mathrm{R}}}{\partial z^2}e^{-ik_{cB}\tau}+\frac{\partial^2 B_{+\mathrm{L}}}{\partial z^2}e^{ik_{cB}\tau}\right)e^{-ik_{zB}z}\\
&+\left(\frac{\partial^2 B_{-\mathrm{R}}}{\partial z^2}e^{-ik_{cB}\tau}+\frac{\partial^2 B_{-\mathrm{L}}}{\partial z^2}e^{ik_{cB}\tau}\right)e^{ik_{zB}z}
\end{aligned}
\qquad \textbf{B.12}
$$

$$
+\frac{k^2\chi}{\ln(b_0/a_0)}\begin{bmatrix}
A_{+\mathrm{R}}(e^{-i(k_{cA}-h_\tau)\tau}+e^{-i(k_{cA}+h_\tau)\tau})(e^{-i(k_{zA}-h_z)z}+e^{-i(k_{zA}+h_z)z})\\
+A_{+\mathrm{L}}(e^{i(k_{cA}+h_\tau)\tau}+e^{i(k_{cA}-h_\tau)\tau})(e^{-i(k_{zA}-h_z)z}+e^{-i(k_{zA}+h_z)z})\\
+A_{-\mathrm{R}}(e^{-i(k_{cA}-h_\tau)\tau}+e^{-i(k_{cA}+h_\tau)\tau})(e^{i(k_{zA}+h_z)z}+e^{i(k_{zA}-h_z)z})\\
+A_{-\mathrm{L}}(e^{i(k_{cA}+h_\tau)\tau}+e^{i(k_{cA}-h_\tau)\tau})(e^{i(k_{zA}+h_z)z}+e^{i(k_{zA}-h_z)z})\\
+B_{+\mathrm{R}}(e^{-i(k_{cB}-h_\tau)\tau}+e^{-i(k_{cB}+h_\tau)\tau})(e^{-i(k_{zB}-h_z)z}+e^{-i(k_{zB}+h_z)z})\\
+B_{+\mathrm{L}}(e^{i(k_{cB}+h_\tau)\tau}+e^{i(k_{cB}-h_\tau)\tau})(e^{-i(k_{zB}-h_z)z}+e^{-i(k_{zB}+h_z)z})\\
+B_{-R}(e^{-i(k_{cB}-h_\tau)\tau}+e^{-i(k_{cB}+h_\tau)\tau})(e^{i(k_{zB}+h_z)z}+e^{i(k_{zB}-h_z)z})\\
+B_{-L}(e^{i(k_{cB}+h_\tau)\tau}+e^{i(k_{cB}-h_\tau)\tau})(e^{i(k_{zB}+h_z)z}+e^{i(k_{zB}-h_z)z})
\end{bmatrix}=0
$$

If we now multiply equation B.12 by $e^{i(k_{zA}z + k_{cA}\tau)}$:

$$
\begin{aligned}
&-2i\left[\left(\frac{\partial A_{+\mathrm{R}}}{\partial z}k_{zA} + \frac{\partial A_{+\mathrm{R}}}{\partial \tau}k_{cA}\right) + \left(\frac{\partial A_{+\mathrm{L}}}{\partial z}k_{zA} - \frac{\partial A_{+\mathrm{L}}}{\partial \tau}k_{cA}\right)e^{2ik_{cA}\tau}\right] \\
&+ 2i\left[\left(\frac{\partial A_{-\mathrm{R}}}{\partial z}k_{zA} - \frac{\partial A_{-\mathrm{R}}}{\partial \tau}k_{cA}\right) + \left(\frac{\partial A_{-\mathrm{L}}}{\partial z}k_{zA} + \frac{\partial A_{-\mathrm{L}}}{\partial \tau}k_{cA}\right)e^{2ik_{cA}\tau}\right]e^{2ik_{zA}z} \\
&-2i\left[\begin{array}{c}\left(\frac{\partial B_{+\mathrm{R}}}{\partial z}k_{zB} + \frac{\partial B_{+\mathrm{R}}}{\partial \tau}k_{cB}\right)e^{i(k_{cA}-k_{cB})\tau} \\ +\left(\frac{\partial B_{+\mathrm{L}}}{\partial z}k_{zB} - \frac{\partial B_{+\mathrm{L}}}{\partial \tau}k_{cB}\right)e^{i(k_{cA}+k_{cB})\tau}\end{array}\right]e^{i(k_{zA}-k_{zB})z} \\
&+2i\left[\begin{array}{c}\left(\frac{\partial B_{-\mathrm{R}}}{\partial z}k_{zB} - \frac{\partial B_{-\mathrm{R}}}{\partial \tau}k_{cB}\right)e^{i(k_{cA}-k_{cB})\tau} \\ +\left(\frac{\partial B_{-\mathrm{L}}}{\partial z}k_{zB} + \frac{\partial B_{-\mathrm{L}}}{\partial z}k_{cB}\right)e^{i(k_{cA}+k_{cB})\tau}\end{array}\right]e^{i(k_{zA}+k_{zB})z} \\
&+\left(\frac{\partial^2 A_{+\mathrm{R}}}{\partial \tau^2} + \frac{\partial^2 A_{+\mathrm{L}}}{\partial \tau^2}e^{2ik_{cA}\tau}\right) + \left(\frac{\partial^2 A_{-\mathrm{R}}}{\partial \tau^2} + \frac{\partial^2 A_{-\mathrm{L}}}{\partial \tau^2}e^{2ik_{cA}\tau}\right)e^{2ik_{zA}z} \\
&+\left(\frac{\partial^2 B_{+\mathrm{R}}}{\partial z^2}e^{i(k_{cA}-k_{cB})\tau} + \frac{\partial^2 B_{+\mathrm{L}}}{\partial z^2}e^{i(k_{cA}+k_{cB})\tau}\right)e^{i(k_{zA}-k_{zB})z} \\
&+\left(\frac{\partial^2 B_{-\mathrm{R}}}{\partial z^2}e^{i(k_{cA}-k_{cB})\tau} + \frac{\partial^2 B_{-\mathrm{L}}}{\partial z^2}e^{i(k_{cA}+k_{cB})\tau}\right)e^{i(k_{zA}+k_{zB})z} \\
&+\frac{k^2\chi}{\ln(b_0/a_0)}\times \\
&\times\left[\begin{array}{c}A_{+\mathrm{R}}(e^{ih_\tau\tau} + e^{-ih_\tau\tau})(e^{ih_z z} + e^{-ih_z z}) \\ +A_{+\mathrm{L}}(e^{i(2k_{cA}+h_\tau)\tau} + e^{i(2k_{cA}-h_\tau)\tau})(e^{ih_z z} + e^{-ih_z z}) \\ +A_{-\mathrm{R}}(e^{ih_\tau\tau} + e^{-ih_\tau\tau})(e^{i(2k_{zA}+h_z)z} + e^{i(2k_{zA}-h_z)z}) \\ +A_{-\mathrm{L}}(e^{i(2k_{cA}+h_\tau)\tau} + e^{i(2k_{cA}-h_\tau)\tau})(e^{i(2k_{zA}+h_z)z} + e^{i(2k_{zA}-h_z)z}) \\ +B_{+\mathrm{R}}(e^{i(k_{cA}-k_{cB}+h_\tau)\tau} + e^{i(k_{cA}-k_{cB}-h_\tau)\tau})(e^{i(k_{zA}-k_{zB}+h_z)z} + e^{i(k_{zA}-k_{zB}-h_z)z}) \\ +B_{+\mathrm{L}}(e^{i(k_{cA}+k_{cB}+h_\tau)\tau} + e^{i(k_{cA}+k_{cB}-h_\tau)\tau})(e^{i(k_{zA}-k_{zB}+h_z)z} + e^{i(k_{zA}-k_{zB}-h_z)z}) \\ +B_{-\mathrm{R}}(e^{i(k_{cA}-k_{cB}+h_\tau)\tau} + e^{i(k_{cA}-k_{cB}-h_\tau)\tau})(e^{i(k_{zA}+k_{zB}+h_z)z} + e^{i(k_{zA}+k_{zB}-h_z)z}) \\ +B_{-\mathrm{L}}(e^{i(k_{cA}+k_{cB}+h_\tau)\tau} + e^{i(k_{cA}+k_{cB}-h_\tau)\tau})(e^{i(k_{zA}+k_{zB}+h_z)z} + e^{i(k_{zA}+k_{zB}-h_z)z})\end{array}\right] \\
&= 0
\end{aligned}
\qquad \textbf{B.13}
$$

and consider the deviation between h_i and k_i to be:

$$[(k_{iA,\,B} \pm k_{iB,\,A}) - h_i] - i\sigma_i \;=\; \delta_{\pm i} - i\sigma_i \qquad \textbf{B.14}$$

where σ_i is the ohmic losses along the *i'th* co-ordinate, and δ_i is the loss-less detuning, substituting for $\delta_i - i\sigma_i$ and taking the slow varying wave approximation, all terms in equation B.13 varying faster than $e^{\pm i(\delta_{\pm z} - i\sigma_z)z} e^{\pm i(\delta_{\pm\tau} - i\sigma_\tau)\tau}$ average to zero, leaving:

$$\begin{aligned} &-2i\left[k_{zA}\frac{\partial A_{+\mathrm{R}}}{\partial z} + k_{cA}\frac{\partial A_{+\mathrm{R}}}{\partial \tau}\right] + \frac{\partial^2 A_{+\mathrm{R}}}{\partial \tau^2} \\ &+\frac{k^2\chi}{\ln(b_0/a_0)}\left[\begin{array}{l}(B_{+\mathrm{R}}e^{-i\delta_{-\tau BA}\tau} + B_{+\mathrm{L}}e^{i\delta_{+\tau}\tau})e^{i\delta_{-z\mathrm{AB}}z} \\ +(B_{-R}e^{-i\delta_{-\tau BA}\tau} + B_{-L}e^{i\delta_{+\tau}\tau})e^{i\delta_{+z}z}\end{array}\right] = 0 \end{aligned} \qquad \textbf{B.15a}$$

Here it should be noted $\delta_{-\tau BA} = -\delta_{-\tau AB}$, $\delta_{-zAB} = -\delta_{-zBA}$ the subscripts mearly denote how the magnitude of the detunings were arrived at for a given coupling between partial waves, i.e. $\delta_{-iAB} = k_{iA} - k_{iB}$, $\delta_{-iBA} = k_{iB} - k_{iA}$. The order of A and B is largely arbitrary but has been chosen to reflect the common assumptions $k_{cA} \ll k_{cB}$, $k_{zA} \gg k_{zB}$.

Following the same procedure, multiplying equation B.12 by, initially, $e^{i(k_{zA}z - k_{cA}\tau)}$, then $e^{-i(k_{zA}z + k_{cA}\tau)}$, $e^{-i(k_{zA}z - k_{cA}\tau)}$, $e^{i(k_{cB}\tau + k_{zB}z)}$, $e^{i(k_{cB}\tau - k_{zB}z)}$, $e^{-i(k_{cB}\tau + k_{zB}z)}$ and $e^{-i(k_{cB}\tau - k_{zB}z)}$, leads to the following:

$$\begin{aligned} &-2i\left[k_{zA}\frac{\partial A_{+\mathrm{L}}}{\partial z} - k_{cA}\frac{\partial A_{+\mathrm{L}}}{\partial \tau}\right] + \frac{\partial^2 A_{+\mathrm{L}}}{\partial \tau^2} \\ &+\frac{k^2\chi}{\ln(b_0/a_0)}\left[\begin{array}{l}(B_{+\mathrm{R}}e^{-i\delta_{+\tau}\tau} + B_{+\mathrm{L}}e^{i\delta_{-\tau BA}\tau})e^{i\delta_{-zAB}z} \\ +(B_{-R}e^{-i\delta_{+\tau}\tau} + B_{-L}e^{i\delta_{-\tau BA}\tau})e^{i\delta_{+z}z}\end{array}\right] = 0 \end{aligned} \qquad \textbf{B.15b}$$

$$\begin{aligned} &2i\left[k_{zA}\frac{\partial A_{-\mathrm{L}}}{\partial z} + k_{cA}\frac{\partial A_{-\mathrm{L}}}{\partial \tau}\right] + \frac{\partial^2 A_{-\mathrm{L}}}{\partial \tau^2} \\ &+\frac{k^2\chi}{\ln(b_0/a_0)}\left[\begin{array}{l}(B_{+\mathrm{R}}e^{-i\delta_{+\tau}\tau} + B_{+\mathrm{L}}e^{i\delta_{-\tau BA}\tau})e^{-i\delta_{+z}z} \\ +(B_{-R}e^{-i\delta_{+\tau}\tau} + B_{-L}e^{i\delta_{-\tau BA}\tau})e^{-i\delta_{-zAB}z}\end{array}\right] = 0 \end{aligned} \qquad \textbf{B.15c}$$

$$2i\left[k_{zA}\frac{\partial A_{\text{-R}}}{\partial z}-k_{cA}\frac{\partial A_{\text{-R}}}{\partial \tau}\right]+\frac{\partial^2 A_{\text{-R}}}{\partial \tau^2}$$
$$+\frac{k^2\chi}{\ln(b_0/a_0)}\left[\begin{array}{l}(B_{+\text{R}}e^{-i\delta_{-\tau BA}\tau}+B_{+\text{L}}e^{i\delta_{+\tau}\tau})e^{-i\delta_{+z}z}\\+(B_{-R}e^{-i\delta_{-\tau BA}\tau}+B_{-L}e^{i\delta_{+\tau}\tau})e^{-i\delta_{-zAB}z}\end{array}\right]=0 \qquad \textbf{B.15d}$$

$$-2i\left[k_{zB}\frac{\partial B_{+\text{R}}}{\partial z}+k_{cB}\frac{\partial B_{+\text{R}}}{\partial \tau}\right]+\frac{\partial^2 B_{+\text{R}}}{\partial z^2}$$
$$+\frac{k^2\chi}{\ln(b_0/a_0)}\left[\begin{array}{l}(A_{+\text{R}}e^{i\delta_{-\tau BA}\tau}+A_{+\text{L}}e^{i\delta_{+\tau}\tau})e^{-i\delta_{-zAB}z}\\+(A_{\text{-R}}e^{i\delta_{-\tau BA}\tau}+A_{\text{-L}}e^{i\delta_{+\tau}\tau})e^{i\delta_{+z}z}\end{array}\right]=0 \qquad \textbf{B.15e}$$

$$2i\left[k_{zB}\frac{\partial B_{\text{-R}}}{\partial z}-k_{cB}\frac{\partial B_{\text{-R}}}{\partial \tau}\right]+\frac{\partial^2 B_{\text{-R}}}{\partial z^2}$$
$$+\frac{k^2\chi}{\ln(b_0/a_0)}\left[\begin{array}{l}(A_{+\text{R}}e^{i\delta_{-\tau BA}\tau}+A_{+\text{L}}e^{i\delta_{+\tau}\tau})e^{-i\delta_{+z}z}\\+(A_{\text{-R}}e^{i\delta_{-\tau BA}\tau}+A_{\text{-L}}e^{i\delta_{+\tau}\tau})e^{i\delta_{-zAB}z}\end{array}\right]=0 \qquad \textbf{B.15f}$$

$$2i\left[k_{zB}\frac{\partial B_{\text{-L}}}{\partial z}+k_{cB}\frac{\partial B_{\text{-L}}}{\partial \tau}\right]+\frac{\partial^2 B_{\text{-L}}}{\partial z^2}$$
$$+\frac{k^2\chi}{\ln(b_0/a_0)}\left[\begin{array}{l}(A_{+\text{R}}e^{-i\delta_{+\tau}\tau}+A_{+\text{L}}e^{-i\delta_{-\tau BA}\tau})e^{-i\delta_{+z}z}\\(A_{\text{-R}}e^{-i\delta_{+\tau}\tau}+A_{\text{-L}}e^{-i\delta_{-\tau BA}\tau})e^{i\delta_{-zAB}z}\end{array}\right]=0 \qquad \textbf{B.15g}$$

$$-2i\left[k_{zB}\frac{\partial B_{+\text{L}}}{\partial z}-k_{cB}\frac{\partial B_{+\text{L}}}{\partial \tau}\right]+\frac{\partial^2 B_{+\text{L}}}{\partial z^2}$$
$$+\frac{k^2\chi}{\ln(b_0/a_0)}\left[\begin{array}{l}(A_{+\text{R}}e^{-i\delta_{+\tau}\tau}+A_{+\text{L}}e^{-i\delta_{-\tau BA}\tau})e^{-i\delta_{-zAB}z}\\+(A_{\text{-R}}e^{-i\delta_{+\tau}\tau}+A_{\text{-L}}e^{-i\delta_{-\tau BA}\tau})e^{i\delta_{+z}z}\end{array}\right]=0 \qquad \textbf{B.15h}$$

Accounting for the ohmic losses σ_i along a given coordinate i (where σ_τ does not have to equal σ_z) and simplifying $\delta_{-\tau BA,\,+\tau}=\delta_\tau$, $\delta_{-zAB,\,+z}=\delta_z$, the previous set of equations can be expressed as:

$$k_{zA}\frac{\partial A_{+\text{R}}}{\partial z}+k_{cA}\frac{\partial A_{+\text{R}}}{\partial \tau}+\frac{i}{2}\frac{\partial^2 A_{+\text{R}}}{\partial \tau^2}$$
$$+i\frac{k^2\chi}{2\ln(b_0/a_0)}\left[\begin{array}{l}(B_{+\text{R}}e^{-i(\delta_\tau-i\sigma_\tau)\tau}+B_{+\text{L}}e^{i(\delta_\tau-i\sigma_\tau)\tau})e^{i(\delta_z-i\sigma_z)z}\\+(B_{-R}e^{-i(\delta_\tau-i\sigma_\tau)\tau}+B_{-L}e^{i(\delta_\tau-i\sigma_\tau)\tau})e^{i(\delta_z-i\sigma_z)z}\end{array}\right]=0 \qquad \textbf{B.16a}$$

$$k_{zA}\frac{\partial A_{+\mathrm{L}}}{\partial z} - k_{cA}\frac{\partial A_{+\mathrm{L}}}{\partial \tau} + \frac{i}{2}\frac{\partial^2 A_{+\mathrm{L}}}{\partial \tau^2}$$

$$+ i\frac{k^2\chi}{2\ln(b_0/a_0)}\left[\begin{array}{l}(B_{+\mathrm{R}}e^{-i(\delta_\tau - i\sigma_\tau)\tau} + B_{+\mathrm{L}}e^{i(\delta_\tau - i\sigma_\tau)\tau})e^{i(\delta_z - i\sigma_z)z} \\ +(B_{-R}e^{-i(\delta_\tau - i\sigma_\tau)\tau} + B_{-L}e^{i(\delta_\tau - i\sigma_\tau)\tau})e^{i(\delta_z - i\sigma_z)z}\end{array}\right] = 0 \qquad \textbf{B.16b}$$

$$k_{zA}\frac{\partial A_{\text{-L}}}{\partial z} + k_{cA}\frac{\partial A_{\text{-L}}}{\partial \tau} - \frac{i}{2}\frac{\partial^2 A_{\text{-L}}}{\partial \tau^2}$$

$$-i\frac{k^2\chi}{2\ln(b_0/a_0)}\left[\begin{array}{l}(B_{+\mathrm{R}}e^{-i(\delta_\tau - i\sigma_\tau)\tau} + B_{+\mathrm{L}}e^{i(\delta_\tau - i\sigma_\tau)\tau})e^{-i(\delta_z - i\sigma_z)z} \\ +(B_{-R}e^{-i(\delta_\tau - i\sigma_\tau)\tau} + B_{-L}e^{i(\delta_\tau - i\sigma_\tau)\tau})e^{-i(\delta_z - i\sigma_z)z}\end{array}\right] = 0 \qquad \textbf{B.16c}$$

$$k_{zA}\frac{\partial A_{\text{-R}}}{\partial z} - k_{cA}\frac{\partial A_{\text{-R}}}{\partial \tau} - \frac{i}{2}\frac{\partial^2 A_{\text{-R}}}{\partial \tau^2}$$

$$-i\frac{k^2\chi}{2\ln(b_0/a_0)}\left[\begin{array}{l}(B_{+\mathrm{R}}e^{-i(\delta_\tau - i\sigma_\tau)\tau} + B_{+\mathrm{L}}e^{i(\delta_\tau - i\sigma_\tau)\tau})e^{-i(\delta_z - i\sigma_z)z} \\ +(B_{-R}e^{-i(\delta_\tau - i\sigma_\tau)\tau} + B_{-L}e^{i(\delta_\tau - i\sigma_\tau)\tau})e^{-i(\delta_z - i\sigma_z)z}\end{array}\right] = 0 \qquad \textbf{B.16d}$$

$$k_{zB}\frac{\partial B_{+\mathrm{R}}}{\partial z} + k_{cB}\frac{\partial B_{+\mathrm{R}}}{\partial \tau} + \frac{i}{2}\frac{\partial^2 B_{+\mathrm{R}}}{\partial z^2}$$

$$+ i\frac{k^2\chi}{2\ln(b_0/a_0)}\left[\begin{array}{l}(A_{+\mathrm{R}}e^{i(\delta_\tau - i\sigma_\tau)\tau} + A_{+\mathrm{L}}e^{i(\delta_\tau - i\sigma_\tau)\tau})e^{-i(\delta_z - i\sigma_z)z} \\ +(A_{\text{-R}}e^{i(\delta_\tau - i\sigma_\tau)\tau} + A_{\text{-L}}e^{i(\delta_\tau - i\sigma_\tau)\tau})e^{i(\delta_z - i\sigma_z)z}\end{array}\right] = 0 \qquad \textbf{B.16e}$$

$$k_{zB}\frac{\partial B_{\text{-R}}}{\partial z} - k_{cB}\frac{\partial B_{\text{-R}}}{\partial \tau} - \frac{i}{2}\frac{\partial^2 B_{\text{-R}}}{\partial z^2}$$

$$-i\frac{k^2\chi}{2\ln(b_0/a_0)}\left[\begin{array}{l}(A_{+\mathrm{R}}e^{i(\delta_\tau - i\sigma_\tau)\tau} + A_{+\mathrm{L}}e^{i(\delta_\tau - i\sigma_\tau)\tau})e^{-i(\delta_z - i\sigma_z)z} \\ +(A_{\text{-R}}e^{i(\delta_\tau - i\sigma_\tau)\tau} + A_{\text{-L}}e^{i(\delta_\tau - i\sigma_\tau)\tau})e^{i(\delta_z - i\sigma_z)z}\end{array}\right] = 0 \qquad \textbf{B.16f}$$

$$k_{zB}\frac{\partial B_{\text{-L}}}{\partial z} + k_{cB}\frac{\partial B_{\text{-L}}}{\partial \tau} - \frac{i}{2}\frac{\partial^2 B_{\text{-L}}}{\partial z^2}$$

$$-i\frac{k^2\chi}{2\ln(b_0/a_0)}\left[\begin{array}{l}(A_{+\mathrm{R}}e^{-i(\delta_\tau - i\sigma_\tau)\tau} + A_{+\mathrm{L}}e^{-i(\delta_\tau - i\sigma_\tau)\tau})e^{-i(\delta_z - i\sigma_z)z} \\ (A_{\text{-R}}e^{-i(\delta_\tau - i\sigma_\tau)\tau} + A_{\text{-L}}e^{-i(\delta_\tau - i\sigma_\tau)\tau})e^{i(\delta_z - i\sigma_z)z}\end{array}\right] = 0 \qquad \textbf{B.16g}$$

$$k_{zB}\frac{\partial B_{+\mathrm{L}}}{\partial z} - k_{cB}\frac{\partial B_{+\mathrm{L}}}{\partial \tau} + \frac{i}{2}\frac{\partial^2 B_{+\mathrm{L}}}{\partial z^2}$$

$$+ i\frac{k^2\chi}{2\ln(b_0/a_0)}\left[\begin{array}{l}(A_{+\mathrm{R}}e^{-i(\delta_\tau - i\sigma_\tau)\tau} + A_{+\mathrm{L}}e^{-i(\delta_\tau - i\sigma_\tau)\tau})e^{-i(\delta_z - i\sigma_z)z} \\ +(A_{\text{-R}}e^{-i(\delta_\tau - i\sigma_\tau)\tau} + A_{\text{-L}}e^{-i(\delta_\tau - i\sigma_\tau)\tau})e^{i(\delta_z - i\sigma_z)z}\end{array}\right] = 0 \qquad \textbf{B.16h}$$

If we now consider the partial-wave amplitudes as being functions of the total detuning from Bragg vectors (c.f. Figure 3.7 and equations 3.34a-3.34d) noting that $k_{si} = k_{ci}$, taking $k_{zA} \gg k_{zB}$, $k_{cA} \ll k_{cB}$, these take the form:

$A_{+\mathrm{R}} = A'_{+\mathrm{R}} e^{i(\delta_z - i\sigma_z)z}$, $A_{+\mathrm{L}} = A'_{+\mathrm{L}} e^{i(\delta_z - i\sigma_z)z}$, $A_{-\mathrm{R}} = A'_{-\mathrm{R}} e^{-i(\delta_z - i\sigma_z)z}$

$A_{-\mathrm{L}} = A'_{-\mathrm{L}} e^{-i(\delta_z - i\sigma_z)z}$, $B_{+\mathrm{R}} = B'_{+\mathrm{R}} e^{i(\delta_\tau - i\sigma_\tau)\tau}$, $B_{-\mathrm{R}} = B'_{-\mathrm{R}} e^{i(\delta_\tau - i\sigma_\tau)\tau}$,

$B_{+\mathrm{L}} = B'_{+\mathrm{L}} e^{-i(\delta_\tau - i\sigma_\tau)\tau}$, $B_{-\mathrm{L}} = B'_{-\mathrm{L}} e^{-i(\delta_\tau - i\sigma_\tau)\tau}$

yielding:

$$\frac{\partial A_{+\mathrm{R,L}}}{\partial z} = \left(i(\delta_z - i\sigma_z) A'_{+\mathrm{R,L}} + \frac{\partial A'_{+\mathrm{R,L}}}{\partial z} \right) e^{i(\delta_z - i\sigma_z)z} \qquad \textbf{B.17a}$$

$$\frac{\partial A_{-\mathrm{R,L}}}{\partial z} = \left(-i(\delta_z - i\sigma_z) A'_{-\mathrm{R,L}} + \frac{\partial A'_{-\mathrm{R,L}}}{\partial z} \right) e^{-i(\delta_z - i\sigma_z)z} \qquad \textbf{B.17b}$$

$$\frac{\partial B_{\pm R}}{\partial \tau} = \left(i(\delta_\tau - i\sigma_\tau) B'_{\pm R} + \frac{\partial B'_{\pm R}}{\partial \tau} \right) e^{i(\delta_\tau - i\sigma_\tau)\tau} \qquad \textbf{B.17c}$$

$$\frac{\partial B_{\pm L}}{\partial \tau} = \left(-i(\delta_\tau - i\sigma_\tau) B'_{\pm L} + \frac{\partial B'_{\pm L}}{\partial \tau} \right) e^{-i(\delta_\tau - i\sigma_\tau)\tau} \qquad \textbf{B.17d}$$

which, on substitution into equations B.16a - B.16h gives:

$$\left(k_{zA} \left(i(\delta_z - i\sigma_z) A'_{+\mathrm{R}} + \frac{\partial A'_{+\mathrm{R}}}{\partial z} \right) + k_{cA} \frac{\partial A'_{+\mathrm{R}}}{\partial \tau} + \frac{i}{2} \frac{\partial^2 A'_{+\mathrm{R}}}{\partial \tau^2} + i \frac{k^2 \chi}{2 \ln(b_0 / a_0)} \left[\begin{array}{l} B'_{+\mathrm{R}} + B'_{+\mathrm{L}} \\ + B'_{-R} + B'_{-L} \end{array} \right] \right) = 0 \qquad \textbf{B.18a}$$

$$\left(k_{zA} \left(i(\delta_z - i\sigma_z) A'_{+\mathrm{L}} + \frac{\partial A'_{+\mathrm{L}}}{\partial z} \right) - k_{cA} \frac{\partial A'_{+\mathrm{L}}}{\partial \tau} + \frac{i}{2} \frac{\partial^2 A'_{+\mathrm{L}}}{\partial \tau^2} + i \frac{k^2 \chi}{2 \ln(b_0 / a_0)} \left[\begin{array}{l} B'_{+\mathrm{R}} + B'_{+\mathrm{L}} \\ + B'_{-R} + B'_{-L} \end{array} \right] \right) = 0 \qquad \textbf{B.18b}$$

$$\left(k_{zA} \left(i(\delta_z - i\sigma_z) A'_{-\mathrm{L}} - \frac{\partial A'_{-\mathrm{L}}}{\partial z} \right) - k_{cA} \frac{\partial A'_{-\mathrm{L}}}{\partial \tau} + \frac{i}{2} \frac{\partial^2 A'_{-\mathrm{L}}}{\partial \tau^2} + i \frac{k^2 \chi}{2 \ln(b_0 / a_0)} \left[\begin{array}{l} B'_{+\mathrm{R}} + B'_{+\mathrm{L}} \\ + B'_{-R} + B'_{-L} \end{array} \right] \right) = 0 \qquad \textbf{B.18c}$$

$$\left(k_{zA}\left(i(\delta_z - i\sigma_z)A'_{-\mathrm{R}} - \frac{\partial A'_{-\mathrm{R}}}{\partial z} \right) + k_{cA}\frac{\partial A'_{-\mathrm{R}}}{\partial \tau} + \frac{i}{2}\frac{\partial^2 A'_{-\mathrm{R}}}{\partial \tau^2} + i\frac{k^2\chi}{2\ln(b_0/a_0)}\begin{bmatrix} B'_{+\mathrm{R}} + B'_{+\mathrm{L}} \\ + B'_{-R} + B'_{-L} \end{bmatrix} \right) = 0 \qquad \textbf{B.18d}$$

$$\left(k_{zB}\frac{\partial B'_{+\mathrm{R}}}{\partial z} + k_{cB}\left(i(\delta_\tau - i\sigma_\tau)B'_{+\mathrm{R}} + \frac{\partial B'_{+\mathrm{R}}}{\partial \tau} \right) + \frac{i}{2}\frac{\partial^2 B'_{+\mathrm{R}}}{\partial z^2} + i\frac{k^2\chi}{2\ln(b_0/a_0)}\begin{bmatrix} A'_{+\mathrm{R}} + A'_{+\mathrm{L}} \\ + A'_{-\mathrm{R}} + A'_{-\mathrm{L}} \end{bmatrix} \right) = 0 \qquad \textbf{B.18e}$$

$$\left(k_{zB}\frac{\partial B'_{-\mathrm{R}}}{\partial z} - k_{cB}\left(i(\delta_\tau - i\sigma_\tau)B'_{-R} + \frac{\partial B'_{-R}}{\partial \tau} \right) - \frac{i}{2}\frac{\partial^2 B'_{-\mathrm{R}}}{\partial z^2} - i\frac{k^2\chi}{2\ln(b_0/a_0)}\begin{bmatrix} A'_{+\mathrm{R}} + A'_{+\mathrm{L}} \\ + A'_{-\mathrm{R}} + A'_{-\mathrm{L}} \end{bmatrix} \right) = 0 \qquad \textbf{B.18f}$$

$$\left(k_{zB}\frac{\partial B'_{-\mathrm{L}}}{\partial z} - k_{cB}\left(i(\delta_\tau - i\sigma_\tau)B'_{-L} - \frac{\partial B'_{-L}}{\partial \tau} \right) - \frac{i}{2}\frac{\partial^2 B'_{-\mathrm{L}}}{\partial z^2} - i\frac{k^2\chi}{2\ln(b_0/a_0)}\begin{bmatrix} A'_{+\mathrm{R}} + A'_{+\mathrm{L}} \\ + A'_{-\mathrm{R}} + A'_{-\mathrm{L}} \end{bmatrix} \right) = 0 \qquad \textbf{B.18g}$$

$$\left(k_{zB}\frac{\partial B'_{+\mathrm{L}}}{\partial z} + k_{cB}\left(i(\delta_\tau - i\sigma_\tau)B'_{+\mathrm{L}} - \frac{\partial B'_{+\mathrm{L}}}{\partial \tau} \right) + \frac{i}{2}\frac{\partial^2 B'_{+\mathrm{L}}}{\partial z^2} + i\frac{k^2\chi}{2\ln(b_0/a_0)}\begin{bmatrix} A'_{+\mathrm{R}} + A'_{+\mathrm{L}} \\ + A'_{-\mathrm{R}} + A'_{-\mathrm{L}} \end{bmatrix} \right) = 0 \qquad \textbf{B.18h}$$

which represent the wave equations for the partial-waves in the region of the reflector.

B.2 Calculation of the Dispersion Curve.

Accounting for the azimuthal structure of the wave-envelope, the partial wave amplitudes can be defined as:

$$A'_{\pm\mathrm{R}}(\tau, z) = \sum_{m' = -\infty}^{\infty} A_{\pm\mathrm{R}}^{m'}(z) e^{ik'_s \tau} \qquad \textbf{B.19a}$$

$$A'_{\pm L}(\tau, z) = \sum_{m'=-\infty}^{\infty} A^{m'}_{\pm L}(z) e^{-ik'_s \tau} \qquad \textbf{B.19b}$$

$$B'_{\pm R}(\tau, z) = \sum_{m'=-\infty}^{\infty} B^{m'}_{\pm R}(z) e^{ik'_s \tau} \qquad \textbf{B.19c}$$

$$B'_{\pm L}(\tau, z) = \sum_{m'=-\infty}^{\infty} B^{m'}_{\pm L}(z) e^{-ik'_s \tau} \qquad \textbf{B.19d}$$

where m' is the azimuthal variation of the wave envelope and $k'_s = m'/r_0$ relates to the aziuthal field structure of the m' eigenmode.

For an arbitrary value of m' this implies:

$$\frac{\partial A^{m'}_{+R,L}}{\partial z} + i\left[(\delta_z - i\sigma_z) + \frac{k_{cA}k'_c}{k_{zA}} - \frac{k'^2_c}{2k_{zA}}\right] A^{m'}_{+R,L} = -i\frac{k^2}{k_{zA}}\kappa[B^{m'}_{\pm R} + B^{m'}_{\pm L}] \qquad \textbf{B.20a}$$

$$\frac{\partial A^{m'}_{-R,L}}{\partial z} - i\left[(\delta_z - i\sigma_z) + \frac{k_{cA}k'_c}{k_{zA}} - \frac{k'^2_c}{2k_{zA}}\right] A^{m'}_{-R,L} = i\frac{k^2}{k_{zA}}\kappa[B^{m'}_{\pm R} + B^{m'}_{\pm L}] \qquad \textbf{B.20b}$$

$$\frac{k_{zB}}{k_{cB}}\frac{\partial B^{m'}_{+R,L}}{\partial z} + i[(\delta_\tau - i\sigma_\tau) + k'_c]B^{m'}_{+R,L} + \frac{i}{2k_{cB}}\frac{\partial^2 B^{m'}_{+R}}{\partial z^2} = -i\frac{k^2}{k_{cB}}\kappa[A^{m'}_{\pm R} + A^{m'}_{\pm L}] \qquad \textbf{B.20c}$$

$$\frac{k_{zB}}{k_{cB}}\frac{\partial B^{m'}_{-R,L}}{\partial z} - i[(\delta_\tau - i\sigma_\tau) + k'_c]B^{m'}_{-R,L} - \frac{i}{2k_{cB}}\frac{\partial^2 B^{m'}_{-R}}{\partial z^2} = i\frac{k^2}{k_{cB}}\kappa[A^{m'}_{\pm R} + A^{m'}_{\pm L}] \qquad \textbf{B.20d}$$

where:

$$\kappa = \frac{\chi}{4\ln(b_0/a_0)} \qquad \textbf{B.21}$$

is the coupling co-efficient.

If we now consider the wave amplitudes to be functions of the solutions of the eigenmodes, in a similar manner to the 1D Bragg reflector case:

$$A^{m'}_{+R,L}(z) = a_{+1R,1L}e^{-ik'_z z} + a_{+2R,2L}e^{ik'_z z} \qquad \textbf{B.22a}$$

$$A^{m'}_{-\mathrm{R,L}}(z) = a_{-1\mathrm{R},1\mathrm{L}}e^{-ik'_z z} + a_{-2\mathrm{R},2\mathrm{L}}e^{ik'_z z} \quad \textbf{B.22b}$$

$$B^{m'}_{+\mathrm{R,L}}(z) = b_{+1\mathrm{R},1\mathrm{L}}e^{-ik'_z z} + b_{+2\mathrm{R},2\mathrm{L}}e^{ik'_z z} \quad \textbf{B.22c}$$

$$B^{m'}_{-\mathrm{R,L}}(z) = b_{-1\mathrm{R},1\mathrm{L}}e^{-ik'_z z} + b_{-2\mathrm{R},2\mathrm{L}}e^{ik'_z z} \quad \textbf{B.22d}$$

the differential terms become:

$$\frac{\partial A^{m'}_{+\mathrm{R,L}}}{\partial z} = -ik'_z(a_{+1\mathrm{R},1\mathrm{L}}e^{-ik'_z z} - a_{+2\mathrm{R},2\mathrm{L}}e^{ik'_z z}) \quad \textbf{B.23a}$$

$$\frac{\partial A^{m'}_{-\mathrm{R,L}}}{\partial z} = -ik'_z(a_{-1\mathrm{R},1\mathrm{L}}e^{-ik'_z z} - a_{-2\mathrm{R},2\mathrm{L}}e^{ik'_z z}) \quad \textbf{B.23b}$$

$$\frac{\partial B^{m'}_{+\mathrm{R,L}}}{\partial z} = -ik'_z(b_{+1\mathrm{R},1\mathrm{L}}e^{-ik'_z z} - b_{+2\mathrm{R},2\mathrm{L}}e^{ik'_z z}) \quad \textbf{B.23c}$$

$$\frac{\partial B^{m'}_{-\mathrm{R,L}}}{\partial z} = -ik'_z(b_{-1\mathrm{R},1\mathrm{L}}e^{-ik'_z z} - b_{-2\mathrm{R},2\mathrm{L}}e^{ik'_z z}) \quad \textbf{B.23d}$$

$$\frac{\partial^2 B^{m'}_{+\mathrm{R,L}}}{\partial z^2} = -k'^2_z(b_{+1\mathrm{R},1\mathrm{L}}e^{-ik'_z z} + b_{+2\mathrm{R},2\mathrm{L}}e^{ik'_z z}) \quad \textbf{B.23e}$$

$$\frac{\partial^2 B^{m'}_{-\mathrm{R,L}}}{\partial z^2} = -k'^2_z(b_{-1\mathrm{R},1\mathrm{L}}e^{-ik'_z z} + b_{-2\mathrm{R},2\mathrm{L}}e^{ik'_z z}) \quad \textbf{B.23f}$$

Substitution into equations B.20a-B.20d yields:

$$\begin{pmatrix} \left(\left[(\delta_z - i\sigma_z) + \frac{k_{cA}k'_c}{k_{zA}} - \frac{k'^2_c}{2k_{zA}} - k'_z\right]a_{+1\mathrm{R},1\mathrm{L}} + \frac{k^2}{k_{zA}}\kappa b_{\pm 1\mathrm{R},1\mathrm{L}}\right)e^{-ik'_z z} \\ + \left(\left[(\delta_z - i\sigma_z) + \frac{k_{cA}k'_c}{k_{zA}} - \frac{k'^2_c}{2k_{zA}} + k'_z\right]a_{+2\mathrm{R},2\mathrm{L}} + \frac{k^2}{k_{zA}}\kappa b_{\pm 2\mathrm{R},2\mathrm{L}}\right)e^{ik'_z z} \end{pmatrix} = 0 \quad \textbf{B.24a}$$

$$\begin{aligned} &\left(\left[(\delta_z - i\sigma_z) + \frac{k_{cA}k'_c}{k_{zA}} - \frac{k'^2_c}{2k_{zA}} + k'_z\right]a_{-1\mathrm{R},1\mathrm{L}} + \frac{k^2}{k_{zA}}\kappa b_{\pm 1\mathrm{R},1\mathrm{L}}\right)e^{-ik'_z z} \\ &+ \left(\left[(\delta_z - i\sigma_z) + \frac{k_{cA}k'_c}{k_{zA}} - \frac{k'^2_c}{2k_{zA}} - k'_z\right]a_{-2\mathrm{R},2\mathrm{L}} + \frac{k^2}{k_{zA}}\kappa b_{\pm 2\mathrm{R},2\mathrm{L}}\right)e^{ik'_z z} \end{aligned} = 0 \quad \textbf{B.24b}$$

$$\left(\left[(\delta_\tau - i\sigma_\tau) + k'_c - \frac{k'_z}{k_{cB}}\left(k_{zB} + \frac{k'_z}{2}\right)\right] b_{+1R,1L} + \frac{k^2}{k_{cB}}\kappa a_{\pm 1R,1L}\right) e^{-ik'_z z}$$
$$+ \left(\left[(\delta_\tau - i\sigma_\tau) + k'_c + \frac{k'_z k_{zB}}{k_{cB}}\left(k_{zB} - \frac{k'_z}{2}\right)\right] b_{+2R,2L} + \frac{k^2}{k_{cB}}\kappa a_{\pm 2R,2L}\right) e^{ik'_z z} = 0 \qquad \textbf{B.24c}$$

$$\left(\left[(\delta_\tau - i\sigma_\tau) + k'_c + \frac{k'_z}{k_{cB}}\left(k_{zB} - \frac{k'_z}{2}\right)\right] b_{-1R,1L} + \frac{k^2}{k_{cB}}\kappa a_{\pm 1R,1L}\right) e^{-ik'_z z}$$
$$+ \left(\left[(\delta_\tau - i\sigma_\tau) + k'_c - \frac{k'_z}{k_{cB}}\left(k_{zB} + \frac{k'_z}{2}\right)\right] b_{-2R,2L} + \frac{k^2}{k_{cB}}\kappa a_{\pm 2R,2L}\right) e^{ik'_z z} = 0 \qquad \textbf{B.24d}$$

Setting

$a_{+1} = a_{+1R} + a_{+1L}$, $a_{-1} = a_{-1L} + a_{-1R}$, $a_{+2} = a_{+2R} + a_{+2L}$, $a_{-2} = a_{-2L} + a_{-2R}$,
$b_{+1} = b_{+1R} + b_{+1L}$, $b_{-1} = b_{-1R} + b_{-1L}$, $b_{+2} = b_{+2R} + b_{+2L}$, $b_{-2} = b_{-2R} + b_{-2L}$

and noting that the exponental terms in equations B.24a-B.24d cannot equal zero:

$$[2k_{zA}[(\delta_z - i\sigma_z) - k'_z] + k'_c(2k_{cA} - k'_c)]a_{+1} = -2k^2\kappa(b_{+1} + b_{-1}) \qquad \textbf{B.25a}$$

$$[2k_{zA}[(\delta_z - i\sigma_z) + k'_z] + k'_c(2k_{cA} - k'_c)]a_{+2} = -2k^2\kappa(b_{+2} + b_{-2}) \qquad \textbf{B.25b}$$

$$[2k_{zA}[(\delta_z - i\sigma_z) + k'_z] + k'_c(2k_{cA} - k'_c)]a_{-1} = -2k^2\kappa(b_{+1} + b_{-1}) \qquad \textbf{B.25c}$$

$$[2k_{zA}[(\delta_z - i\sigma_z) - k'_z] + k'_c(2k_{cA} - k'_c)]a_{-2} = -2k^2\kappa(b_{+2} + b_{-2}) \qquad \textbf{B.25d}$$

$$[2k_{cB}[(\delta_\tau - i\sigma_\tau) + k'_c] - k'_z(2k_{zB} + k'_z)]b_{+1} = -2k^2\kappa(a_{+1} + a_{-1}) \qquad \textbf{B.25e}$$

$$[2k_{cB}[(\delta_\tau - i\sigma_\tau) + k'_c] + k'_z(2k_{zB} - k'_z)]b_{+2} = -2k^2\kappa(a_{+2} + a_{-2}) \qquad \textbf{B.25f}$$

$$[2k_{cB}[(\delta_\tau - i\sigma_\tau) + k'_c] + k'_z(2k_{zB} - k'_z)]b_{-1} = -2k^2\kappa(a_{+1} + a_{-1}) \qquad \textbf{B.25g}$$

$$[2k_{cB}[(\delta_\tau - i\sigma_\tau) + k'_c] - k'_z(2k_{zB} + k'_z)]b_{-2} = -2k^2\kappa(a_{+2} + a_{-2}) \qquad \textbf{B.25h}$$

Setting:

$$q_1 = 2k_{zA}[(\delta_z - i\sigma_z) - k'_z] + k'_c(2k_{cA} - k'_c) \quad \textbf{B.26a}$$

$$q_2 = 2k_{zA}[(\delta_z - i\sigma_z) + k'_z] + k'_c(2k_{cA} - k'_c) \quad \textbf{B.26b}$$

$$q_3 = 2k_{cB}[(\delta_\tau - i\sigma_\tau) + k'_c] - k'_z(2k_{zB} + k'_z) \quad \textbf{B.26c}$$

$$q_4 = 2k_{cB}[(\delta_\tau - i\sigma_\tau) + k'_c] + k'_z(2k_{zB} - k'_z) \quad \textbf{B.26d}$$

simplifies equations B.25b-B.25h to:

$$a_{+1} = -\frac{2k^2\kappa}{q_1}(b_{+1} + b_{-1}) \quad \textbf{B.27a}$$

$$a_{+2} = -\frac{2k^2\kappa}{q_2}(b_{+2} + b_{-2}) \quad \textbf{B.27b}$$

$$a_{-1} = -\frac{2k^2\kappa}{q_2}(b_{+1} + b_{-1}) \quad \textbf{B.27c}$$

$$a_{-2} = -\frac{2k^2\kappa}{q_1}(b_{+2} + b_{-2}) \quad \textbf{B.27d}$$

$$b_{+1} = -\frac{2k^2\kappa}{q_3}(a_{+1} + a_{-1}) \quad \textbf{B.27e}$$

$$b_{+2} = -\frac{2k^2\kappa}{q_4}(a_{+2} + a_{-2}) \quad \textbf{B.27f}$$

$$b_{-1} = -\frac{2k^2\kappa}{q_4}(a_{+1} + a_{-1}) \quad \textbf{B.27g}$$

$$b_{-2} = -\frac{2k^2\kappa}{q_3}(a_{+2} + a_{-2}) \quad \textbf{B.27h}$$

giving:

$$b_{-1} = \frac{q_3}{q_4}b_{+1},\ b_{-2} = \frac{q_4}{q_3}b_{+2},\ a_{-1} = \frac{q_1}{q_2}a_{+1},\ a_{-2} = \frac{q_2}{q_1}a_{+2}$$

and so:

$$a_{+1} = -\frac{2k^2\kappa}{q_1 q_4}(q_4 + q_3)b_{+1} \qquad \textbf{B.28a}$$

$$a_{+2} = -\frac{2k^2\kappa}{q_2 q_3}(q_3 + q_4)b_{+2} \qquad \textbf{B.28b}$$

$$b_{+1} = -\frac{2k^2\kappa}{q_3 q_2}(q_2 + q_1)a_{+1} \qquad \textbf{B.28c}$$

$$b_{+2} = -\frac{2k^2\kappa}{q_4 q_1}(q_1 + q_2)a_{+2} \qquad \textbf{B.28d}$$

which leads to the relation:

$$q_1 q_2 q_3 q_4 = 4k^4\kappa^2(q_1 + q_2)(q_3 + q_4) \qquad \textbf{B.29}$$

If we now consider the difference between δ_z and δ_τ as:

$$\delta_\tau = \delta_z + \Delta k - \Delta h + i\Delta\sigma \qquad \textbf{B.30}$$

where $\Delta k = k_c - k_z$, $\Delta\sigma = \sigma_\tau - \sigma_z$, the LHS of equation B.29 gives:

$$q_1 q_2 q_3 q_4 = \begin{pmatrix} \delta_z^4(p_1 p_4) + \delta_z^3(p_1 p_5 + p_2 p_4) + \delta_z^2(p_1 p_6 + p_2 p_5 + p_3 p_4) \\ + \delta_z(p_2 p_6 + p_3 p_5) + p_3 p_6 \end{pmatrix} \qquad \textbf{B.31}$$

where:

$$p_1 = k_{zA}^2 \qquad \textbf{B.32a}$$

$$p_2 = k_{zA}k'_c(2k_{cA} - k'_c) - 2i\sigma_z k_{zA}^2 \qquad \textbf{B.32b}$$

$$p_3 = 2i\sigma_z k_{zA}k'_c\left(\frac{k'_c}{2} - k_{cA}\right) - k_{cA}k'^2_c\left(\frac{4k_{cA} - k'_c(2 + k'_c)}{4}\right) - k_{zA}^2(k'^2_z + \sigma_z^2) \qquad \textbf{B.32c}$$

$$p_4 = k_{cB}^2 \qquad \textbf{B.32d}$$

$$p_5 = k_{cB}^2[k'_c - i\sigma_\tau + 2(\Delta k - \Delta h + i\Delta\sigma)] - k_{cB}k'^2_z \quad \textbf{B.32e}$$

$$p_6 = \begin{array}{c} k_{cB}\left[k_{cB}(k'^2_c - \sigma_\tau^2) + k'_z\left(\frac{2k_{zB} - k'_z}{2}\right)\right] \\ + [\Delta k - \Delta h + i\Delta\sigma][k_{cB}^2(k'_c - i\sigma_\tau + [\Delta k - \Delta h + i\Delta\sigma]) - k_{cB}k'^2_z] \end{array} \quad \textbf{B.32f}$$

and the RHS of equation B.29 gives:

$$4k^4\kappa^2(q_1 + q_2)(q_3 + q_4) = 4k^4\kappa^2(\delta_z^2 p_7 + \delta_z p_8 + p_9) \quad \textbf{B.33}$$

where:

$$p_7 = 4k_{zA}k_{cB} \quad \textbf{B.34a}$$

$$p_8 = \begin{array}{c} 2k_{zA}(2k_{cB}[\Delta k - \Delta h - i\sigma_z + k'_c] - k'^2_z) \\ + 2k_{cB}[k'_c(2k_{cA} - k'_c) - 2i\sigma_z k_{zA}] \end{array} \quad \textbf{B.34b}$$

$$p_9 = [k'_c(2k_{cA} - k'_c) - 2i\sigma_z k_{zA}](2k_{cB}[\Delta k - \Delta h - i\sigma_z + k'_c] - k'^2_z) \quad \textbf{B.34c}$$

which gives a quartic equation of the form:

$$\left(\begin{array}{c} \delta_z^4(p_1p_4) + \delta_z^3(p_1p_5 + p_2p_4) \\ + \delta_z^2(p_1p_6 + p_2p_5 + p_3p_4 - 4k^4\kappa^2 p_7) \\ + \delta_z(p_2p_6 + p_3p_5 - 4k^4\kappa^2 p_8) + p_3p_6 - 4k^4\kappa^2 p_9 \end{array}\right) = 0 \quad \textbf{B.35}$$

which yields four roots following numerical solving. Plots of these roots can be seen in Figures 3.14 - 3.15.

B.3 Reflection Coefficient in 2D Bragg Reflectors.

Regarding diffractive effects as being negligible in calculation of the reflection coefficient, equations B.18a-B.18h reduce to:

$$\frac{\partial A'_+}{\partial z} + i(\delta_z - i\sigma_z)A'_+ + ik\kappa(B'_+ + B'_-) = 0 \quad \textbf{B.36a}$$

$$\frac{\partial A'_-}{\partial z} - i(\delta_z - i\sigma_z)A'_- - ik\kappa(B'_+ + B'_-) = 0 \quad \textbf{B.36b}$$

$$\frac{\partial B'_{+}}{\partial \tau} + i(\delta_\tau - i\sigma_\tau)B'_{+} + ik\kappa(A'_{+} + A'_{-}) = 0 \qquad \textbf{B.36c}$$

$$\frac{\partial B'_{-}}{\partial \tau} - i(\delta_\tau - i\sigma_\tau)B'_{-} - ik\kappa(A'_{+} + A'_{-}) = 0 \qquad \textbf{B.36d}$$

where $B'_{+} = B'_{+\mathrm{R}} + B_{+\mathrm{L}}$ and $B'_{-} = B'_{-\mathrm{R}} + B'_{-\mathrm{L}}$, taking $k_{zA} \approx h_z$ $(k_{zB} \approx 0)$ and $k_{cB} \approx h_\tau$ $(k_{cA} \approx 0)$.

One may then consider the wave-amplitudes, as functions of the azimuthal structure of the eigenmodes, in the simplified form:

$$A'_{\pm}(\tau, z) = \sum_{m' = -\infty}^{\infty} A_{\pm}^{m'}(z) e^{ik'_s \tau} \qquad \textbf{B.37a}$$

$$B'_{\pm}(\tau, z) = \sum_{m' = -\infty}^{\infty} B_{\pm}^{m'}(z) e^{ik'_s \tau} \qquad \textbf{B.37b}$$

yielding:

$$\frac{\partial A_{+}^{m'}}{\partial z} + i(\delta_z - i\sigma_z)A_{+}^{m'} + ik\kappa(B_{+}^{m'} + B_{-}^{m'}) = 0 \qquad \textbf{B.38a}$$

$$\frac{\partial A_{-}^{m'}}{\partial z} - i(\delta_z - i\sigma_z)A_{-}^{m'} - ik\kappa(B_{+}^{m'} + B_{-}^{m'}) = 0 \qquad \textbf{B.38b}$$

$$B_{+}^{m'} = -\frac{k\kappa(A_{+}^{m'} + A_{-}^{m'})}{(\delta_\tau - i\sigma_\tau + k'_s)} \qquad \textbf{B.38c}$$

$$B_{-}^{m'} = -\frac{k\kappa(A_{+}^{m'} + A_{-}^{m'})}{(\delta_\tau - i\sigma_\tau - k'_s)} \qquad \textbf{B.38d}$$

which reduces to:

$$\frac{\partial A_{+}^{m'}}{\partial z} + i(\delta_z - i\sigma_z)A_{+}^{m'} - 2i\frac{k^2\kappa^2}{(\delta_\tau - i\sigma_\tau)^2 - k'^2_s}(A_{+}^{m'} + A_{-}^{m'}) = 0 \qquad \textbf{B.39a}$$

$$\frac{\partial A_{-}^{m'}}{\partial z} - i(\delta_z - i\sigma_z)A_{-}^{m'} + 2i\frac{k^2\kappa^2}{(\delta_\tau - i\sigma_\tau)^2 - k'^2_s}(A_{+}^{m'} + A_{-}^{m'}) \;=\; 0 \qquad \textbf{B.39b}$$

We may now consider the remaining partial-wave amplitudes as functions of the solutions of the eigenmodes as:

$$A_{+}^{m'} \;=\; a_{+1}e^{\Lambda z} + a_{+2}e^{-\Lambda z} \qquad \textbf{B.40a}$$

$$A_{-}^{m'} \;=\; a_{-1}e^{\Lambda z} + a_{-2}e^{-\Lambda z} \qquad \textbf{B.40b}$$

giving:

$$\begin{aligned}&\Lambda(a_{+1}e^{\Lambda z} - a_{+2}e^{-\Lambda z}) + i(\delta_z - i\sigma_z)(a_{+1}e^{\Lambda z} + a_{+2}e^{-\Lambda z})\\ &-2i\frac{k^2\kappa^2}{(\delta_\tau - i\sigma_\tau)^2 - k'^2_s}([a_{+1} + a_{-1}]e^{\Lambda z} + [a_{+2} + a_{-2}]e^{-\Lambda z}) \;=\; 0\end{aligned} \qquad \textbf{B.41a}$$

$$\begin{aligned}&\Lambda(a_{-1}e^{\Lambda z} - a_{-2}e^{-\Lambda z}) - i(\delta_z - i\sigma_z)(a_{-1}e^{\Lambda z} + a_{-2}e^{-\Lambda z})\\ &+2i\frac{k^2\kappa^2}{(\delta_\tau - i\sigma_\tau)^2 - k'^2_s}([a_{+1} + a_{-1}]e^{\Lambda z} + [a_{+2} + a_{-2}]e^{-\Lambda z}) \;=\; 0\end{aligned} \qquad \textbf{B.41b}$$

which, as the exponential terms cannot equal zero, give the relations:

$$a_{+1}[([\delta_\tau - i\sigma_\tau]^2 - k'^2_s)(\Lambda + i[\delta_z - i\sigma_z]) - 2ik^2\kappa^2] \;=\; 2ik^2\kappa^2 a_{-1} \qquad \textbf{B.42a}$$

$$a_{+2}[([\delta_\tau - i\sigma_\tau]^2 - k'^2_s)(i[\delta_z - i\sigma_z] - \Lambda) - 2ik^2\kappa^2] \;=\; 2ik^2\kappa^2 a_{-2} \qquad \textbf{B.42b}$$

$$a_{-1}[([\delta_\tau - i\sigma_\tau]^2 - k'^2_s)(i[\delta_z - i\sigma_z] - \Lambda) - 2ik^2\kappa^2] \;=\; 2ik^2\kappa^2 a_{+1} \qquad \textbf{B.42c}$$

$$a_{-2}[(\Lambda + i[\delta_z - i\sigma_z])([\delta_\tau - i\sigma_\tau]^2 - k'^2_s) - 2ik^2\kappa^2] \;=\; 2ik^2\kappa^2 a_{+2} \qquad \textbf{B.42d}$$

and setting:

$$q_1 \;=\; [([\delta_\tau - i\sigma_\tau]^2 - k'^2_s)(\Lambda + i[\delta_z - i\sigma_z]) - 2ik^2\kappa^2] \qquad \textbf{B.43a}$$

$$q_2 \;=\; [([\delta_\tau - i\sigma_\tau]^2 - k'^2_s)(i[\delta_z - i\sigma_z] - \Lambda) - 2ik^2\kappa^2] \qquad \textbf{B.43b}$$

gives $a_{+1} = \frac{2ik^2\kappa^2}{q_1}a_{-1}$, $a_{+2} = \frac{2ik^2\kappa^2}{q_2}a_{-2}$ and equations B.40a-B.40b the form:

$$A_+^{m'}(z) = \frac{2ik^2\kappa^2}{q_1}a_{-1}e^{\Lambda z} + \frac{2ik^2\kappa^2}{q_2}a_{-2}e^{-\Lambda z} \quad \textbf{B.44a}$$

$$A_-^{m'}(z) = a_{-1}e^{\Lambda z} + a_{-2}e^{-\Lambda z} \quad \textbf{B.44b}$$

Noting the boundary conditions $A_+^{m'}(z)\big|_{z=0} = 1$, $A_-^{m'}(z)\big|_{z=l_{2D}} = 0$, where l_{2D} is the length of the corrugation:

$$a_{-1} = -a_{-2}e^{-2\Lambda l_{2D}} \quad \textbf{B.45}$$

and so:

$$A_+^{m'}(z) = 2i\frac{k^2\kappa^2}{q_1q_2}(q_1e^{-\Lambda z} - q_2e^{\Lambda(z-2l_{2D})})a_{-2} \quad \textbf{B.46a}$$

$$A_-^{m'}(z) = a_{-2}(e^{-\Lambda z} - e^{\Lambda(z-2l_{2D})}) \quad \textbf{B.46b}$$

The reflection co-efficient can be determined as:

$$|R(z)| = \left|\frac{A_-^{m'}(z)}{A_+^{m'}(z)}\right| = \left|-i\frac{q_1q_2(e^{\Lambda(z-2l_{2D})} - e^{-\Lambda z})}{2k^2\kappa^2(q_1e^{\Lambda(z-2l_{2D})} - q_2e^{-\Lambda z})}\right| \quad \textbf{B.47}$$

Multiplying through by $e^{l_{2D}}/e^{l_{2D}}$:

$$|R(z)| = \left|-i\frac{q_1q_2(e^{\Lambda(z-l_{2D})} - e^{-\Lambda(z-l_{2D})})}{2k^2\kappa^2(q_1e^{\Lambda(z-l_{2D})} - q_2e^{-\Lambda(z-l_{2D})})}\right| \quad \textbf{B.48}$$

and using the relations $e^{\pm x} = \cosh(x) \pm \sinh(x)$:

$$|R(z)| = \left|-i\frac{q_1q_2\sinh(\Lambda(z-l_{2D}))}{2k^2\kappa^2[(q_1-q_2)\cosh[\Lambda(z-l_{2D})] + (q_1+q_2)\sinh(\Lambda(z-l_{2D}))]}\right| \quad \textbf{B.49}$$

Finally, division by $\sinh(\Lambda(z-l_{2D}))$ yields:

$$|R(z)| = \left| -i \frac{q_1 q_2}{2k^2\kappa^2[(q_1-q_2)\coth(\Lambda(z-l_{2D}))+q_1+q_2]} \right| \quad \textbf{B.50}$$

with the magnitude of the transmission co-efficient ($|T(z)|$) obtained via:

$$|T|^2 = 1-|R|^2-|\Omega|^2 \quad \textbf{B.51}$$

where Ω is the total system losses as before.

Appendix C: Calibration of the High-Voltage Power Supply

Proper calibration of the FEM power supply was important for two reasons. Firstly, for proper operation of the FEM experiment the power supply must be capable of delivering reproducible pulses for a given set of starting conditions and secondly, misuse of such a high-voltage (potentially $1.5MV$) power supply may lead to permanent damage of the constituent components, many of which cannot be easily replaced. The inclusion of additional diagnostics, for the $3.5kA$ 2D-1D FEM experimental run, allowed for monitoring of the electron accelerating potential at three key stages as it evolved through the FEM power supply. A simple resistive divider probe monitored the discharge voltage from the Marx-bank (c.f. Section 6.2.1.1) while the potential of the transmission line was monitored using a capacitive divider probe located just before the connection to the output spark-gap (c.f. Section 6.2.2). The shaped voltage pulse, applied across the diode by the transmission line, was monitored using a purpose built non-shielded resistive divider probe (c.f. Section 6.2.1.3).

The traces recorded for a typical voltage pulse, as it evolved through the power supply, are given in Figure C.1 The charging voltage on the Marx-bank capacitors was $50kV$.

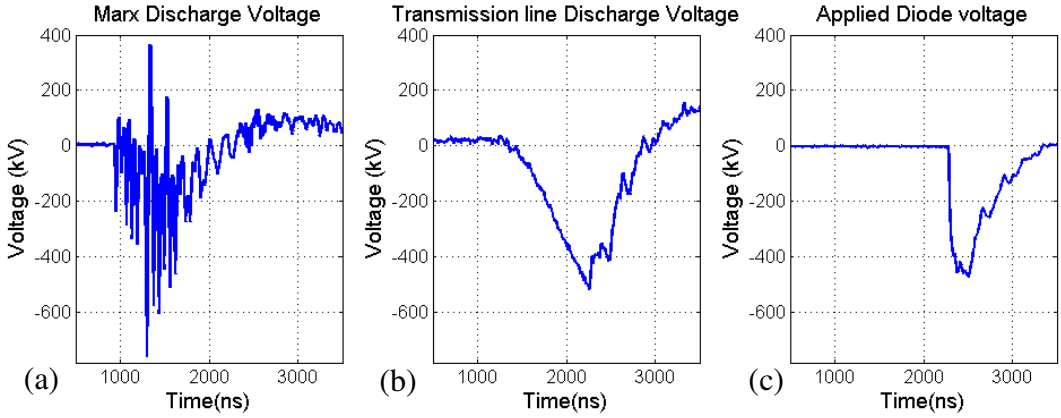

Figure C.1: Shows (a) the output voltage from the Marx-bank (b) the voltage discharge from the transmission line (c) the voltage applied to the gun diode for a charging voltage of *50kV* per capacitor on the Marx-bank.

Coupling of noise, from the closing spark-gaps of the Marx-bank to the co-axial lead of the probe, resulted in the distortion seen in Figure C.1a. This prevents determination of the absolute magnitude of the Marx-bank discharge pulse, but does not render the diagnostic useless, as the positive swing of the voltage trace can be monitored to improve calibration of the power supply.

Comparing Figures C.1a and C.1b, it can be seen that the positive voltage swing on the Marx-bank diagnostic corresponds to the point where the output spark-gap closes and transmission line begins to discharge to the diode. This indicates the magnitude of the reflected pulse incident on the Marx-bank, tied directly to the breaking voltage of the output spark-gap, i.e. as the pressure in the spark-gap is increased to its optimum level, for a given potential on the transmission line, the magnitude of the reflected pulse can be seen to decrease at the Marx-bank.

The traces shown in Figure C.2 correspond to a set of Marx-bank discharges, all charged at $50kV$ per capacitor, with the pressure on the output spark-gap increased by $1Bar$ each time. Figures C.3 and C.4 show the corresponding pulses recorded using the transmission line and diode probes respectively:

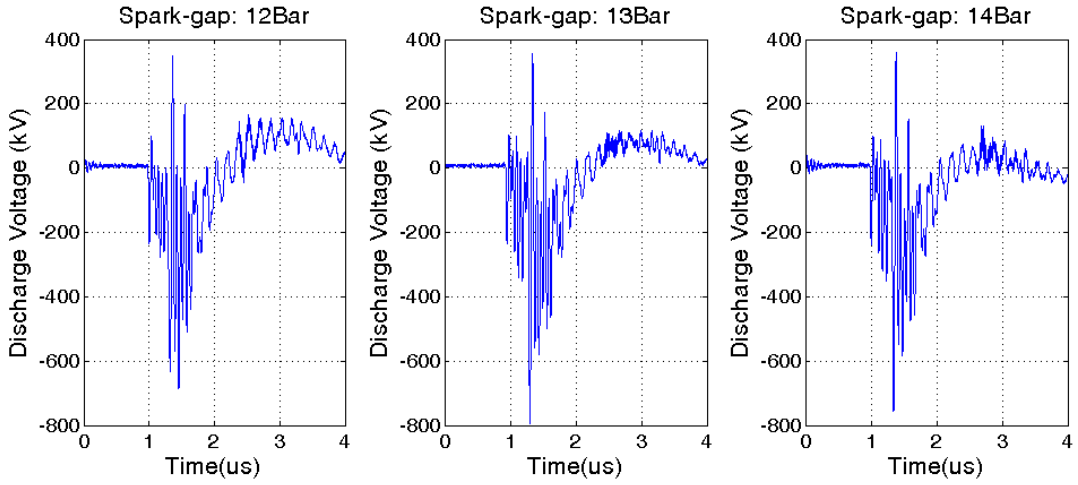

Figure C.2: Shows a set of traces for the Marx-bank discharge, recorded for different pressures of Nitrogen gas in the output spark-gap of the transmission line.

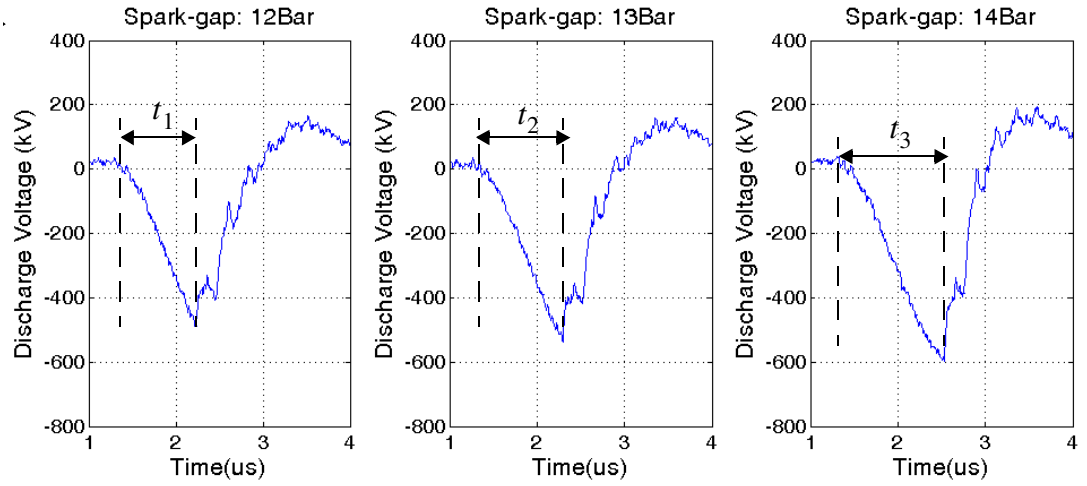

Figure C.3: Shows the voltage traces, recorded using the capacitive probe on the transmission line, corresponding to the Marx-bank discharge traces of Figure C.2. The rise time (charging time until the output spark-gap closed) in each case is noted.

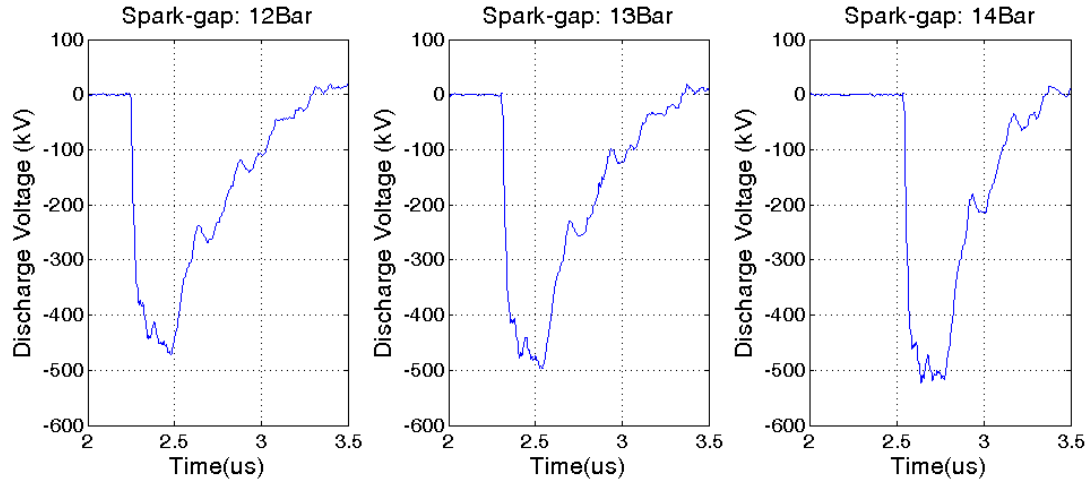

Figure C.4: Shows the applied diode potentials corresponding to the Marx-bank and transmission line discharges shown in Figures C.2 and C.3 respectively.

Regarding Figures C.2, C.3 and C.4 as a whole, the influence of the output spark-gap pressure on the potential imposed across the gun diode can be seen to be quite significant; as the spark-gap pressure increased the rise-time of the transmission line (that is; the time over which the transmission line is charged before the output spark-gap closes) can be seen to increase (compare $t_{1,2,3}$ in Figure C.3) with a corresponding decrease in the amplitude of the reflected pulses seen at the Marx-bank.

Improvements in the diode pulse can also be observed with increasing spark-gap pressure, specifically in the absolute magnitude and in over-all pulse shape; the stepped decay of the pulse reduces.

If one compares Figures C.2a &b with Figures C.3a & b, it can be seen that the more readily identifiable trend is offered by measurement of the reflected pulse on the Marx-bank diagnostic. Monitoring of the diode pulse for calibration purposes was discounted for much the same reason as monitoring of the transmission line diagnostic.

In calibrating the power supply, using the Marx-bank diagnostic, the following steps were followed:

- Before charging of the Mark-bank both the Marx-bank spark-gap column and the output spark-gap of the transmission line were vented, then pressurised with fresh, pure, Nitrogen gas. The pressures in both cases were allowed to settle to the desired value and were controlled to ~$\pm 10\%$.
- For a given charging voltage on the Marx-bank capacitors the pressure on the output spark-gap was set $2-3bar$ below that expected for optimum operation, with the pressure increased by $0.25-0.5bar$ on a shot by shot basis until the reflected pulse seen on the Marx diagnostic had the desired profile (see Fig. C.2c).
- When the reflected pulse observed in the Marx diagnostic was observed to be minimized, but still observable, the output spark-gap pressure was recorded and checked for consistency.

It should be noted that in calibrating the power supply the aim was not to completely remove the reflected pulse seen at the Marx-bank, only to minimise it. If the pressure on the output spark-gap had been increased beyond $14bar$ (for a charging voltage of $50kV$), say to $16bar$, the output spark-gap would fail to close, resulting in the full discharge voltage from the Marx-bank being reflected back to the source. The Marx-bank is protected, to a degree, from reflected pulses by a set of dump-resistors ($R4$ in Figure 5.2) which provide a preferential route to ground compared to the Marx capacitor stack, however the magnitude of the pulse in this case carries with it a risk of a sizeable mechanical shock wave, risking serious damage to the Marx-bank

components. By monitoring the size of the reflected pulse on the Marx-bank diagnostic, a balance can therefore be found where the reflected pulse is minimised but maintained.

In regards to the discharge from the transmission-line (see FigureC.3), when the pressure of the output spark-gap is set correctly, the peak voltage (denoting the breaking voltage of the output spark-gap) is a good approximation of the peak discharge voltage of the Marx-bank, allowing some monitoring of this value despite the noise seen on the Marx diagnostic itself.

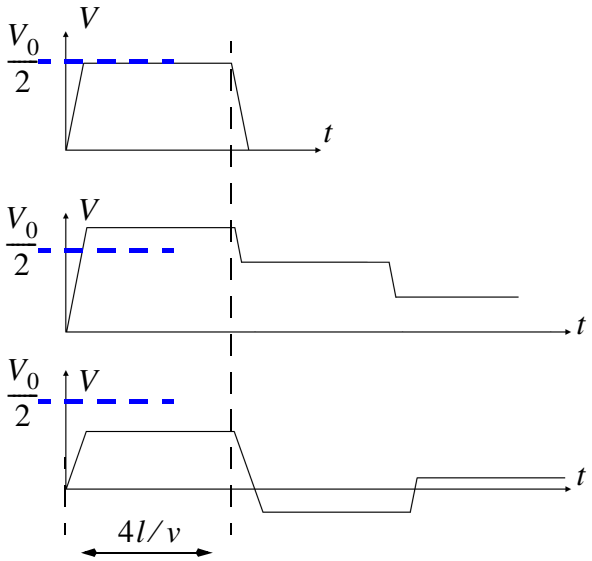

Figure C.5: Shows schematic pulse decays for (a) $Z_0 = Z_L$, (b) $Z_0<Z_L$, (c) $Z_0>Z_L$, where $V_0/2$ is the matched peak output voltage, l is the physical line length and v is the velocity of the pulse through the filling medium of the line.

In addition to the changes in peak voltage seen in Figure C.4, changes in the definition of the trailing edge to the pulse can be observed, indicating the impedance presented by the load was dependent on both the matching resistors and the pressure of output spark-gap, with the effect due to the resistors dominating as the optimum spark-gap pressure was approached. A stepped discharge was expected in this diagnostic as the load (Z_L) and line (Z_0) impedances were deliberately miss-matched to provide $> V_0/2$ across the diode, reducing the charging voltage required on the Marx-bank capacitors. The dependence of the transmission line pulse on the relation between Z_0 and Z_L is presented in Figure C.5.

Authors Publications.